A University of Sussex DPhil thesis

Available online via Sussex Research Online:

http://sro.sussex.ac.uk/

This thesis is protected by copyright which belongs to the author.

This thesis cannot be reproduced or quoted extensively from without first obtaining permission in writing from the Author

The content must not be changed in any way or sold commercially in any format or medium without the formal permission of the Author

When referring to this work, full bibliographic details including the author, title, awarding institution and date of the thesis must be given

Please visit Sussex Research Online for more information and further details

Photoelectrochemical Water Splitting and Gas Ionisation Sensing Using Metal Oxide Nanostructures

By

Wei Cheat Lee

A Thesis Submitted for the Degree of Doctor of Philosophy

School of Life Sciences

University of Sussex

June 2015

Declaration

I hereby declare that this work has not been submitted in any substance to another University for the award of any other degree or other academic or professional distinction.

Signature:

Wei Cheat Lee

Acknowledgements

First of all, I would like to express my sincere gratitude to my main supervisor, Dr Qiao Chen for his invaluable support and guidance whilst completing my research.

I would also like to thank my co-supervisor, Dr Mark Osborne for his support and helpful advice throughout my time at Sussex.

I would like to thank Public Service Department of Malaysia for giving me this golden opportunity to pursue my PhD study at the University of Sussex. I hope my work will benefit my country in the future.

I would like to express my special thanks to my amazing and understanding nano group members, Yuanxing Fang, Giacomo Canciani, Brnyia Alwhshe, Thomas Draper, Dr Rantej Kler, Dr Ali Shahroozi and Dr Zainab Abdullah. I would like to acknowledge the former MChem students, Joshua Fellowes, Christy Tuohy, Anna Crosby, Edward Hills, Charles Readman, Samuel Pearce and Thomas Samuels, for their assistance in our group during their MChem projects.

I am thankful to Alex Burns and Barry Jackson for their help in constructing the gas ionisation sensor setup. Many thanks to Mike Henry, Chris Dadswell and Fran Chick for their help in the teaching lab.

Last but not least, I would especially like to thank my family and my closest friends for their love, support and continued encouragement!

University of Sussex

Wei Cheat Lee

Doctor of Philosophy

Photoelectrochemical Water Splitting and Gas Ionisation Sensing Using Metal Oxide Nanostructures

Summary

Energy harvesting directly from sunlight has attracted tremendous attention owing to its great potential for low-cost and clean hydrogen production. However, the current photoconversion efficiency from nanostructured metal oxides remains low due to a number of factors, such as low surface area, limited light absorption, poor electron mobility and high electron-hole recombination. In this research, a number of approaches have been carried out to overcome these difficulties.

Firstly, changing the morphology of nanomaterials will help to increase the effective surface area of the photoanodes. ZnO nanotubes were prepared and the photoelectrochemical measurements revealed an efficiency of 3 times higher than their nanorod counterparts. In addition, the combination of ZnO nanorods with a 3D metal substrate, stainless steel mesh, showed a further enhancement in the water splitting efficiency by two-fold when compared with that on a planar substrate.

Secondly, the hybridisation of two different metal oxides was studied by creating a heterojunction to improve the charge separation, extending the light absorption and increasing the total surface area of the electrode. In this work, both

urchin-like ZnO nanorod arrays on TiO_2 hollow hemispheres and 1D $BiVO_4$/ZnO nanorod films displayed synergistic enhancement in photoelectrochemical water splitting efficiency.

Thirdly, doped ZnO nanostructures with different optical and/or electrical properties were tailored for photoelectrochemical water splitting and gas ionisation sensing applications. The photoelectrochemical water splitting performances of the doped ZnO nanostructures was improved by at least 27% due to increased light absorption. Conductive Y-doped ZnO nanorods were prepared and applied in gas ionisation sensor application. The measurements revealed that both the selectivity and sensitivity of Y-doped ZnO nanorods were enhanced with respect to undoped ZnO nanorods. Furthermore, the effect of UV illumination on gas sensitivity was also investigated.

In summary, different approaches and namomaterials have been adapted and demonstrated in this thesis, for the design of specific photoanodes/electrodes for specific applications.

Table of Contents

List of Abbreviations

α	Absorption coefficient
h	Planck's constant [6.63×10^{34} J/s]
v	Frequency of light
σ	Conductivity
ρ	Resistivity
η	Photoconversion efficiency
τ	Transient time constant
h^+	hole
e^-	electron
0D	Zero dimensional
1D	One dimensional
1L	1 layer of M60mW33
2D	Two dimensional
2L	2 layers of M60mW33
3D	Three dimensional
3L	3 layers of M60mW33
4L	4 layers of M60mW33
AC	Alternating current
Ag/AgCl	Silver/silver chloride reference electrode
AM1.5 G	Air mass 1.5 global
ATR–FTIR	Attenuated total reflectance–Fourier transform infrared
CBD	Chemical bath deposition

CNT	Carbon nanotubes
Co-Pi	Cobalt phosphate
CVD	Chemical vapour deposition
D	Normalised parameter
DC	Direct current
DI	Deionised
DSSC	Dye-sensitised solar cell
E_u	Urbach energy
EDX	Energy dispersive X-rays spectroscopy
EIS	Electrochemical impedance spectroscopy
eV	Electron volt
FTO	Fluorine doped tin oxide
FWHM	Full width half maximum
GIS	Gas ionisation sensor
HHS	Hollow hemisphere
HMT	Hexamethylenetetramine
HOMO	Highest occupied molecular orbital
HP	Hydrolysis-precipitation
ICP–MS	Inductively coupled plasma–mass spectroscopy
IPA	Isopropanol
I_{in}	Initial photocurrent
I_{st}	Steady-state photocurrent
I_t	Time-dependent photocurrent
I–t	Current–time

ITO	Indium doped tin oxide
I–V	Current–voltage
JCPDS	Joint Committee on Powder Diffraction Standards
LED	Light emitting diode
LUMO	Lowest unoccupied molecular orbital
M	Molar
M30mW33	ZnO NRs grew on SS mesh for 30 minutes by PACBD at 33.0W
M60mW33	ZnO NRs grew on SS mesh for 60 minutes by PACBD at 33.0W
M90mW33	ZnO NRs grew on SS mesh for 90 minutes by PACBD at 33.0W
M120mW33	ZnO NRs grew on SS mesh for 120 minutes by PACBD at 33.0W
MOD	Metal organic decomposition
M–S	Mott–Schottky
MW	Molecular weight
N_D	Donor density
NHE	Normal hydrogen electrode
NM	Nitromethane
NP	Nanoparticle
NR	Nanorod
NT	Nanotube
NW	Nanowire
OEC	Oxygen evolution catalyst
P	Surface porosity
P15h	ZnO NRs grew on SS plate for 15 hours by CBD
PACBD	Power assisted chemical bath deposition

PEC	Photoelectrochemical
PEG	Polyethylene glycol
PMMA	Polymethylmethacrylate
PTFE	Polytetrafluoroethylene
PVA	Polyvinyl alcohol
RHE	Reversible hydrogen electrode
rpm	Revolutions per minute
SAVR	Surface area to volume ratio
SEM	Scanning electron microscopy
SS	Stainless steel
TC	Texture coefficient
TTIP	Titanium tetraisopropoxide
UV	Ultraviolet
V_{FB}	Flatband potential
Vis	Visible
VLS	Vapour liquid solid
VOC	Volatile organic compound
VS	Vapour solid
W	Width of the space-charge layer
wt%	Weight percentage%
XPS	X-ray photoelectron spectroscopy
XRD	X-ray diffraction
YZO	Y-doped ZnO
ZA	1.0 M zinc acetate

ZAP	1.0 M zinc acetate with 6 wt% of PVA
ZT 400	ZnO NRs arrays on TiO_2 HHS annealed at 400°C
ZT 500	ZnO NRs arrays on TiO_2 HHS annealed at 500°C
ZT 600	ZnO NRs arrays on TiO_2 HHS annealed at 600°C
ZT 700	ZnO NRs arrays on TiO_2 HHS annealed at 700°C
ZT 750	ZnO NRs arrays on TiO_2 HHS annealed at 750°C
ZT 800	ZnO NRs arrays on TiO_2 HHS annealed at 800°C

List of Figures

List of Tables

List of Publications

1. W. C. Lee, Y. X. Fang, R. Kler, G. E. Canciani, T. C. Draper, Z. T. Y. Al-Abdullah, S. M. Alfadul, C. C. Perry, H. Y. He and Q. Chen, *Mater. Chem. Phys.*, 2015, **149-150**, 12-16.
2. W. C. Lee, G. E. Canciani, B. O. S. Alwhshe and Q. Chen, *Int. J. Hydrogen Energ.*, 2015, submitted.
3. Y. X. Fang, W. C. Lee, G. E. Canciani, T. C. Draper, Z. F. Al-Bawi, J. S. Bedi, C. C. Perry and Q. Chen, *Mater. Sci. Eng., B*, 2015, submitted.
4. W. C. Lee, Y. X. Fang, J. F. C. Turner, J. S. Bedi, C. C. Perry, H. Y. He and Q. Chen, *Chem. Mater.*, 2015, submitted.

Chapter 1 Introduction

1.1 Metal Oxide Semiconductors

Metal oxides have received great attention from researchers over the past few decades and have played an important role in many areas of chemistry, physics and materials science.[1-4] Due to the difference in the electronic structure, metal oxides can be either a conductor, a semiconductor or an insulator. For a conductor, the valence band is filled and the conduction band is partially filled by electrons; these electrons are free to conduct. A material is categorised as a semiconductor when its band gap can be surpassed by thermal and/or optical excitations to create electron-hole pairs in the conduction and valence bands. For a material with band gap energy larger than 4 eV, it is classified as an insulator since it cannot be easily overcome to generate charge carriers.

The electronic structure of a metal oxide can be described by the formation of molecular orbitals through the linear combination of multiple periodically arranged atomic orbitals. When a large number of orbitals overlap, they form primarily continuous bands with s, p and d orbital character. The valence band is formed through the overlapping of the highest occupied molecular orbitals (HOMOs) whilst the higher energy conduction band is created through the overlapping of the lowest unoccupied molecular orbitals (LUMOs). The separation between these two bands is associated with the band gap, which defines as the minimum energy required for an electronic transition in the material.

In general, metal oxide semiconductors can be categorised into two different groups which are n-type and p-type semiconductors. For an n-type semiconductor,

electrons are the majority charge carriers and conversely, holes are the majority charge carriers for a p-type semiconductor. In addition, the nature of semiconductor can be altered by introducing different types of dopants. In case of an intrinsic semiconductor, the Fermi level is approximately midway between the minimum energy of its conduction band and the maximum energy of its valence band. For n-type doping, the Fermi level shifts towards the conduction band, whereas for p-type doping, the Fermi level shifts towards the valence band.[5, 6]

Since the first discovery of carbon nanotubes (CNTs) by Iijima S. in 1991,[7] the exploitation of nanostructured inorganic materials has received great interest.[8-10] Metal oxide nanomaterials have stimulated great interest due to their importance in basic scientific research and have possessed many unique properties linked to the nanometre dimensions.[11-13] Nanomaterials are generally classified as having three different morphologies or nanostructures: 0D, 1D and 2D nanostructures. 0D nanostructures are usually named as nanoparticles (NPs) with the possible morphology of dots and spheres. Meanwhile, 1D nanostructures have been called by a variety of names including nanorods (NRs), nanotubes (NTs), nanowires (NWs), nanowhiskers and nanofibres. For 2D nanostructures, they are usually thin films and some nanoplatelets.[14]

The dimensions of nanomaterials are ranging from several nanometres to several hundred nanometres. It is important to note that the change of the size and dimensionality of the nanomaterials will result in a change in the structural characteristics and electronic structures of the materials.[1] These properties of nanostructured metal oxides lead to the wide applications as energy storage, harvesting devices, optoelectronic devices and photocatalysts for environmental treatment, such as lithium ion batteries,[15] fuel cells,[16] solar cells,[17] light emitting devices (LEDs),[18] water

and air purification,[19] hydrogen production by water photolysis,[1] photodetectors[20] and sensors.[21]

Metal oxide based nanostructures such as ZnO, TiO_2 and their derivatives are the focus of current research efforts in nanotechnology due to their availability since Zn and Ti are the most common minerals on the Earth and have tremendous potential applications.[11] In addition, these metal oxide nanomaterials are biocompatible and can be synthesised into various nanostructures with different chemical and physical properties. In this thesis, ZnO, TiO_2 and $BiVO_4$ are the three main metal oxides being explored. Therefore, in the following sections, the properties of each material, methods of synthesis and their potential applications will be discussed in details.

1.2 Zinc Oxide (ZnO)

1.2.1 ZnO Properties

ZnO is one of the metal oxide materials that have received broad attention owing to its notable performance in electronics, optics and photonics. ZnO is an II-VI wide band gap semiconductor. The crystal structures of ZnO are mainly in either zincblende or wurtzite structure, as schematically shown in Figure 1.1B and 1.1C. Rocksalt ZnO (Figure 1.1A) can be synthesised under high pressure but it is not stable under ambient conditions. Both zincblende and wurtzite ZnO structures have the zinc cation surrounded by four oxygen anions at the corners of a tetrahedron, and vice versa.[22] Wurtzite ZnO has a hexagonal structure (space group $P6_3mc$) with lattice parameters $a = b = 3.250$ Å and $c = 5.207$ Å (JCPDS # 36-1451). Meanwhile, zincblende ZnO has a cubic structure (space group $F\bar{4}3m$) with lattice parameters $a = b = c = 4.580$ Å (JCPDS # 65-2880).

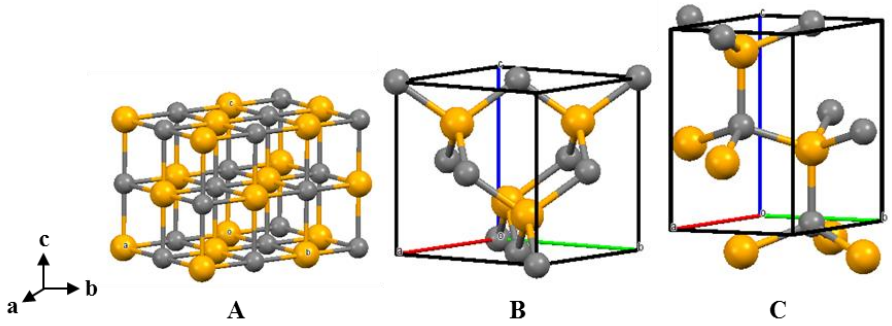

Figure 1.1 Schematic diagrams of ZnO unit cell in (A) rocksalt, (B) zincblende and (C) wurtzite crystal structures. Zinc and oxygen are grey and orange, respectively.

At normal temperature and pressure, ZnO exhibits wurtzite crystal structure since it is thermodynamically more stable than zincblende.[23] The zincblende ZnO structure can be stabilised only by growth on a cubic substrate. Wurtzite ZnO has a direct optical band gap of 3.37 eV.[24] The lack of the centre of symmetry in wurtzite ZnO (Figure 1.1C) results in strong piezoelectric and pyroelectric properties.[25] Another important characteristic of ZnO is the polar surfaces. The alternating stacking of the oppositely charged ions, Zn^{2+} and O^{2-} leads to the formation of positively charged Zn-terminated (0001) and negatively charged O-terminated $(000\bar{1})$ surfaces, resulting in spontaneous polarisation along the c-axis and difference in surface energy.[26] Due to the high surface energy of the Zn-terminated (0001) plane, the anions are favourably absorbed on this polar surface. Hence, it causes a fast growth along the [0001] direction and results in the formation of 1D ZnO nanostructures such as NRs, NWs or nanobelts (Figure 1.2). In addition, different crystal planes have different kinetic parameters, therefore the growth direction of ZnO can be tuned by varying the growth conditions in order to obtain the desired nanostructures such as polar ZnO nanobelt (Figure 1.2C).[27]

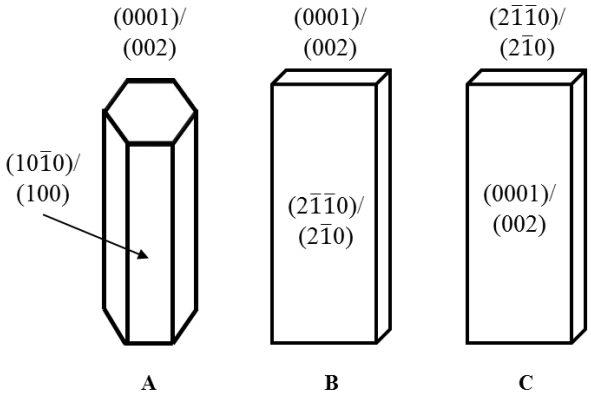

Figure 1.2 Typical growth morphologies of 1D ZnO nanostructures and the corresponding facets, (A) NR or NW, (B) nanobelt and (C) polar nanobelt.

ZnO has a large exciton binding energy of 60 meV which offers higher exciton populations under stimulation. This makes it useful for room temperature optoelectronic devices such as laser diodes and LEDs.[28] In addition, ZnO has high electron mobility and high thermal conductivity. Crystalline ZnO has a long hole diffusion length (also known as minority carrier diffusion length) of 125 nm which reduces the recombination rate of the electron-hole pairs.[29] Without contact with acid, ZnO is generally chemically stable with a high melting point of 1975°C.[30] It resists radiation damage, including irradiation by high energy electrons and heavy ions.[31, 32] Additionally, ZnO is nontoxic and completely biocompatible which make it suitable to be used in biomedical applications.[33]

1.2.2 Synthesis of ZnO Nanostructures

Various physical and chemical routes have been proposed to synthesise ZnO nanostructures. By controlling the experimental conditions, different forms of ZnO nanostructures, such as NPs, NRs, NTs, NWs, nanobelts, nanorings, nanoflowers, nanocombs, nanohelices, nanocups, nanocages, nanospirals and nanopencils can be

prepared.[25, 34-36] Here, the advantages and disadvantages of different synthesis methods and their specific applications will be discussed in details.

1.2.2.1 Chemical Vapour Deposition

Chemical vapour deposition (CVD) of ZnO is a chemical process that involves condensation of thermally vaporised zinc onto a pre-seeded substrate in a controlled oxygen environment to produce high purity, crystallised thin films.[37] This can be achieved by either vapour liquid solid (VLS) or vapour solid (VS) mechanisms. The difference between VS and VLS is that VS growth does not involve a liquid catalyst. Both pathways take place in a tube furnace at high temperature. In a typical CVD process, zinc precursor is vaporised in a crucible near the closed end of a tube furnace. Usually two different types of zinc precursors are being used which are either zinc powder (VS) or a mixture of ZnO and graphite powder (VLS). Upon heating, zinc vapours will be produced and a carrier gas (*e.g.* oxygen or argon) is flowed through the reaction chamber. This carrier gas will transport the zinc vapour to the substrate which is at relative lower temperature to form ZnO nanostructures. Figure 1.3 is a schematic diagram illustrates the CVD process.

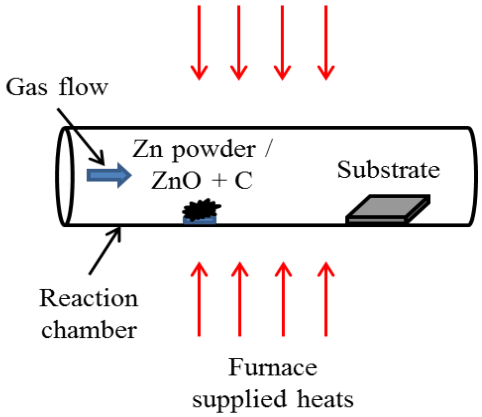

Figure 1.3 A schematic diagram of the CVD process.

For VS and VLS growth, the ZnO solidifies and grows preferentially along the [0001] direction to form 1D nanostructures. This is due to the oppositely charged ions (Zn^{2+} and O^{2-}) leading to the formation of the positively charged (0001) and negatively charged ($000\bar{1}$) surfaces, which results in a large surface energy for these polar surfaces. During the CVD reaction, the incoming vapours favourably adsorb on the polar surface and therefore 1D ZnO nanostructures, rather than thin films, are created. There are number of reports for the synthesis of ZnO nanostructures by the CVD method.[37-40] One of the parameters that can cause a change in the morphology of ZnO is the distance between zinc precursor and substrate. Yao B. D. *et al.* have reported that needle-like, ribbon-like and wire-like ZnO nanostructures can be obtained in a CVD process depending on the temperature of the substrate. This is because different substrate temperatures will lead to different nucleation and different growth kinetics.[41]

The ZnO nanostructures created through CVD method are usually highly crystalline and densely packed. However high operating temperatures (> 650°C) are required and this restricts the choice of substrate. In addition, CVD method has a difficulty of introducing dopant with well controlled stoichiometry using multiple element precursors, since the rates of evaporation of different precursors are different.[42]

1.2.2.2 Spray Pyrolysis Deposition

Spray pyrolysis deposition is one of the techniques widely used to prepare ceramic films. It is a simple and cost effective way to create large size thin films of any composition. A typical spray pyrolysis setup consists of a spray nozzle, precursor solution, atomiser, substrate heater and temperature controller. The process involves three steps which are; (i) atomisation of precursor solution, (ii) aerosol transport of

droplets and (iii) decomposition of the precursor to initiate film growth.[43] Figure 1.4 is a schematic diagram for spray pyrolysis deposition process.

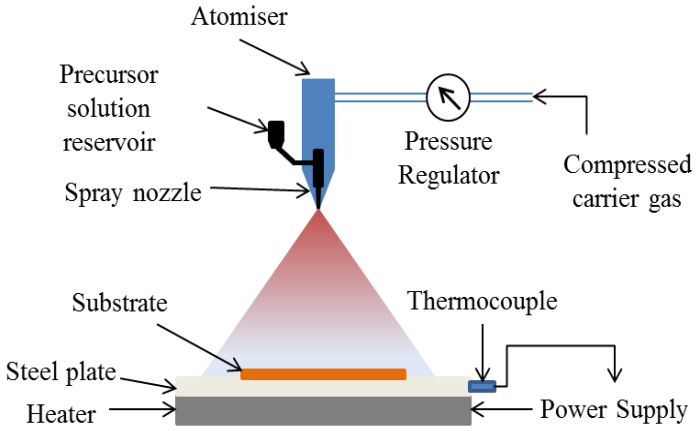

Figure 1.4 A schematic diagram of the spray pyrolysis deposition process.

The atomiser will generate droplets from a precursor solution and send them toward the substrate surface by the compressed carrier gas. When the droplets reach the surface of the heated substrate, they will be decomposed and deposited onto the substrate forming a film. The final morphology of thin films by spray pyrolysis method is defined by a few key parameters such as the deposition temperature, type of atomiser and properties of precursor solution (*e.g.* pH and solvent). This method can produce relatively uniform and high quality metal oxide films with the possibility of doping.

Although the delivery of the metal precursors in spray pyrolysis is different from CVD method, the growth mechanism is actually very similar. Vertically aligned ZnO NRs were created on glass substrate through spray pyrolysis method using zinc precursors by Shinde S. D. *et al.*[44] They used a mixture of 10 ml of methanol, 5 ml DI water and a 0.1 M zinc acetate aqueous solution as zinc precursor. A spray rate of 5 ml min^{-1} was used, driven by the compressed air as a carrier gas. The substrate was held at 350°C for the deposition of ZnO nanostructured film. The substrate temperature

determines the pyrolysis rate which should be matched with the spray rate aiming for a high quality of ZnO NRs. A high sprayer rate with low substrate temperature could result a featureless thin film. The influence of precursor pH and substrate temperature on the growth and morphology of ZnO films have been reported by Quintana *et al*.[45] The change of precursor pH from 2 to 5 causes a change in the shape of the particles from planar to spherical. Meanwhile, increasing the deposition temperature leads to an increase in the particles size.

1.2.2.3 Chemical Bath Deposition

ZnO nanostructures are commonly prepared using solution methods. One of the solution synthesis methods which has garnered great interest for the synthesis of ZnO nanostructures is chemical bath deposition (CBD). This method was first developed by Vayssieres L. in 2003 for the solution growth of arrayed NRs and NWs of ZnO.[46] The aqueous solution of zinc nitrate hexahydrate, zinc acetate or zinc chloride was used as zinc precursor. Hexamethylenetetramine (HMT) or ethylenediamine was used as the hydroxide anion source. CBD process is operated at a mild temperature of 85°C. Upon heating, HMT or ethylenediamine will decompose to yield OH^- which will then react with Zn^{2+} to precipitate ZnO. For the growth of vertically aligned array ZnO nanostructures, a layer of ZnO seeding particles should be used to initiate the growth of ZnO NRs. The details of the growth mechanism is proposed in section 3.4.2.

Different morphologies of ZnO nanostructures can be obtained by changing the experimental parameters, including the concentration of zinc and hydroxide anion precursors, duration of reactions and the additional of surfactant. Xu S. *et al.* have studied the effect of growth temperature, concentration of zinc precursor and duration of reaction on the morphology of ZnO nanostructures by seedless CBD.[47] The results

showed that an increase in the duration of reaction and concentration of the zinc precursor caused the formation of longer and larger ZnO NRs, respectively. Meanwhile, increase in the growth temperature caused a change in the NR morphology from hexagonal to tapered-like. This indicates that the growth rate can be significantly affected by the growth temperature through the rate of the decomposition of amines.

Alternatively, CBD growth can also use the strong oscillation energy generated in an ultrasonic bath, which is known as the sonochemical method. The synthesis nutrient solution is similar to the one used in thermal CBD, however the solution is being placed in an ultrasonochemical apparatus. During the ultrasonication, a large amount of energy, temperatures and pressures are released from the collapse of microbubbles. The generated energy will overcome the energy barriers that are needed for the growth of various ZnO nanocrystals. The power of ultrasonic wave and duration of ultrasonic treatments can change the size, shape and morphology of ZnO nanostructures, such as NRs, nanoflowers, nanocups, nanodiscs and various nanoarchitectures.[48]

The advantages of CBD method are that it operates at mild conditions (< 100°C and normal pressure) and can be used for a large area deposition on variety of substrates. It is a cost effective and environmental friendly technique which requires no organometallic or hazardous components and no special equipment and apparatus other than a heating source.

1.2.2.4 Hydrothermal Method

Hydrothermal is another solution method which has been widely used for the synthesis of ZnO nanostructures with aqueous zinc solution as a precursor. A Teflon lined stainless steel (SS) autoclave is used as the thermal reactor, as shown in Figure

1.5. Since the reaction chamber is sealed and heated, a high pressure will be created in the chamber and thus results in the formation of high crystalline ZnO nanostructures.[49] The growth mechanism of ZnO nanostructures through hydrothermal synthesis is similar to that of aqueous CBD growth.

Figure 1.5 A photograph of Teflon lined stainless steel chamber for the hydrothermal reaction.

The concentration of zinc precursor, solvent used, concentration of surfactant and pH of the reaction mixture are some of the key parameters to control the size, shape, morphology and crystallinity of the as-synthesised ZnO nanostructures through hydrothermal route. In addition, the morphology of ZnO nanostructures can also be tuned by changing the operating temperature and duration of hydrothermal reaction. Liu B. and Zeng H. C. have reported the growth of ZnO NRs in the diameter regime of 50 nm through hydrothermal synthesis.[50] Tong Y. *et al.* have studied the influence of seeding and growth duration on the morphology of ZnO nanostructures.[51] The results revealed that a variety of ZnO nanostructures, including nanotowers, nanovolcanoes, NRs, NTs and nanoflowers, could be achieved by controlling the reaction time and the seeding conditions.

The aspect ratio of ZnO NRs can be tuned by adding potassium chloride in the growth solution.[52] This is because either the (100) or (002) planes of ZnO are passivated by the chloride ions, depending on the concentration of the potassium chloride, resulting in the formation of NWs or nanoplatelets. Flower-like ZnO nanostructures were also created through hydrothermal method with the presence of polyethylene glycol (PEG).[53] The formation of flower-like ZnO structures was due to the PEG adsorbed the primary ZnO nuclei causing the oriented growth of ZnO nanosheets. The difference in the surface energy causes the ZnO nanosheets to rearrange and results in the formation of ZnO microflowers.

1.2.3 Applications of ZnO Nanostructures

1.2.3.1 Optics and Electronics

ZnO nanostructured semiconductor has shown some interesting optoelectrical properties. Optically and electron stimulated emission and lasing of ZnO nanostructures, including NRs, NWs as well as epitaxial layers have been previously reported.[54-56] It has been demonstrated the potential as a laser material to produce intense, monochromatic and coherent light sources since it has a much higher exciton binding energy at room temperature (60 meV)[11] as compared to other wide band gap semiconductor (*e.g.* GaN; 25 meV).[57] Compared to bulk semiconductor, the nanostructured semiconductor has the additional benefit for more efficient in stimulated emission and lasing. Meanwhile, the threshold potential for lasing will also decrease with decrease in the dimension of the materials. Therefore, ZnO nanostructures become an ideal candidate for the development of semiconductor lasers.

Recently, ZnO nanomaterials have also been developed into new generation phosphor–free high efficiency LEDs with interesting spectral coverage from blue to the

deep UV.[25] The quantum efficiency could approach as high as 90%.[25] Compared to GaN based LEDs, there are two main advantages of ZnO based LEDs as follows:

(i) ZnO has a superior material quality. It has been demonstrated that by growth of high purity of ZnO with defect densities below 105 cm^{-3}.[58]

(ii) The performance of ZnO based LEDs can be improved by doping to reduce the activation energy. ZnO film doped with arsenic, a p-type dopant, has an activation energy of 120 meV,[5] which is much less than that of 209 meV for p-type GaN doped with magnesium.[59]

For ZnO nanostructures, NRs or NWs, it can be grown easily on different types of substrates such as glass, polymers, plastics, and metal oxide dielectric substrates. For optical applications, ZnO nanostructures are usually grown on a transparent conductive substrate, such as indium or fluorine doped tin oxide (ITO or FTO) coated glass.

1.2.3.2 Sensors

ZnO nanomaterials have also been widely used as active layers for gas sensors.[60] The conductance, optical response and surface vibrational properties of ZnO can be strongly affected by the environmental conditions or the presence of adsorbed molecules. Nanomaterials with larger surface area offers additional advantage of high sensitivity as more molecules can be adsorbed.

Many types of ZnO nanomaterials based sensors have been reported, including gas,[60] temperature,[61] pressure,[62] humidity,[63] and chemical sensors.[44] The mechanisms of these gas sensors are based on the conductivity change upon gas exposure, measured by an electrical current passing through the ZnO nanostructures. The adsorbed molecules will affect the oxidation or reduction state of the ZnO which in turn decreases or increases its conductivity. ZnO nanomaterials have also been applied as biological

sensors to detect urea and glucose as well as the sequence of bases in DNA.[64-67] A highly sensitive pressure sensor can also be created using the piezoelectric effects which can measure the forces in the range of nano to pico Newtons. This phenomenon is used to fabricate micro pressure sensors for monitoring blood flow rate and pressure generated in the veins.[68]

Recently, ZnO NRs or NWs have been applied in the field ionisation gas sensors.[69-71] In such devices, the gas electrical breakdown voltage and current are used to identify the gas species and to measure its concentration. The first nanomaterials based gas ionisation sensor (GIS) were CNTs, however it has a poor stability due to CNTs oxidised in oxygen environment and degraded at high current.[69, 72] ZnO nanostructures have been proved to have an outstanding stability as GIS owing to its high melting point (1975°C) and chemical resistance towards oxidation.[69] However, in comparison with CNTs, the pristine ZnO based GISs still require a much higher voltage to breakdown the targeted gas species. This is due to the limited conductivity of ZnO which can be overcome with doped ZnO as discussed in Chapter 7 comprehensively.

1.2.3.3 Photovoltaic and Photoelectrochemical Cells

Metal oxide semiconductors with controllable band gaps can be used as efficient photocatalysts. Applications, such as dye sensitised solar cells (DSSCs) and photoelectrochemical (PEC) water splitting, have been developed for new generation of renewable energy sources. For DSSCs, metal oxide films or nanostructures prepared on ITO or FTO glass substrate with adsorbed dyes are used as the photoanode, a platinum coated glass serves as a counter electrode, and a liquid electrolyte is used to electrically connect the two electrodes. The commonly used electrolyte is the mixture of iodine and iodide solution.[26] An example of the DSSC process is presented in Figure 1.6.

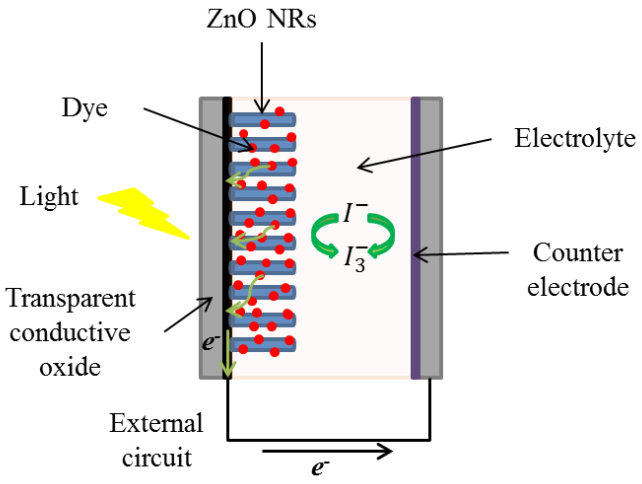

Figure 1.6 A schematic diagram illustrating the DSSC process.

As demonstrated in Figure 1.6, a monolayer of dye molecule absorbs on the surface of ZnO NRs will create excited electrons and holes upon illumination. The photogenerated electrons are injected into the conduction band of ZnO, while the holes are released by redox couples in the electrolyte. 1D ZnO nanostructures are one of the promising materials for an efficient solar cell since it not only possesses a large surface area, high carrier mobility and good crystallinity but also provides a good geometry for light absorption and electrolyte transportation.[1] The large surface area of the ZnO will also benefit for the loading of dye molecules which will improve the effective light absorption leading to high photoconversion efficiency. Naturally, DSSCs based on various ZnO nanostructures such as ordered and disordered NRs, nanotetrapods, NWs, nanoflowers, NPs and other nanostructures will have different light conversion efficiencies.[73]

As a photocatalyst, nanostructured ZnO has also been widely explored for its potential in electrochemical photolysis of water for hydrogen generation. Hydrogen is an efficient source of clean and renewable energy where it has the potential to replace fossil fuels. There are number of reports for the use of ZnO nanostructures, including

thin films, NRs, NWs, NPs and nanopencils as photoanodes for photoelectrolysis water splitting application.[34, 74-79] However, the solar-to-hydrogen conversion efficiency achieved by ZnO nanostructures is still very low due to its wide band gap which only absorbs the UV light. To overcome this drawback, dopants can be used to reduce the band gap energy of ZnO and increase the photoconversion efficiency, which will be discussed in detail in Chapter 5.

To utilise hydrogen as an energy source, the challenge for storage and transportation of high pressure explosive gas has to be addressed. Recent studies revealed that ZnO nanostructures were able to reversibly absorb and desorb hydrogen at ambient temperature.[80, 81] Wan Q. *et al.* have first reported that ZnO NWs absorb 0.83 wt% of hydrogen at room temperature and ~30 atm hydrogen pressure, however only ~0.6 wt% of the stored hydrogen has been released during the desorption.[81] Pan H. *et al.* have reported that the hydrogen storage characteristic of ZnO can be improved with the introduction of magnesium.[80] Their experimental results revealed that magnesium doped ZnO samples show a faster hydrogen uptake and release kinetics than pristine ZnO.

1.3 Titanium Dioxide (TiO_2)

1.3.1 TiO_2 Properties

Titanium dioxide, TiO_2, or commonly known as titania, has also attracted tremendous attention due to its low cost, harmless, good chemical stability and more importantly its excellent photocatalytic activity.[3, 9, 82] Three main types of TiO_2 structures can be formed, namely tetragonal rutile, tetragonal anatase and orthorhombic brookite, as shown in Figure 1.7. These three crystal structures are made up of distorted octahedral in which titanium cation is at the centre with oxygen anions positioned at the

corners. Brookite is obtained as mineral but it cannot be formed under normal laboratory conditions. For anatase and rutile, the unit cell vectors (*a*, *b* and *c*) and the symmetry of the crystal determine the spacing of individual crystal planes. For tetragonal anatase TiO_2, the TiO_6 octahedron is slightly more distorted than that of rutile TiO_2, where the lattice parameter dimensions of anatase are $a = b = 3.785$ Å and $c = 9.514$ Å (JCPDS # 21-1272). Meanwhile, tetragonal rutile TiO_2 has the lattice parameters of $a = b = 4.593$ Å and c = 2.959 Å (JCPDS # 21-1276).

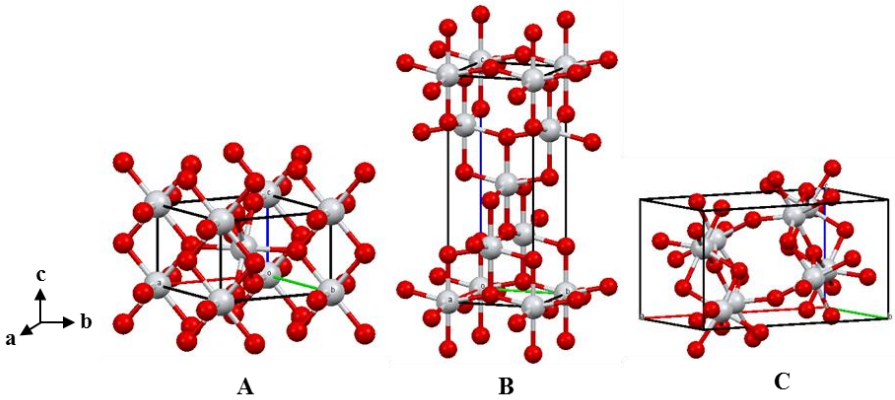

Figure 1.7 Crystal structures of TiO_2, (A) rutile, (B) anatase and (C) brookite. Titanium and oxygen are white and red, respectively.

When the amorphous TiO_2 is annealed at 280°C, anatase phase of TiO_2 is formed first. The rutile phase is formed at 650°C and above. The size dependence of the stability of various TiO_2 phases has been reported.[83] For NPs larger than 35 nm, rutile phase of TiO_2 is the most stable phase while for the NPs less than 11 nm, anatase is the most stable phase.[84] TiO_2 is a wide band gap semiconductor where the anatase and rutile phase of TiO_2 have band gap energies of 3.2 eV and 3.0 eV, respectively.[85] In addition, TiO_2 is stable in both acidic and basic conditions, except in hydrofluoric solutions, and is resistance to the corrosion by common gas.

1.3.2 Synthesis of TiO_2 Nanostructures

Different morphologies of TiO_2 nanostructures such as NPs, NTs, NRs, NWs, nanofibres, nanobelt and nanosheets can be prepared in the form of powders, thin films and crystals.[86-89] There are many methods have been proposed for the fabrication of TiO_2 nanostructures, either by chemical or physical routes. Here I will discuss the principle of a variety techniques and analyse their advantages and disadvantages.

1.3.2.1 Hydrothermal Method

One of the widely used techniques for the preparation of TiO_2 nanostructures is hydrothermal method.[89] Hydrothermal synthesis of TiO_2 nanostructures is normally conducted in autoclaves with Teflon liners under controlled temperature and pressure with the reaction in aqueous solutions. The reaction temperature can be elevated above the boiling point of water, reaching high pressure of vapour saturation. The amount of internal pressure of the autoclave is strongly affected by the operating temperature and the amount of solution added. This method is also commonly used in the ceramics industry for the production of small particles.

Many groups have reported the creation of TiO_2 NPs using hydrothermal route using titanium alkoxide in an acidic ethanol-water solution.[90, 91] TiO_2 NTs can also be prepared through hydrothermal method. Kasuga *et al.* were the first group reported the synthesis of anatase TiO_2 NTs with an outer diameter of 8 nm (wall thickness of 2~3 nm) and a specific surface area of 400 $m^2 g^{-1}$ via the hydrothermal method.[92] A sol-gel solution was first prepared by mixing titanium tetraisopropoxide and tetraethyl orthosilicate in a molar ratio of 8:2. The gel was then calcined at 600°C for 2 hours followed by a hydrothermal reaction in 10 M NaOH solution at 110°C for 20 hours. TiO_2 NTs were obtained by removing the amorphous SiO_2 in 0.1 M HCl solution. Other

than that, TiO_2 nanocrystals and NRs can also been synthesised through hydrothermal synthesis with the presence of zinc powder in titanium trichloride aqueous solution.[93, 94] The functions of zinc powder in the solution were to prevent the oxidation of Ti^{3+} and to tune the oxygen vacancy and the crystalline phase. When the amount of zinc powder is lower than 0.5 mmol, mainly anatase phase of TiO_2 nanocrystals in truncated octahedron structure were formed. As increased the amount of zinc powder to 1.5 mmol and above, rutile TiO_2 NRs were created.

1.3.2.2 Sol-gel Method

TiO_2 powders, membranes and thin films can be synthesised using sol-gel method. In a typical sol-gel process, a colloidal suspension or a sol, is formed from the hydrolysis and polymerisation reactions of the titanium precursors. The precursors are mainly made up of inorganic metal salts or metal organic compounds such as metal alkoxides. The liquid sol will transform into solid gel phase after the completion of polymerisation and loss of solvent.

Sol-gel method is mainly divided into two different routes which are alkoxide and non-alkoxide methods. For non-alkoxide method, inorganic salts such as nitrates, chlorides, acetates, carbonates and acetylacetonates are used in the solution.[95] This method requires an additional step to remove the inorganic anions. Meanwhile, the alkoxide route uses metal alkoxides as the starting material where metal oxide nanostructures are obtained by hydrolysis and condensation of the metal alkoxides.[96] In general, a thin film of TiO_2 nanostructures are prepared through either spin coating or dip coating. The solution was used to perform a coating on the surface of substrate, and the wet gel is converted into a solid film either by drying or thermal treatment.

The sol-gel method has many advantages. Firstly, it is an easy method to produce TiO_2 thin films with high purity. Secondly, sol-gel method offers a flexibility in introducing dopants in high concentrations or stoichiometry control over the desired composition. Thirdly, when compared to other synthesis techniques, sol-gel method has the advantage in producing large and complex area coating.

1.3.2.3 Electrochemical Anodisation

One of the promising ways to obtain organised and well-aligned TiO_2 NTs is through electrochemical anodisation. Anodic oxidation of titanium foil for the creation of TiO_2 NTs was first reported by Dong G. *et al.* in 2001.[97] By controlling the anodisation parameters, it is possible to control the shape, wall thickness, length as well as the outer and inner diameters of the NTs. For an electrochemical anodisation setup, it consists of two electrodes, where two clean titanium plates are used as anode and cathode. Both of the electrodes were immersed in a fluoride containing electrolyte at a fixed separation. A power supply was used to apply a constant voltage or a constant current during the anodisation process. Figure 1.8 is a schematic diagram illustrates the electrochemical anodisation setup.

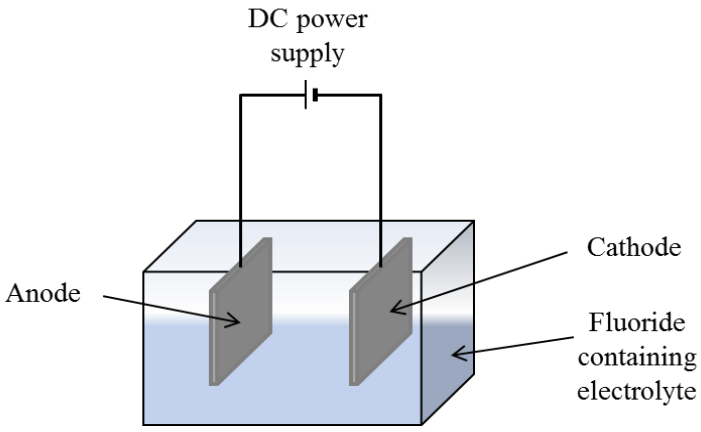

Figure 1.8 Electrochemical anodisation unit with a two-electrode cell.

The electrolyte composition of electrochemical anodisation plays a critical role in determining the resultant NT morphology. The pH and the composition of the electrolyte determine both the rate of formation of NT arrays and also the rate at which the resultant oxide is dissolved. For the formation of TiO_2 NTs, a fluoride ion containing electrolyte is needed. The general understanding for the anodisation of titanium in fluoride electrolyte is that titanium is oxidised forming an oxide barrier layer on the anode surface. As the oxide layer gets thicker, it decreases the oxidation electrical field, reducing the oxidation rate. In the presence of fluoride ion, a field directed dissolution of TiO_2 causes thinning the oxide barrier layer, resulting in an immediate formation of etching pits, which are then developed deeper into NTs.[98, 99] The chemical processes of oxidation and dissolution reactions are described below:

$$Ti_{(s)} + 2H_2O_{(l)} \rightarrow TiO_{2(s)} + 2H_{2(g)} \quad \text{(Equation 1.1)}$$

$$TiO_{2(s)} + 6F^-_{(aq)} + 4H^+_{(aq)} \rightarrow TiF_6^{2-}{}_{(aq)} + 2H_2O_{(l)} \quad \text{(Equation 1.2)}$$

The oxidation is facilitated by the water in the electrolyte (Equation 1.1). The formation of soluble fluoro-complexes (TiF_6^{2-}) in the electrolyte is aided by the electric field, which moves fluoride anions toward the anode and release TiF_6^{2-} into the electrolyte (Equation 1.2). The dissolution of the barrier oxide layer at the bottom of the NTs maintains the oxidation process active. Consequently, optimal TiO_2 NTs growth rate is achieved when the oxidation rate at the interface of the metal and oxide is balanced to the dissolution rate.

There are a number of factors which can affect the formation of TiO_2 NTs, including the applied voltage, electrolyte concentration and anodisation temperature.[91, 97] Larger applied voltage and higher operating temperature will result a faster growth

and larger diameter of the NTs.[100] The oxidation and dissolution rates of the anodisation process are determined by the concentration of water and fluoride ions, respectively. Therefore, for the creation of highly ordered TiO_2 NTs, the precise control of the anodisation parameters is essential.

1.3.2.4 Electrospinning Method

Electrospinning method was first studied by Zeleny J. in 1914.[101] It is a technique commonly carried out for the creation of ultrafine fibres with outer diameters in micrometre to nanometre range. In a typical electrospinning process, an external electrical field is applied in between the tip of a spinneret and a drop of polymeric fluid. When the strength of electric field increases, the hemispherical surface of the solution at the tip elongates to form a convex meniscus, also known as the Taylor cone.[102, 103] The repulsive electrical forces will overcome the surface tension of the drop when the applied electric field reaches a critical value. A charged jet of solution is then ejected from the tip of the Taylor cone and a rapid and unstable whipping of the jet occurs between the tip and drum collector. This leads to the evaporation of the solvent and results in the formation of ultrafine fibres on the drum collector. There are three main components in an electrospinning setup, which are a high voltage power supply (kV), a spinneret (a syringe or pipette tip) and a grounded collector (a metal plate or a rotating metal drum), as shown in Figure 1.9.

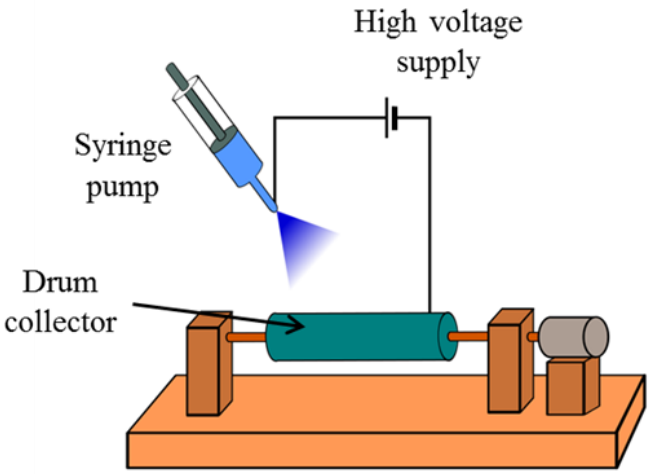

Figure 1.9 Scheme of a typical setup for electrospinning process.

Electrospinning method has attracted renewed attention due to its potential for the creation of metal oxide nanomaterials, such as nanofibres, which possess high surface to volume aspect ratios, leading to low density and high pore volume, and excellent mechanical strength.[103] The morphology of the created nanostructures is strongly dependent on the solution parameters, including the concentration, viscosity, solvent used, molecular weight of polymer, surface tension, and processing parameters such as diameter of pipette orifice, applied voltage, feed rate and distance between the nozzle and the drum collector.[104] Various morphologies of TiO_2 nanostructures can be produced through the electrospinning method with the titanium precursors dissolved in polymer solutions followed by calcination, for instance, nonwoven, aligned or patterned nanofibres, nanoribbons, nanospheres, nanocups, NRs and nanocrystals.[103-105]

There a number of advantages of using electrospinning method to create metal oxide nanostructures. Firstly, it is a simple and robust technique to produce large quantities of metal oxide nanomaterials. Secondly, it is cost effective and has high degree of reproducibility for the obtained materials. Thirdly, electrospinning method

can be used for a large area deposition and it has the ability to manipulate nanomaterial composition in order to get desired properties and functions.

1.3.3 Applications of TiO_2 Nanostructures

1.3.3.1 Photoelectrochemical Cells and Photovoltaic

Similar to ZnO nanostructures, TiO_2 nanomaterials have been used for photovoltaics and hydrogen generation through photocatalytic electrochemical photolysis of water. In 1972, Fujishima A. and Honda K. have demonstrated photocatalytic of water by an n-type TiO_2 single crystal thin film for solar energy conversion and storage in the form of hydrogen.[106] In order to increase the photoconversion efficiency of TiO_2, one of the approaches is to increase the effective surface area of the photoanode by fabricating various nano morphologies of TiO_2, including NRs, NTs, NWs, nanofibres, hollow spheres and NPs.[9, 89, 94, 107, 108] The details of the photocatalytic water splitting mechanism and experimental setup will be discussed in section 1.5.1 and 2.6, respectively.

Similar to ZnO photoanode, the solar conversion efficiency of TiO_2 photoanode is also limited due to its large band gap (3.0–3.2 eV) which only allows it to absorb UV part of the solar emission. Numerous attempts have been carried out to improve the conversion efficiencies of the PEC cells such as extending the absorption spectrum of TiO_2 to the visible range by dye sensitisation or doping with species that introduce additional dopant state within the band gap of TiO_2. A number of dopants, such as nitrogen, carbon, sulphur, tin and the oxygen vacancy have been used to reduce the band gap of TiO_2 which lead to the increase of the PEC water splitting efficiencies.[3, 89, 109, 110] Xu M. *et al.* have reported that the introduction of tin into TiO_2 lattice caused a

reduction in the band gap energy and resulting in a two-fold enhancement in the solar-to-photon conversion efficiency when compared to the pristine TiO_2 photoanode.[110]

In 1991, Gratzel M. *et al.* reported a DSSC where a monolayer of charge transfer dyes has been deposited on the surface of TiO_2 crystals to increase the light harvesting and increase the solar conversion efficiency.[111] Other than organic dyes, quantum dots (*e.g.* CdSe and CdS) have also been introduced onto the surface of TiO_2 nanostructures to increase the solar conversion efficiency.[112]

1.3.3.2 Water and Air Purification

TiO_2 is the most commonly used photocatalysts for environmental applications. TiO_2 Degussa P-25 powder, consisting of 80% anatase and 20% of rutile with an average particle size of 30 nm, is widely used in the treatment of contaminated wastewater. Upon UV illumination, TiO_2 photocatalysts are able to generate superoxide radicals and hydroxide radicals which can oxidise most of the organic pollutants. Water purification processes are usually carried out in a photocatalytic reactor consisting a quartz tube, with an inlet tube for oxygen purging during photocatalysis and another outlet for the collection of samples from the reactor at different time intervals. A known amount of photocatalyst and a known concentration of pollutant(s) are mixed with DI water and poured into the photoreactor. During the reaction under light illumination, the concentration of the pollutant(s) is monitored as a function of time. Figure 1.10 is a schematic diagram of a typical photocatalytic reactor.

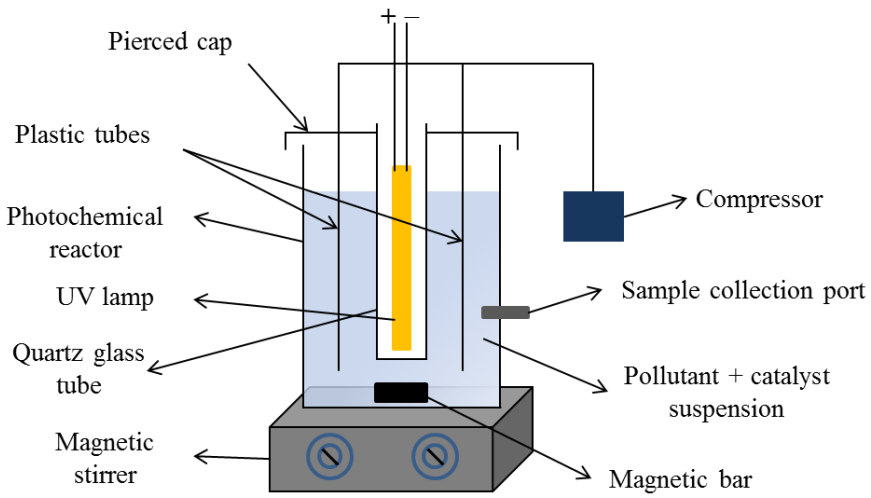

Figure 1.10 A schematic diagram of photocatalytic reactor.

Most of the organic pollutants in water can be completely degraded and mineralised at the surface of UV-excited TiO_2 photocatalysts, including alkanes, haloalkanes, aliphatic alcohols, carboxylic acids, alkenes, aromatics, haloaromatics, polymers, surfactants, herbicides, pesticides, and dyes.[86] Other than water pollutants, TiO_2 nanomaterials have also been used in degrading gaseous pollutants. One of the major air pollutants is volatile organic compounds (VOCs), which is originating mainly from industrial processes. It has been reported that the use of illuminated TiO_2 can not only effectively decompose VOCs, but also convert nitrogen oxides and sulphur oxides in the air.[113] Upon UV illumination, TiO_2 photocatalysts are able to oxidise and decompose the gaseous pollutants into carbon dioxide, water vapour and mineral acids.[86]

1.3.3.3 Biomedical Treatment

TiO_2 has also been widely used for medical purposes since it is nontoxic, biocompatible and chemically stable with excellent mechanical properties.[114] Porous TiO_2 nanostructures have been used for drug eluting coating for orthopaedic implants,

stimuli-responsive therapeutic systems, dental implants and vascular (coronary) stents.[114] Drug therapy is required for most of the medical procedures such as hip replacements, dental implants or vascular stents, in order to prevent infection, control clotting or decrease inflammation.[115] Delivery of drugs locally from an implant surface rather than systemically can reduce side effects. One of the commonly used strategies for drug elution is through a drug-loaded polymer coating for slow release. However, polymer degradation may induce in inflammatory response, activating phagocytes and increasing vascular smooth muscle proliferation, which can lead to implant failure.[114] Therefore, non-polymer based drug delivery implant platforms, such as nanoporous aluminium oxide and nanotubular TiO_2 are the focus in the newest development in drug eluting.[116]

TiO_2 NTs have an open end which can be used to carry drugs as a capsule for drug delivery. These tubes can be coated with proteins that can recognise viruses or cells which results in self-guided drug delivery. The drug release can also be controlled by UV light or X-ray radiation for *in vivo* treatments through living tissue.[117] Song Y.Y. *et al.* have proposed the use of amphiphilic tube layers in a payload filling and release mechanism.[118] These NTs have been loaded with hydrophilic drugs and are protected by a hydrophobic cap. The hydrophobic cap can be removed by photocatalytic oxidation, allowing aqueous body fluids to enter the tubes and flush out the desired drugs.

TiO_2 has also been used in cancer treatment. In 1986, Fujishima A. *et al.* demonstrated the use of strong oxidising power of illuminated TiO_2 to kill tumour cells.[119] Animal experiments implanting cancer cells under the skin of mice to cause the formation of tumour cells were conducted by Cai R. *et al.*[120] The experimental results showed that TiO_2 particles significantly supressed the growth of HeLa cells implanted in nude mice, however this technique was not effective in stopping a cancer that had

grown beyond a certain size. The experiments also showed that the photoactivity is effected by the illumination of the near UVA and UVB lights, with wavelengths in the range of 300–400 nm, which did not cause mutation to the healthy cell.

1.4 Bismuth Vanadate ($BiVO_4$)

1.4.1 Properties of $BiVO_4$

In order to study the visible light excited photocatalysis, we are also interested in metal oxides with a narrow band gap. $BiVO_4$ is an n-type semiconductor of bright yellow colour with band gap energies in the range of 2.9 to 2.4 eV, capable of absorbing green to blue light.[121] It has been identified as one of the most promising photoanode materials for photocatalytic water splitting due to its appropriate band edges.[121] There are three main types of $BiVO_4$ crystal structures which are pucherite (orthorhombic), scheelite (monoclinic or tetragonal) and zircon (tetragonal),[121] as shown in Figure 1.11. $BiVO_4$ prepared in the laboratory are usually crystallised either in a scheelite or a zircon type structure. Pucherite is obtained as mineral but it cannot be formed under normal laboratory conditions. For a zircon structure, vanadium ion is stabilised by four oxygen atoms in a tetrahedral site and bismuth is coordinated by eight oxygen atoms from six VO_4 units. For a scheelite structure, each vanadium ion is coordinated by four oxygen atoms in a tetrahedral site and each bismuth ion is coordinated by eight oxygen atoms from eight different VO_4 tetrahedral units. The only difference between tetragonal and monoclinic scheelite structure is that the local environments of vanadium and bismuth ions of monoclinic structure are more significantly distorted.

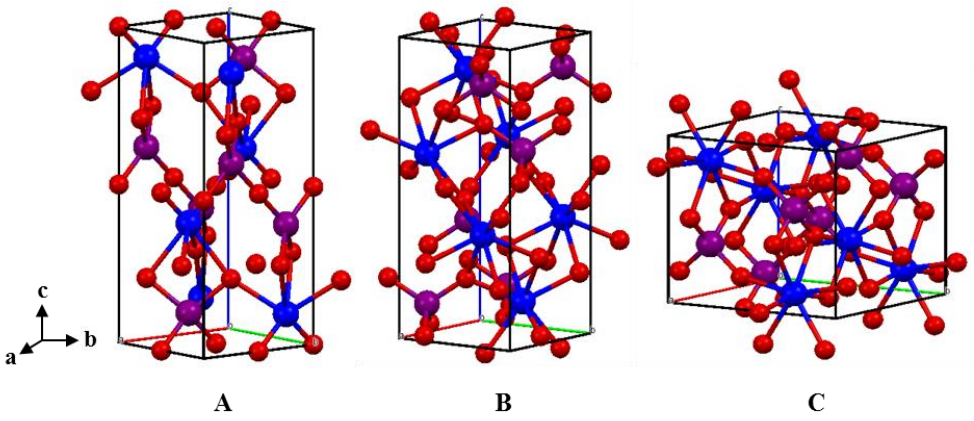

Figure 1.11 Crystal structures of $BiVO_4$, (A) pucherite, (B) scheelite and (C) zircon. Bismuth, vanadium and oxygen are purple, blue and red, respectively.

For tetragonal zircon-type $BiVO_4$, it has the lattice parameters $a = b = 7.303$ Å and c = 6.584 Å. Meanwhile, a tetragonal scheelite $BiVO_4$ has the lattice parameter dimensions $a = b = 5.147$ Å and c = 11.722 Å, whereby the monoclinic scheelite $BiVO_4$ has the lattice parameters $a = 5.194$ Å, $b = 5.090$ Å and $c = 11.697$ Å.[121] Tetragonal zircon-type structure of $BiVO_4$ is formed at low synthesis temperature, for instance, precipitation at room temperature. A phase transition from tetragonal zircon to monoclinic scheelite was reported to occur irreversibly at 400–500°C.[122] For scheelite structures, the phase transformation between the monoclinic and tetragonal structures was observed to occur reversibly at 255°C.[121] Both the tetragonal zircon phase and monoclinic scheelite phase of $BiVO_4$ were reported to have direct band gap energies of 2.9 eV and 2.4 eV, respectively.[122]

1.4.2 Synthesis of $BiVO_4$ Nanostructures

There are a number of different synthesis methods have been proposed for the fabrication of $BiVO_4$ nanostructures.[123] Different morphologies of $BiVO_4$ nanostructures have been reported, for instance, NRs, NWs, NTs, nanosheets,

nanoellipsoids, hollow spheres, worm-like nanoporous films, nanoplates, buckhorn-like nanodots, butterfly-like microparticles and microtubes.[123-127] In the following sections, the principle of synthesis techniques and the advantages and disadvantages will be studied.

1.4.2.1 Electrochemical Deposition Method

One of the simple solution methods for the creation of $BiVO_4$ nanostructures is electrochemical synthesis. In a typical electrochemical synthesis method, it consists of three electrodes which are a working electrode, a counter electrode and a reference electrode. These electrodes were immersed into a plating solution that contains ions and molecules that will participate in the electrochemical reactions, as shown in Figure 1.12. When an electrochemical potential is applied, a reduction (cathodic deposition) or oxidation reaction (anodic deposition) occurs on the working electrode. The species produced by the oxidation and reduction reactions trigger the deposition of desired materials onto the surface of working electrode.

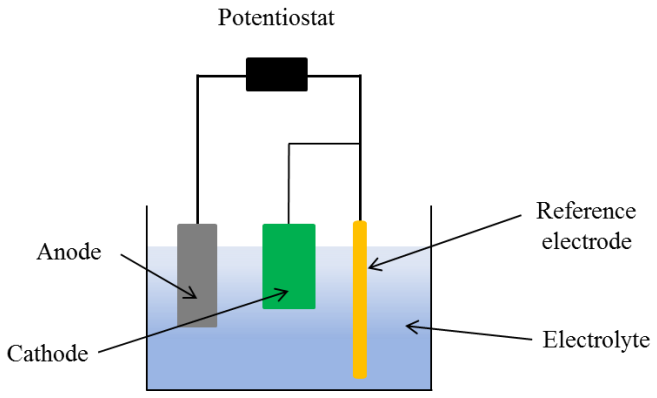

Figure 1.12 A schematic diagram of electrochemical deposition setup.

The first electrochemical synthesis of $BiVO_4$ was achieved by Myung N. *et al.* where the anodisation of a bismuth metal coated platinum electrode resulted in generation of Bi^{3+} ions, which reacted with V^{5+} in the solution and precipitated crystalline $BiVO_4$ on the working electrode.[128] Seabold *et al.* have reported the creation of $BiVO_4$ thin films using a different electrolyte.[129] In the experiment, a plating solution containing Bi^{3+} and V^{4+} ions was used. When the V^{4+} ions were oxidised to V^{5+} ions upon application of an appropriate voltage, the V^{5+} ions promptly reacted with Bi^{3+} ions to form an amorphous Bi–V–O film with a Bi:V ratio of 2:3. The film was thermally converted to crystalline $BiVO_4$ and V_2O_5. A pure $BiVO_4$ film was obtained by removing the V_2O_5 phase with 1.0 M KOH solution.

1.4.2.2 Metal Organic Decomposition Method

Metal organic decomposition (MOD) is the most commonly used technique for the preparation of $BiVO_4$ electrodes.[125, 130] In general, organometallic species containing Bi^{3+} and V^{3+} or V^{5+} ions are dissolved into a solution. The commonly used precursors are bismuth nitrate and vanadium acetylacetonate. The resulting solution is deposited onto a conducting substrate either by spin coating or spray pyrolysis, and crystalline $BiVO_4$ film is formed by heat treatment at a moderately high temperature (350–500°C) to decompose the organic precursors.

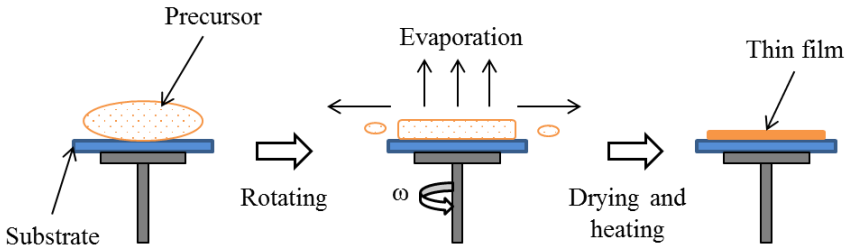

Figure 1.13 A schematic diagram representing the spin coating process.

MOD/spin coating method is the most widely employed technique for the fabrication of $BiVO_4$ electrodes, which was first reported by Sayama K. *et al.* in 2003.[131] Figure 1.13 is a schematic diagram illustrates the spin coating process. One of the advantages of the MOD/spin coating method is the easy composition tuning. Different dopants can be introduced into $BiVO_4$ films by adding dopant ions in the precursor solution. For example, Luo W. *et al.* have reported the creation of molybdenum doped $BiVO_4$ by adding molybdenum acetylacetonate into the precursor solution.[130] Similarly, Zhong D. K. *et al.* have reported the formation of tungsten doped $BiVO_4$ by incorporating tungstic acid into the precursor solution.[132]

1.4.2.3 Vacuum Deposition Method

$BiVO_4$ electrodes can also be synthesised through gas phase route by vacuum deposition methods such as ballistic deposition and reactive ballistic deposition. In these processes, a high vacuum chamber equipped with two electron beam evaporators are required to deposit bismuth and vanadium atoms in a 1:1 ratio onto a substrate.[133] The only difference between ballistic deposition and reactive ballistic deposition is that oxygen was introduced into the deposition chamber for reactive ballistic deposition as reactant gas.[121] The crystalline $BiVO_4$ electrodes were obtained by annealing the as-deposited films at 500°C in air. Recently, Berglund S. P. *et al.* have reported the fabrication of tungsten and molybdenum doped $BiVO_4$ electrodes through ballistic deposition where tungsten or molybdenum metal was co-evaporated with bismuth and vanadium metals.[134]

1.4.3 Applications of $BiVO_4$ Nanostructures

1.4.3.1 Photoelectrochemical Cells

As mentioned before (Section 1.4.1), $BiVO_4$ exists in three different types of structures, however only the thermodynamically stable monoclinic scheelite $BiVO_4$ exhibits good photocatalytic behaviour.[123] This is because monoclinic scheelite $BiVO_4$ owned a smaller band gap energy (2.4 eV) with a conduction band more negative than 0 V and a valence band more positive than 1.23 V with respect to normal hydrogen electrode (NHE). In addition, it has been reported that the distortion in monoclinic scheelite $BiVO_4$ could probably affect the charge separation and delocalisation of photogenerated electrons and holes, and thus improved the photocatalytic activity under visible light irradiation.[135]

Various morphologies of monoclinic scheelite $BiVO_4$ have been prepared and utilised as photoanodes for PEC water splitting application.[126, 127, 132] The theoretical solar-to-hydrogen conversion efficiency of $BiVO_4$ photoanode under AM1.5 G solar light has been calculated to be ~9.2% with a maximum photocurrent density of 6.3 mA cm^{-2}.[136] To date, however, the actual conversion efficiency achieved by $BiVO_4$ photoanodes is far smaller than the theoretical maximum value. This is because $BiVO_4$ has slow charge transportation, which leads to approximately 60%–80% of electron-hole pairs recombination before they reach at interfaces.[123] There are a number of approaches have been designed to overcome such problems. The incorporation of dopants with $BiVO_4$ films have been reported to increase the photoconversion efficiency. Luo W. *et al.* have shown that molybdenum doped $BiVO_4$ films exhibit a much higher PEC performance in water splitting than pristine $BiVO_4$.[130] The significant enhancement in PEC water splitting efficiency by doped $BiVO_4$ electrodes was due to the dopant increasing the carrier concentration and reducing the resistance. Another

effective way to address the poor electron mobility of $BiVO_4$ is forming a composite structure or heterojunction, which will be discussed in details in Chapter 8.

1.4.3.2 Water Purification

Other than photoelectrolysis of water, $BiVO_4$ nanomaterials have also been used as photocatalysts for water decontamination processes. $BiVO_4$ nanostructures have been used to decompose organic compounds such as methylene blue, rhodamine B and 4-*n*-nonylphenol in water.[137-139] Kohtani S. *et al.* compared the photocatalytic degradation of toxic surfactant 4-*n*-nonylphenol using $BiVO_4$ and TiO_2 (P-25) under simulated sunlight.[139] The results revealed that, under excess oxygen environment, a faster degradation of 4-*n*-nonylphenol was observed for $BiVO_4$, while similar activities to TiO_2 were found in air saturated medium. However, in contrast with TiO_2, there is no carbon dioxide evolution was observed with $BiVO_4$.

In order to further improve the photocatalytic activity, chemical modification of $BiVO_4$ with silver, platinum, palladium or copper oxide has also been tried.[137] Kohtani S. *et al.* have demonstrated the photocatalytic degradation of various aqueous pollutants using silver loaded $BiVO_4$.[140] The results showed that the silver loaded $BiVO_4$ has a higher photocatalytic degradation performance than pure $BiVO_4$, as well as a higher mineralisation degree. The enhancement was possibly due to either improved generation of superoxide radicals from silver or the improved charge separation from $BiVO_4$.

1.5 Specific Applications Used in This Thesis

1.5.1 Photoelectrochemical Water Splitting

The use of solar energy to split water for the generation of hydrogen from a photoelectrochemical (PEC) cell is one of the promising developments to replace fossil fuels.[141, 142] This is an ideal method to supply a clean and sustainable fuel since water is the only combustion product with high energy density (140 MJ kg^{-1}).[78] Metal oxide nanostructures have been widely explored and used as photoanodes for PEC water splitting due to their relative low cost, large surface area and scalability for production purposes.[142, 143]

The split of water into hydrogen and oxygen is an uphill reaction where a standard Gibbs free energy of 237 kJ mol^{-1} or 1.23 eV is required. To facilitate this reaction, the band gap of the photocatalyst should be larger than 1.23 eV.[142, 144] More important, the reduction and oxidation potentials of water should lie in between the band edges of the photocatalyst. Thus, the conduction band of the photocatalyst has to be more negative than the reduction potential of H^+/H_2 (0 V versus NHE), whereas the valence band has to be more positive than oxidation potential of O_2/H_2O (1.23 V_{NHE}). Other than having an appropriate band edge energy, there are some other critical criteria for an efficient water oxidation photocatalyst/photoanode, such as (i) high light absorption efficiency over a broad wavelength to make full use of the solar energy; (ii) effective charge carrier transfer and charge separation to suppress charge recombination; (iii) sufficient surface area to provide enough active sites; (iv) fast surface reaction kinetics for oxygen evolution; and (v) high chemical stability in electrolytes.[123]

Water photoelectrolysis using a PEC involves several processes within the photoelectrodes and at the photoelectrode/electrolyte interface.[145] In general, the

processes in photocatalytic generation of hydrogen of photocatalysts consists of three steps, including:

1. Upon illumination, photoexcited electrons and holes will be created at the conduction and valence bands, respectively.
2. The photoexcited electrons will migrate to the surface of counter electrode, meanwhile the photogenerated holes will move to the surface of the photocatalysts.
3. These separated electrons and holes will carry out redox reactions at the electrode surfaces with the chemical species (electron donors or acceptors) in the electrolyte to generate hydrogen and oxygen.

For an n-type semiconductor photocatalyst, the holes at the valence band created by band gap excitation of the film will migrate to the electrode surface to oxidise water to oxygen (Equation 1.3).

$$4h^+ + H_2O_{(aq)} \rightarrow O_{2_{(gas)}} + 4H^+{}_{(aq)} \qquad \text{(Equation 1.3)}$$

$$4H^+{}_{(aq)} + 4e^- \rightarrow 2H_{2_{(gas)}} \qquad \text{(Equation 1.4)}$$

Meanwhile, the conduction band electrons will travel through the underlying substrate to reach to the counter electrode, platinum foil, to reduce the water to hydrogen, as shown in Equation 1.4. On the contrary, for a p-type semiconductor photocatalyst, the opposite reaction will occur where oxygen and hydrogen will be evolved at the counter electrode and photocathode, respectively.

Currently, the photocatalytic water splitting research is focused on the low-cost and Earth-abundant elements that exhibit promising solar-to-hydrogen conversion efficiencies. To date, the highest photoconversion efficiency of 14% was achieved by

using a titanium dioxide-coated indium phosphide photocathode.[146] Lately, Earth-abundant transition metal based materials have also been widely studied as oxygen evolution catalysts (OECs). These catalysts can effectively overcome the oxygen evolution overpotentials of the photoanodes and thus improve the overall water splitting efficiency.[10, 147, 148] For instance, Kim T. W. and Choi K.-S. have demonstrated the use of dual-layer OECs (FeOOH and NiOOH) on the nanoporous $BiVO_4$ photoanode to achieve a photoconversion efficiency of 1.72%.[10] Recently, Luo J. *et al.* have achieved a solar-to-hydrogen conversion efficiency of 12.3% driven by perovskite photovoltaics.[147] These recent studies show the potential towards commercial PEC water splitting devices.

1.5.2 Gas Ionisation Sensor

In the past decades, gas sensors based on the metal oxide semiconductors have been studied in diverse field for wide applications.[70, 149] Various nanostructured metal oxides have been applied in gas sensor such as SnO_2,[8] TiO_2,[150] ZnO,[151] WO_3,[152] Fe_2O_3[153] and In_2O_3.[154] There are two different types of gas sensors, which are chemical type and physical type of sensors. For a chemical type gas sensor, it is operated through the adsorption and desorption of gas molecules on the surface of the sensing materials, which affects the conductivity of the nanomaterials. Meanwhile, the physical type gas sensor detects gas through electric field ionisation. In general, there are a few basic criteria for a high quality and efficient gas sensing system: (i) high sensitivity and selectivity; (ii) fast response time and recovery time; (iii) low operating voltage and temperature and (iv) high stability in performance.

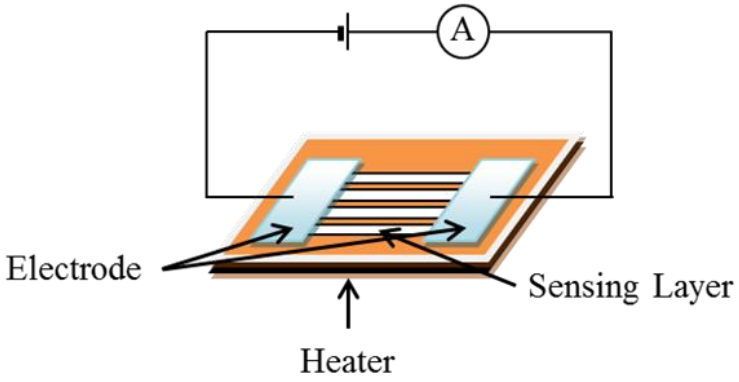

Figure 1.14 A schematic diagram of a chemical type gas sensor device.

To date, most of the conventional gas sensors are chemical type and the active layer are usually made up of metal oxide nanostructures,[69] porous silicon[155] and CNT[21, 156]. The sensing mechanism of this type of sensor is based on the changes in the electrical properties by the adsorption of gas molecules on the surface of the active layer, which causes a large variation in the electrical resistance.[157, 158] Figure 1.14 is a schematic diagram illustrates the chemical type of gas sensor device. In this device, a heating element is used to elevate the sensor's temperature in order to increase the responses and to reduce the recovery times. For the sensing layer, two different types of metal oxide nanostructures, n-type and p-type, are widely used.[159-161] The electrical resistance of these types of metal oxide nanostructures decreases when the temperature increases due to their semiconducting properties and the increasing of the surface oxygen vacancies.[60] There were however, some drawbacks for this type of gas sensors, where it suffers from selectivity issues. A high working temperature also restricts its applications.[162, 163] In addition, chemical type sensors have difficulty in detecting gas with poor adsorption.[70, 164]

In this work, we focus on the physical type gas sensors, gas ionisation sensors (GISs), which operate at room temperature. Its principle is based on the fingerprint ionisation energy of different gases.[162] When compared to chemical type gas sensors,

GISs are not restricted by the electrophilicity or adsorption energy of the gases. Since the first demonstration of miniaturised GISs using CNTs in 2003,[72] much attention has been paid to metal oxide nanostructures, including CuO NWs,[164] TiO_2 NTs,[165] Si NWs,[166] ZnO NRs[167] and NWs,[168] as they are more stable towards oxidation in oxygen environment. For a high performance GIS, the electric field should be focused on the top surface of the nanomaterials and this can be achieved by using vertically aligned metal oxide NRs or NWs with sharp tips and with high conductivities.[71]

1.6 Thesis Overviews

The thesis is devised of 10 chapters, the first 2 of which will provide the review of relevant metal oxide nanomaterials. Both the synthetic methods and their applications are discussed in Chapter 1. The characterisation techniques used in this work, including scanning electron microscopy (SEM), X-ray diffraction (XRD), UV-visible (UV-vis) spectroscopy and electrochemical impedance spectroscopy (EIS) will be discussed in Chapter 2. Additionally, the experimental setup of photocatalytic water splitting and gas ionisation sensing will also be explained in Chapter 2.

The experimental details for the preparation of ZnO NTs and NRs through CBD method will be described in Chapter 3. The purpose of growing ZnO NTs was to increase the effective surface area of ZnO NRs and thus enhanced the photocatalytic water splitting performance. In this experiment, the growth mechanism and optical properties of the created NRs and NTs were studied. The effect of the volume of growth solution on the morphology of NRs and NTs were explored. The performances of ZnO NRs and NTs as photoanodes in PEC water splitting were evaluated.

After the growth of ZnO NRs, a novel nanomaterial, urchin-like ZnO NR arrays on TiO_2 hollow hemispheres (HHSs) were created through the combination of

electrospinning and CBD methods. The aim of employing two different metal oxides as the photoanode material was to create dipole at the interface for reducing the electron-hole recombination which thus increased the photoconversion efficiency. In Chapter 4, the growth mechanism and a series of calcination studies for the urchin-like composite samples were studied. The effect of the calcination temperature on the PEC water splitting performance was investigated.

Although the urchin-like sample revealed a significant improvement in the photocatalytic water splitting activity, the large band gap energies of TiO_2 and ZnO only allow them to absorb UV light. In order to improve the light absorption for photocatalytic water splitting, Chapter 5 concentrates on the synthesis of doped ZnO NRs using the CBD method. A number of dopants were used in this experiment and the effects of the dopants on the morphologies and optical properties of the doped samples were studied. The photocatalytic water splitting performances of the doped ZnO NRs were measured and compared with the pristine ZnO NRs.

In Chapter 6, a novel direct heating method for the growth of ZnO NRs onto a stainless steel (SS) mesh has been developed. The purpose of growing ZnO NRs on SS mesh was to overcome the problem of poor light absorption, small effective surface area and high electron-hole recombination rate by a planar photoanode. Here, the growth mechanism of the NRs using this novel method was proposed. A comparison of the PEC performances between ZnO NRs prepared on SS mesh and that prepared on SS plate was also carried out. In order to increase the light harvesting and thus increase the photoconversion efficiency, multilayers of ZnO NRs on SS meshes were used as a photoanode for photoelectrolysis of water.

In order to increase the gas sensitivity and selectivity of ZnO NRs based gas ionisation sensors, the effect of ZnO conductivity was studied by introducing yttrium

atoms into ZnO. Chapter 7 concentrates on the preparation of Y-doped ZnO NRs through the hydrothermal method and its application as gas ionisation sensor. The effect of Y concentration on the morphology, optical properties and electrical properties of the created nanomaterials were examined. The undoped and Y-doped ZnO NRs were used as anodes in gas ionisation sensing applications. The effect of UV illumination on the gas sensors was examined.

A highly ordered 1D $BiVO_4$ nanoporous film coated on ZnO NRs was created through the combination of MOD/spin coating and CBD methods, as described in Chapter 8. The purpose of employing two different metal oxides as the photoanode material is to extend the light absorption of the sample to the visible region of solar spectrum. A comparison of the photocatalytic water splitting performances between the hybrid sample, bare ZnO NRs and $BiVO_4$ nanoporous film was performed.

Chapter 2 Characterisation

2.1 Abstract

In this chapter, I will discuss the technical details of the instruments and methods used to characterise the structures and properties of the nanomaterials created in this project. The materials prepared in this thesis are novel in morphology and composition. Scanning electron microscope was used to quantitatively study the morphology of the nanostructures. Energy dispersive X-rays spectroscopy was used to evaluate the chemical compositions of the composite materials. The crystal structure and crystal orientation of the materials were characterised by powder X-ray diffraction. The optical properties of the materials were examined by UV-visible spectrophotometer. The intrinsic properties of the materials were determined by electrochemical impedance spectroscopy. Photoelectrochemical testing is an important characterisation technique to evaluate the efficiency of the created materials as photoanode in photocatalytic water splitting. Gas ionisation sensing is another crucial application for determining the selectivity and sensitivity of the created materials as anode of gas ionisation sensor.

2.2 Scanning Electron Microscopy

Scanning electron microscope (SEM) is one of the commonly used instruments to analyse the morphology and to characterise the chemical composition of the as-prepared materials.[169] Electron microscopy is like optical microscopy but it gives a better resolution by using high energy and short wavelength electron beam. This interaction will generate signals which contain information about the sample's surface

composition and topography. For our SEM, a high energy electron is generated from a tungsten filament through thermionic emission,[170] accelerated at a typical energy in the range 10–30 kV. This high energy electron beam is finely focused through several electrostatic and electromagnetic lenses before reaching onto the sample.

In SEM, it is an inelastic scattering (secondary electrons) which provides morphological information on the specimen to be analysed. After the bombardment, both backscattered electrons and secondary electrons are released from atoms close to the surface of the sample to construct a SEM micrograph. In addition, X-ray can also be emitted by relaxation of electrons to the lower orbitals which give elemental information of the sample.

Secondary electron image is the most commonly used signal in SEM with high resolution. Secondary electrons are low energy electrons (typically 10–300 eV) which are emitted a few nanometres from the sample surface (< 10 nm). This signal provides the topographic details on the surface. Secondary electrons are generated through the Auger process by a high energy electron beam scattering process. The incidence of the high energy electrons cause the ionisation by losing an electron at the core level. The upper level electron will relax into the core level causes the emission of another electron, which is called as Auger electron. The advantage of using secondary electrons to image the surface is that the low energy of the electron allows it to be separated from the primary electron (beam) in the background, achieving a good image contrast.

Backscattered electrons are high energy incident electrons which undergo elastic interactions with the sample surface. The backscattered electron detector (not installed in our SEM) is usually positioned very close to both the target surface and electron beam. Unlike secondary electrons, backscattered electrons are generated from the electrons penetrate a few microns depth from the sample surface. The intensity of the

backscattered electrons is related to the density and the atomic number of the sample. Therefore it gives additional contrast due to the difference in atomic species.

In addition to secondary electron and backscattered electron detections, SEM can also be used to identify the composition of the materials based on X-ray fluorescence by an X-ray detector. The energy dispersive X-ray (EDX) detector measures the X-ray energy created through the bombardment of the electrons striking the surface of sample. These X-rays are emitted after a core electron is emitted and an upper electron relaxes to the core level. The energy of the emitted X-rays is distinctive for each atom and can be used to determine the chemical composition. The intensity of the fluorescence is proportional to the amount of the element in the sample.

2.3 X-ray Diffraction

Crystal structure and crystal orientation of nanomaterials can be identified using an X-ray diffractometer (XRD). The diffraction technique depends on the interference between waves reflected from the periodic arrangement of atoms within the crystals.[171] The X-rays strike on the surface of a crystal structure and are partially reflected by the atoms in the lattice. This will cause the occurrence of constructive or destructive interference of the diffracted waves at certain angles. The angle at which constructive interference occurs is defined by the spacing between the planes of the lattice and the wavelength of the X-ray; following the Bragg's law:[172]

$$n\lambda = 2d\ sin\theta \qquad \text{(Equation 2.1)}$$

where *n* is an integer, λ is the wavelength of the X-ray (Cu–K_α = 1.54056Å), *d* is the spacing in between the planes in the atomic lattice and θ is the angle of incidence X-ray. Figure 2.1 is a schematic diagram illustrates the reflective diffraction geometry.

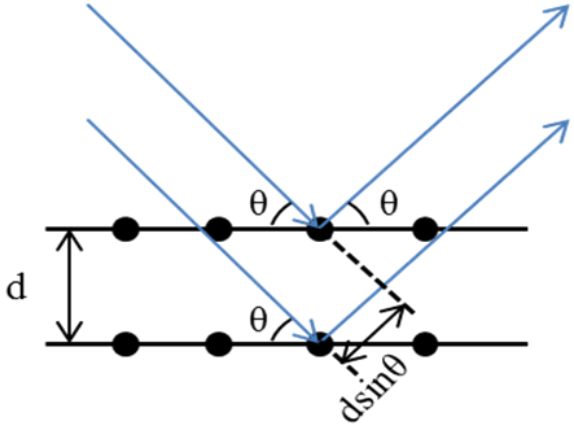

Figure 2.1 A schematic diagram illustrates Bragg's law.

In a powder diffraction, the crystal structure of the sample can be identified by the characteristic diffraction peaks. The position of the peaks are determined by the lattice spacing of the sample and this can be used to calculate the lattice constants of the nanostructures. In this work, ZnO is the main metal oxide being used and the structure of ZnO is hexagonal, thus the separation between crystal planes follows:[173]

$$\frac{1}{d^2} = \frac{4}{3}\left(\frac{h^2 + hk + k^2}{a^2}\right) + \frac{l^2}{c^2} \qquad \text{(Equation 2.2)}$$

where *h*, *k* and *l* are the Miller indices representative of a particular set of equivalent parallel planes, *a* and *c* are the lattice constants. Based on the calculated lattice constants 'a' and 'c', the bond length of the sample can be evaluated using the following relationship:[174]

$$L = \left[\frac{a^2}{3} + \left(\frac{1}{2} - u\right)^2 c^2\right]^{1/2} \quad \text{(Equation 2.3)}$$

where the u parameter depends on the structure of the materials. For ZnO, it is wurtzite structure and can be expressed as:

$$u = \frac{a^2}{3c^2} + 0.25 \quad \text{(Equation 2.4)}$$

In addition, the diffraction peaks also show a different line width, which is corresponding to the crystal grain size and is also affected by the density of defects. The peak width is inversely proportional to the averaged crystal size of the materials. The crystal domain of the nanostructures can be quantitatively described by Scherrer's equation:[175]

$$D = \frac{K\lambda}{\beta\ cos\theta} \quad \text{(Equation 2.5)}$$

where D is the crystalline diameter, K is the shape factor (0.89 in this work), λ is the wavelength of the X-ray source (Cu target, λ = 1.541 Å), θ is the Bragg angle of the diffraction peak (in degrees) and β is the linewidth of the diffraction peak corrected for instrument broadening (in radians), defined as:

$$\beta = \sqrt{B_M^2 - B_I^2} \quad \text{(Equation 2.6)}$$

where B_M is the measured linewidth (FWHM in radians) and B_I is the instrumental broadening (also in radians) which is determined by the linewidth (FWHM) from standard crystallised particles of size > 200 nm.

For oriented nanostructures, for instance, ZnO NRs or NWs, the peak height will be intense at Bragg angle corresponding to the preferred orientation. Based on the normalised intensities of these diffraction peaks, the degree of orientation of the nanostructures can be determined by the relative texture coefficient. For ZnO nanostructures, [0001] is the most favoured growth direction, which is along the (002) plane, thus the equation is proposed below:[176]

$$TC_{002} = \frac{I_{002}/I^{\circ}_{002}}{I_{002}/I^{\circ}_{002} + I_{101}/I^{\circ}_{101}} \qquad \text{(Equation 2.7)}$$

where TC_{002} is the relative texture coefficient of diffraction peaks (002) over (101), I_{002} and I_{101} are the measured diffraction intensities of (002) and (101) planes, respectively. I°_{002} and I°_{101} are the corresponding values of standard PDF measured from randomly oriented NR. The relative texture coefficient achieved by ZnO powder with random crystallographic orientation is 0.50. For a perfect vertically aligned NRs or NTs, the texture coefficient is 1.0.

2.4 UV-Visible Spectrophotometry

The optical properties of the metal oxide semiconductors are usually examined by UV-visible (UV-vis) spectrophotometer. The light absorption properties of the materials are of major interest in semiconductor nanomaterials since it can be used to calculate the optical band gap energy. Band gap determination of nanomaterials using

this spectroscopic technique may allow one to test and optimise the band gaps with the aim of harvesting a large solar spectrum when they are used as photoanodes in photovoltaic application.

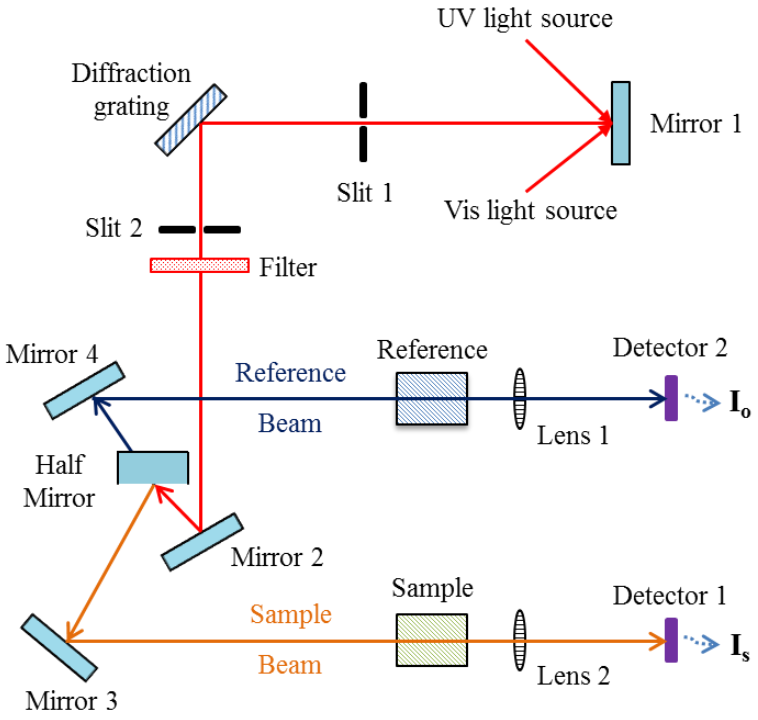

Figure 2.2 A schematic diagram of UV-vis spectrophotometer.

The principle of a double beam UV-vis spectrophotometer is relatively straight forward, as presented in Figure 2.2. UV and/or visible light source generate a beam of light (red) and is focused onto a diffraction grating which spreads the incoming light into its component colours of different wavelengths as a function of exit angle. The monochromated beam is then split into two equal intensity beams (blue and orange) by a half mirror device. One of the beam will be used to study the absorption of sample, meanwhile the other beam will be used to determine the absorption of reference. The intensities of these light beams are then measured by detectors, and the resultant light intensities are named as I_o for reference and I_s for sample. After the sample absorbs part

of the light, the intensity of the beam detected, I_s, will be less than I_o and this difference will be plotted on a graph as a function of wavelength. The transmittance and absorbance of the sample is defined:[177]

$$T = \frac{I_s}{I_o} \quad \text{(Equation 2.8)}$$

$$A = -\log_{10}\frac{I_s}{I_o} \quad \text{(Equation 2.9)}$$

where *T* and *A* are the transmittance and the absorbance of the sample. The absorbance of a sample will be proportional to its molar concentration and optical path length. Thus, a corrected absorption value, molar absorptivity, is used when comparing the spectra of different compounds and is defined as the Beer-Lambert Law:[177]

$$\alpha = \frac{A}{bc} \quad \text{(Equation 2.10)}$$

where α is the molar absorptivity, *b* is the length of the beam in the absorbing medium and *c* is the concentration of the absorbing species.

For metal oxide semiconductors, each material exhibits different absorption edge and this value corresponds to their band gap energy. The optical band gap of the samples can be related to the absorption coefficient and photon energy from the following Tauc expression:[178, 179]

$$(\alpha h\upsilon)^{1/n} = A_o\left(h\upsilon - E_g\right) \quad \text{(Equation 2.11)}$$

where E_g is the band gap energy, α is the absorption coefficient, h denotes the Planck's constant, υ represents the frequency of the incident photon, A_o is a constant that depends on the electron-hole mobility of the material and n depends on the nature of transitions of the semiconductor. n has the values of ½ and 2 for allowed direct and indirect transitions, respectively. For a thin film, the absorption coefficient can be defined as below:[180]

$$\alpha = \left(\frac{1}{t}\right) ln\left(\frac{1}{T}\right) \qquad \text{(Equation 2.12)}$$

where t is the film thickness as measured from the cross-sectional SEM image, and T is the optical transmittance. The band gap energy of a direct band gap material can be estimated from the x-intercept of the tangent line in the plot of $(\alpha h\upsilon)^2$ versus $h\upsilon$.[180]

The Tauc plot method was initially derived and proposed by Tauc J. for calculating the band gap of amorphous semiconductors with an indirect transition.[180] There are many modern examples of such use to determine the band gaps of both amorphous and crystalline semiconductors, for instance, crystalline rutile TiO_2,[181] amorphous selenium-antimony thin films,[182] and the effects of temperature on crystallinity of zinc-indium-tin oxide films.[183] Earlier analysis by Tauc *et al.* in 1966 found that the momentum is not conserved in a direct transition,[184] however recently researchers proved that this type of plot can still be used for semiconductors with direct band gaps.[181, 183]

Crystal defects or dopant ions in the lattice of semiconductors will cause the formation of band tailing in the band gap, resulting in an exponential tail at the edge of the optical absorption.[185] This tail is defined as the Urbach tail corresponding to the width of the localised state available in the optical band gap that affects the optical band

gap structure and optical transitions. In the exponential edge region, Urbach rule is expressed as below:[186]

$$\alpha = \alpha_o \exp\left(\frac{h\upsilon}{E_u}\right) \quad \text{(Equation 2.13)}$$

where α_o is a absorption constant of a defect free single crystal, E_u is the Urbach energy which characterises the slope of the exponential edge. The Urbach plot and the following relation were used for the E_u calculation of the samples:

$$E_u = \left[\frac{d(\ln \alpha)}{d(h\upsilon)}\right]^{-1} \quad \text{(Equation 2.14)}$$

The value of the E_u was obtained from the inverse of the slope of ln α as a function of $h\upsilon$. A large E_u value indicates the presence of structural disorder and defects in the film.[187] The E_u values can be reduced by increasing the crystal quality of the materials through annealing process.

2.5 Electrochemical Impedance Spectroscopy

Electrochemical impedance spectroscopy (EIS) is an instrument which is carried out to assess the electrochemical behaviour of electrode and/or electrolyte materials.[188] In general, electrical stimulus (a known voltage or current) is applied to the electrode and the response is recorded (the resulting current or voltage). When the electrode/cell is electrically stimulated, there are a number of processes take place which include the transport of electrons through the electronic conductors, the transfer of electrons at the

interface of electron and electrolyte and the flow of charged atoms or atom agglomerates via defects in the electrolyte.[189, 190]

EIS can be used to study any intrinsic property that affects the conductivity of an electrode-materials system or an external stimulus. Usually two categories of parameters can be derived from EIS spectrum which are: (i) those related to the materials itself only, for instance, conductivity, dielectric constant, carrier mobility and bulk generation-recombination rates; and (ii) those pertinent to the interface of electrode and electrolyte/gas, such as rate constants of adsorption reactions, diffuse coefficient of neutral species in the electrode and capacitance of the interface region.[189] For an EIS measurement, a small amplitude of sinusoidal alternating current (AC) voltage is added on a direct current (DC) bias $V(t)$, and the amplitude and phase angle (θ; relative to the applied voltage) of the resulting current, $I(t)$ is measured. Based on this, the impedance, $Z(\omega)$, can be determined by using Ohm's law:[191]

$$V(t) = V_o + V_m \sin(\omega t) \quad \text{(Equation 2.15)}$$

$$I(t) = I_o + I_m \sin(\omega t + \theta) \quad \text{(Equation 2.16)}$$

$$Z(\omega) = \frac{V(t)}{I(t)} \quad \text{(Equation 2.17)}$$

where V_o and I_o are the DC bias potential and the steady-state DC current flowing through the electrode, respectively, V_m and I_m are the amplitude of AC voltage and current. θ is the phase difference between applied AC voltage and the resultant current. The $Z(\omega)$ can be simplified in terms of orthogonal system of axes rather than polar coordinates:

$$Z(\omega) = Z' + jZ'' \quad \text{(Equation 2.18)}$$

where the j is the imaginary number $\left(j = \sqrt{-1}\right)$, Z' is the real part of impedance and Z'' is the imaginary part of impedance. This may be plotted in the plane with either rectangular or polar coordinates,[189] as shown in Figure 2.3.

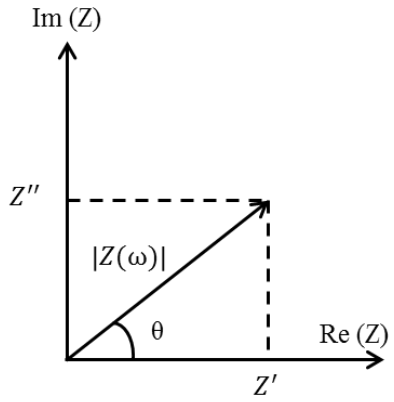

Figure 2.3 The impedance, Z plotted as a planar vector using polar coordinates.

Here, the real and imaginary parts of impedance can be expressed as follow:

$$Z' = |Z(\omega)|\cos(\theta) \quad \text{(Equation 2.19)}$$

$$Z'' = |Z(\omega)|\sin(\theta) \quad \text{(Equation 2.20)}$$

with the phase angle, θ and the total impedance, $|Z(\omega)|$ can be defined as:

$$\theta = \tan^{-1}\frac{Z''}{Z'} \quad \text{(Equation 2.21)}$$

$$|Z(\omega)| = [(Z')^2 + (Z'')^2]^{1/2} \quad \text{(Equation 2.22)}$$

In order to analyse the response of the charge mobility within the material, an AC signal with a range of frequencies, ω, can be applied to generate an impedance spectrum. Generally, the range of the frequencies are from 10 kHz to 100 mHz and the amplitude of sinusoidal bias is set at 10 mV. The resulting real and imaginary impedance data is used to evaluate the kinetics of charge transfer properties of the materials at the interface of electrode and electrolyte. A curve of imaginary part of impedance (Z'') versus real part of impedance (Z') is plotted, named as Nyquist plot. The smaller the semicircle/arc radius of the EIS Nyquist plot indicates the larger the oxide layer capacitance which may lead to higher charge density at the interface of electrode and electrolyte.[192] This will increase the interfacial charge transfer to the electron donor and/or electron acceptor, thus a slower rate of charge recombination.[34, 193]

Other than that, EIS is commonly used to measure the capacitance of materials in the electrolyte in the dark. The capacitances at the interface of semiconductor and electrolyte are calculated by an equivalent electrical circuit. Based on the measured capacitances, the flatband potential and the carrier density of the semiconductor material can be evaluated using Mott–Schottky (M–S) equation:[125]

$$\frac{1}{(C_{SC})^2} = \frac{2(V_E - V_{FB} - {kT}/{e})}{e\varepsilon\varepsilon_o N_D A^2} \qquad \text{(Equation 2.23)}$$

where C_{SC} is the capacitance between semiconductor and electrolyte, V_E is the applied voltage, V_{FB} is the flatband potential, k is the Boltzmann constant, T is the temperature, e is the electron charge, ε is the dielectric constant of the semiconductor, ε_o is the permittivity of free space, N_D is the number of donor density and A is the area contacted

with electrolyte. A linear plot of $\frac{1}{(C_{SC})^2}$ versus V_E is generated, named as M–S plot. The V_{FB} can be determined from the intercept on the *x*-axis from the M–S plot. V_{FB} is the potential that has to be imposed over the interface between the electrode and electrolyte to make the bands flat.[192]

Additionally, the slope of the M–S plot can be used to determine whether the material is an n-type or p-type semiconductor. For n-type semiconductors, positive M–S slopes will be obtained and conversely, negative M–S slopes will be attained by p-type semiconductors. The slope of the M–S plot can also be used to calculate the charge carrier density of the material using the following equation:[194]

$$N_D = \frac{2}{e\varepsilon\varepsilon_o}\left[\frac{d\left(1/C^2\right)}{dV}\right]^{-1} \qquad \text{(Equation 2.24)}$$

where e is 1.6×10^{-19} C, ε_o is 8.86×10^{-14} F cm^{-1} and ε is the dielectric constant of the material. The smaller the slope of the M–S plot suggests the larger the carrier concentration.

Once the V_{FB} and donor density of the samples are determined, the width of the space-charge layer (W) at the interface of semiconductor and electrolyte can also be derived from M–S plot relationship as:[195]

$$W = \left[\frac{2\varepsilon\varepsilon_o(V - V_{FB})}{e_o N_D}\right]^{1/2} \qquad \text{(Equation 2.25)}$$

The formation of space-charge layer is due to the electrolyte containing strong oxidising species, so electrons will pass through the interface between the electrode and electrolyte from the semiconductor into the solution until an equilibrium is achieved (Fermi level is equal to redox potentials). This electron transfer from semiconductor to electrolyte will cause the conduction or valence band to move relative to the Fermi level. Therefore, a band bending is formed, resulting in a "space charge region" or a depletion layer.[196]

2.6 Photoelectrochemical Water Splitting

In this thesis, a standard three-electrode configuration photoelectrochemical (PEC) cell was used in the photocatalytic water splitting measurements, as illustrated in Figure 2.4. A semiconductor thin film was used as a photoanode and a platinum foil was used as a counter electrode. In this work, a KCl saturated Ag/AgCl electrode was used as a reference. There are several scales in which the potential can be referenced to, and the most common form is the reversible hydrogen electrode (RHE).

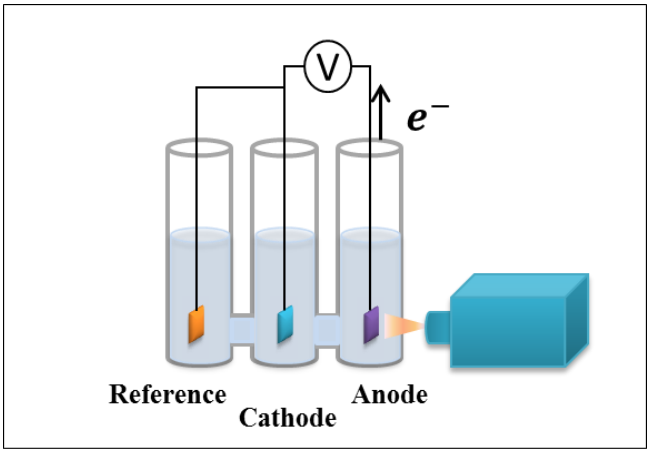

Figure 2.4 A schematic diagram illustrating the principle of a PEC cell using a standard three-electrode configuration.

The pH of electrolyte will cause a shift in the oxidation and reduction potentials of water with respect to the RHE according to the Nernst equation:[197]

$$E_{RHE} = E_{Ag/AgCl} + 0.059pH + E^{\circ}_{Ag/AgCl} \quad \text{(Equation 2.26)}$$

where E_{RHE} is the potential versus RHE, $E_{Ag/AgCl}$ is the measured potential versus Ag/AgCl reference electrode and $E^{\circ}_{Ag/AgCl}$ is 0.1976 V at 25°C. Different electrolytes were used in this work determined by the chemical stability of the metal oxide in different pH environments. Two different electrolyte solutions, 1.0 M KOH (pH 13.6) and 0.5 M Na_2SO_4 (pH 6.8), have been used in this work. The potentials of 1.23 V_{RHE} for these electrolytes are equivalent to 0.23 $V_{Ag/AgCl}$ and 0.63 $V_{Ag/AgCl}$, respectively.

The performance of the PEC cells is determined by calculating its photoconversion efficiency. The photon-to-hydrogen efficiency of the photoanode can be calculated from the following equation:[78, 198]

$$\eta\ (\%) = \frac{J_p\left(E^{\circ}_{rev} - E_{app}\right)}{I_o} \times 100 \quad \text{(Equation 2.27)}$$

where η is the conversion efficiency of the photoanode, J_p is the photocurrent density (mA cm^{-2}), E°_{rev} = 1.23 V, $E_{app} = E_{meas} - E_{oc}$ where E_{meas} is the working electrode potential (versus Ag/AgCl) and E_{oc} is the working electrode potential (versus Ag/AgCl) under the open circuit condition (J_p = 0 mA cm^{-2}) whilst illuminated, and I_o is the incident light power intensity. In this work, the sunlight was simulated with a 300 W xenon arc lamp with an AM1.5 G filter. The output light power intensity was adjusted

to 100 mW cm^{-2}. The optical power density was calibrated by a power meter (Newport 1830-C) with a wide band sensor (Newport 818-UV attenuated).

2.7 Gas Ionisation Sensor

The physical type sensor, gas ionisation sensor (GIS) device is made up of a counter electrode (usually Al or Cu), a sensing layer (metal oxide NRs) sandwiched between two conductive electrodes and an insulating spacer with a thickness between 50~200 μm, as demonstrated in Figure 2.5. When a voltage is applied between two electrodes, individual metal oxide will create a high electric field near the tips, which will ionise gases flowing between two electrodes.[35, 199, 200]

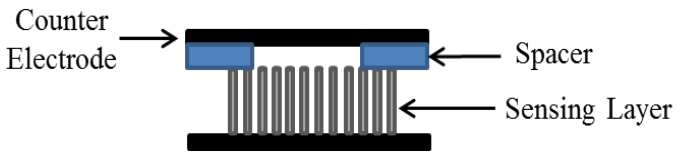

Figure 2.5 A schematic diagram of a metal oxide based GIS device.

The ionisation of the detected gas are caused by the collisions of the molecules with accelerated electrons.[201] This induces the formation of a self-sustaining inter-electrode discharge at breakdown voltage. The breakdown voltage of the gases is determined by the bonding energy of the gas molecules, which is unique for each type of gas molecule. The discharge current is dominated by the amount of gas molecules per unit volume and is related to the partial pressure of gas molecules.[149]

Chapter 3 Marangoni Ring-templated Growth of Vertically Aligned ZnO Nanotube Arrays with Enhanced Photocatalytic Hydrogen Production

3.1 Abstract

We report the facile synthesis of vertically aligned hexagonal ZnO NT arrays and their use as photoanodes in the photoelectrochemical (PEC) generation of hydrogen from water splitting. A polymer based seeding solution was coated onto titanium substrates to form ring structures through the Marangoni mechanism, guiding the growth of ZnO NTs with aqueous chemical bath deposition (CBD). The correlation between the amount of the growth solution and the nanostructure morphologies was investigated. With increased amount of growth solution, the diameter, wall thickness and length of the NTs were increased linearly. The PEC measurements revealed that the ZnO NT anode (0.45%) was about three times more effective than the ZnO NR anode (0.15%) in the photoenergy conversion in water splitting. The results demonstrated that the tubular ZnO arrays have substantial potential for PEC generation of hydrogen applications.

3.2 Introduction

The large ion transport channels and good electrical contact with the substrates of the nanostructured tubular materials (micro-, and nano-tubes) have attracted extensive investigation for almost two decades.[7, 143, 202-204] Since carbon nanotubes (CNTs) were first reported in 1991,[7] a great number of metal oxide semiconductor

tubular microstructures and nanostructures have also been designed and synthesised, which lead to the development of wide potential applications.[205-207]

Among the various inorganic tubular materials, microtubes and NTs of ZnO have received great attention.[208-212] This is because ZnO semiconductor has many outstanding properties and has shown promising potential in various applications, due to the direct band gap of 3.37 eV, large exciton binding energy (60 meV) and its piezoelectric effect.[213] Different approaches have been reported for the fabrication of ZnO tubular structures. The first one is a dissolution method which involves a two-step process.[214] Solid forms of 1D crystallised ZnO NRs were formed followed by dissolution of the polar (002) plane of the rod structures.[215, 216] In this method, a precise control of the dissolution kinetics and sufficient ion transportation were essential, which limits reproducible good quality NT morphology. The second strategy is to use metallic zinc NWs as a template where ZnO was formed on the surfaces of NWs. The metallic cores were then removed by thermal evaporation and subsequently the tubular structures of ZnO were formed.[217, 218] Unfortunately, the hollow ZnO structures fabricated using this technique is likely to be polycrystalline,[217-219] which could affect the charge mobility. The third technique used is vapour phase deposition with pulsed laser deposition[220] or chemical vapour deposition (CVD).[204, 221] The growth process normally involves expensive high vacuum systems and requires a high processing temperature (> 500ºC) which will restrict the choices of substrates.

The study of novel methods such as direct growth of ZnO NTs in solution represents a new challenge in this field of research. Here we demonstrate a bottom-up direct synthesis of high quality crystallised ZnO NTs in a cost effective CBD process at mild temperature (< 100ºC). The initial circular ring structured templates were formed with Marangoni mechanism, which guided the formation of NTs. Using our approach,

the central vacant space of ZnO NTs was created through limited crystal growth instead of the reported dissolution processes. Such direct growth method leads to the formation of vertically aligned, crystallised ZnO NTs with uniform diameters and wall thicknesses. Compared with ZnO NR photoanode, the photoactivity measurements have revealed increased photoconversion efficiency in hydrogen generation from ZnO NT photoanode by a factor of three.

3.3 Experimental Details

3.3.1 Preparation for Growing ZnO Nanostructures

All the chemicals used were analytical grade and purchased from Sigma-Aldrich. The titanium plates/glass substrates ($2 \times 2\ cm^2$) were sonicated in an isopropanol (IPA) bath for 15 minutes and dried in air before they were used to form a seeding layer on the substrate surface by spin coating. Two different seeding solutions were prepared. The first solution (ZA) was formed by dissolving 2.195 g of zinc acetate in 10 ml of deionised (DI) water and magnetically stirred for 2 hours to form a 1.0 M seeding solution. The second solution (ZAP) has the same concentration of zinc acetate with addition of 0.6 g of polyvinyl alcohol (PVA, MW ~25,000, 88% hydrolysed) in 10 ml solution with increased viscosity. In order to compensate the difference in viscosity, the coating of ZA solution was operated at lower spin speed (300 rpm), while the coating of ZAP solution was operated at 800 rpm.

The coated sample was then annealed in air at a constant heating rate of $10°C\ min^{-1}$ to 350°C. This temperature was held for an hour to remove PVA and to convert the zinc acetate into ZnO nanocrystal seeds. Vertically aligned ZnO NTs and NRs were grown via CBD method in a nutrient solution consisting of a 1:1 molar ratio of zinc nitrate hexahydrate and hexamethylenetetramine (HMT) in DI water. The final

concentration of Zn^{2+} in the growth solution was 10.0 mM. The seeded titanium plates were placed in glass beakers containing 40~100 ml of growth solution for 16 hours at 85°C. The samples were allowed to cool to room temperature, rinsed three times with DI water and air dried.

3.3.2 Characterisation

Step-wise temperature dependent attenuated total reflectance–Fourier transform infrared spectroscopy (ATR-FTIR, Perkin Elmer Spectrum One) measurements were carried out to monitor the PVA decomposition process of the seeding layer. The surface morphologies were studied by SEM (JSM 820M, Jeol). The crystallinity and structure orientation of the nanostructures were analysed by powder XRD (Siemens D500). The UV-vis absorption spectra were recorded using UV-vis spectrophotometer (Thermospectronic UV 300). The average diameters and average film thicknesses were measured from top- and side-view SEM images using Image J (National Institutes of Health, USA). The PEC water splitting was measured using a standard three-electrode configuration in a 1.0 M KOH electrolyte. A platinum foil was used as counter electrode and a KCl saturated Ag/AgCl electrode was used as a reference. A USB potentiostat (eDAQ) was used to control and record the photocurrent as a function of electrochemical potential. Sunlight was simulated with a 300W xenon arc lamp with an AM1.5 G filter and the output light power density was adjusted to 100 mW cm^{-2}.

3.4 Results and Discussion

3.4.1 Growth of ZnO NRs

A clean substrate is required for spin coating in order to avoid any residual particles which will cause uneven spreading of the seeding solution. The annealing of the sample at 350°C after spin coating is to thermally degrading zinc precursor into ZnO nano seeds. An experiment was carried out for a non-annealed sample where no vertically aligned ZnO NRs or NTs were found; instead, some inhomogeneous precipitates, microcrystals and microrods were randomly formed. Hence, ZnO nano seeds are essential for CBD growth of homogenous ZnO nanostructures.

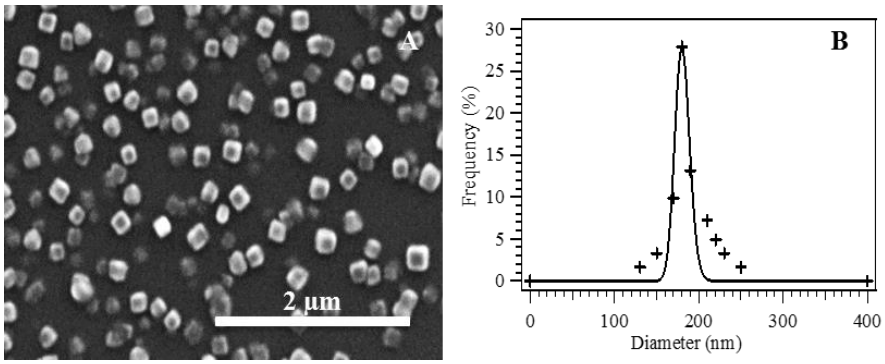

Figure 3.1 (A) Top view SEM image of seeding layer from ZA solution annealed at 350°C with a heating rate of 10°C min^{-1} and (B) size distributions of the ZnO nano seeds.

Figure 3.1A is the SEM image of ZnO seeding layer on a polished titanium substrate with ZA solution. The formed seed crystals are having a cubic morphology, which corresponds to a typical cubic zincblende structure of ZnO. The average size and mean error of the seeds were evaluated from 100 measurements through their top view SEM images. The size distributions of the cubic seed is relative narrow with an average dimension of 186 nm and a full width half maximum (FWHM) of 22 nm (Figure 3.1B).

The high density seed crystals are well dispersed on the substrate surface with their (100) face parallel to the substrate. The cubic zincblende seeds are readily convert to the hexagonal wurtzite ZnO structure during the growth process since wurtzite is more thermodynamically stable.

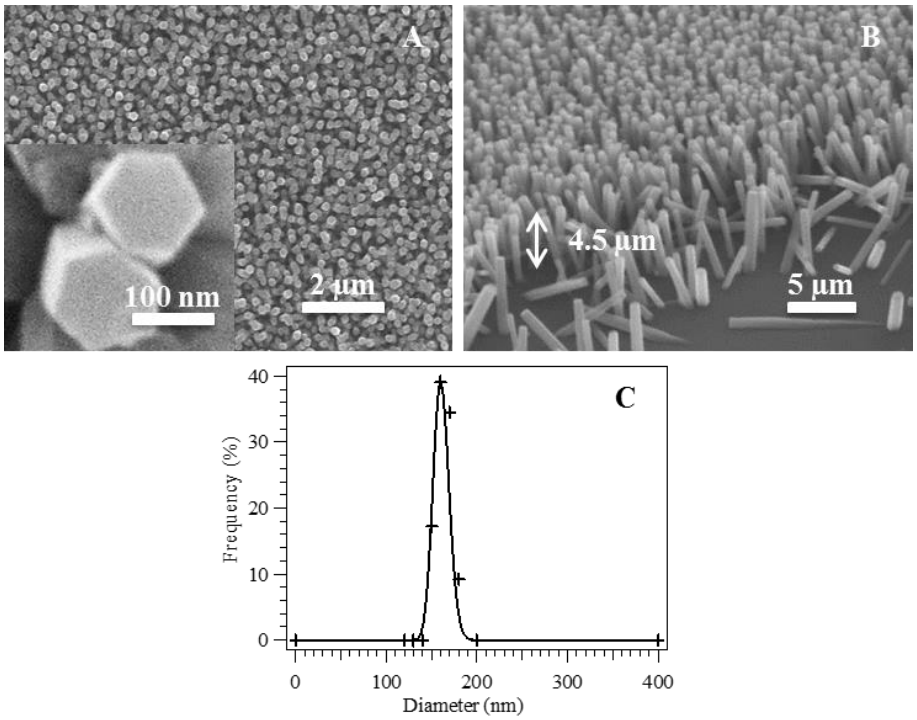

Figure 3.2 SEM images of ZnO NRs grown in 60 ml of growth solution, (A) top view (The inset is the corresponding higher resolution of SEM image) and (B) tilted view. (C) Diameter distributions of NRs.

ZnO NRs, shown in Figure 3.2, were successfully grown through CBD method using ZA seeding and 60 ml of growth solution. It is clearly shown that the ZnO NRs are hexagonal in shape. The top hexagonal face corresponds to the reactive polar (002) surface. The vertical growth of the ZnO crystal is the direct result of the higher reactivity of the (002) face, which allows the 1D growth along the c-axis. The growth kinetics and rods morphology are controlled by the density of the ZnO seeds. At high

density, the growth rate is limited by the rate of hydrolysis of Zn^{2+}. All seeds have the same steady growth rate thus a uniform height of the NRs were formed with an average length of 4.5 μm, as shown in Figure 3.2B. Figure 3.2C demonstrates that the formed ZnO NRs are monodispersed in their diameter (157 nm) with a FWHM of 30 nm, corresponding to a ±9% dispersion (100 measurements through the top view SEM images).

The crystal structure and crystal orientation of the as grown ZnO NRs were investigated by powder XRD. Since the as grown ZnO NRs is relatively thin, thus the sample is analysed by a small incidence angle in order to enhance the diffraction signal and minimise the contribution from the substrate. With normal incidence angle, the strong substrate signal could overshadow the signal from ZnO film. This reduced incident X-ray angle diffraction is called glancing angle XRD. In our experiment, the incidence angle was fixed at 3° (detector scan) from the surface and the diffraction spectrum is shown in Figure 3.3. The XRD pattern of ZnO NRs is analysed based on the standard XRD database (JCPDS #36-1451) for wurtzite hexagonal ZnO. All the XRD peaks are matched with the standard spectrum except for the three peaks located at 38.56°, 40.32° and 53.24° (T), which can be assigned to metal substrate in the form of alpha-titanium (JCPDS #44-1294). The hexagonal wurtzite ZnO NRs give the diffraction peaks located at 2θ = 31.93°, 34.82°, 36.65°, 47.97° and 56.83°, corresponding to the (100), (002), (101), (102) and (110) crystal planes. The strongest diffraction intensity from (002) plane is consistent to the fact that [0001] is the most favoured growth direction for the 1D ZnO nanomaterials. This observation is in agreement with the hexagonal morphology of the ZnO NRs observed in SEM.

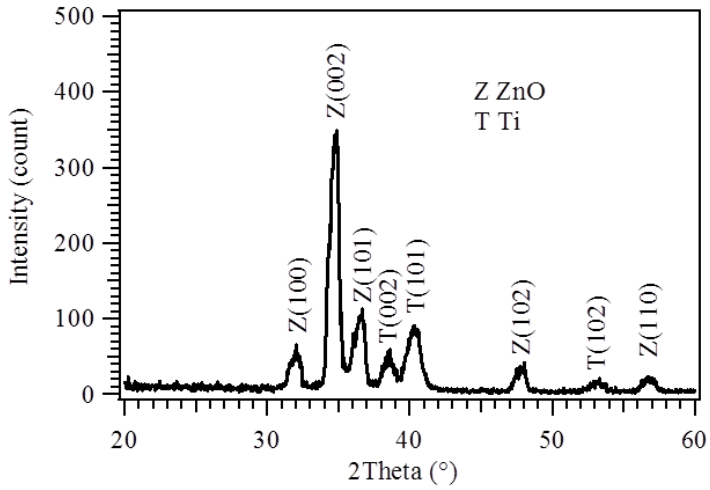

Figure 3.3 Glancing angle (3° incidence) XRD pattern of ZnO NRs on titanium plate. The miller indices of the crystal planes are labelled where Z and T are ZnO and titanium, respectively.

The XRD spectrum also shows a different line width for different diffraction peaks of ZnO, which corresponding to the crystal nature of the well aligned rod morphology. The crystal domain of the sample was calculated using Scherrer equation (Equation 2.5, Section 2.3). From the diffraction spectrum shown in Figure 3.3, the (002) peak is the narrowest peak with a FWHM of 0.3419º, which corresponds to a crystal domain size of 26.4 nm. Most of the other peaks have a FWHM of 0.472º, which corresponds to a smaller crystal domain of 17.5 nm. This suggests that the crystal quality of the (002) plane is much better than other planes. Large crystal domain with less defects is essential for high charge mobility with less probability of charge recombination.

3.4.2 Growth Mechanism of ZnO NRs

The growth mechanism of ZnO NRs by CBD method has been widely studied. It was suggested that the growth of ZnO NRs proceeded in the following steps:[47]

$$(CH_2)_6N_4 + 6H_2O \rightleftharpoons 4NH_3 + 6HCHO \quad \text{(Equation 3.1)}$$

$$NH_3 + H_2O \rightleftharpoons NH_3 \cdot H_2O \quad \text{(Equation 3.2)}$$

$$NH_3 \cdot H_2O \rightleftharpoons NH_4^+ + OH^- \quad \text{(Equation 3.3)}$$

$$Zn^{2+} + 2OH^- \rightleftharpoons Zn(OH)_2 \quad \text{(Equation 3.4)}$$

$$Zn(OH)_2 \rightleftharpoons ZnO + H_2O \quad \text{(Equation 3.5)}$$

In this process, the thermal reaction of HMT with water yields NH_4^+ and OH^-, which increase the solution pH (Equations 3.1 to 3.3). At higher pH, Zn^{2+} will be hydrolysed into $Zn(OH)_2$ which will then be deposited onto the nucleation sites (seeds) as ZnO (Equations 3.4 and 3.5). The balance between the precipitation rate and the growth rate is the key for the formation of good quality ZnO crystal. Thus, the decomposition of HMT seems to play an important role for the growth of ZnO NRs. Previous work[222] applied in-situ near edge X-ray absorption structure spectroscopy to investigate the deposition process of ZnO by CBD. The experiment confirmed that, during the heating process, HMT decomposed into formaldehyde and ammonia with a gradual release of OH^-. Meanwhile, the formation of $Zn(OH)_2$ and ZnO also helped to maintain the pH of the growth solution. A kinetic profile of the sequential growth process can be represented by the concentration evolution as a function of time, as shown in Figure 3.4.

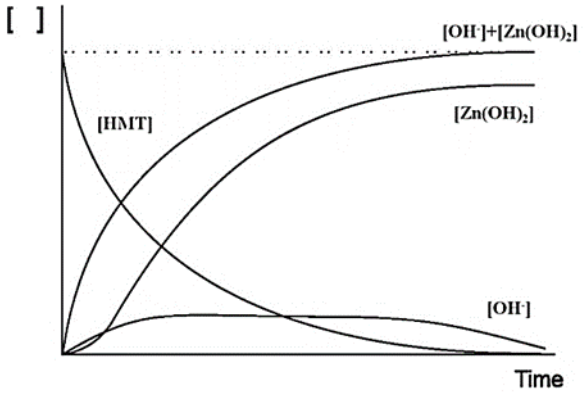

Figure 3.4 A schematic kinetic profile of the CBD growth process.

In such sequential kinetic process, the reaction rate law can be described as:

$$\mathrm{HMT} \overset{k_1}{\rightarrow} \mathrm{OH^-} \overset{k_2}{\rightarrow} \mathrm{Zn(OH)_2} \qquad \text{(Equation 3.6)}$$

where k_1 and k_2 are the rate constants for the formation of $\mathrm{OH^-}$ and $\mathrm{Zn(OH)_2}$ reactions, respectively. Normally, the rate of decomposition of HMT and formation of $\mathrm{OH^-}$ are controlled by the CBD temperature (~85ºC). Under such condition, the overall reaction rate is limited by this step, since the subsequent formation of $Zn(OH)_2$ is a kinetic favourable process. This suggests that k_2 will always be larger than k_1, which results in a stationary concentration of the intermediate species of $\mathrm{OH^-}$. The Zn^{2+} ions consume the $\mathrm{OH^-}$ ions to form $Zn(OH)_2$ which is constantly released by the decomposition of HMT. This condition is critical for the formation good quality of ZnO crystals and morphology as a stable growth condition (constant pH) is maintained at optimised growth temperature. At higher temperature, the rate of decomposition of HMT will be faster. This will cause the rapid increase of solution pH and the faster, unstable growth of ZnO crystals, which will affect the crystal quality.

3.4.3 Effect of Growth Solution Volume on the Morphology of ZnO NRs

The diameter and the length of ZnO NRs determine the total surface area accessible for ions, which can in turn affect their reactivity. Here, we investigated the correlation between the morphology of ZnO NRs and the initial volume of nutrient solution in a CBD process. All other parameters, such as the seed densities and solution concentrations were maintained as constant. Initial growth solutions of 40 ml, 60 ml, 80 ml and 100 ml were used.

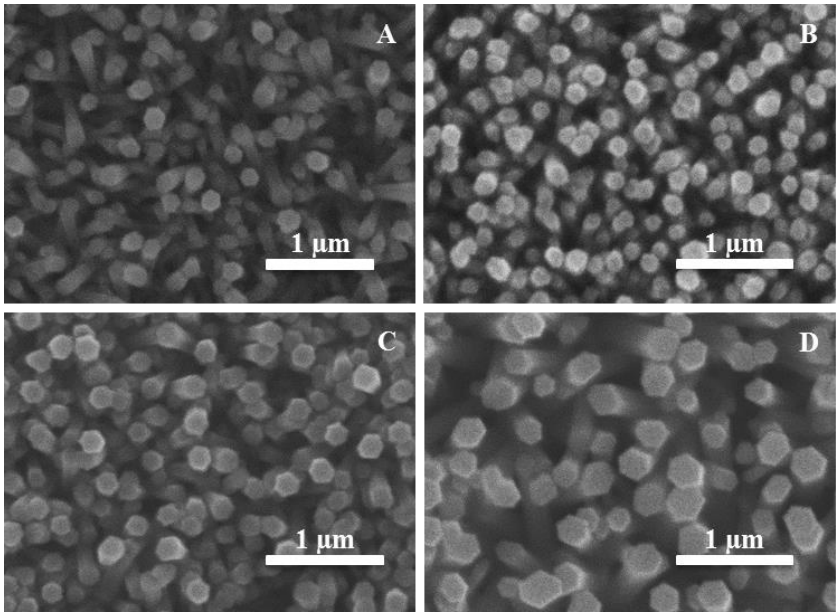

Figure 3.5 Top view SEM images of ZnO NRs formed at different volumes of growth solutions, (A) 40 ml, (B) 60 ml, (C) 80 ml and (D) 100 ml.

It is noticeable that the diameter of ZnO NRs increases as the volume of growth solution increases (Figure 3.5). The water content of growth solution is reduced via evaporation throughout the reaction at 85°C and the concentrations of the reactants will increase gradually. Thus, for a higher volume of growth solution it is expected to have a higher concentration once part of the solvent is evaporated, resulting in a higher growth rate. In addition, for the higher volume of growth solution, the number of moles of Zn^{2+}

is relatively higher which will cause the increasing of the diameter and also the length of the ZnO NRs.

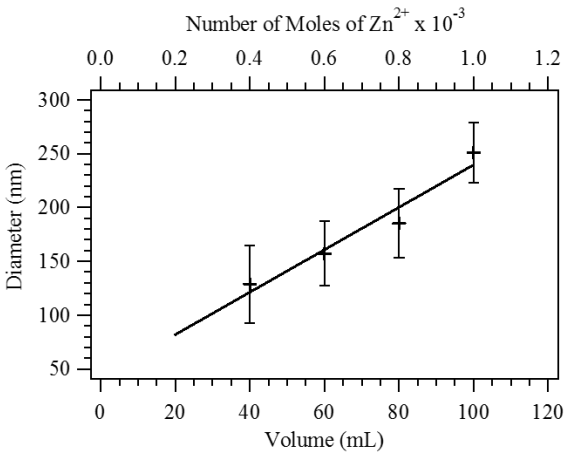

Figure 3.6 Plot of average diameter with respect to the volume of growth solution and number of moles of Zn^{2+}.

The average diameters of the samples were quantified with the top view SEM images (100 measurements). The measurements confirm that the diameter of ZnO NRs increases as the volume of growth solution increases. The average diameters of the ZnO NRs that grew in 40 ml, 60 ml, 80 ml and 100 ml of growth solution were measured to be 129±36, 157±30, 185±32 and 252±28 nm, respectively. A graph of the ZnO NRs diameter versus the volume of growth solution is plotted in Figure 3.6. The plot shows a reliable linear relationship between the diameter of ZnO NRs and volume of growth solution. The linear curve can be extrapolated to pass the origin (0, 0) with a small offset, which suggests that linear relationship could be scaled in a wider volume range.

3.4.4 Growth of ZnO NTs

The surface area of ZnO NRs can be further increased in the form of NTs. Here, we report the growth of vertically aligned ZnO NT arrays through CBD method with the addition of PVA in the seeding solution, ZAP. Without PVA, only cubic crystalline ZnO seeds were formed and consequently, ZnO NRs were formed, as we demonstrated above. This suggests that PVA plays an important role in the formation of tubular structure of ZnO.

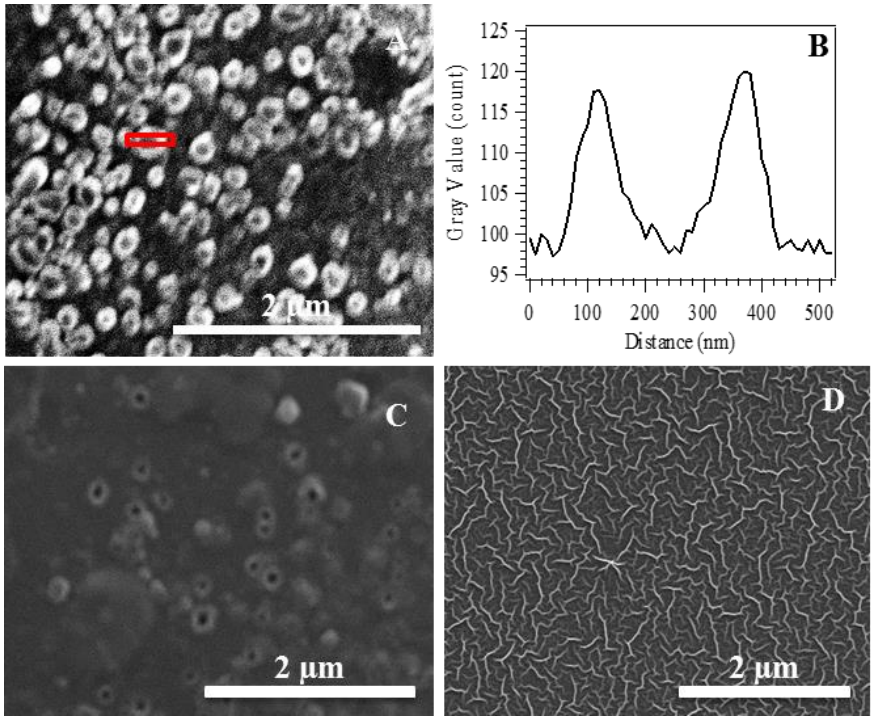

Figure 3.7 Top view SEM images of seeding layer by ZAP solution annealed at (A) 350°C (10°C min^{-1}), (C) 300°C (10°C min^{-1}) and (D) 350°C (15°C min^{-1}) for an hour. (B) Line profile of the marked ring (red) in Figure 3.7A.

The structure of the ZAP seeded layer was investigated by SEM, as shown in Figure 3.7. The optimal experimental conditions for the formation of ZnO rings were with a heating rate of 10°C min^{-1} to 350°C, as shown in Figure 3.7A. In order to prove

that the formed structure is a ring, a line profile of the ring structure was plotted as shown in Figure 3.7B. There are two peaks for the line profile which confirms the structure formed is a ring with a vacancy. The rings were measured to have an average outer diameter of 380 nm.

It is important to note that the ring formation is strongly dependent on both the annealing temperature and the heating rate. As shown in Figure 3.7C, with a lower annealing temperature of 300°C, only a small number of rings were formed. If the heating rate was too rapid (15°C min^{-1}), webs, rather than the rings, were formed as shown in Figure 3.7D. This suggests that the PVA evaporation rate was faster than the inflow of the molten polymer. The ring formation may be explained by the Marangoni mechanism[223] through the convective evaporation-decomposition process. During the annealing, the PVA film begins to melt and forms drops due to the dewetting on the polished titanium plate before decomposition. The dome profile of the droplet causes an increasing temperature gradient from the centre to the edge of the droplet. This results in the decomposition of the PVA at the pinned circular edge.[223] The liquid removed from the edge is replenished by an outward flow of the molten PVA and zinc acetate, at a slowly increasing temperature.[224] After the calcination, PVA is removed and ZnO seeds remain in a ring-like structure. Such ZnO ring structure acts as a template for the growth of ZnO NTs in CBD process, rather than ZnO NRs.

An ATR-FTIR was used to monitor the decomposition of PVA content in the seeding layer on a glass substrate. Figure 3.8 represents the ATR-FTIR spectra of seeding layer at various temperatures of 25°C, 150°C, 250°C and 350°C.

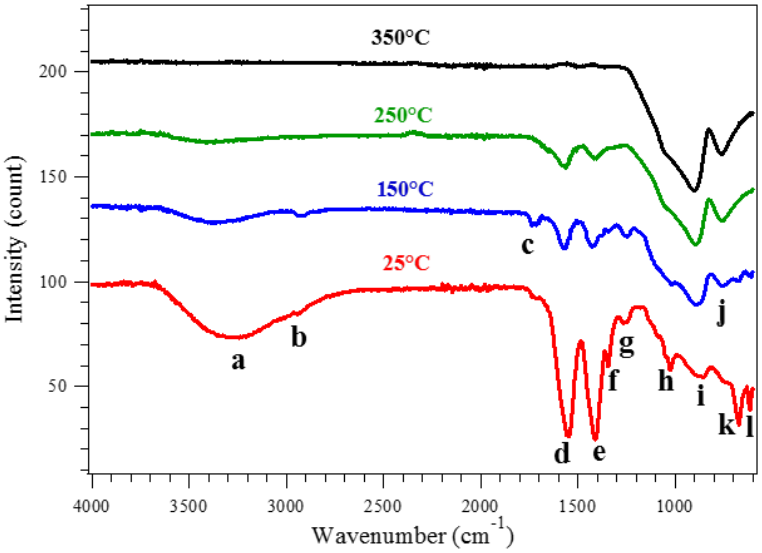

Figure 3.8 ATR-FTIR spectra of ZAP seeding layer at various annealing temperatures.

The broad peak at 3500–3000 cm^{-1} (**a**) is typical for the hydrogen bonding between the hydroxyl groups within the PVA polymer. The small peak at 2940 cm^{-1} (**b**) can be assigned to the C–H stretching mode, which is also contributed from the PVA molecular chain. The intense peak at 1570 cm^{-1} (**d**) is normally absent for the PVA solution.[225] Thus, we assigned it to C=O stretching modes, originated from zinc acetate. Meanwhile, the weak peak at 1720 cm^{-1} (**c**) can be associated with the C=O stretching from the polyvinyl acetate within the PVA due to the incomplete hydroxylation of the PVA polymer. The intense peak at 1410 cm^{-1} (**e**) is the in plane bending of the O–H group from PVA polymer. The peak at 1342 cm^{-1} (**f**) is assigned to the coupling of the O–H in plane bending mode with the C–H wagging mode.[226] The peak at 1260 cm^{-1} (**g**) is the stretching of the C–O group from PVA polymer while the peak at 1023 cm^{-1} (**h**) is the stretching of the C–O group by zinc acetate. The two broad and medium intense peaks at 888 cm^{-1} (**i**) and 747 cm^{-1} (**j**) are the peaks contributed from the glass substrate. The sharp peaks at 670 cm^{-1} (**k**) and 610 cm^{-1} (**l**) are corresponding to the O–H out-of-plane bending which is contributed from PVA polymer.[226]

When the annealing temperature is increased, the vibrational peak intensities from both the PVA and zinc acetate were reduced. At room temperature (25ºC), peaks at 1570 cm^{-1} (zinc acetate) and 1410 cm^{-1} (PVA) had similar intensity. At 150ºC, the zinc acetate peak intensity became stronger. This indicates that PVA polymer began to decompose at a relatively lower temperature. After annealing at 350ºC, most of the organic molecular peaks, associated with C and O disappeared. At this temperature, PVA was completely decomposed and zinc acetate has converted to ZnO nano seeds. The residual vibrational peaks were contributed from the glass substrate which became more intense as the polymer layer getting thinner.

Although the boiling point of PVA is 228°C, there are still some hydrocarbon residue remaining after the sample plate is annealed to 250°C. This is evidenced from the temperature dependent FTIR spectra shown in Figure 3.8. Only after annealing to a temperature higher than 350°C, the PVA polymer was fully decomposed. Under this condition, the sample colour changed from clear to pale yellowish opaque. Therefore, all samples were annealed at 350°C for an hour with a heating rate of 10°C per minute after coating with ZAP seeding solution. Here, the high temperature thermal treatment is necessary for both removing the PVA content and oxidising the zinc acetate into crystallised ZnO nano seeds.

Figure 3.9A displays ZnO NTs were successfully prepared using the ZAP seeding solution and 60 ml of nutrient solution. Similar to ZnO NRs, the high quality, close-packed, vertically aligned ZnO NTs were formed with hexagonal morphology. The average outer diameter and average wall thickness of the NTs were measured (100 measurements through the top view SEM images) to be 159 ± 24 nm and 41 ± 12 nm, shown in Figure 3.9C and 3.9D, respectively. Figure 3.9B demonstrates that the length

of the ZnO NTs is about 5.0 μm and the average inner diameter of the ZnO NTs was calculated to be 83 nm, about half of its outer diameter.

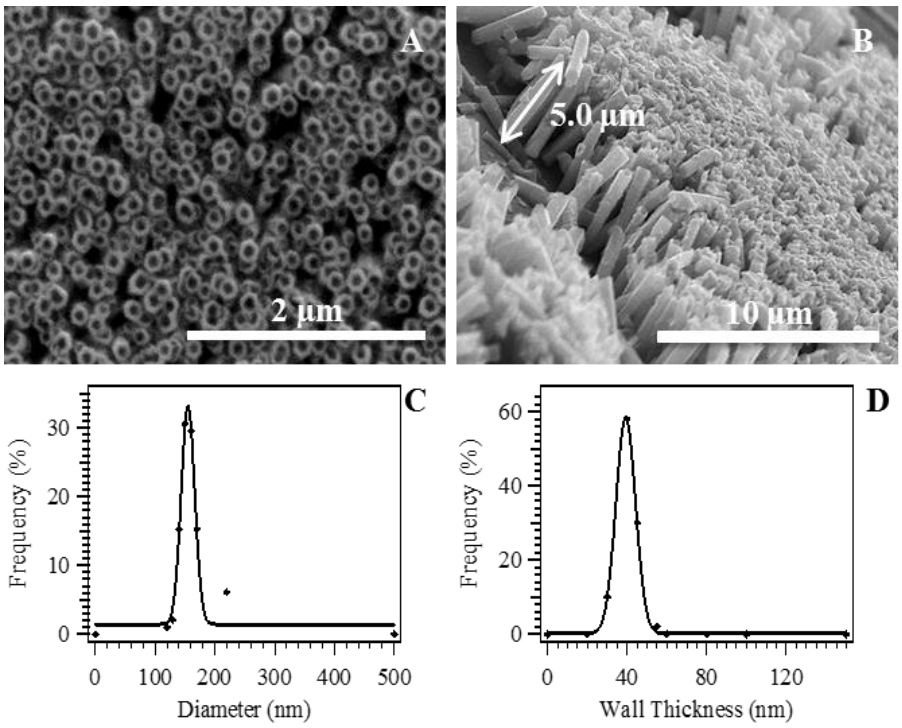

Figure 3.9 SEM images of ZnO NTs grew in 60 ml of nutrient solution, (A) top view and (B) tilted view. (C) Diameter distributions and (D) wall thickness distributions of NTs.

Powder XRD measurements were carried out to study the crystallinity and crystal orientation of the ZnO NT arrays. Similar to ZnO NRs, the thickness of as grown ZnO NT film was relatively thin (5 μm), therefore, fixed small incident angle XRD configuration was used in order to increase its surface sensitivity. A typical diffraction spectrum with labelled miller indices is shown in Figure 3.10.

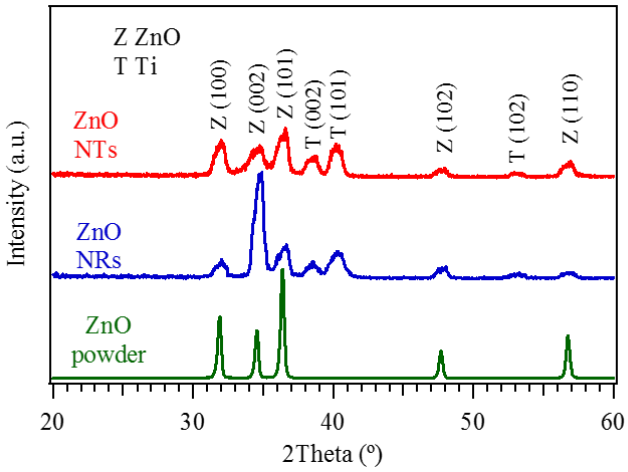

Figure 3.10 Surface XRD spectra of ZnO NTs and NRs on titanium plates with a film thickness of ~5 μm in comparison with ZnO powder. The miller indices of the crystal planes are labelled where Z and T are ZnO and titanium, respectively.

Similar to the XRD pattern of ZnO NRs, all the XRD peaks from ZnO NTs are matched for wurtzite hexagonal ZnO. The diffraction pattern from ZnO powder was also included as a reference. In comparison with the ZnO powder, the (002) peak is dominant for the NRs. This is contributed from the vertical orientation of NRs with their (002) planes parallel to the substrate. However, NTs display a much lower (002) peak intensity due to the reduced scattering from the (002) plane at the tube centre. Quantitative analysis of the diffraction intensities reveals that the intensity ratio of the ZnO powder is 1.0:0.7:1.5 for (100):(002):(101) planes. This ratio changes to 1.0:1.0:1.2 for ZnO NTs. This analysis suggests that the NTs are possibly aligned perpendicular to the substrate. For ZnO NTs, the linewidth of the (100) and (101) peaks are narrower (FWHM of 0.351º and 0.272º) than the (002) peak (FWHM of 0.551º). Therefore, larger crystal sizes are formed for the (100) and (101) planes (26.4 nm and 30.4 nm), while a smaller crystal domain of 21.2 nm is identified for the (002) plane.

This indicates that the crystal quality of the (100) and (101) planes are much better than the (002) plane.

3.4.5 Effect of Growth Solution Volume on the Morphology of ZnO NTs

The effect of the volume of growth solution on the morphology of ZnO NTs were also investigated. While maintaining other growth parameters, the relationship between the volume of growth solution and morphology of ZnO NTs is shown in Figure 3.11. Similar to ZnO NRs, the average diameter of ZnO NTs is increased when the volume of growth solution is increased.

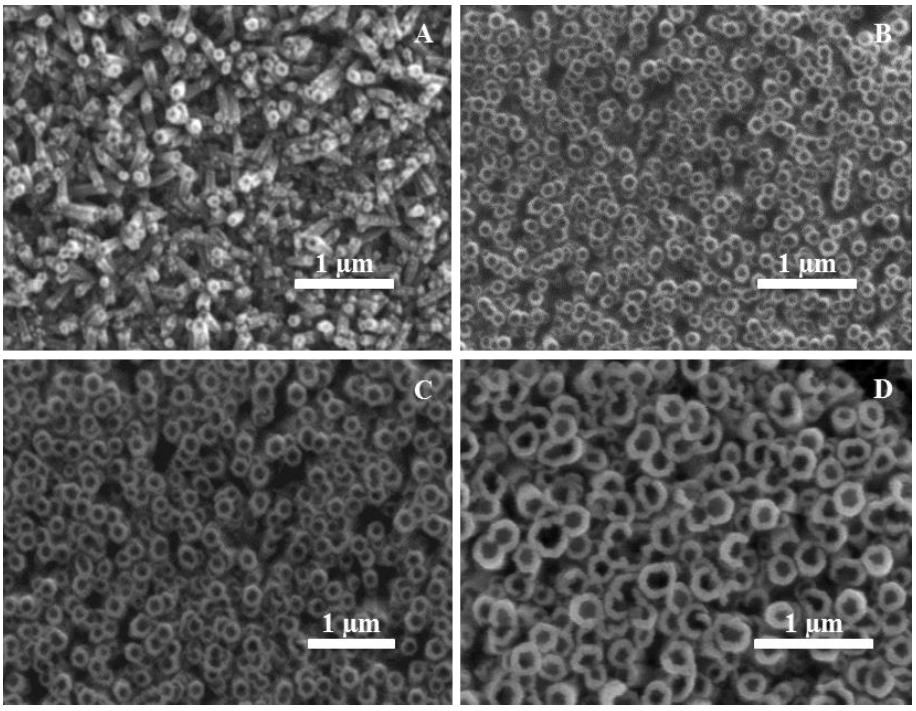

Figure 3.11 Top view SEM images of ZnO NTs formed at different volumes of growth solutions, (A) 40 ml, (B) 60 ml, (C) 80 ml and (D) 100 ml.

The average outer diameters and wall thicknesses of the samples were evaluated from 100 measurements through their top view and side view SEM images (Figure

3.11). The average outer diameters of the ZnO NTs for that grew at 40, 60, 80 and 100 ml of growth solutions were measured to be 98 ± 38, 159 ± 36, 192 ± 40 and 235 ± 42 nm, respectively. As shown in Figure 3.11, increased in the volume of growth solution will also increase the wall thickness, as well as the inner diameter of NTs. It is worth noting that the ratio between the outer and inner diameters of the NTs was sustained at a factor of two and the density of the NTs maintained constant. Thus, for higher volume of growth solution, larger NTs will be formed with reduced the gap between the neighbouring NTs. In some cases, the adjacent tubes are even coalesced into double tubes, as shown in Figure 3.11D. Closely packed NTs will help to improve the overall alignment of ZnO NTs. On the contrary, at low initial solution volume, 40 ml, randomly tilted NTs were formed (Figure 3.11A).

3.4.6 Optical Properties of ZnO NRs and NTs

The UV-vis absorption was used to measure the band gap of the ZnO nanostructures. For this experiment, both the ZnO NRs and NTs were prepared on glass substrates and the absorption spectra are presented in Figure 3.12A.

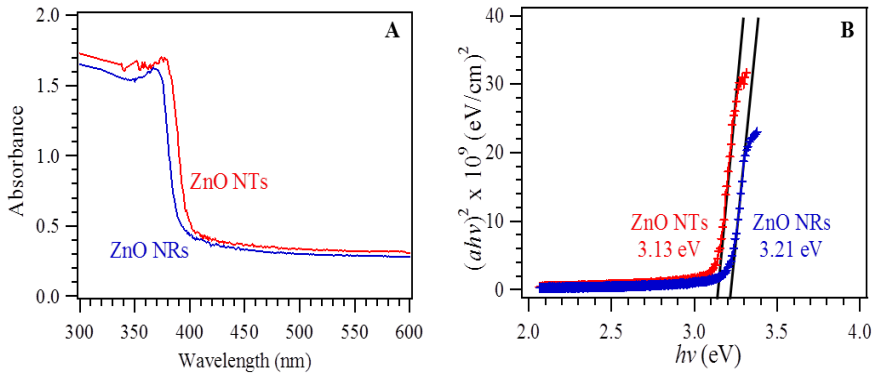

Figure 3.12 (A) UV-vis absorption spectra and (B) Tauc plots of ZnO NTs and NRs.

Figure 3.12A reveals that the UV-vis absorption onset of the ZnO NTs is shifted to a longer wavelength (~404 nm) as compared to the ZnO NRs (~392 nm). The red shift of the ZnO NTs indicates that the optical band gap of the NTs is smaller than the NRs. The optical band gap of the samples can be related to the absorption coefficient and photon energy from the following Tauc expression (Equation 2.11, Section 2.4). The linear nature of the Tauc plots (Figure 3.12B) at the absorption edge confirms that the films are semiconductors with direct band gaps. The band gaps of ZnO NTs and NRs were estimated to be 3.13 and 3.21 eV, respectively. The smaller band gap can be attributed to the high density of crystal defects originated from the small crystal domain and thin wall thickness of NTs. This suggests that the NT films may be superior to the NR films for solar light absorption.

3.4.7 Structural Morphology of ZnO NTs and NRs

In order to assess the difference in structural morphology between the NT and NR arrays, we calculated and compared the surface porosity densities as well as the surface area to volume ratios for both structures. The aspect ratios (length/outer diameter)[227] of achieved ZnO NTs and NRs grew in 60 ml of growth solution were almost identical with a value of about 30. For hexagonal NT arrays organised in hexagonal patterns, the surface porosity (P) can be calculated by using equation 3.7.

$$P_{NT} = 1 - \frac{3(w^2 + dw)}{l^2} \qquad \text{(Equation 3.7)}$$

where w is the wall thickness, d is the inner diagonal length and l is the average distance between the centre of adjacent NTs. For vertically aligned hexagonal NRs, the surface porosity follows equation 3.8.

$$P_{NR} = 1 - \frac{3D^2}{4l^2} \qquad \text{(Equation 3.8)}$$

where l is the same parameter as in equation 3.7 and D is the diagonal width of the hexagonal rods. The structural parameters are indicated in Figure 3.13 and the average values of the parameters were evaluated from 100 measurements through their top view SEM images. Our measurements indicated the porosities of ZnO NT and ZnO NR arrays are 53% and 43%, respectively. The measurements reveal that the P_{NT} is ~23% larger than that of the P_{NR}. The surface porosity indicates the percentage of open surface in the total top surface. This parameter determines the kinetics for the electrolyte transportation. The larger surface porosity of NTs results in a faster mass transportation.

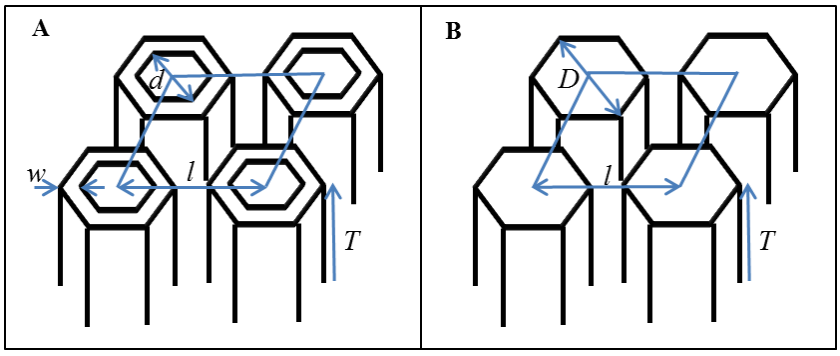

Figure 3.13 Schematic diagrams of NTs and NRs labelled with critical morphological parameters used in equations 3.7 to 3.10.

The other critical morphological parameter is the surface area to volume ratio (*SAVR*), which determines the reaction kinetics for gas or liquid at porous solid surface. Porous nanomaterials with large *SAVR* offer a large number of surface reaction centres and lead to faster reactions. For the photocatalytic applications, a large *SAVR* results in more effective charge transfer from photoexcited semiconductor to the electrolyte. For vertically aligned hexagonal NT arrays, the *SAVR* follows equation 3.9.

$$SAVR_{NT} = \frac{\left(4\sqrt{3} + 3\,w/T\right)(d + w)}{l^2} \qquad \text{(Equation 3.9)}$$

where the parameters *w*, *d* and *l* are the same as in equation 3.7, and *T* is the NT length. For hexagonal NRs, the *SAVR* follows a simpler formula:

$$SAVR_{NR} = \frac{D\left(2\sqrt{3} + \frac{3D}{4T}\right)}{l^2} \qquad \text{(Equation 3.10)}$$

where the parameters *l*, *D* and *T* are the same as in equations 3.7 and 3.8.

Using equations 3.9 and 3.10, based on the measured morphological dimensions, the *SAVR* values were calculated as 0.027 nm^{-1} and 0.017 nm^{-1} for NT and NR arrays respectively. Thus, the *SAVR* of a NT array is about 59% higher than a NR array for the photocatalytic oxidation of water. The combination of large *P* with higher *SAVR* is essential for optimisation of catalytic reactions kinetics involving gases and liquids on solid surfaces.

3.5 PEC Water Splitting of ZnO NTs and NRs

The water photoelectrolysis activity of ZnO NTs photoanode was evaluated by measuring the photocurrent in 1.0 M KOH aquatic electrolyte (pH 13.6) under the illumination of a 100 mW cm^{-2} solar simulator with an AM1.5 G filter. The photocatalytic activity was compared with that from vertically aligned ZnO NRs, grown under the same conditions (60 ml growth solution at 85ºC), without PVA in the seeding solution (ZA). The overall shape of both samples are very similar, apart from NTs are 0.5 μm longer than NRs. We chose growth with 60 ml 10 mM solution to avoid structural complications, such as the coalescence between adjacent NTs or NRs.

Figure 3.14A shows the current–voltage (*I*–*V*) curves for ZnO NTs and NRs photoanodes in dark and under simulated sunlight in the potential range from –0.5 to 1.0 $V_{Ag/AgCl}$. For an electrolyte of 1.0 M KOH with pH 13.6, the reversible oxygen standard potential is at 0.23 $V_{Ag/AgCl}$, marked with a vertical red line in Figure 3.14A. For both NTs and NRs, the dark current is negligible in the measurement potential range (0.01 mA cm^{-2} at 0.23 $V_{Ag/AgCl}$), as for typical for n-type semiconductors.

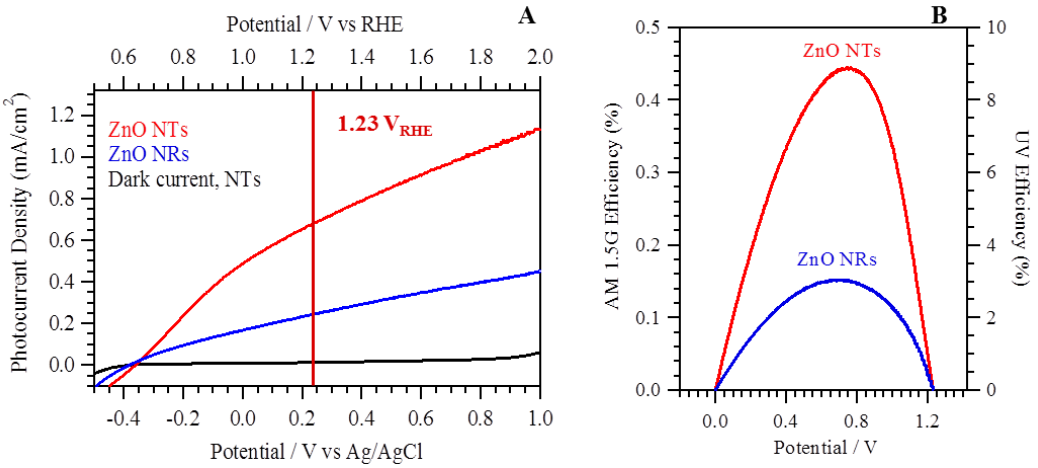

Figure 3.14 (A) Photocurrent generated from ZnO NTs and ZnO NRs together with the dark current measured from ZnO NTs in 1.0 M KOH electrolyte (pH 13.6) under the illumination of a 100 mW cm^{-2} solar simulator with an AM1.5 G filter and (B) corresponding UV (UG11, Schott) and AM1.5 G efficiency.

With light on, the photocurrent from both the ZnO NTs and NRs increases steeply at lower potential with onset potentials (open circuit potentials) at –0.36 $V_{Ag/AgCl}$ for NTs and –0.38 $V_{Ag/AgCl}$ for NRs. The small difference in the water oxidation onset potentials can be explained by the better crystal quality (*i.e.* with fewer crystal defects) of NRs, as indicated by the powder XRD data. However, the photocurrent density generated from the NTs increases much faster than the NRs at more positive potentials.

For measurements at 1.23 V_{RHE}, ZnO NT electrode generated a photocurrent density of 0.67 mA cm^{-2}, but ZnO NRs photoanode generates only 0.24 mA cm^{-2}. Amperometric studies were carried out for both the NT and NR photoanodes in 1.0 M KOH electrolyte (pH 13.6) at an applied voltage of 0.2 $V_{Ag/AgCl}$ under light on-off cycles for 600 s, shown in Figure 3.15 There is no obvious decrease in the photocurrents, which confirms that both NT and NR photoanodes are stable under our experimental conditions.

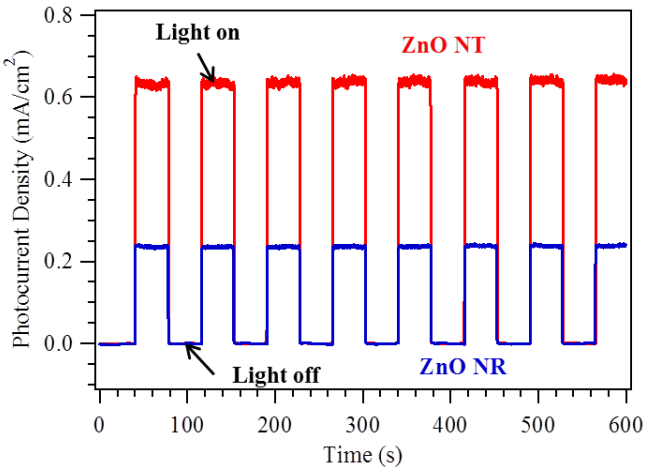

Figure 3.15 Amperometric current–time (*I–t*) curves of ZnO NTs and NRs in 1.0 M KOH electrolyte (pH 13.6) at an applied voltage of 0.2 $V_{Ag/AgCl}$ at 100 mW cm^{-2} for 600 s with repeated light on-off cycles.

A comparison of the PEC output powers of ZnO NR and NT photoanodes were carried out and is presented in Figure 3.14B. As ZnO NTs and NRs have band gaps larger than 3.1 eV (Figure 3.12B), only UV part of the light was absorbed. As such, we calculated the photoconversion efficiency against the energy densities from both the UV and the full solar spectrum (Equation 2.27, Section 2.6). Under AM1.5 G illumination, NTs anode achieves a higher conversion power than NRs anode, with a maximum output power of 0.45 mW cm^{-2}, instead of 0.15 mW cm^{-2}. These correspond to

AM1.5 G efficiencies of 0.45% (NTs) and 0.15% (NRs) and UV photoconversion efficiencies of 9% (NTs) and 3% (NRs). The photoconversion efficiency of our ZnO NTs electrode was compared with the ZnO NTs prepared by electrochemical method.[228] The efficiency of our NTs is three times higher for water splitting, which could be due to their limited tube length, poor orientation and poor crystal quality.

The higher photoconversion efficiency of ZnO NTs, relative to ZnO NRs, can be explained in several ways. We believe that, under our controlled experimental conditions, the small difference in length between the NTs (5.0 μm) and NRs (4.5 μm) is not enough to account for the significant increase in the photoenergy conversion. The morphological difference between the NTs and NRs could, however, play a key role. First, the NT thin film offers a more porous structure with a void dimension of ~80 nm. This is associated with a larger *P* defined by equations 3.7 and 3.8, with a value of 53%, compared with 43% for the NRs. Thus, the NT structure offers additional nano-channels for the transport of electrolytes, allowing a deep penetration of electrolytes inside the film. This maximises the access of effective surface for the photocatalytic oxidation.

Secondly, the vertically aligned NTs have 59% larger effective *SAVR* values than that of NRs. This could increase the number of available reaction centres for the oxidation of water at the solid-liquid-gas interface. Thirdly, our ZnO NTs have a wall thickness of 41 nm, while the NRs have a solid diameter of 157 nm. This difference can significantly affect the light absorption as well as the electron-hole recombination and therefore affect the photoconversion efficiency. The UV light normally can penetrate into the ZnO crystal about 50 nm (α = 200000 cm^{-1} at 370 nm)[229] and the hole diffusion length for crystalline ZnO is about 125 nm.[29, 230] Thus, a full 3D UV illumination within the film is expected for ZnO NTs while this is restricted in the NRs. Therefore, the light absorption is expected to be higher for the thin wall NTs. The wall thickness of NT

(41 nm) is much smaller than the minority carrier diffusion length (125 nm), whereas the lateral dimension of the NRs (157 nm) is comparable to this critical parameter. Photogenerated holes have to travel to the surface to carry out water oxidation reactions. So electron-hole recombination is expected to be much lesser for the NTs than for the NRs and allowing effective transfer of photoexcited electrons towards the conductive substrate in the NTs. Most importantly, ZnO NTs benefit from a smaller band gap (due to defects), so that intense longer wavelength light can be absorbed.

In summary, the combined effects of small band gap, large *P*, large *SAVR*, and small hole transfer pathway have contributed to the increase of PEC hydrogen generation efficiency of ZnO NTs by three-fold.

3.6 Conclusions

ZnO NRs and NTs were successfully prepared using CBD method. ZnO NTs were formed with the presence of PVA in the seeding solution, without PVA, only ZnO NRs were created. The morphology of ZnO NTs and NRs can be manipulated by simply varying the growth conditions. Increased in the volume of growth solution resulted in increased both the length and the outer (inner) diameter of the NRs (NTs). The UV-vis absorption measurements revealed that the band gap energy of ZnO NTs (3.13 eV) is 0.08 eV smaller than that of ZnO NRs (3.21 eV), which can be attributed to the high density of crystal defects originated from small crystal domain size and thin wall thickness of NTs. The calculations demonstrated that, with the similar growth conditions, the *P* and *SAVR* of NT anodes are ~23% and ~59% larger than their NR counterparts, respectively. The photocatalytic water splitting measurements revealed that NTs anode was about three times more efficient than NRs anode with similar dimensions. Possible mechanisms for the high efficiency were also discussed.

Chapter 4 Enhanced Photoelectrochemical Water Splitting by 3D Uchin-like ZnO Nanorod Arrays on TiO_2 Hollow Hemispheres

4.1 Abstract

Urchin-like hybrid metal oxide nanostructures were successfully synthesised from vertically aligned, crystallised ZnO NRs grown on the surface of TiO_2 hollow hemisphere (HHS) nanostructures. A technique combining electrospinning and aqueous chemical bath deposition (CBD) was used. SEM and XRD confirmed the hybrid system contained a mixture of crystallised ZnO NRs, TiO_2 HHSs and zinc titanate (Zn_2TiO_4) thin film by annealing the hybrid sample at 700ºC. Zn_2TiO_4 was formed at the interface between ZnO NRs and TiO_2 HHSs which was verified through SEM, EDX and XRD characterisation, following the removal of the ZnO with acid. The PEC measurements revealed that, with the formation of a Zn_2TiO_4 interface layer (1.07%), the photoconversion efficiency was increased by 76% with respect to the hybrid urchin structures without Zn_2TiO_4 (0.61%). By analysing the interface band gap structures between ZnO, Zn_2TiO_4 and TiO_2, Zn_2TiO_4 was proposed to act as a barrier layer to improve charge separation which results in an enhancement of the PEC water splitting efficiency.

4.2 Introduction

Hydrogen is an ideal clean fuel with high energy density values per mass of 140 MJ/kg.[78] In order to preserve the fossil fuel as a raw chemical resource for the future and limit carbon dioxide emission, hydrogen is an ideal candidate as a future energy source. Currently hydrogen is produced by steam reforming of natural gas,

which consumes fossil fuel and generates greenhouse gases.[78] Therefore, there has been the motivation to develop efficient processes for hydrogen fuel production to replace currently used carbon emitting technologies. The field of nanotechnology has been rapidly growing, in an attempt to address this issue.

Out of many techniques, PEC water splitting is one of the promising solutions to harvest and store solar energy into hydrogen fuels. Since TiO_2 was first reported to have ability in photocatalysis of water splitting in 1972,[106] a great number of 1D nanoarchitectures of metal oxide semiconductors, such as NRs,[231] NTs[93] and NWs,[232] have been designed and prepared for improving the solar to hydrogen conversion efficiency. Semiconductor nanostructures (*e.g.* ZnO,[233] $BiVO_4$,[130] WO_3,[234] SnO_2[235] and GaN[236]) possess large surface areas, excellent electron transportation and good electrical contact with the substrates have attracted extensive investigation for their potential applications in PEC water splitting.[237-239] Among various semiconductors, ZnO and TiO_2 have received great attention due to their wide direct band gap[240, 241] and have been shown to have potential applications in photovoltaic[17, 242] and PEC water splitting.[241, 243]

For the creation of a highly efficient PEC cell, one of the important factors is the design of the nanostructured photoanode, which should have excellent light harvesting ability with high surface area. Although 1D nanostructures based electrodes offer direct and fast electron transportation path, their photoconversion efficiency is still lower than that of NP based PEC cells, due to their smaller effective surface area.[244] Consequently, a number of strategies have been developed to optimise the effective surface area of the electrodes by creating 3D heterogeneous nanostructured electrodes to promote the photocatalytic performances.[87, 245]

Herein, we report the creation of urchin shaped hybrid ZnO NRs grown on the TiO_2 HHSs through a combination of electrospinning and aqueous CBD methods. The

calcination studies of the 3D urchin-like structure revealed the presence of a thin layer of zinc titanate (Zn_2TiO_4) at the interface by annealing the sample at 700°C. The PEC performance of the hybrid sample was ~60% higher than the sum of the output power of ZnO NRs and TiO_2 HHSs. More important, with the presence of a Zn_2TiO_4 interface layer, the photoconversion efficiency was further increased by ~76% with respect to the hybrid urchin structures without Zn_2TiO_4.

4.3 Experimental Details

4.3.1 Preparation for TiO_2 HHSs

All the chemicals used were analytical grade and purchased from Sigma-Aldrich. The HSS was synthesised and deposited onto a titanium substrate using electrospinning technique. The process was developed based on collaboration with my colleague, Yuanxing Fang. The titanium substrates ($2 \times 2\ cm^2$) were polished and sonicated in an IPA bath for 15 minutes, and dried in air before they were used. The averaged molecular weight of poly(methyl methacrylate) (PMMA) is 35,000 $g\ mol^{-1}$, determined by gel permeation chromatography performed by the supplier.

In the electrospinning process, the PMMA was first dissolved in nitromethane (NM) to form a 10 wt% solution. Then, 4 wt% of titanium tetraisopropoxide (TTIP) and 1 wt% of acetylacetone were added to the PMMA solution. Here, acetylacetone was used to stabilise the TTIP in NM solution. The solution was magnetically stirred at room temperature for 24 hours under dark surrounding until the colour of the solution becomes a transparent light yellow. The mixture was loaded into a plastic syringe with a needle inner diameter of 0.270 mm for the electrospinning process at a constant flow rate of 2.0 ml hr^{-1}, controlled by a syringe pump. A positive bias of 25 kV was applied at the metallic needle while the collector (polished titanium substrate) was grounded.

The distance between the tip of the needle and the titanium plate was maintained at 12 cm. The duration of the electrospinning process was 4 hours, during which a white homogeneous thin film of HHSs was formed on the substrate. Then, the as-prepared HHSs were hydrolysed by dipping in DI water, followed by steam bath at 80ºC for an hour. The sample was then calcined at 400ºC for 18 hours, with a heating rate of 1ºC min^{-1}. During the calcination process, the thin film turned brown at 300ºC and then became white-yellow at 400ºC.

4.3.2 Growth of ZnO NRs on TiO_2 HHSs

The method used for growing ZnO NRs on the surface of TiO_2 HHSs is the aqueous CBD. The seeding solution was prepared by dissolving 0.219 g of zinc acetate in 10.0 ml of DI water and magnetically stirred for 2 hours to form a 0.10 M seeding solution. The annealed TiO_2 HHSs were soaked in the seeding solution for an hour. The seeded samples were then annealed at 350°C for an hour to convert the zinc acetate into ZnO nano seeds, followed by the CBD growth process. The nutrient solution for CBD growth was composed of a 1:1 molar ratio of zinc nitrate hexahydrate and hexamethylenetetramine (HMT) in DI water. The Zn^{2+} final concentration of the solution was 10.0 mM. The as-prepared samples were vertically aligned in glass beakers containing 150 ml of growth solution at 85°C for 4, 15 and 24 hours. The samples were then rinsed three times with DI water, dried at room temperature, and annealed to 400~800°C.

4.3.3 Acid Treatment of Urchin-like ZnO/TiO_2 Sample Annealed at 700°C

The urchin-like ZnO NRs on TiO_2 HHSs annealed at 700°C (ZT 700) sample was subjected to hydrochloric acid (HCl) in order to reveal the structures underneath the

ZnO NRs by gradually dissolving the ZnO NRs. HCl with a pH value of 1.0 was used in this experiment. The ZT 700 sample was dipped in the HCl solution for 10 s followed by five rinses with DI water. This step was repeated until all the ZnO NRs were dissolved by HCl solution.

4.3.4 Characterisation

SEM (JSM 820M, Jeol) was used to examine the surface morphology and structure of the samples. Power XRD (Siemens D500) was carried out to analyse the crystallinity of the nanostructures. The elemental analysis of the samples was analysed by EDX. The diameters of the ZnO NRs and TiO_2 HHSs were measured using Image J software (National Institutes of Health, USA). PEC water splitting was undertaken to identify the photocatalytic activity of the samples in a 1.0 M aqueous KOH electrolyte solution (pH 13.6). A KCl saturated Ag/AgCl electrode was used as the reference and a platinum foil was used as the counter electrode. Sunlight was simulated with a 300W xenon arc lamp with an AM1.5 G filter and the output light power density was adjusted to 100 mW cm^{-2}. The cyclic voltammetry measurements were taken by USB potentiostat using eDAQ software.

4.4 Results and Discussion

4.4.1 Preparation for Electrospinning and CBD

A polished and cleaned substrate is required for electrospinning process in order to ensure the conductivity of the titanium plate. ZnO seeding was introduced to the surface of TiO_2 HHSs by soaking in the zinc acetate solution for an hour followed by annealing the sample at 350°C to thermally degrading zinc precursor into ZnO nano seeds.

4.4.2 Electrospinning of TiO_2 HHSs

Mesoporous TiO_2 HHSs, as shown in Figure 4.1, were successfully formed through the electrospinning method previously developed within the group. Based on these investigations, the diameters of TiO_2 HHSs are controllable and optimised by tuning the experimental parameters.

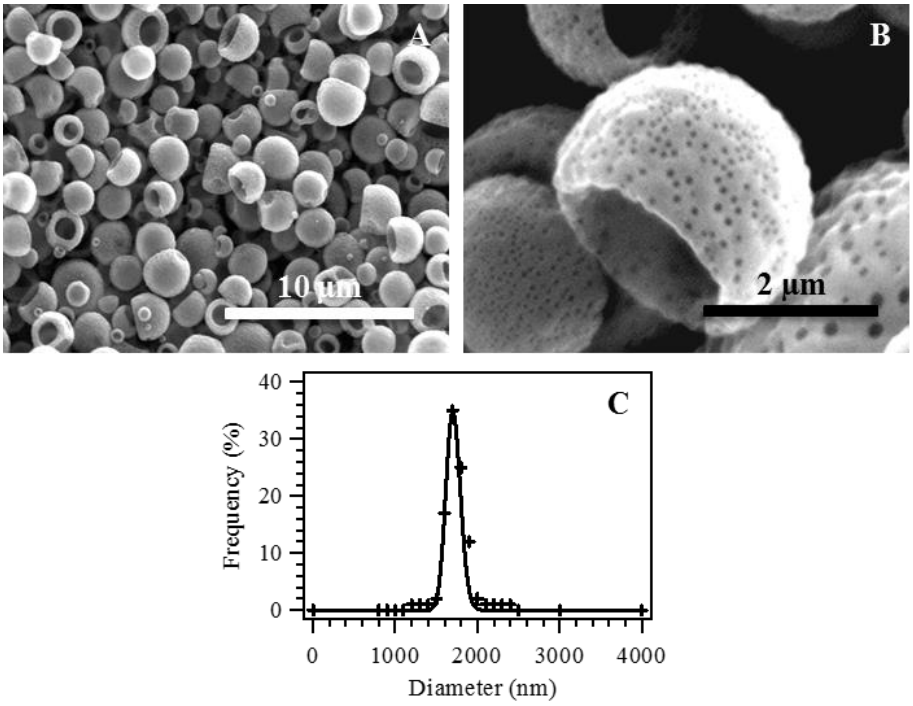

Figure 4.1 SEM images of TiO_2 HHSs annealed at 400ºC for 18 hours with an initial heating rate of 1ºC min^{-1}, (A) top view and (B) high magnification. (C) Diameter distributions of TiO_2 HHSs.

For the formation of nanopores on the surface of TiO_2 HHSs, the as-prepared sample needs to undergo hydrolysis-precipitation (HP) treatment by dipping the sample in DI water, followed by a steam bath reaction for an hour, which converts the TTIP to titanium hydroxide crystals. The HP treated sample was then annealed at 400ºC for 18 hours, with an initial heating rate of 1ºC min^{-1} in order to retain the structure of the

sample after calcination. TTIP has a boiling point of 232ºC, which is similar to the decomposition temperature of PMMA (between 200–300ºC). Rapidly increasing the annealing temperature would cause considerable evaporation of TTIP, resulting in deformation of TiO_2 HHS and significant aggregation.

It is noticeable that TiO_2 HHSs were homogenously electrospun onto a titanium substrate, as shown in Figure 4.1A. Figure 4.1B reveals the created TiO_2 HHSs are having nanopores on the surface. The average diameters and mean errors of the TiO_2 HHSs and nanopores were evaluated from 100 measurements through their top view SEM images, which were measured to be 300±35 and 70±20 nm, respectively. Figure 4.3C shows the as-spun TiO_2 HHSs are monodispersed in the diameter (2500 nm) with a FWHM value of 300 nm, corresponding to a ±6% dispersion.

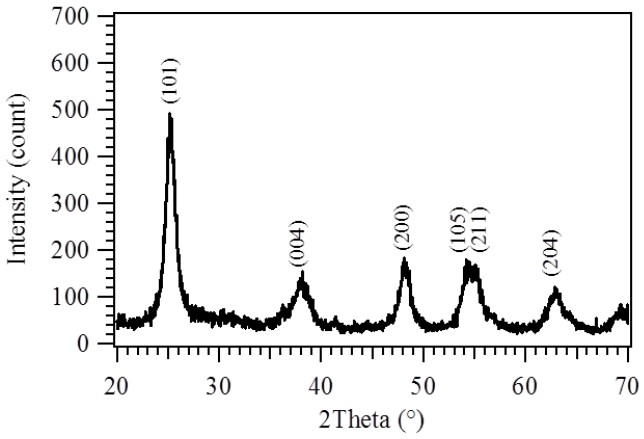

Figure 4.2 XRD pattern of TiO_2 HHSs annealed at 400°C for 18 hours with an initial heating rate of 1ºC min^{-1}. The miller indices of the crystal planes are labelled.

Powder XRD was used to confirm the crystal structure of the annealed TiO_2 HHSs. The XRD pattern of TiO_2 HHSs is analysed based on the standard XRD database for the anatase phase of TiO_2 (JCPDS # 21-1272). All of the peaks can be assigned to the anatase phase of TiO_2. The TiO_2 HHSs give the diffraction peaks located at 2θ =

25.27°, 37.70°, 47.98°, 54.76°, 55.69° and 62.95°, corresponding to (101), (004), (200), (105), (211) and (204) crystal planes. Figure 4.2 demonstrates (101) is the most intense diffraction peak with a FWHM value of 0.7085º, which gives a crystal domain size of 11.2 nm.

4.4.3 Effect of Growth Duration on the Morphology of ZnO NRs

A duration dependent experiment was conducted to determine the optimal duration for the growth of ZnO NRs on the surface of TiO_2 HHSs to form the urchin-like structures. All the other experiment parameters were held constant, while the duration of reaction is varied from 4, 15 to 24 hours. Figure 4.3 shows the top view SEM images of the samples grown at different durations.

Urchin shaped hybrid ZnO NRs on TiO_2 HHSs were successfully created through the combination of electrospinning and CBD methods. Figure 4.3A shows the ZnO NRs formed after 4 hours of growth are randomly oriented with a small diameter. Additionally, there are only a small number of NRs grew on the surface of TiO_2 HHS. When the growth duration is increased to 15 hours, more ZnO NRs were deposited onto the surface of TiO_2 HHSs, with larger diameters, and becoming more vertically aligned after 24 hours growth (Figure 4.3C). It is clearly shown that ZnO NRs formed were homogenously vertically aligned array on the surface of TiO_2 HHSs.

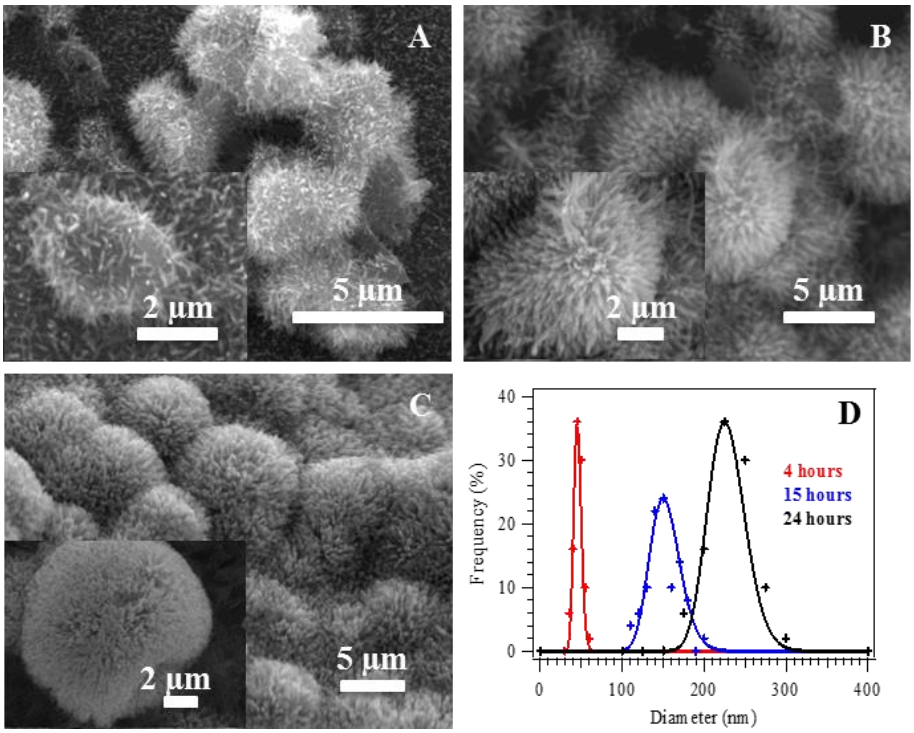

Figure 4.3 SEM images of urchin-like ZnO NR arrays on TiO_2 HHSs grown in 150 ml of nutrient solution at different growth durations, (A) 4 hours, (B) 15 hours and (C) 24 hours (The inset is the corresponding higher resolution of SEM image). (D) Diameter distributions of ZnO NRs at different growth durations.

The diameters, lengths and mean errors of ZnO NRs of the hybrid samples were quantified using the top view and cross sectional view SEM images (100 measurements). The measurements demonstrate the average diameters of the NRs are increasing proportionally to the growth duration. The diameter distributions of ZnO NRs for that grew for 4, 15 and 24 hours show monodispersion in their diameter with an average diameter of 50±12, 150±50, and 220±64 nm, respectively (Figure 4.3D). Meanwhile, the average length of the NRs increases from 0.76 µm to 3.15 µm when the growth duration increased from 4 to 24 hours.

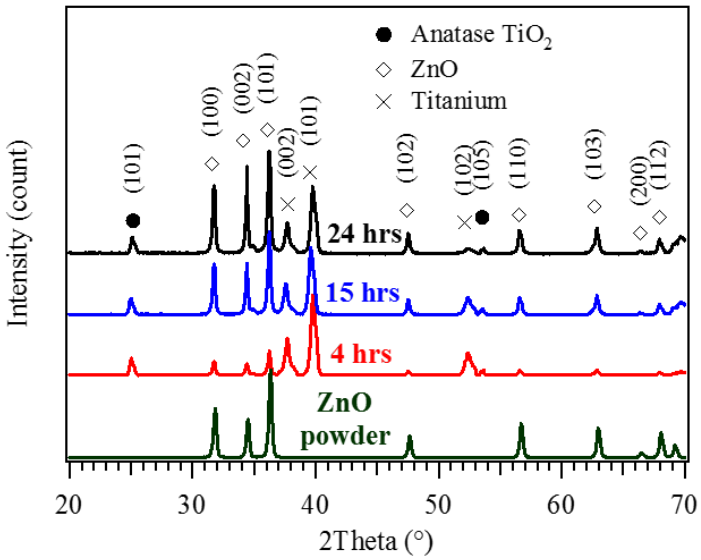

Figure 4.4 XRD patterns of urchin-like ZnO NRs on TiO_2 HHSs on titanium plate after different growth durations together with XRD pattern of ZnO powder. The miller indices of the crystal planes are labelled where ●, ◊ and × are anatase phase of TiO_2, ZnO and titanium, respectively.

The XRD patterns of the urchin-like ZnO NRs array vertically on TiO_2 HHSs (Figure 4.4) are analysed based on the standard XRD database for anatase phase of TiO_2 (JCPDS # 21-1272), wurtzite ZnO (JCPDS # 36-1451) and alpha-titanium (JCPDS # 44-1294). The anatase phase of TiO_2 gives the diffraction peaks located at $2\theta = 25.42°$ and 54.05° (●), corresponding to (101) and (105) crystal planes. The wurtzite ZnO gives the diffraction peaks located at $2\theta = 31.82°$, 34.58°, 36.40°, 47.67°, 54.37°, 62.96°, 66.46° and 68.08° (◊), corresponding to (100), (002), (101), (102), (110), (103), (200) and (112) crystal planes. The alpha-titanium gives the diffraction peaks located at $2\theta = 38.12°$, 39.89° and 52.42° (×), corresponding to (002), (101) and (102) crystal planes.

As growth duration increases, the intensities of the ZnO diffraction peaks are increased. This is in agreement with the SEM images, where increase in the growth duration results in longer and wider ZnO rods, since more ZnO is deposited onto the

nucleation sites. The SEM images also demonstrate the ZnO NRs are vertically aligned on the surface of TiO_2 HHSs. This indicates the favoured growth direction for the ZnO NRs is along the [0001] direction, which is perpendicular to the surface of TiO_2 HHSs. However, the strongest diffraction peak of the urchin-like ZnO/TiO_2 sample is (101) plane, instead of (002) plane as shown in Figure 4.4. This can be attributed to the fact that the ZnO NRs are being grown on the curved surface of TiO_2 HHSs. Therefore, most of the X-rays are shone on the side facets of the hexagonal rods, resulting in low (002) peak intensity. It is important to mention that the quantitative analysis of the diffraction intensities reveals that the intensity ratios of the ZnO powder are 1.0:0.7:1.5 for (100):(002):(101) planes. This ratio changes to 1.0:1.0:1.1, 1.0:1.0:1.2 and 1.0:1.1:1.2 for the ZnO NRs grew on TiO_2 HHSs for 4, 15 and 24 hours, respectively. These measurements reveal that the NRs are possibly vertically aligned on the surface of TiO_2 HHSs.

The crystal domain sizes of the samples were quantitatively described by the Scherrer equation (Equation 2.5, Section 2.3). Crystal sizes of 17.2, 25.6 and 33.7 nm were calculated for that grew at 4 hours, 15 hours and 24 hours, respectively. Other than that, the degree of orientation of ZnO nanostructures can also be obtained from the XRD spectra. The preferred orientation of the film can be illustrated by the relative texture coefficient (Equation 2.7, Section 2.3). The relative texture coefficients of ZnO NRs for urchin-like samples at different growth durations were estimated to be 0.54, 0.64 and 0.68. In comparison to ZnO powder (0.50), our samples exhibit higher relative texture coefficient values, which suggests that the NR arrays on TiO_2 HHSs are relatively more c-oriented. This is in agreement with the SEM images in Figure 4.3, where the ZnO rods are grown radially outward on the surface of TiO_2 HHSs.

4.4.4 Calcination Study of Urchin-like ZnO/TiO_2 Sample

The effect of annealing temperatures on the urchin-like ZnO/TiO_2 sample was investigated. A series of calcination studies were performed where the optimised urchin-like ZnO/TiO_2 sample (grew for 24 hours) was annealed from 400 to 800°C for an hour. The XRD patterns of all the samples are matched with the standard database for anatase phase of TiO_2 (JCPDS # 21-1272), rutile phase of TiO_2 (JCPDS # 21-1276), wurtzite ZnO (JCPDS # 36-1451), Zn_2TiO_4 (JCPDS # 25-1164) and alpha-titanium (JCPDS # 44-1294).

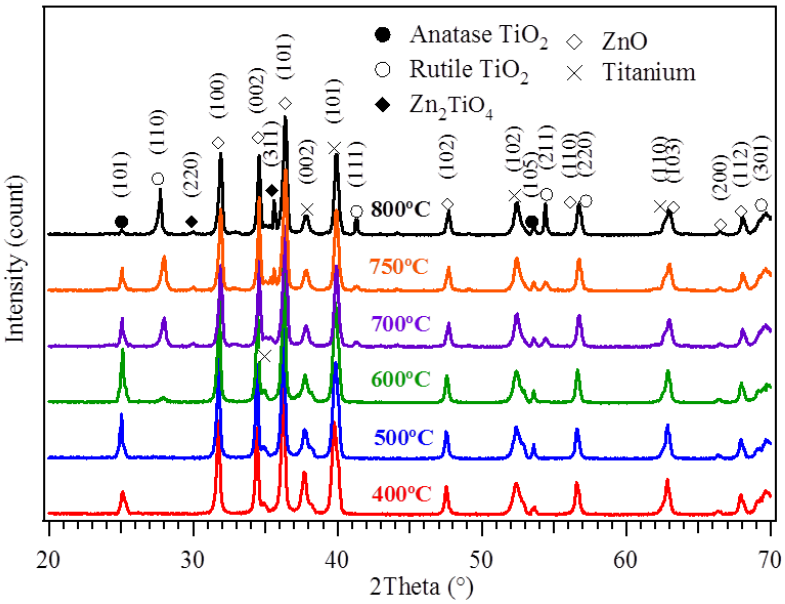

Figure 4.5 XRD patterns of urchin-like ZnO/TiO_2 sample grew at 24 hours at different annealing temperatures. The miller indices of the crystal planes are labelled where ●, ○, ♦, ◊ and × are anatase phase of TiO_2, rutile phase of TiO_2, Zn_2TiO_4, ZnO and titanium, respectively.

As shown in Figure 4.5, the diffraction peaks intensities for anatase phase of TiO_2 increase from 400°C to 500°C and start to decrease when the annealing

temperature is at 600°C and above. At 600°C, a few additional diffraction peaks appeared at 2θ = 27.56°, 41.36°, 54.37°, 56.69° and 69.05° (○), corresponding to (110), (111), (211), (220) and (301) crystal planes for the rutile phase of TiO_2. The initial increase of anatase diffraction intensity indicates the improvement of the crystallinity of the TiO_2. The decreasing of the anatase peaks intensities at 600°C were due to the conversion of anatase phase of TiO_2 to rutile phase of TiO_2, which is thermodynamically more stable.[246] Meanwhile, the intensity of ZnO diffraction peaks remain unchanged when the annealing temperature is increased from 400°C to 600°C. It is important to note that the intensities of ZnO peaks start to decrease slightly when the sample is annealed at 700°C. Meanwhile, there are two small peaks appeared at 2θ = 29.90° and 35.43° (♦). These two peaks correspond to the (220) and (311) crystal planes of Zn_2TiO_4, which are the dominant peaks of Zn_2TiO_4. It is noteworthy that the intensity of Zn_2TiO_4 diffraction peaks (marked as ♦) are weak (Figure 4.5), which indicates the Zn_2TiO_4 film formed in the urchin-like ZnO/TiO_2 sample at 700°C is relatively thin. The intensities of the Zn_2TiO_4 peaks became more intense when the annealing temperature was increased to 800°C. This explains why the intensity of ZnO peaks start reducing at 700°C as some of the ZnO has reacted with TiO_2 to form Zn_2TiO_4. Cai Z. Y. *et al.* have also reported that Zn_2TiO_4 starts to form in their sample mixture, containing zinc acetate and TTIP, annealed at 700°C.[247] This phenomenon is similar to our experiment since the urchin-like ZnO/TiO_2 sample contains a mixture of ZnO and TiO_2 at the interfaces.

4.4.5 Acid Treatment of ZT 700 Sample

In order to confirm that Zn_2TiO_4 is formed at the interface between ZnO NRs and TiO_2 HHSs, an acid treatment experiment was conducted for the ZT 700 sample.

The purpose of this acid treatment experiment was to gradually dissolve ZnO NRs from the ZT 700 sample, since both TiO_2 and Zn_2TiO_4 are stable in acid.[110, 248]

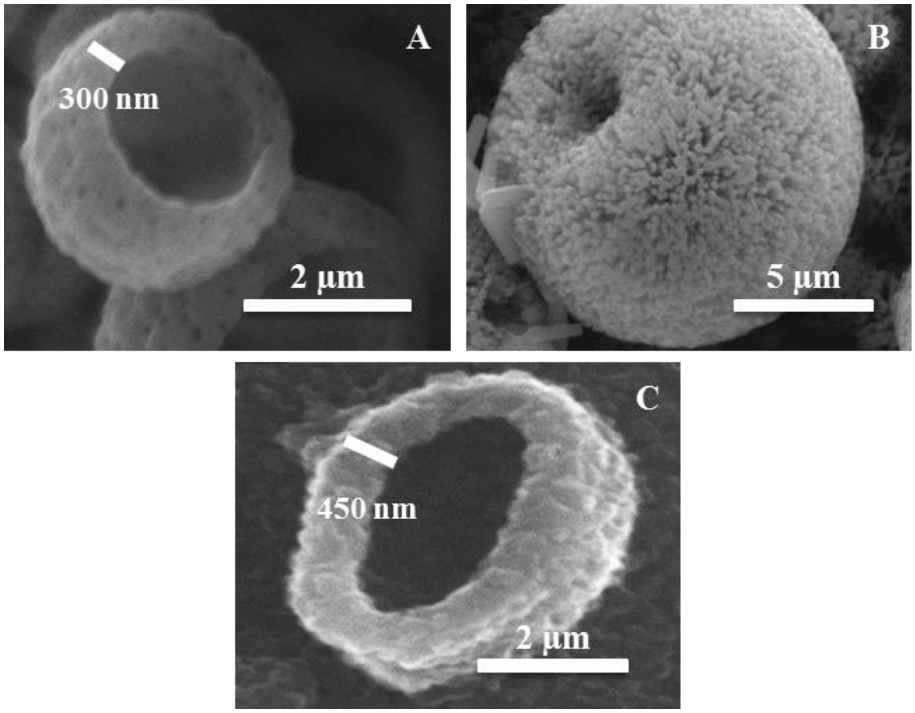

Figure 4.6 SEM images of (A) TiO_2 HHS, (B) ZT 700 and (C) ZT 700 after 80 s of acid treatment.

Figure 4.6C shows the ZnO NRs of ZT 700 sample were fully removed after dipping in HCl solution of pH 1 for 80 s. The reaction of the experiment is as below:

$$ZnO_{(s)} + 2HCl_{(aq)} \rightarrow ZnCl_{2(aq)} + H_2O_{(l)} \quad \text{(Equation 4.1)}$$

By comparing the morphology of as-spun TiO_2 HHS (Figure 4.6A) with ZT 700 sample after the removal of ZnO NRs (Figure 4.6C), it is noticeable that there are a few changes on the HHSs surface. One of the obvious changes is that the smooth surface with nanopores of the as-prepared TiO_2 HHS is now changed to a layer of cubical

nanostructures. In addition, the wall thickness of the HHS for ZT 700 sample is increased by 150 nm as compared to the as-prepared TiO_2 HHS. This measurement reveals that a thin film (75 nm) of Zn_2TiO_4 is possibly formed at the interface between ZnO NRs and TiO_2 HHSs. To further confirm the cubical nanostructures formed are Zn_2TiO_4, EDX was carried out to determine the elemental composition of ZT 700 sample before and after 80 s of acid treatment.

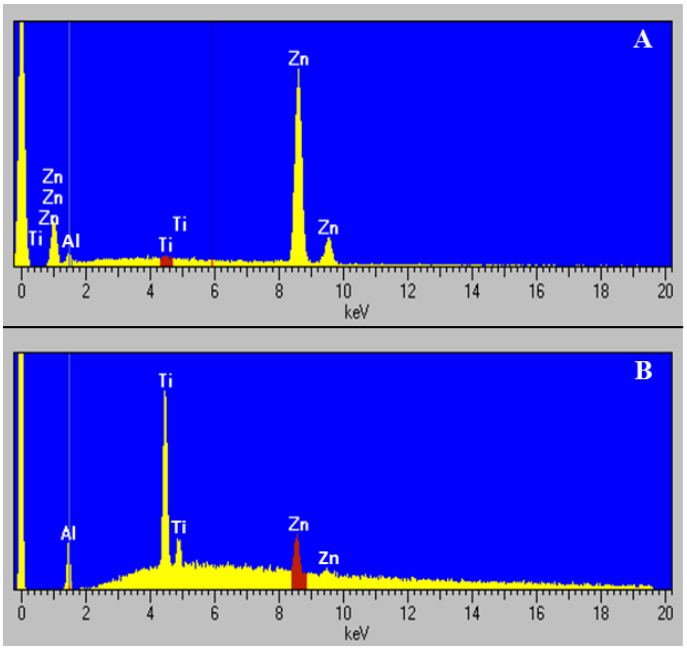

Figure 4.7 EDX spectra of ZT 700 sample, (A) before and (B) after 80 s of acid treatment.

For this experiment, ZT 700 sample was scratched down from the titanium substrate onto an aluminium foil before the EDX analysis. This is to prevent the EDX analysis from recording titanium element from the substrate instead of the sample. As shown in Figure 4.7, both EDX spectra display the dominant elements presented in the ZT 700 samples before and after 80 s of acid treatment are zinc and titanium. The quantitative analysis reveals an atomic composition of 3.08% titanium and 96.92% zinc

for that before acid treatment, meanwhile an atomic composition of 72.33% titanium and 27.67% zinc was obtained for that after 80 s of acid treatment. As shown in Figure 4.7A, the zinc element of the untreated sample is about 30 times higher than that of titanium. After all the ZnO NRs are removed, the EDX spectrum (Figure 4.7B) still presented a small amount of zinc in the sample. These results further confirm the formation of acid stable cubical nanostructures of Zn_2TiO_4. To further support the existence of Zn_2TiO_4 in the ZT 700 sample, XRD measurements were ran in parallel with the acid treatment experiment.

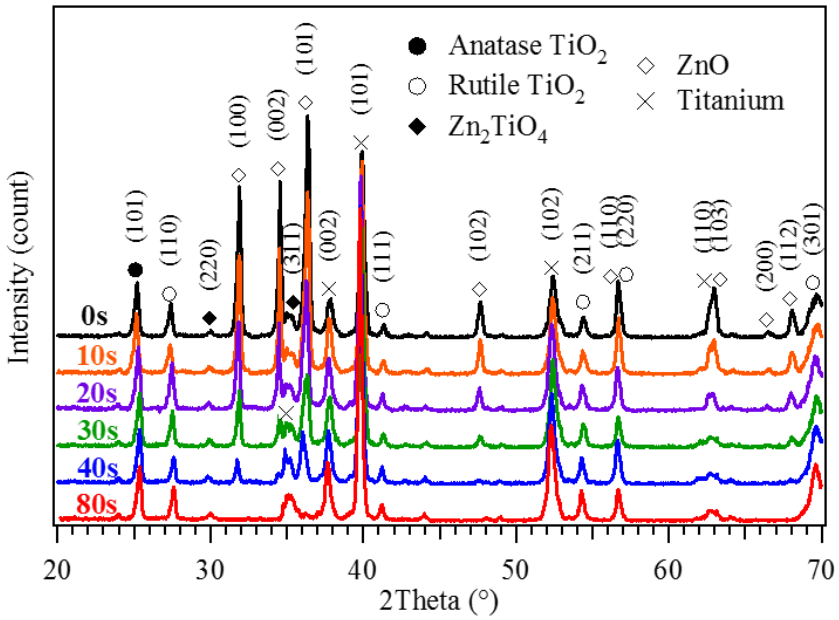

Figure 4.8 XRD patterns of ZT 700 sample at different durations of acid treatment. The miller indices of the crystal planes are labelled where ●, ○, ♦, ◊ and × are anatase phase of TiO_2, rutile phase of TiO_2, Zn_2TiO_4, ZnO and titanium, respectively.

ZnO NRs are gradually dissolved by HCl solution as confirmed by the XRD spectra, shown in Figure 4.8. The intensity of ZnO peaks are steadily decreased as acid treatment duration increases, while the rest of the diffraction peaks remain unchanged.

By comparing the XRD patterns of the untreated ZT 700 sample (0 s, black spectrum) with that after 80 s of acid treatment (red spectrum), it is noticeable that the diffraction peaks of Zn_2TiO_4 (♦) become more intense while the diffraction peaks of ZnO (◊) disappear. It is noteworthy that the diffraction peak intensities of titanium (×) increase as well as the duration of acid treatment increases. This is consistent with the dissolving of ZnO NRs by HCl solution, resulting in a thinner oxide layer on titanium substrate. The main diffraction peak intensities of ZnO [(100), (002), (101)] together with the Zn_2TiO_4 [(311), (200)] as a function of acid treatment duration were measured and plotted in Figure 4.9.

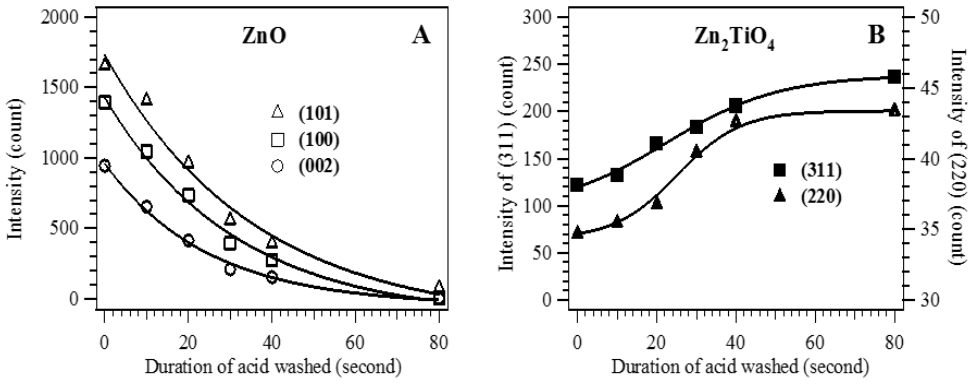

Figure 4.9 Plots of XRD diffraction peak intensities with respect to the duration of acid treatment for (A) ZnO and (B) Zn_2TiO_4.

Figure 4.9A demonstrates the three main diffraction peak intensities of ZnO decrease exponentially throughout the acid treatment. The ZnO was fully dissolved after dipping in the acid solution for 80 s. Meanwhile, the two dominant diffraction peaks of Zn_2TiO_4 steadily increase as the acid treatment continues, reaching a constant value after 40 s of acid treatment (Figure 4.9B). The diffraction peak intensities of Zn_2TiO_4 increase during the acid treatment experiment because they were previously overshadowed by the diffraction from ZnO.[249]

4.4.6 Growth Process of Urchin-like ZnO/TiO_2 Sample

Based on the growth duration dependent experiment, calcination study and acid treatment with SEM and XRD of the urchin-like ZnO/TiO_2 sample, schematic diagrams are deduced to illustrate the growth process of the sample, as presented in Figure 4.10.

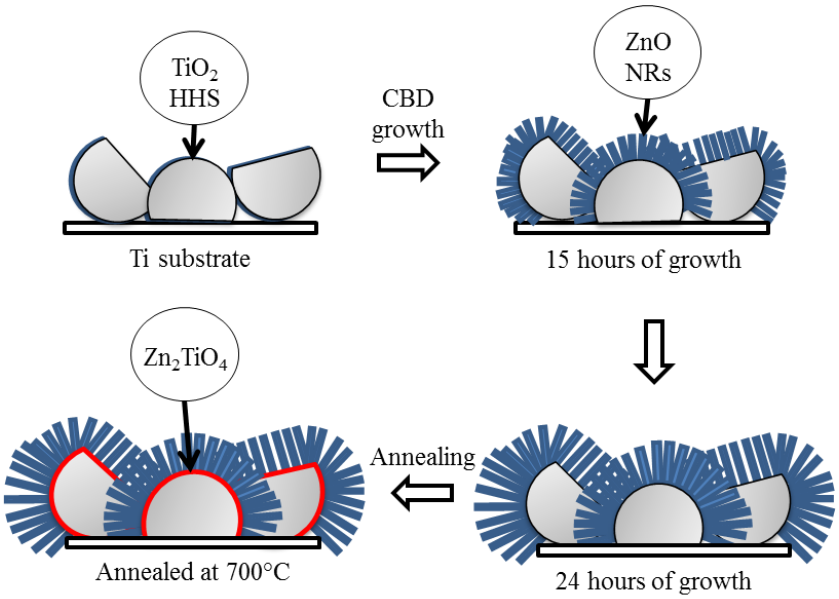

Figure 4.10 Schematic diagrams demonstrating the growth process of the urchin-like ZnO/TiO_2 sample.

Firstly, TiO_2 HHSs were electrospun onto a titanium substrate followed by the CBD growth of ZnO NRs. The ZnO NRs are growing along the [0001] direction on the seeded TiO_2 HHSs. As the growth duration increased, the ZnO NRs formed will be longer with a larger diameter. When the urchin-like ZnO/TiO_2 sample is annealed to 700°C (ZT 700), Zn_2TiO_4 is formed in the sample, as confirmed by powder XRD. We propose that the Zn_2TiO_4 layer should be form at the interface between ZnO NRs and TiO_2 HHSs, where ZnO and TiO_2 are contacted.

4.5 PEC Hydrogen Generation Study

4.5.1 Effect of Calcination on the PEC Activity of ZnO/TiO_2 Sample

The PEC performance of the urchin-like ZnO/TiO_2 sample was optimised by controlling the crystallinity. The hybrid sample annealed at elevated temperatures, ranging from 400–800ºC, was examined as photoanode (named as ZT 400–ZT 800) in 1.0 M KOH electrolyte (pH 13.6) under the illumination of a 100 mW cm^{-2} solar simulator with an AM1.5 G filter.

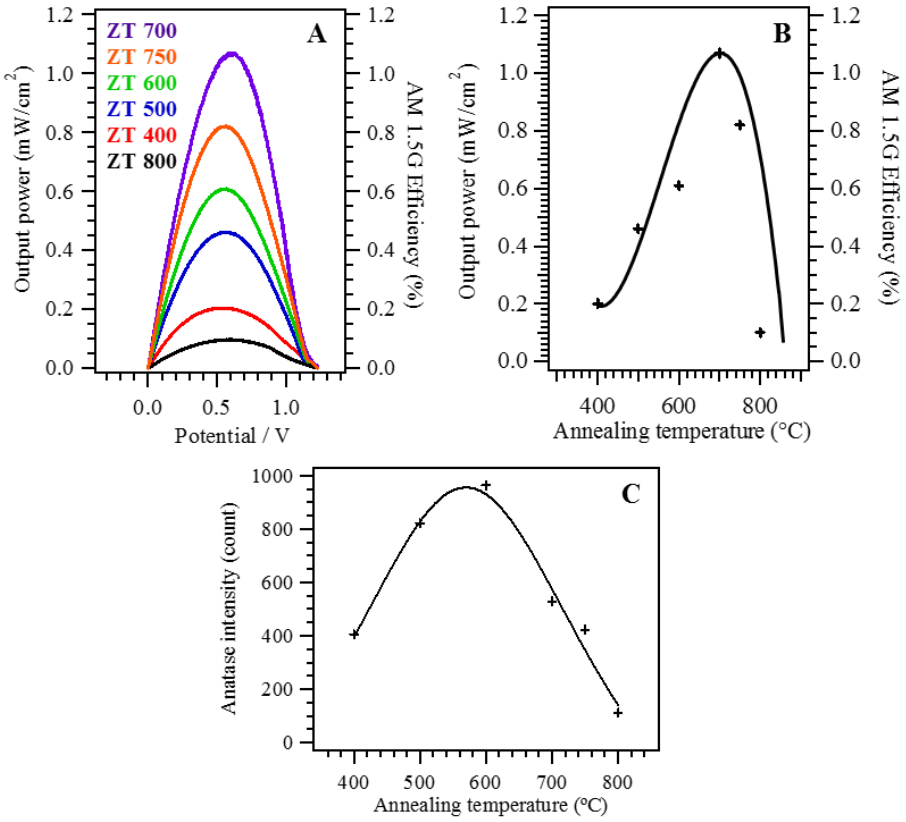

Figure 4.11 (A) Output power and AM1.5 G efficiency of urchin-like ZnO/TiO_2 sample at different calcination temperatures, (B) photoconversion output power and AM1.5 G efficiency and (C) (101) peak intensity for anatase phase of TiO_2 as a function of calcination temperature.

Figure 4.11A represents the PEC output power as a function of calcination temperature from 400 to 800ºC and Figure 4.11B demonstrates the maximum output power from the urchin-like ZnO/TiO_2 sample. It is clear that the hydrogen generation efficiency increased initially as the annealing temperature increases, with a maximum output power of 1.07 mW cm^{-2} achieved at 700ºC.

It has been reported that the ratio of anatase and rutile phase of TiO_2 plays an important role in determining the photocatalytic performance of the sample.[250] In order to demonstrate how the crystallinity of TiO_2 affects the photocatalytic activity, the (101) peak intensity of anatase as a function of annealing temperature is extracted from Figure 4.5, shown in Figure 4.11C. Initially, the increasing in calcination temperature improves the crystal quality of the TiO_2 HHS, while above 600ºC, the anatase is subjected to a phase transition to rutile TiO_2. The anatase diffraction intensity curvature is very similar to the maximum output power curve in Figure 4.11B. This reveals some correlation between the crystal quality and the photoconversion output power of TiO_2 HHSs in the urchin-like ZnO/TiO_2 sample. Such correlation can be explained as the crystallinity improves, the crystal defect decreases and thus the charge mobility increases. However, it is important to note that the maximum output power is achieved at a higher temperature of 700°C. Literature showed that the highest photocatalytic activity of TiO_2 is at 650°C.[251] Our higher temperature for maximum output power could not be exclusively explained by the crystal quality of TiO_2 but could also be contributed from the presence of a layer of Zn_2TiO_4 at the interface of the urchin-like ZnO/TiO_2 sample. This will be further evidenced by comparison of the optimal PEC performance from ZnO NRs, TiO_2 HSS and ZT700 photoanodes in the following section.

A decrease in the photoconversion output power is observed when the annealing temperature of the urchin-like ZnO/TiO_2 sample is further increased to 750ºC (ZT 750;

Figure 4.11A). This can be explained by the increase in rutile phase of TiO_2 in the urchin-like ZnO/TiO_2 sample, resulting in an increase in the charge recombination.[82] Alternatively, it could also be due to the increase of the Zn_2TiO_4 layer thickness, as confirmed by temperature dependent XRD (Figure 4.5). The formation of a thick layer of Zn_2TiO_4 at the interface presents a long pathway and thick barrier for limiting the photogenerated electrons to migrate to the conductive substrate and the photogenerated holes to migrate to the ZnO surface.[252] Therefore, it is unfavourable for overall charge separation which will result in a decrease in the photocatalytic efficiency.

4.5.2 PEC Activity of ZnO NRs, TiO_2 HHSs, ZT 600 and ZT 700

In order to check whether the urchin-like ZnO/TiO_2 sample displays a synergistic effect, a comparison of the photocatalytic activity between ZnO NRs, TiO_2 HHSs, ZT 600 and ZT 700 photoanodes was carried out. In order to achieve optimal photoconversion efficiency, ZnO NRs and TiO_2 HHSs were calcined at 400°C and 650°C, respectively. The length, diameter and density of the ZnO NRs were similar to those grown on TiO_2 HHSs, since identical experimental conditions were applied. Figure 4.12A represents the *I*–*V* curves of ZnO NRs (blue curve), TiO_2 HHSs (red curve), ZT 600 (green curve) and ZT 700 (purple curve) under simulated sunlight (100 mW cm^{-2} with an AM1.5 G filter) in the potential range from –0.8 to 1.0 $V_{Ag/AgCl}$ together with the dark current measured from ZT 700 in 1.0 M KOH electrolyte.

At a typical potential of 0.4 $V_{Ag/AgCl}$, the photocurrents generated from ZnO NRs, TiO_2 HHSs, ZT 600 and ZT 700 electrodes were measured to be 0.23, 0.59, 1.34 and 2.12 mA cm^{-2}, respectively. It is worth noting that the onset potentials of ZT 600 and ZT 700 photoanodes are more negative than that of ZnO NRs and TiO_2 HHSs photoanodes. The onset potentials of ZnO NRs, TiO_2 HHSs, ZT 600 and ZT 700

photoanodes were estimated to be –0.39, –0.42, –0.63 and –0.72 $V_{Ag/AgCl}$, respectively. The negative shift in the photocurrent onset potential can be attributed to the improved in the charge separation which thus reduced the electron-hole recombination.[253, 254]

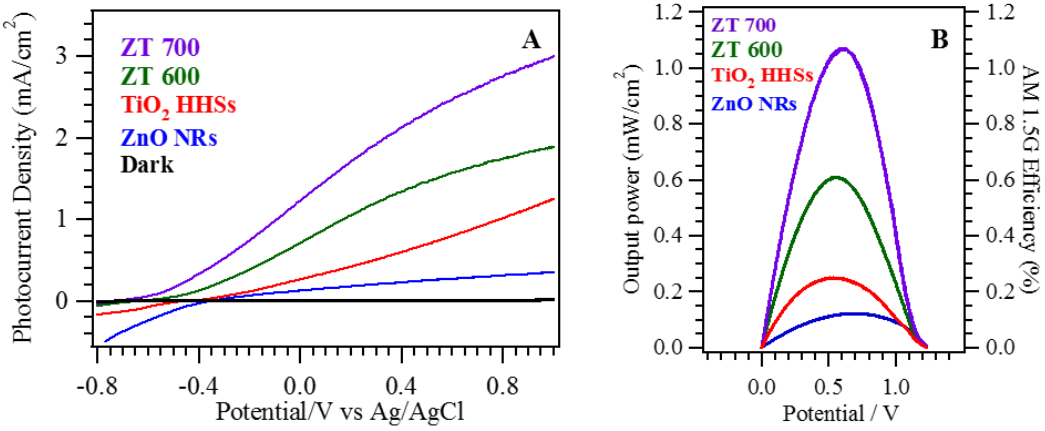

Figure 4.12 (A) *I–V* curves of ZnO NRs, TiO_2 HHSs, ZT 600 and ZT 700 together with dark current measured from ZT 700 in 1.0 M KOH electrolyte (pH 13.6) under simulated sunlight of 100 mW cm^{-2} with an AM1.5 G filter and (B) corresponding PEC output power and conversion efficiency under AM1.5 G full solar spectrum irradiation.

A comparison of the PEC output powers (Equation 2.27, Section 2.6) of the samples are presented in Figure 4.12B. The photoconversion efficiencies of ZnO NRs, TiO_2 HHSs, ZT 600 and ZT 700 photoanodes were calculated to be 0.12, 0.25, 0.61 and 1.07%, respectively. These results reveal that ZT 600 displays a synergic enhancement, resulting in its output power being ~60% higher than the sum of the output power of ZnO NRs and TiO_2 HHSs. More important, the photoconversion efficiency of ZT 700 photoanode is 76% higher than that of ZT 600 photoanode.

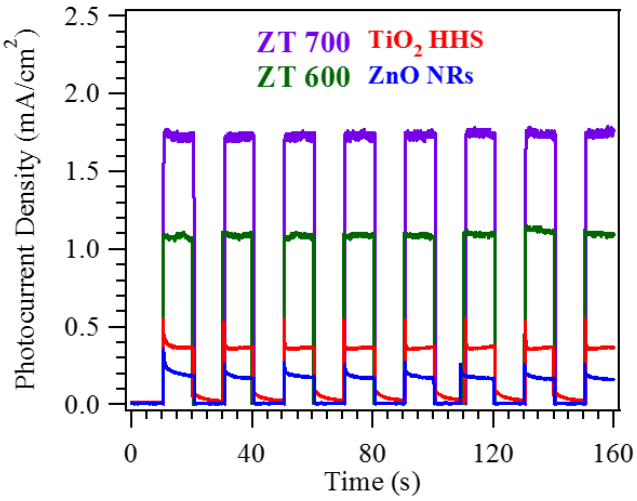

Figure 4.13 Amperometric *I–t* curves of ZnO NRs, TiO_2 HHSs, ZT 600 and ZT 700 photoanodes in 1.0 M KOH electrolyte (pH 13.6) at an applied voltage of 0.23 $V_{Ag/AgCl}$ at 100 mW cm^{-2} for 160 s with repeated light on-off cycles.

In addition, amperometric studies were carried out for ZnO NRs, TiO_2 HHSs, ZT 600 and ZT 700 photoanodes in 1.0 M KOH electrolyte (pH 13.6) at an applied voltage of 0.23 $V_{Ag/AgCl}$ under light on-off cycles for 160 s. Figure 4.13 demonstrates there is no obvious decrease in the photocurrent density for all the photoanodes, which confirms the stability of the photoanods under our experimental conditions in 1.0 M KOH electrolyte (pH 13.6) at room temperature.

It is worth noting that all the photoanodes, in particular the TiO_2 HHS and ZnO NRs, show an anodic photocurrent spike under the sudden illumination. The formation of these anodic photocurrent spikes was due to the bulk separation of the photoexcited electron and hole pairs that accumulated at the interface of semiconductor and electrolyte, resulting from the slow oxygen evolution reaction kinetics and carrier oxidised trap states of the semiconductor.[255, 256] Therefore, these anodic photocurrent spikes can be used to assess the lifetime of the charge carrier of the photoanodes which can be related to the general rate of charge recombination of the samples. The charge

recombination behaviour of the samples can be quantitatively determine by the normalised parameter (D) as below:[257]

$$D = \frac{(I_t - I_{st})}{(I_{in} - I_{st})} \qquad \text{(Equation 4.2)}$$

where I_t, I_{st}, and I_{in} are the time-dependent, steady-state and initial photocurrent, respectively, as labelled in Figure 4.14A.

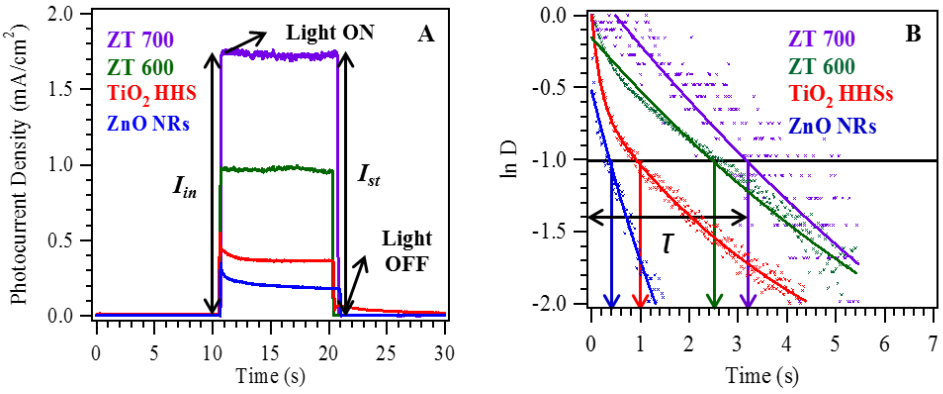

Figure 4.14 (A) Anodic photocurrent dynamics of the photoanodes recorded in 1.0 M KOH electrolyte (pH 13.6) at an applied potential of 0.23 $V_{Ag/AgCl}$ at 100 mW cm^{-2} and (B) normalised plots of ln D as a function of illumination time.

Figure 4.14B is the normalised plots of ln D as a function of illumination time for ZnO NRs, TiO_2 HHSs, ZT 600 and ZT 700 photoanodes. The transient time constant (τ) is defined as the time when ln D = –1, which reflects the lifetime of the charge carriers of the sample. The τ values of ZnO NRs, TiO_2 HHSs, ZT 600 and ZT 700 photoanodes were determined to be 0.38, 0.97, 2.42 and 3.18 s, respectively. These measurements demonstrate that the charge recombination of ZT 600 photoanode is

about 6.3 times and 2.5 times slower than that of ZnO NRs and TiO_2 HHSs photoanodes, respectively.

The possible reasons for the enhanced in the photocurrent density of ZT 600 may be attributed to the unique urchin-like morphology which facilitates a large effective surface area. Such geometry offers a large number of surface reaction sites for the oxidation of water. In addition, the 3D structure of urchin-like ZnO/TiO_2 sample offers improved light scattering ability which results in enhanced light harvesting.[245, 258] Other than that, the combination of ZnO NRs and TiO_2 HHSs can improve the electrolytes infiltration helping maintaining the electrolyte concentration at the vicinity of the reaction sites, which may also contribute to the improvement in the PEC efficiency.

More important, the recombination of photogenerated electrons and holes for the ZT 600 photoanode is reduced significantly as identified from Figure 4.14. This can be attributed to the appropriate alignment in the band gaps of ZnO and TiO_2 (Figure 4.15A). Both ZnO and TiO_2 have the similar band gap energies of 3.2 eV, however the conduction band of ZnO is 0.13 eV higher than TiO_2's due to the difference in Fermi levels. This will improve the charge separation rate since the injections of the photogenerated electrons from ZnO to TiO_2 and the photogenerated holes from TiO_2 to ZnO are thermodynamically favourable.[259] The misalignment between the conduction band of ZnO and TiO_2 will prevent the back flow of the electrons. According to Lee W. *et al.*,[260] TiO_2 NTs with a thin ZnO energy barrier in cadmium selenide quantum-dot-sensitised solar cells caused an increase in the total efficiency by 25.9%. The enhancement is attributed to the charge-collecting efficiency being improved, and the charge recombination being reduced. As a result, the possibility of electron-hole pair recombination is reduced and consequently increases the occurrence of redox processes

for the ZnO/TiO_2 composite material. This can be one of the dominate mechanisms for improved photocurrent density of the ZT600 photoanode over the ZnO NRs and TiO_2 HHSs photoanodes.

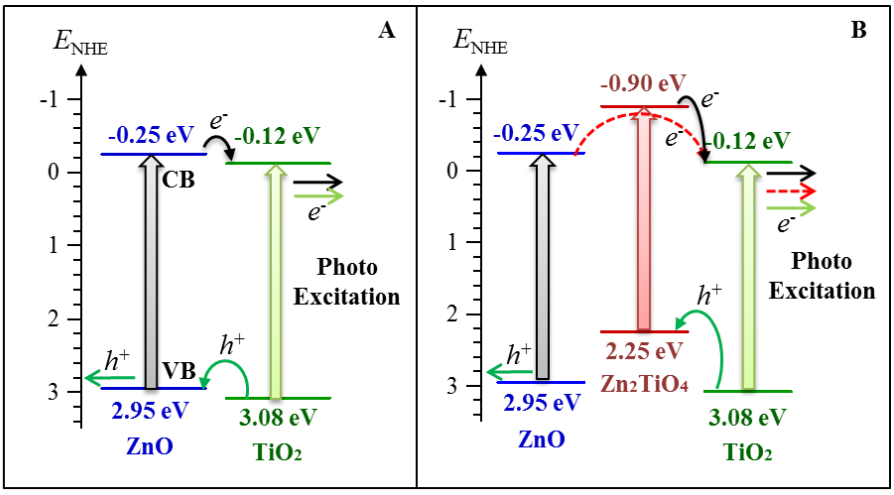

Figure 4.15 Band gap schematic diagrams representing the charge-transfer process in (A) ZT 600 and (B) ZT 700.[261, 262]

As mentioned before, there is further increased in the photoconversion efficiency from the ZT 600 to ZT 700 photoanodes, shown in Figure 4.12B. This significant enhancement cannot be simply accredited to the change in the ratio of anatase and rutile phase of TiO_2, but instead relates to the formation of a thin layer of Zn_2TiO_4 at the interface of ZnO NRs and TiO_2 HHSs. Here, the thin layer of Zn_2TiO_4 acts as a barrier to improve charge separation, resulting in an enhancement of the PEC water splitting efficiency. Figure 4.14B shows the lifetime of the charge carriers of the ZT700 photoanode is about 1.3 times longer than that of the ZT 600 photoanode. This suggests the rate of charge recombination of the ZT 700 photoanode is much less than that of the ZT 600 photoanode. The decrease in the rate of electron-hole recombination of the ZT 700 electrode can be explained by the interface band gap structures between

ZnO, Zn_2TiO_4 and TiO_2, as shown in Figure 4.15B. Theoretical study has shown that the conduction band of the Zn_2TiO_4 is more negative than those of the TiO_2 and ZnO.[262] Therefore, the presence of Zn_2TiO_4 forms an electron barrier layer which also helps to reduce the electron-hole recombination. As the energy gap between the conduction bands of the Zn_2TiO_4 and TiO_2 is larger (0.78 eV) than that between the Zn_2TiO_4 and TiO_2, as illustrated in Figure 4.15B, the back flow of photogenerated electron from the TiO_2 to ZnO is restricted.

In addition, it is believed, quantum tunnelling of electrons were occurred in the ZT 700 electrode, when the Zn_2TiO_4 barrier layer is relatively thin. Quantum tunnelling is a phenomenon whereby the height of the barrier is greater than the total energy of the particle, and the particle 'tunnels' through the barrier to the other side regardless. Some of the electrons may exhibit quantum effects[263] and tunnel through the Zn_2TiO_4 barrier to reach at the conduction band of TiO_2, shown in Figure 4.15B by the red dashed arrows. In order to achieve quantum tunnelling of electrons in the ZT 700 sample, the Zn_2TiO_4 barrier layer should be thin since the tunnelling current follows exponential decay as a function of gap distance or barrier thickness.[264] In our case, the Zn_2TiO_4 formed at the interface layer is relatively thin (about 75 nm), confirmed by the SEM image of the acid treated sample. Therefore, it is believed that some of the electrons might penetrate through the Zn_2TiO_4 barrier to reach the conduction band of TiO_2 through quantum tunnelling. For calcination temperature higher than 700°C, a thicker layer of Zn_2TiO_4 could be formed and most of the anatase phase of TiO_2 HHSs will be converted to the rutile phase of TiO_2 HSSs. Under both conditions, the overall PEC efficiency will decrease as we observed in Figure 4.11B.

In summary, 3D urchin-like ZnO/TiO_2 sample demonstrates an improved in the PEC water splitting as compared to ZnO NRs and TiO_2 HHSs. The enhanced in the

PEC hydrogen generation efficiency can attributed to the combined effects of large effective surface area, enhanced light harvesting, improved charge separation, reduced electron-hole recombination, increased the electrolytes infiltration and enhanced the electron transportation. Therefore, the proposed technique to synthesise 3D urchin-like ZnO NR aligned arrays on TiO_2 HHSs represents a significant advance for PEC hydrogen generation applications.

4.6 Conclusions

In this study, aligned arrays of ZnO NR were successfully created on seeded porous TiO_2 HHSs, forming a 3D urchin-like structure through the combination of electrospinning and aqueous CBD methods. The optimum duration for the growth of ZnO NRs on TiO_2 HHSs was 24 hours. The calcination study revealed a thin layer of Zn_2TiO_4 was formed in the hybrid sample at 700°C. The acid treatment experiment showed that Zn_2TiO_4 layer was formed at the interface between ZnO NRs and TiO_2 HHSs, which was then further characterised by SEM, EDX and XRD. The PEC water splitting measurements revealed that the ZT 600 electrode displayed a synergistic effect whereby its output power was ~60% higher than the sum of the output power of ZnO NRs and TiO_2 HHSs photoanodes. More important, the presence of a thin layer of Zn_2TiO_4 film in the ZT 700 sample caused an increased in the photoconversion efficiency by 76% (1.07%), compared to that without Zn_2TiO_4 (0.61%). The possible mechanisms for the higher PEC water splitting performance of the 3D urchin-like ZnO/TiO_2 sample were also discussed.

Chapter 5 Enhanced Photoelectrochemical Water Oxidation by $Zn_{1-x}M_yO$ (M = Ni, Co, K, Na) Nanorod Arrays

5.1 Abstract

Here we report on a facile approach for the one-pot solution growth of doped ZnO NR arrays vertically by chemical bath deposition (CBD) method. The effect of the dopant ions on the final morphologies of ZnO nanostructures was examined. With the introduction of dopants, the optical band gap energies of the samples were reduced. The PEC water splitting performances of the doped and undoped ZnO NRs were tested. When compared with pristine ZnO NRs (0.11%), all the doped ZnO NRs (0.14 ~ 0.29%) demonstrated an improved in PEC water splitting efficiency by at least 27%. The highest photoconversion efficiency was achieved by the Na-doped ZnO NRs photoanode (0.29%), where it was 2.6 times greater than the pristine ZnO NRs electrode (0.11%).

5.2 Introduction

Fossil fuels have been extensively used for several decades and it has resulting in increased the greenhouse gases and pollutants. Therefore, the development of sustainable and renewable resources is vital for future energy security. The use of semiconductor materials for solar PEC and photocatalytic water splitting offers one of environmental friendly processes for generating renewable energy. Among the nanoscaled materials, 1D photocatalyts have been widely explored due to they possessed large surface area and short diffusion lengths for photogenerated minority carriers.[4, 79, 89, 265]

Many different metal oxide nanostructures such as ZnO,[266] TiO_2,[3] Fe_2O_3[267] and WO_3,[268] have been studied for their potential application in PEC water splitting. Out of many semiconductors, ZnO has been recognised as a promising photoanode material owing to its appropriate band edges, high electron mobility, low electrical resistance and high electron-transfer efficiency.[2, 79] However, the photoconversion efficiency of ZnO nanomaterials is substantially limited due to its large band gap (3.37 eV), which only absorb light in the UV region and rapid charge recombination due to high density of trap states.[269] Thus, many efforts have been focused on to increase the absorption of ZnO in the visible region, including sensitisation with dyes or quantum dots, and doping with heteroatoms.[79, 194, 265, 269, 270]

Impurity doping has been widely investigated in the past as one of the effective methods to increase the electrical conductivity and to narrow the band gap energy of the semiconductors.[187, 271-273] So far, various types of extrinsic dopants, for instance, metal cations[187, 273, 274] and non-metal anions[52, 275, 276] have been introduced into ZnO for enhancing the photoconversion efficiency. There are a range of techniques have been reported for the creation of doped ZnO NRs. The first method used for the growth of doped ZnO nanostructures is hydrothermal synthesis.[52, 277] Hydrothermal method has been extensively used since it requires low temperature to synthesise high quality of metal oxide nanostructures. However, it is difficult to monitor and control the growth process. The second technique used is metal vapour vacuum arc ion source implanter.[194] The growth process usually involves expensive high vacuum systems and operates under high voltage and current supply. The third strategy used chemical vapour deposition (CVD)[276] or high-pressure pulsed-laser deposition.[278] It is a complex process where high temperature (> 600°C) and high pressure are required for these methods, restricting the choices of substrates.

The study of growing doped ZnO nanostructures using a cost effective CBD process at low temperature (< 100°C) represents a relatively new challenge in this field of research. In the present work, we demonstrate a one-pot solution synthesis of high quality crystallised doped ZnO NRs based on an adapted CBD method. The method is capable of homogenous deposition of NRs over a large surface area, and allowing precisely control concentrations of dopants. In this project, various dopants (Co, K, Na and Ni) have been introduced into ZnO structures. The effects of dopant ions on the morphologies and optical properties of the created ZnO nanostructures were investigated. All the doped ZnO NRs show a reduced in their band gap energy as compared to the undoped ZnO NRs. The PEC measurements reveal that the photoconversion efficiency of doped ZnO nanostructures is enhanced by at least 27% with respect to the pristine ZnO NRs in PEC water splitting.

5.3 Experimental Details

5.3.1 Preparation for Growing Undoped and Doped ZnO NRs

All the chemicals used were analytical grade and purchased from Sigma-Aldrich. The substrates, titanium plates (2×2 cm^2) were polished and cleaned under sonication in an IPA bath for 15 minutes, and dried in air before they were used for growing ZnO nanostructures.

The synthesis process has two main steps which are seeding and growth processes. The seeding solution was prepared by dissolving 0.219 g of zinc acetate in 10.0 ml of DI water and magnetically stirred for 2 hours to form a 0.10 M seeding solution. The resulting precursor solution was spin cast (speed≈300 rpm, time≈30 s) onto titanium plate to form a seed layer. The seeded samples were then annealed at 350°C for an hour to convert the zinc acetate into ZnO nano seeds, followed by the

CBD growth process. The nutrient solution for CBD growth was composed of a 1:1 molar ratio of zinc acetate and hexamethylenetetramine (HMT) in DI water. The final concentration of the solution was 20.0 mM.

For the doped ZnO nanostructures, four different chemicals were used as doping precursors, which are cobalt acetate tetrahydrate, potassium nitrate, nickel acetate tetrahydrate and sodium nitrate. Doping was carried out by adding dopant ions into the growth solution resulting in a 1:4 molar ratio of dopant and zinc acetate. Each compound powder was weighed and placed in glass beakers, to which the pre-made nutrient solutions of 20 mM zinc acetate and HMT were added and magnetically stirred until the dopants had completely dissolved. The seeded substrates were vertically aligned in glass beakers containing 100 ml of growth solution at 85°C. After 12 hours, the samples were rinsed three times with DI water, dried at room temperature, and annealed at 400°C for an hour.

5.3.2 Characterisation

The surface morphologies were studied by SEM (JSM 820M, Jeol). The crystallinity and structure orientation of the nanostructures were analysed by powder XRD (Siemens D500). The UV-vis absorption spectra were recorded using UV-vis spectrophotometer (Thermospectronic UV 300). The average diameters and average film thicknesses were measured from top- and side-view SEM images using Image J (National Institutes of Health, USA). The actual concentrations of zinc and dopants were measured using inductively coupled plasma mass spectroscopy (ICP-MS; Agilent 7500ce). The PEC water splitting was measured using a standard three-electrode configuration in a 1.0 M KOH electrolyte (pH 13.6). A platinum foil was used as counter electrode and a KCl saturated Ag/AgCl electrode was used as a reference. A

USB potentiostat (eDAQ) was used to control and record the photocurrent as a function of electrochemical potential. Sunlight was simulated with a 300W xenon arc lamp with an AM1.5 G filter and the output light power density was adjusted to 100 mW cm^{-2}. Electrochemical impedance spectroscopy (EIS; Palmsens 3.0) measurements were carried out in 0.5 M Na_2SO_4 solution (pH 6.8) and the amplitude of the sinusoidal wave was set at 10 mV.

5.4 Results and Discussion

5.4.1 Morphologies of Undoped and Doped ZnO Nanostructures

Undoped, pure ZnO and doped ZnO NRs, as shown in Figure 5.1 and 5.3, were successfully synthesised through CBD method. The top view SEM images in Figure 5.1 demonstrate the morphologies of homogenously deposited ZnO nanostructures with no detectable micro-cracks. After the introduction of different dopants, shown in Figure 5.1B–E, the as-grown NRs still present the typical ZnO hexagonal cross section with variable rod density. It is worth noting that the morphologies of the Co- and Ni-doped ZnO NRs are quite different from the pure ZnO NRs. For the Ni-doped ZnO sample, the rods formed are relatively bigger in diameter, which forming a close-packed structure (Figure 5.1D). Meanwhile, the cross sections of the Co-doped ZnO NRs (Figure 5.1B) are less well defined as compared to the pristine ZnO NRs.

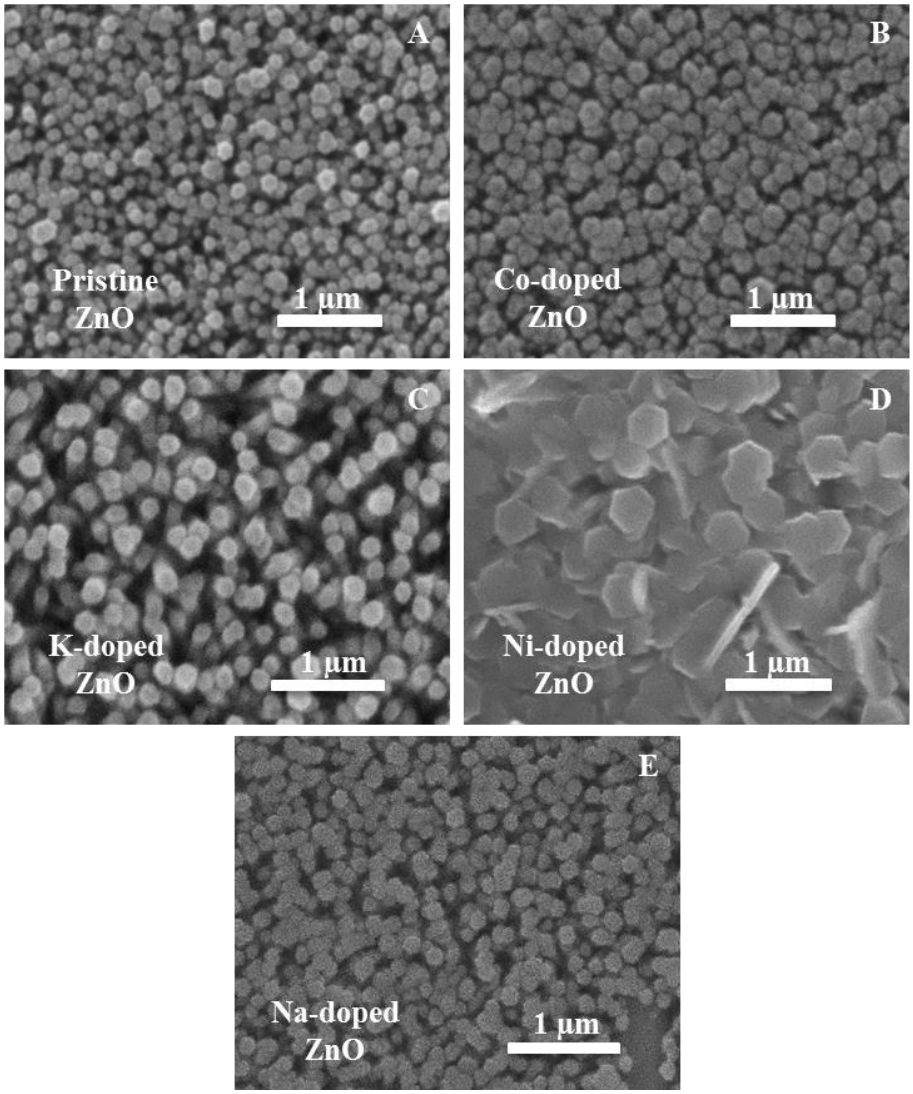

Figure 5.1 Top view SEM images of (A) undoped, (B) Co-, (C) K-, (D) Ni- and (E) Na-doped ZnO nanostructures grew in 100 ml of growth solution at 85°C.

The average diameters and mean errors of the doped and undoped ZnO NRs were evaluated from 100 measurements through their top view SEM images. As shown in Figure 5.2, the diameter distributions of the doped and undoped ZnO NRs are monodispersed in their diameters. The average diameters of the undoped, Co-, K-, Ni- and Na-doped ZnO NRs were measured to be 160, 200, 180, 440 and 170 nm with FWHM values of 22, 24, 21, 66 and 24 nm, respectively.

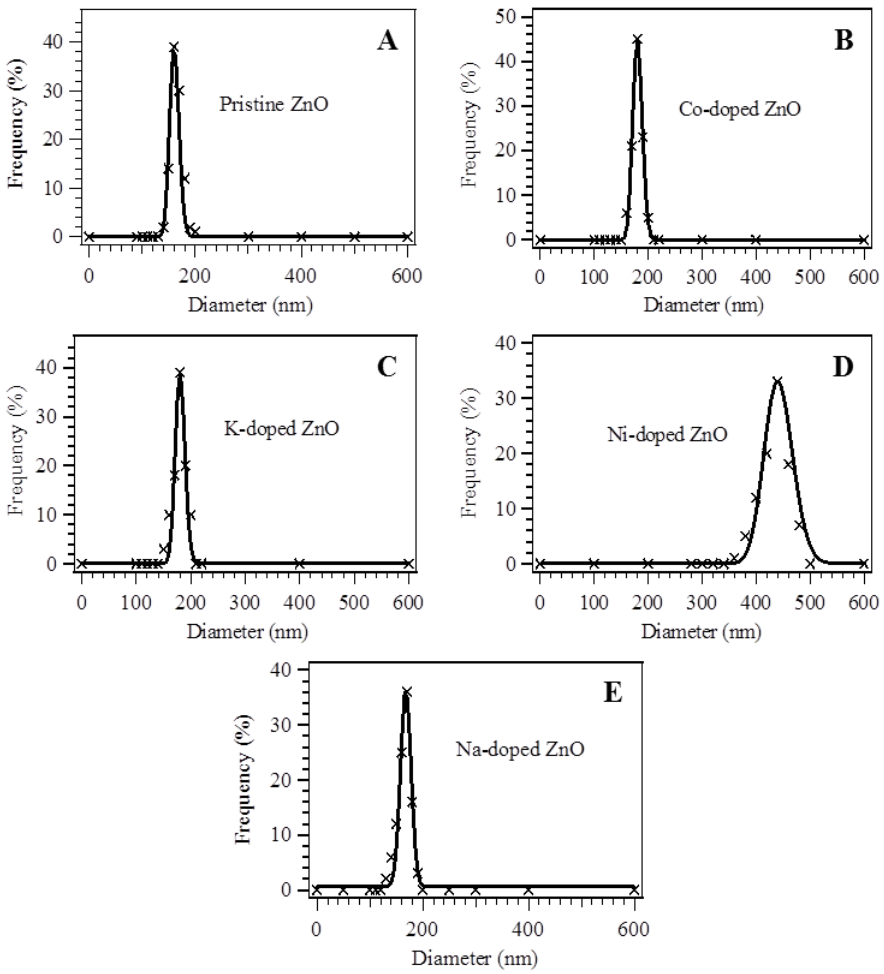

Figure 5.2 Diameter distributions of (A) undoped, (B) Co-, (C) K-, (D) Ni- and (E) Na-doped ZnO nanostructures grew in 100 ml of growth solution at 85°C.

Other than the outer diameters of the NRs, the introduction of dopants can also affect the length of the NRs. Figure 5.3 shows the cross section view SEM images of the NRs with measured film thickness. It is noticeable that all the observed NRs for the doped and undoped ZnO samples are grown along the [0001] direction, which is directly resulted from the highly reactivity of the polar (002) surface. The average lengths of the undoped, Co-, K-, Ni- and Na-doped ZnO NRs were determined to be 4.0, 3.1, 3.6, 2.2 and 3.8 μm, respectively.

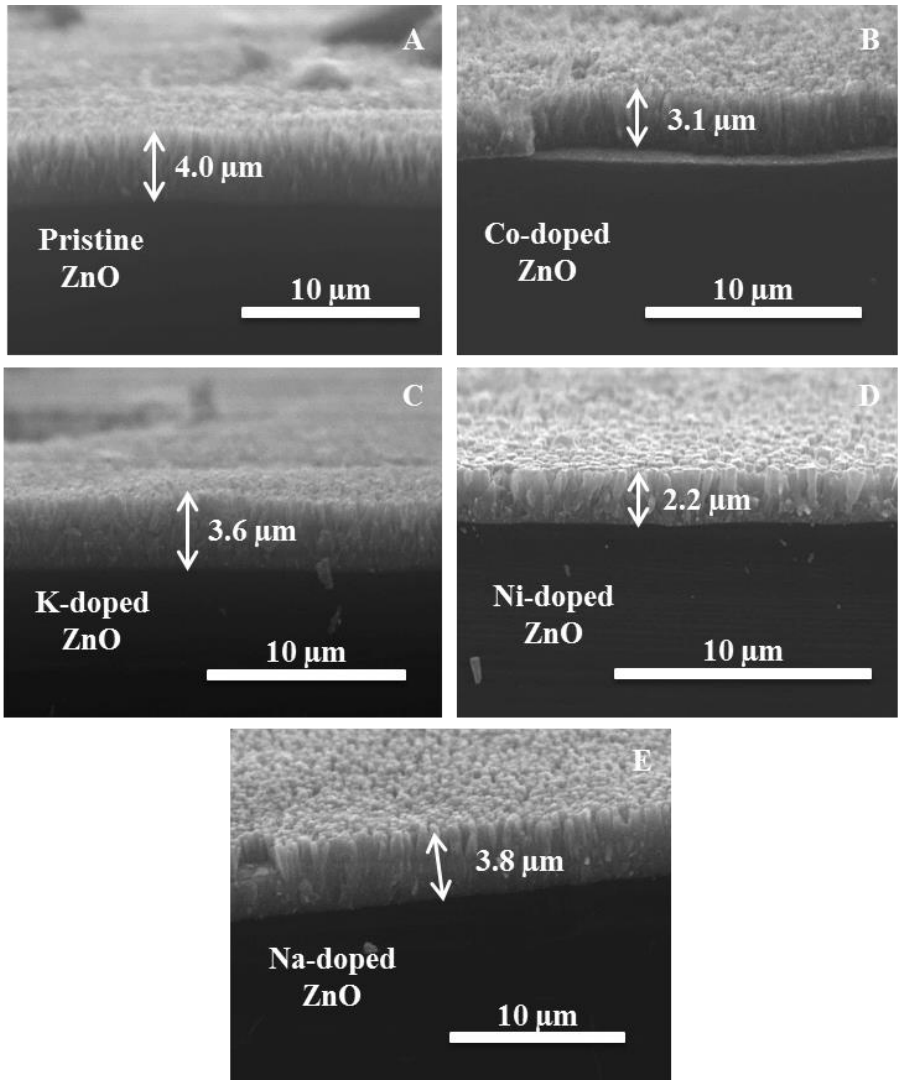

Figure 5.3 Cross-sectional SEM images of (A) undoped, (B) Co-, (C) K-, (D) Ni- and (E) Na-doped ZnO nanostructures grew in 100 ml of growth solution at 85°C.

For the Na- and K-doped ZnO nanostructures, the average lengths of the NRs are almost similar to that of pristine ZnO NRs. However, the Co- and Ni-doped ZnO NRs are shorter in comparison to the pristine ZnO NRs. The length of the Co-doped ZnO NRs is reduced by ~22.5%, while the length of the Ni-doped ZnO NRs is about half of that from the pristine ZnO NRs. The large NR diameter of the Ni-doped ZnO NRs is consistent to the observation of shorter NR. In order to establish the NR surface

density, the volume of individual NR (V) was calculated and the results are presented in Table 5.1, using the following equation:

$$V = \frac{3\sqrt{3}(r^2)t}{2} \qquad \text{(Equation 5.1)}$$

where r and t are the radius and length of the NR, respectively.

Table 5.1 Morphological parameters and volume of individual NR.

NR samples	Dimensions (μm)			V (μm^3)
	Radius	Length	Distance between adjacent NRs	
Pristine ZnO	0.08	4.0	0.17	0.0665
Co-doped ZnO	0.10	3.1	0.20	0.0805
Ni-doped ZnO	0.22	2.2	0.18	0.2766
Na-doped ZnO	0.09	3.8	0.38	0.0713
K-doped ZnO	0.09	3.6	0.18	0.0799

As shown in Table 5.1, the results reveal that most of doped NRs have similar volume for a single rod, except for the Ni-doped ZnO sample which has a much larger volume. This can be attributed to the effect of large cross section diameter of the (002) plane. In addition, the large NR volume of the Ni-doped ZnO also indicates that the number density of the NRs is much less than other ZnO samples, which suggests that coalescence between the adjacent NRs could be happened to result a large diameter in the Ni-doped ZnO sample.

5.4.2 Effect of Dopants on the Morphology of ZnO NRs

The CBD growth mechanism of ZnO NRs was discussed in section 3.4.2. The doping precursor could be embedded during the formation of NRs and a bulk doping would be expected. From Figure 5.1 and 5.3, the introduction of different dopant ions into the growth solutions could clearly affect the morphology of the NRs. Previous findings reported that different dopants will form different type of charged complex ions (cation or anion) in the nutrient solutions, which will then create electrostatic interaction with the zinc reactants and ZnO surfaces to alter the NRs morphology bidirectionally (increasing or decreasing the aspect ratio).[279-281]

For ZnO crystals, the dopants can be divided into two types, A-type and B-type ions, based on how they affect the crystal morphology. A-type metal ions tend to inhibit NR growth along the vertical (002) plane, causing an increase of deposition onto the sidewalls (100), resulting in larger diameter but shorter overall film thickness. Conversely, B-type dopants cause inhibition of the sidewall (100) deposition, resulting increased the favourability towards the growth of the vertical (002) plane.[279] In such case, the as-grown NR will be longer with a smaller diameter, forming a needle-like nanostructure.

Atomic force microscopy measurements showed that the (002) surface plane is negatively charged and (100) sidewalls plane is positively charged on the ZnO NR.[279] Cations, such as Mg^{2+}, Ca^{2+}, Cu^{2+} and Cd^{2+}, generally behave like A-type dopant and would be attracted to the negative top face, (002) plane, thus inhibiting the vertical growth. On the contrary, cations, such as Al^{3+}, In^{3+} and Ga^{3+}, form negatively charged complex in solution at pH 11, which will be attracted to inhibit the deposition onto the (100) sidewall plane.[279]

In this experiment, two different groups of metal ions, alkaline and transition metal ions, were introduced into the growth solutions. The addition of alkaline cations (Na^+ and K^+), only increases the diameters of NRs by 6.25% (Na^+) and 12.5% (K^+) respectively, in comparison with the pristine ZnO NRs. This suggests that both the Na^+ and K^+ could possibly classified as weak A-type metal ions.

With Co^{2+} and Ni^{2+} doping, the diameters of the NRs increase by 25% (Co^{2+}) and 175% (Ni^{2+}) with significant effect on the overall length of the NRs as well. This suggests that both the Co^{2+} and Ni^{2+} are A-type metal ions, which can effectively inhibit the growth of the NRs along the (002) direction, resulting in large diameter NRs. The significant different effects between the Co^{2+} and Ni^{2+} can be attributed to the difference in the binding energies of Co^{2+} and Ni^{2+} on the oxygen terminated of ZnO (002) plane. Experimental measurements revealed that the formation enthalpy of NiO is about 2.5 kJ mol^{-1} more negative than CoO. Therefore, we could expect that Ni will bind more strongly to the ZnO (002) plane and thus resulting in large diameter NRs.[282]

5.4.4 XRD Characterisation of Doped ZnO NRs

After examining the morphologies of undoped and doped ZnO NRs, powder XRD was used to investigate the crystal structure and crystal orientation of the samples. The XRD patterns of undoped and doped ZnO nanostructures were compared with standard XRD database for wurtzite ZnO (JCPDS # 36-1451) and alpha-titanium (JCPDS # 44-1294).

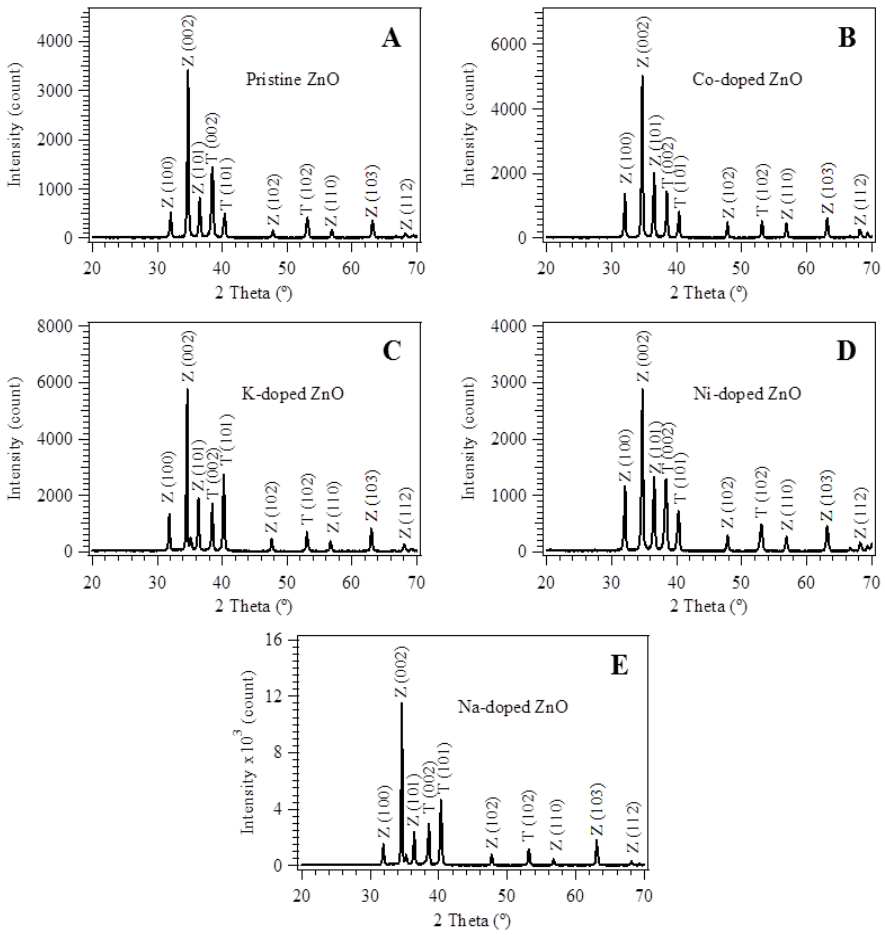

Figure 5.4 XRD patterns of (A) undoped, (B) Co-, (C) K-, (D) Ni- and (E) Na-doped ZnO NRs grew in 100 ml of growth solution at 85°C. The miller indices of crystal planes are labelled where Z and T are ZnO and titanium, respectively.

As shown in Figure 5.4, all samples present the typical the wurtzite ZnO diffraction peaks located at 2θ = 31.92°, 34.75°, 36.55°, 47.84°, 56.90°, 63.12° and 68.26° (Z) corresponding to (100), (002), (101), (102), (110), (103) and (112) crystal planes. Meanwhile, the alpha-titanium gives the diffraction peaks located at 2θ = 38.16°, 39.89° and 52.42° (T), corresponding to (002), (101) and (102) crystal planes. The sharp and intense diffraction peaks revealed the high quality crystal structure. It is important to note that there is no dopant metal oxides phases were observed in the XRD patterns. This indicates the dopants are homogenously distributed into the ZnO NRs.

As shown in the XRD spectra, all the samples are having a dominant (002) peak, which suggesting the NRs are grown along the [0001] direction. The relative texture coefficient values (Equation 2.7, Section 2.3) of the undoped and doped ZnO samples were determined. The relative texture coefficients of undoped, Co-, K-, Ni- and Na-doped ZnO NRs were calculated to be 0.90, 0.85, 0.87, 0.82 and 0.92, respectively. This suggests that the Co- and Ni-doped ZnO NRs have a poor c-axis orientation with respect to the surface normal. This finding is in good agreement with the SEM images in Figure 5.3. Since the Co- and Ni-doped ZnO NRs have larger diameters, it is expected that the coalescence of the adjacent vertically aligned NRs could only be achieved by gradually tilting of NRs at later stage of the growth. This behaviour will decrease the degree or the crystal alignment leading to a lower relative texture coefficient.

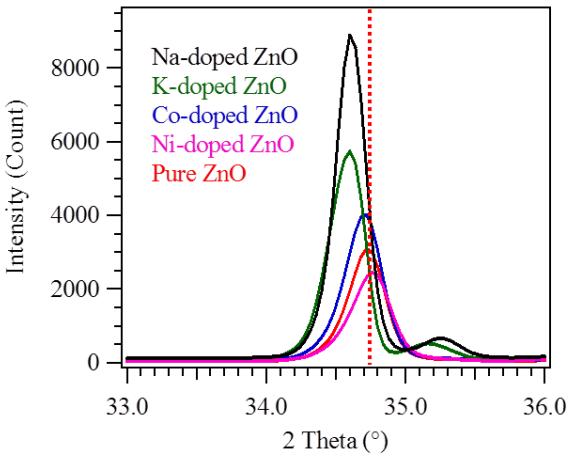

Figure 5.5 Enlarged (002) diffraction peaks of undoped and doped ZnO NRs.

It is noteworthy that, in comparison to undoped ZnO NRs, the (002) peak of the doped ZnO samples are generally broader, as shown in the magnified (002) XRD peak in Figure 5.5. This indicates that the dopants could decrease the overall crystallinity

with smaller single crystal size. The crystal domain sizes (Equation 2.5, Section 2.3) of the undoped, Co-, K-, Ni- and Na-doped ZnO NRs were calculated to be 29.45, 22.72, 24.85, 22.72 and 26.51 nm, respectively. The smaller crystal domain size can be attributed to the formation of surface defects (oxygen or zinc vacancies) in the doped samples after the incorporation of dopants into the ZnO lattice, since with respect to ZnO, the dopant ions have different valence charges, ionic radii and native oxide crystal structures. In comparison to Na and K doping, the Co- and Ni-doped ZnO NRs have the smallest crystal sizes. This probably can be explained by the higher dopant concentrations inside the ZnO as identified in Table 5.2. Such higher dopant concentration suggests that Co^{2+} and Ni^{2+} have higher binding energy on ZnO surface, which is also supported by significant morphology variations of the Co- and Ni-doped ZnO NRs, observed in Figure 5.1 and 5.3.

In addition, from Figure 5.5, when compared to pristine ZnO, the (002) peak positions of the Na- and K-doped ZnO samples are having an obvious shift of ~0.1° toward a lower angle, while the Ni- and Co-doped ZnO samples show very little shift. The shift of the (002) peak position can be attributed to the distortion of the ZnO lattice after incorporation with dopants. Here, the c-lattice constants (Equation 2.2, Section 2.3) of the undoped and doped ZnO samples were determined. The lattice constants 'c' of undoped, Co-, K-, Ni- and Na-doped ZnO NRs were calculated to be 5.163, 5.162, 5.181, 5.160 and 5.179 Å, respectively.

The shift of the (002) peak to a lower angle for the K- and Na-doped ZnO NRs is due to the ionic radii of these dopants are larger than Zn^{2+}. According to Shannon R.D., the ionic radii of Zn^{2+}, Na^{+} and K^{+} are 0.74, 1.18 and 1.51 Å, respectively.[283] When the zinc sites are being substituted by these alkaline metal ions, the ZnO lattice will be enlarged with some crystal strains.[79] This is consistent with the calculated c-

lattice constant where the K- and Na-doped ZnO NRs showed an increase of ~0.3% in the c-lattice parameter as compared to the pristine ZnO NRs. The obtained results are consistent with the previous findings.[272, 284] Such analysis also suggests that some of the dopants occupy the substitution positions by replacing Zn^{2+} in the lattice, which is essential for band gap engineering.

For the Co- and Ni-doped ZnO samples, there is much less crystal lattice expansion. This may be due to the ionic radii of Ni^{2+} ion (0.69 Å) and Co^{2+} ion (0.72 Å)[285] are slightly smaller or similar to the ionic radius of Zn^{2+} ion (0.74 Å).[283] Therefore, the substitution of Ni^{2+} or Co^{2+} ions into the zinc sites will not cause much distortion of the ZnO lattice. Both Chiu H. S. *et al.*[286] and Ma P. *et al.*[287] have obtained the similar XRD spectra for their recent investigation in the solution growth of Ni- and Co-doped ZnO nanostructures.

5.4.4 Actual Dopant Concentrations of Doped ZnO NRs

In order to further confirm that Na, K, Co and Ni metal ions were successfully doped into the ZnO lattice, ICP–MS was used to determine the actual dopant concentrations in the NRs. The ICP–MS samples were prepared by dissolving NRs in 2 ml of 1.5% nitric acid then being diluted to 50 ml with DI water. The results are shown in Table 5.2. The measurements reveal the presence of dopant (Co^{2+}, Ni^{2+}, Na^{+} and K^{+}) ions in the doped ZnO samples, which suggests that these dopants were successfully doped into the ZnO lattice.

It is noticeable that the actual dopant/Zn molar ratios are much lower than that in the nutrient solutions. The low-level of doping concentration can be attributed to the solubility of these dopants in ZnO.[273, 286] It has been reported that the dopant solubility increases with increasing the operating temperature since the diffusion of the dopant

ions into the ZnO crystals is favoured at high temperature.[288] In our experiment, the CBD reacts at a rather low temperature (~85°C), thus the solubilities of the dopant ions are expected to be much lower. Similar low temperature behaviour for transition metal ion doping in ZnO nanocrystals has been reported.[273, 289]

Table 5.2 ICP-MS analysis of doped ZnO NRs.

NR samples	Dopant concentration (%)		Doping efficiency (%)
	Solution	Film	
Co-doped ZnO	25.0	2.95±0.28	11.80
Ni-doped ZnO	25.0	3.23±0.26	12.92
Na-doped ZnO	25.0	2.17±0.42	8.68
K-doped ZnO	25.0	1.98±0.36	7.92

In comparison with Na^+ and K^+ doping, Co^{2+} and Ni^{2+} have achieved relative higher dopant concentrations. This observation can be explained by the high binding energy of the Co^{2+} and Ni^{2+} and large ion radii of Na^+ and K^+. This is consistent with the observation of morphology variation, lattice constants enlargement, crystal textures and crystal domain sizes for our Na-, K-, Co- and Ni-doped ZnO.

5.4.5 Optical Properties of Undoped and Doped ZnO NRs

The possible effect of doping on the optical band gap energy of ZnO was investigated using UV-vis spectrophotometer. Each samples were prepared on glass substrates and were annealed to 400^{o}C before the UV-vis transmission and absorption measurements.

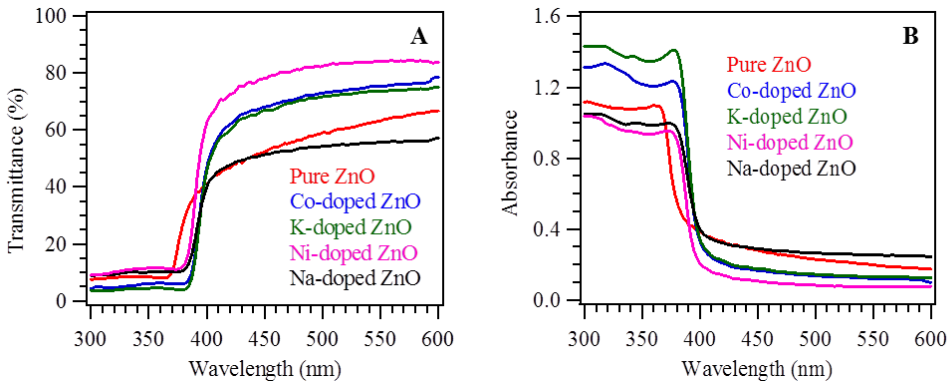

Figure 5.6 (A) Optical transmission and (B) absorption spectra of the undoped and doped ZnO NRs.

The average values of the optical transmission of the undoped and doped ZnO samples at 300–600 nm were estimated ranging from 50–85% (Figure 5.6A). As shown in Figure 5.6B, the UV-vis absorption onset of the doped ZnO NRs are shifted to a longer wavelength (> 400 nm) when compared to the pristine ZnO NRs (~387 nm). The red shift in the absorptions of the doped ZnO samples indicate that the optical band gaps of the doped ZnO nanostructures are smaller than the pure ZnO NRs. This reveals a significant enhancement in the absorption of solar light toward the visible region. The band gap energies of the samples can be calculated from the recorded optical transmission spectra using the Tauc equation (Equation 2.11, Section 2.4).

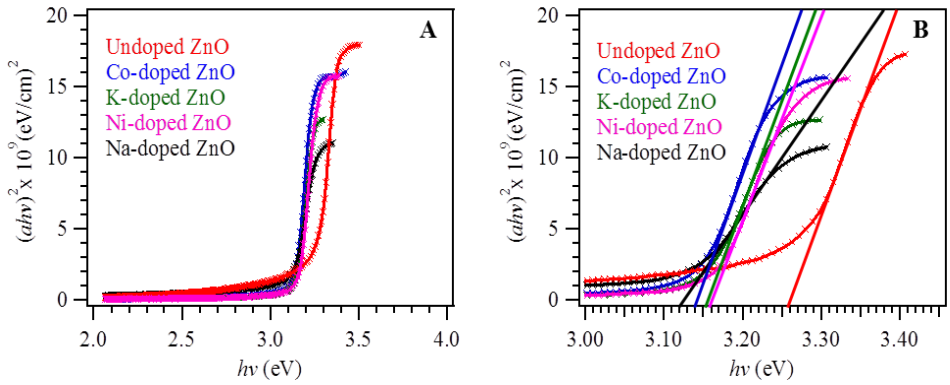

Figure 5.7 Tauc plots of undoepd and doped ZnO NRs, (A) full spectra and (B) enlarged region between 3.0–3.45 eV.

Figure 5.7 presents the plots of $(\alpha hv)^2$ vs hv for the undoped and doped ZnO nanostructures. The linear nature of the Tauc plots at the absorption edges confirms that both the undoped and doped ZnO NRs are semiconductors with direct band gaps. The magnified Tauc plots in Figure 5.7B show the band gap energies of the pure ZnO, Co-, K-, Ni- and Na-doped ZnO NRs were 3.26, 3.14, 3.15, 3.16 and 3.12 eV, respectively. The measurements reveal that all the doped ZnO NRs possessed a smaller band gaps than the pure ZnO NRs.

There are two possible reasons that cause the reduced band gap energies for the doped ZnO samples. Firstly, it may be caused by the creation of oxygen vacancies and defect centres within the ZnO structure induced by the dopants.[278] Secondly, the existence of impurities (Co^{2+}, K^+, Na^+ or Ni^{2+}) in the ZnO structure lead to the formation of impurity bands inside the band gap region of ZnO, which caused the shrinkage effect in the band gaps of the doped samples.[271, 272]

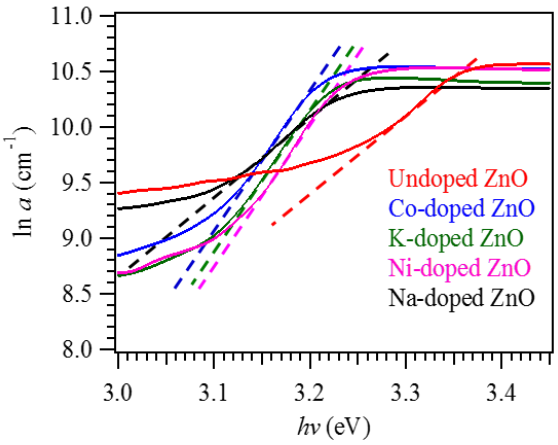

Figure 5.8 Plots of ln α as a function of photon energy for undoped and doped ZnO nanostructures.

The formation of band tailing in the band gap is often observed when there is impurity incorporate into the semiconductor, which is also known as Urbach tail. The Urbach tails of the samples can be calculated using the Urbach rule (Equation 2.13, Section 2.4). The Urbach energy (E_u) of the sample was obtained from the inverse of the slope of ln α as a function of $h\upsilon$, as shown in Figure 5.8. This is equivalent as assuming the Urbach tail follows an exponential curvature defined by the E_u. The E_u values of undoped, Co-, K-, Ni- and Na-doped ZnO NRs were calculated to be 94.5, 112.6, 163.2, 105.8 and 169.4 meV, respectively. The obtained E_u value of pristine ZnO NRs is comparable with the reported value.[187] The E_u values change inversely with optical band gaps of the nanostructures. It is important to note that all the doped ZnO NRs are having a higher E_u value as compared to that of pure ZnO. The larger the E_u value indicates an increased in the structural disorder and the number of defects in the created nanostructures.[187] These measurements further confirm that the dopants (Na, K, Co and Ni metal ions) were successfully substituted into the ZnO lattice.

5.5 PEC Hydrogen Generation Study of Undoped and Doped ZnO NRs

The PEC water splitting performances of the undoped and doped ZnO NRs were investigated. Figure 5.9A represents the photocurrents generated from pure ZnO (red curve), Ni-doped ZnO (pink curve), Co-doped ZnO (blue curve), K-doped ZnO (green curve) and Na-doped ZnO (black curve) under simulated sunlight (100 mW cm^{-2} with an AM1.5 G filter) between potentials of –0.5 and 1.0 $V_{Ag/AgCl}$ together with the dark current measured from Na-doped ZnO NRs (orange curve) in 1.0 M KOH electrolyte (pH 13.6).

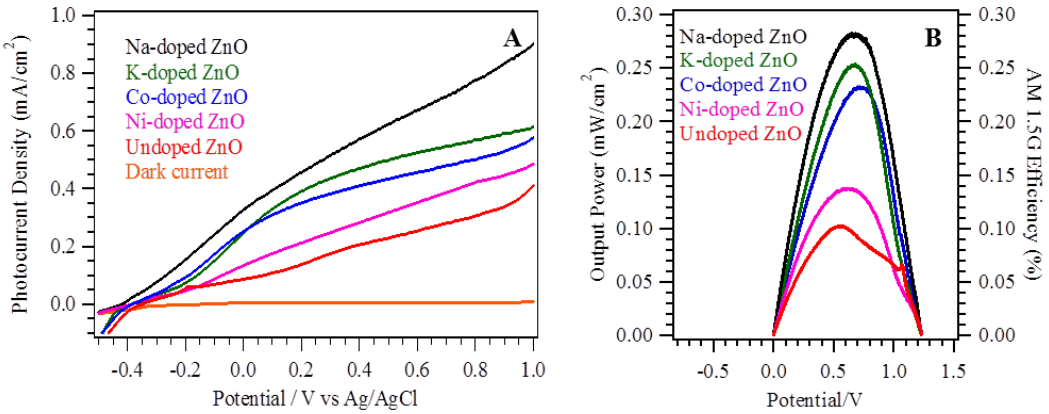

Figure 5.9 (A) Photocurrents generated from pristine and doped ZnO NRs in 1.0 M KOH electrolyte (pH 13.6) under simulated sunlight of 100 mW cm^{-2} with an AM1.5 G filter and (B) the corresponding output power and photoconversion efficiency under AM1.5 G full solar spectrum irradiation.

In comparison to the pure ZnO NRs photoanode, it is obvious that all the doped ZnO NRs demonstrated a significant improvement in the photocurrent density. At a typical potential of 1.0 $V_{Ag/AgCl}$, the photocurrents generated from pure ZnO, Ni-, Co-, K- and Na-doped ZnO NRs photoanodes were measured to be 0.42, 0.48, 0.58, 0.62 and 0.90 mA cm^{-2}, respectively. It is worth noting that the onset potentials of all the doped

ZnO NR photoanodes are more negative than that of pristine ZnO NR photoanode. The onset potentials of pure ZnO, Ni-, Co-, K- and Na-doped ZnO NRs were –0.35, –0.39, –0.38, –0.39 and –0.42 $V_{Ag/AgCl}$, respectively. The onset potential is determined by the slow kinetics of water oxidation, where it is used to remove four electrons and four protons from two water molecules to form one molecule of oxygen. Therefore, the photogenerated electrons and holes will accumulate at the surface of the electrode and surface recombination will occur until sufficient positive potentials are applied.[79] For the doped ZnO samples, the shift of the onset potentials to a more negative value can be attributed to the created defects (oxygen vacancies) of the electrodes after the introduction of dopants, causing in lowering the kinetic barrier to interfacial charge transfer.[79] Therefore, a smaller overpotential will be required and thus the *I*–*V* curves of the doped ZnO samples are shifted to the left.

The photoconversion efficiency of the sample can be calculated from the ratio of electrochemical energy density to the input of photoenergy density (Equation 2.27, Section 2.6), as presented in Figure 5.9B. The maximum photoconversion efficiencies of the Ni-, Co-, K- and Na-doped ZnO NRs were calculated to be 0.14, 0.24, 0.26 and 0.29%, respectively, which were 1.3, 2.2, 2.4 and 2.6 times higher than that of undoped ZnO NRs (0.11%). The higher photoconversion efficiencies suggest that the doped ZnO NRs electrodes are more efficient in light absorption and converting it to the electricity than the pure ZnO NRs electrode.

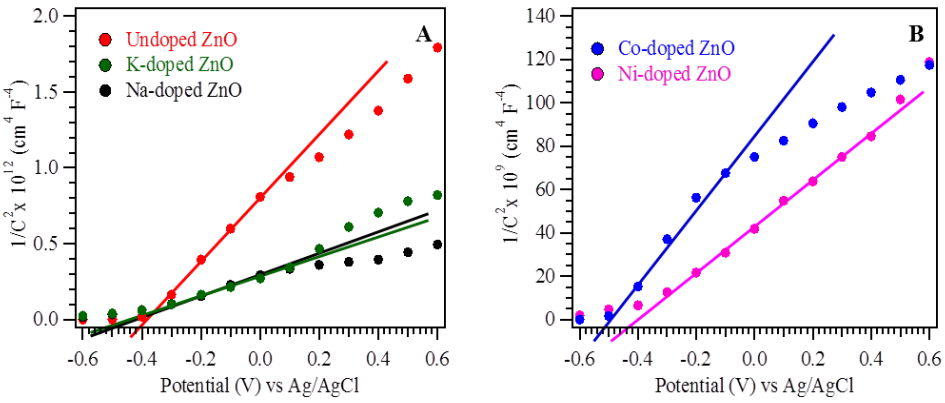

Figure 5.10 M–S plots of (A) undoped, K- and Na-doped ZnO NRs and (B) Co- and Ni-doped ZnO NRs in 0.5 M of Na_2SO_4 (pH 6.8). The amplitude of the sinusoidal wave was set at 10 mV at a frequency of 1 kHz.

In addition, EIS measurements were carried out to measure the capacitances of the NRs in 0.5 M of Na_2SO_4 (pH 6.8) in the dark with an AC voltage of 10 mV at a fixed frequency of 1 kHz. As shown in Figure 5.10, both the undoped and doped ZnO samples show positive slopes in the Mott–Schottky (M–S) plots, which confirm the n-type semiconductor behaviour of the electrodes. The flatband potential, V_{FB}, of the photoanodes can be obtained by M–S analysis (Equation 2.23, Section 2.5). The V_{FB} values of the photoanodes were determined by extrapolation of *x*-intercepts in M–S plots. The values of V_{FB} of the undoped, Co-, Ni-, K- and Na-doped ZnO NRs were measured to be –0.41, –0.52, –0.44, –0.53 and –0.50 $V_{Ag/AgCl}$. The measurements reveal that the V_{FB} values of the doped ZnO photoanodes are more negative than the pristine ZnO photoanode. This suggests the charge separation of the doped ZnO NRs is better than that of pristine ZnO NRs. This is because the doped ZnO samples have a lower potential barrier to overcome, resulting in a reduction of the charge transfer resistance and an enhancement in the charge transfer.[79] The measurements are consistent with the photocurrent onset measured from Figure 5.9A where all the doped samples are having

a more negative potential than the undoped ZnO NRs. It is important to note that the obtained onset potentials of the samples are more positive than the V_{FB} values. This can be accredited to the interfacial charge transport limitations of the samples.[290]

In addition, the doped ZnO electrodes show substantially smaller gradients of the M–S plots as compared to the pristine ZnO electrode. This implies the donor densities of the doped ZnO samples are increased. The slopes of the M–S plots were used to derive the charge carrier density of the photoanodes (Equation 2.24, Section 2.5). For ZnO, it has a relative dielectric constant value of 10 [291] and the donor densities of pure ZnO, Co-, Ni-, K- and Na-doped ZnO were calculated to be 7.16×10^{18}, 1.05×10^{20}, 1.34×10^{20}, 2.48×10^{19} and 2.20×10^{19} cm^{-3}, respectively. In comparison with the dopant concentrations identified from ICP–MS in Table 5.2, the large donor densities for the doped ZnO samples may be due to the oxygen vacancies, which are known as electron donor for oxide-based semiconductors.[89] The increased in the electron density will improve the electron transfer at the interface between the ZnO and titanium substrate, as well as the charge transport within the ZnO. In addition, the Fermi level of the doped ZnO samples is expected to shift toward the conduction band due to the increased of the electron density. This will facilitate the charge separation at the interface of semiconductor and electrolyte by increasing the degree of band bending at the ZnO surface.[265] Therefore, the PEC water splitting performances of the doped ZnO NRs are improved.

Other than that, the optical band gap of the sample also plays an important role in determining the photocatalytic water splitting. As discussed in section 5.4.5, all the doped ZnO NRs owned a smaller band gap energy than that of pristine ZnO NRs (Figure 5.7). The smaller band gap energy will extend the absorption region and increase the number of solar excited electrons and holes, thus resulting in a higher PEC

water splitting efficiency. This increased population of excitons will benefit from the increased donor densities and improved the charge mobility. In addition, Zou Z. *et al.* have reported that the improvement of photocatalytic of the nanostructures doped with transition metals could be due to the *d-d* transition induce the electron-hole separation and improved the generation of hydrogen and oxygen.[292] However, the mechanism on how the *d*-orbitals enhanced the photoexcitation and photocatalytic activity is still remained unknown.

Another possible parameter that affect the PEC water splitting activity is the surface area to volume ratio (*SAVR*) of the sample, which determines geometry effects on the reaction kinetics for gas or liquid at solid surface.[293] Based on the measured morphological dimensions, the *SAVR* values (Equation 3.10, Section 3.4.7) were calculated as 0.0181, 0.0175, 0.0184, 0.0110 and 0.0194 nm^{-1} for pristine ZnO, Co-, K-, Ni- and Na-doped ZnO NR arrays, respectively. Consistent with the findings, Na- and K-doped ZnO NR arrays with the highest *SAVR* values achieved highest photocurrent densities and photoconversion efficiencies.

In summary, the reduced band gap energy, increased carrier concentration, improved interfacial catalysis and increased *SAVR* are believed to be the major reasons for the improvement in photoactivity of PEC water splitting for the doped ZnO NRs.

5.6 Conclusions

Doped ZnO NRs were successfully created through the aqueous CBD method. The surface morphology of ZnO nanostructures was strongly affected by the type of charged ions formed by the dopants, which will alter the NRs morphology, either increasing or decreasing the aspect ratio. All the doped ZnO samples demonstrated a reduced in the optical band gap energy. An efficient solar hydrogen system was

developed based on the doped ZnO NRs photoanodes. When compared with the pristine ZnO NRs photoanode, all the doped ZnO NRs electrodes revealed at least ~27% enhancement in the photoconversion efficiency. Among these photoanodes, Na-doped ZnO NRs electrode exhibited the highest PEC water splitting efficiency, which was 2.6 times more efficient than the pristine ZnO NRs photoanode. The improvement in photoactivity of PEC water splitting may be attributed to the increased *SAVR*, reduced band gaps, improved charge separation, increased donor densities and improved the interfacial charge-transfer kinetics.

Chapter 6 Enhanced Hydrogen Production through 3D ZnO Nanorods Array on Stainless Steel Meshes

6.1 Abstract

Here we report on a novel approach for the direct growth of vertically aligned ZnO NRs array on stainless steel (SS) mesh by power-assisted chemical bath deposition method, forming a 3D configuration. The effect of the applied powers on the final morphologies of ZnO nanostructures was examined. The correlation between the growth durations and the final morphologies of ZnO nanostructures was investigated. With increased growth duration, both the diameter and length of the NRs were linearly increased. The photocatalytic activity of the synthesised nanostructures was tested in a PEC water splitting process. When compared with 2D array of ZnO NRs (0.13%), which grown on SS plate, 3D array of ZnO NRs (0.28%) demonstrated an improved in PEC water splitting efficiency by two-fold. The photoconversion efficiency was further enhanced by folding the number of the 3D array where four layers (0.80%) of 3D array of ZnO NRs revealed a photoconversion efficiency enhancement of ~158% as compared to that using single mesh (0.31%) of 3D array of ZnO NRs.

6.2 Introduction

The development of alternative energy has steadily grown to replace conventional fossil fuel energy source. PEC water splitting is one of the promising solutions to harvest and store the solar energy into hydrogen fuels. Photocatalysts possessed large surface areas, excellent electron transportation, low charge carrier recombination and good electrical contact with the substrates are essential for producing

high photoenergy conversion.[9] Predominantly, surface area of the nanostructures is one of the crucial factors that affect the photocatalytic efficiency. A large effective surface area of a photoanode is expected to achieve a higher photoconversion efficiency since the amount of photocatalytic material and interface area with the electrolyte is increased. As such, one of the approaches to increase the surface area of the electrode is to combine three-dimensionality of the substrate with metal oxide nanostructures. Since it was first reported that the deposition of TiO_2 nanoparticles on SS mesh have shown to increase the DSSCs efficiency,[294] a great number of 1D metal oxide nanostructures, such as NRs,[295] NTs[296], nanosheets[297] and NWs,[76] have been designed and prepared on metal wires[296, 298] or meshes[299, 300] for improving the conversion efficiency.

Other than TiO_2, ZnO has received renewed attention due to the wide direct band gap and excellent electron transportation.[240] Furthermore, ZnO has a longer hole diffusion length (~125 nm)[29] when compare to TiO_2 (~100 nm)[234] and its electron mobility is typically 10–100 times higher than that of TiO_2.[73, 266] So far, only a few groups have reported the growth of ZnO nanostructures on metal meshes through the traditional CBD, hydrothermal and CVD methods and those samples were mainly applied in photocatalytic degradation of dyes and DSSCs applications.[301-303]

In the present work, we report for the first time, a single-step CBD to synthesise vertically aligned crystalline ZnO NR arrays on the SS meshes with the assisting of power, which we named it as power-assisted CBD (PACBD) method. The morphology and length of the NRs can be controlled by tuning the parameters of PACBD. The PEC measurements reveal that the 3D arrays of ZnO NRs electrode is roughly two times more efficient than the 2D arrays of ZnO NRs electrode. In addition, the PEC water splitting efficiency is further improved by folding the number of 3D arrays of ZnO NRs.

6.3 Experimental Details

6.3.1 Preparation of SS Meshes

All the chemicals used were analytical grade and purchased from Sigma-Aldrich. The SS meshes (Alfa Aesar) used in this experiment had a mesh count of 100, where the opened area is 0.142 mm by 0.142 mm with a wire diameter of 0.112 mm. The SS meshes (1 cm × 3 cm) were degreased and cleaned under sonication in an IPA bath for 15 minutes, and dried in air before they were used for growing ZnO NRs on the surfaces.

6.3.2 Preparation for Growing ZnO NRs on SS Meshes by PACBD

A typical setup for PACBD growth of ZnO NRs is shown in Figure 6.1.

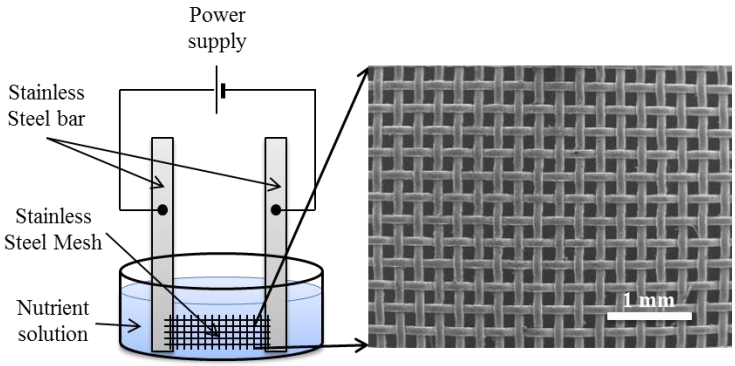

Figure 6.1 Typical PACBD setup for growing ZnO NRs on SS mesh with a top view SEM image of clean SS mesh.

Firstly, a cleaned SS mesh (1 × 3 cm^2) was spot welded onto two SS bars followed by connecting it to a power supply. The whole setup was then immersed into a glass beaker containing 150 ml of nutrient solution for growing ZnO NRs. The nutrient solution was composed of a 1:1 molar ratio of zinc nitrate hexahydrate (1.78 g) and hexamethylenetetramine (HMT; 0.84 g) in 300 ml DI water. The final concentration of

the solution was 20.0 mM. ZnO NRs were grown on SS meshes at different applied powers and different growth durations, ranging from 14.0 to 60.0W and 30 to 120 minutes, respectively. No additional heating of the growth solution is needed. The as-prepared samples were rinsed three times with DI water and air dried.

6.3.3 Characterisation

SEM (JSM 820M, Jeol) was used to examine the surface morphologies of the samples. Power XRD (Siemens D500) was carried out to analyse the crystallinity and structure orientation of the nanostructures. UV-vis spectrophotometer (Thermospectronic UV 300) was used to record both the optical absorption and transmission of the samples. The average diameters and average film thicknesses were measured from top- and side-view SEM images using Image J (National Institutes of Health, USA). The PEC water splitting was measured using a standard three-electrode configuration in a 1.0 M KOH electrolyte (pH 13.6). A platinum foil was used as counter electrode and a KCl saturated Ag/AgCl electrode was used as a reference. A USB potentiostat (eDAQ) was used to control and record the photocurrent as a function of electrochemical potential. Sunlight was simulated with a 300W xenon arc lamp with an AM1.5 G filter and the output light power density was adjusted to 100 mW cm^{-2}, 200 mW cm^{-2} and 300 mW cm^{-2}. The optical power density was calibrated by a power meter (Newport 1830-C) with a wide band sensor (Newport 818-UV attenuated). EIS (Palmsens 3.0) measurements were carried out in 0.5 M Na_2SO_4 solution (pH 6.8) and the amplitude of the sinusoidal wave was set at 10 mV.

6.4 Results and Discussion

6.4.1 Growth of ZnO NRs on SS Meshes by PACBD

Figure 6.2A and 6.2B represent the photographs of SS meshes before and after the growth of ZnO NRs in 150 ml of nutrient solution for 60 minutes at an applied heating power of 33.0W (M60mW33). The photographs reveal that the colour of the SS mesh has changed from shinny grey to white-greyish after the deposition of ZnO NRs with reduced transparency.

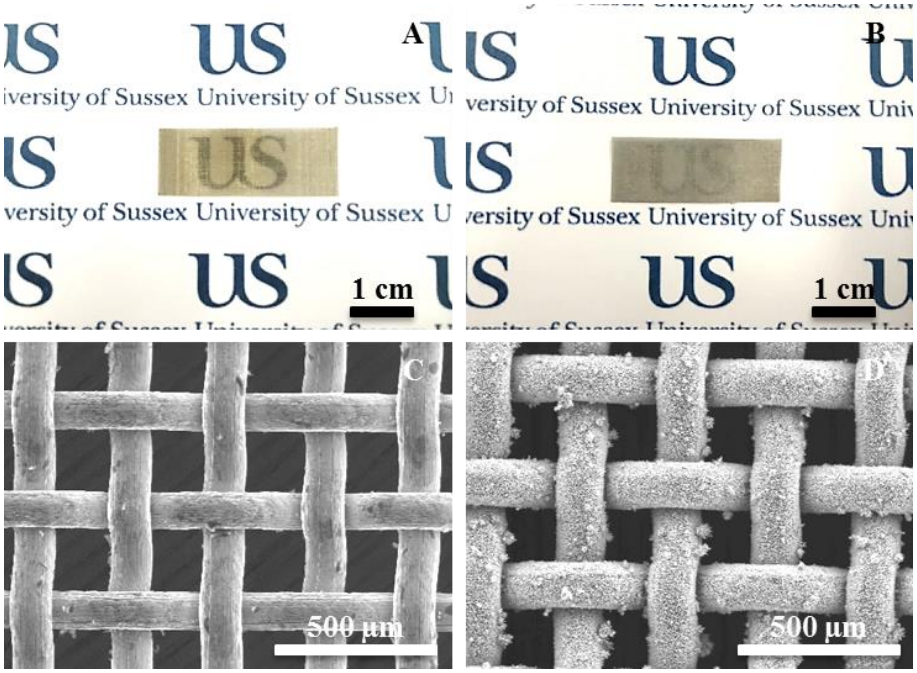

Figure 6.2 Photographs of SS meshes (A) before and (B) after the growth of ZnO NRs in 150 ml nutrient solution for 60 minutes at an applied heating power of 33.0W (M60mW33). (C) and (D) are their corresponding top view SEM images.

The low magnification SEM images of the SS mesh before and after the growth of ZnO NRs are shown in Figure 6.2C and 6.2D. The SS mesh has an opened area of 0.14 mm by 0.14 mm with a wire diameter of 0.11 mm. After 60 minutes of PACBD reaction, ZnO NRs were uniformly deposited in a radially outward direction on the

surface of SS wires throughout the SS mesh without any obvious cracks, featuring a 3D configuration (Figure 6.2D). The length of the NRs and the diameter of SS wire are measured to be 9.6 μm and 129.2 μm, respectively.

It is worth noting that the SS mesh is still translucent after the growth of ZnO NRs for 60 minutes, shown in Figure 6.2B. The percentages of projected open area (*A*) of the samples can be calculated using the following equation:

$$A\ (\%) = \left(\frac{O_{ss} - 2L}{O_{ss} + D_{ss}}\right)^2 \times 100 \qquad \text{(Equation 6.1)}$$

where O_{ss} is the opening of SS mesh (mm), D_{ss} is the diameter of SS wire (mm) and *L* is the length of the NRs (mm). As shown in equation 6.1, the projected open area of the sample is directly correlated to the NR length. When the length of the NR is increased, the projected open area of the sample will be decreased due to the deposition of ZnO NRs will reduce the opening distance. The resulting projected opening areas of the M60mW33 and the clean SS mesh are calculated to be ~23.4% and ~31.3%, where the projected open area of the M60mW33 is slightly less than the clean SS mesh.

The growth of ZnO NRs on SS meshes using PACBD method offers several advantages. Firstly, PACBD is a one-step experiment where the seeding process is occurred during the growth process. Unlike PACBD, traditional CBD requires a seed layer for the growth of vertically aligned arrays of ZnO NR. Secondly, PACBD is a much faster growth process compared to the traditional CBD. For example, the time needed for traditional CBD to grow ZnO NRs with length of ~5 μm is about 15 hours while with PACBD, it only needs 30 minutes. Thirdly, PACBD offers a homogenous deposition of ZnO NRs throughout a large surface area. For traditional CBD, there will be a temperature gradient in the nutrient solution which will cause an uneven deposition

of ZnO nanostructures on the surface of substrate. On the contrary, PACBD is an in-situ heating process where the heat was consistently generated on the surface of SS mesh driven by the applied heating current through the SS wires. The concentrated heat on the SS mesh wires will rapidly decompose the HMT and accelerate the deposition of ZnO onto the surface, resulting in fast growth of homogenous NR films.

6.4.2 Effect of Applied Heating Power on the Morphology of ZnO NRs

It has been reported that one of the parameters that will affect the morphology of the ZnO nanostructures is the growth temperature. For PACBD process, the growth temperature is determined by the applied heating power. Hence, the correlation between the morphology of ZnO NRs and applied power in PACBD process was investigated. All the experiment parameters, such as the dimension of SS mesh (1×3 cm^2), growth duration (60 minutes) and volume of nutrient solution (150 ml) were maintained as constant. The applied heating powers were operated ranging from 14.0W to 60.0W.

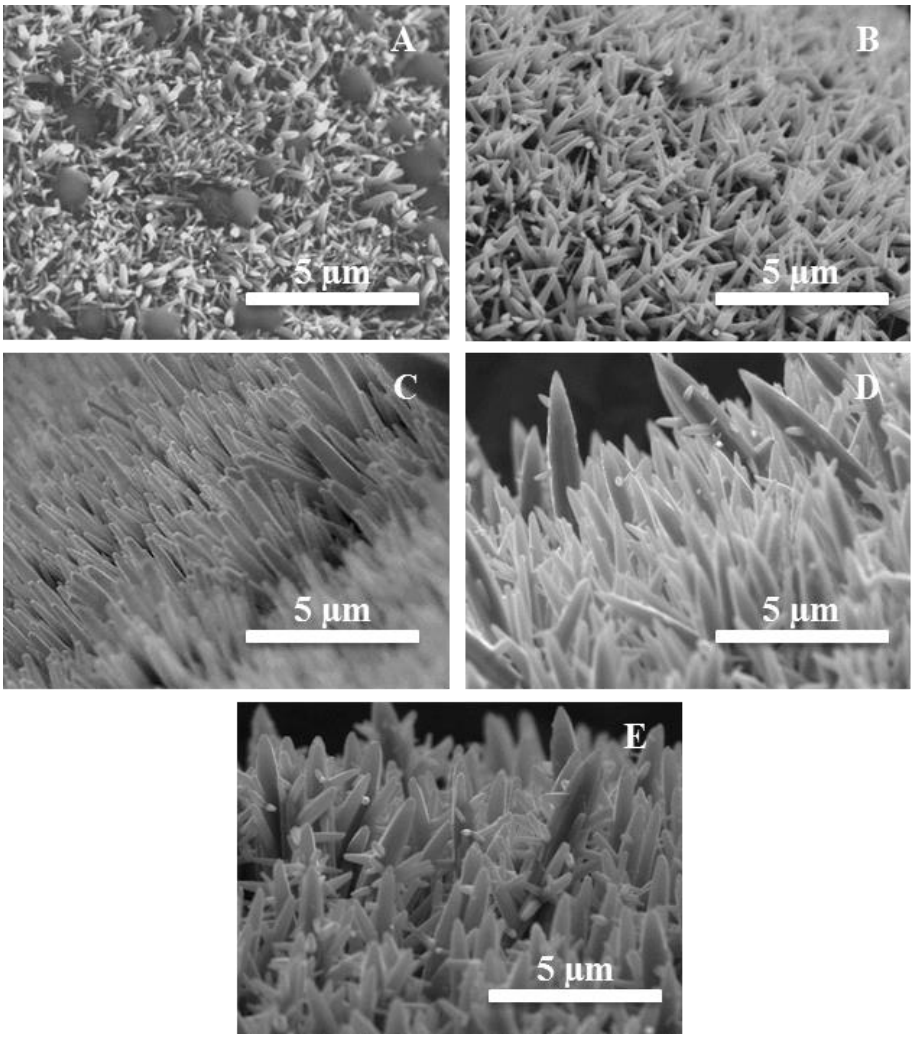

Figure 6.3 Tilted view SEM images of ZnO NRs grown on SS meshes in 150 ml of nutrient solution for 60 minutes at different applied heating powers, (A) 14.0W, (B) 22.5W, (C) 33.0W, (D) 45.5W and (E) 60.0W.

Figure 6.3 demonstrates that the final morphology of ZnO NRs is strongly affected by the applied heating power. At a low applied power (14.0W), only some sparse randomly oriented ZnO NRs were formed on the surfaces of SS mesh with the presence of some big crystals (Figure 6.3A). Further increased the applied power to 33.0W resulted in the formation of higher density and well-ordered ZnO NRs. The rods formed are relatively vertically aligned on the surface of SS mesh. When the applied power was 45.5W, tapered-like ZnO nanostructures with small branches were created

on the SS mesh. With the heating power above 45.5W, the tree-like, branched ZnO NRs were formed.

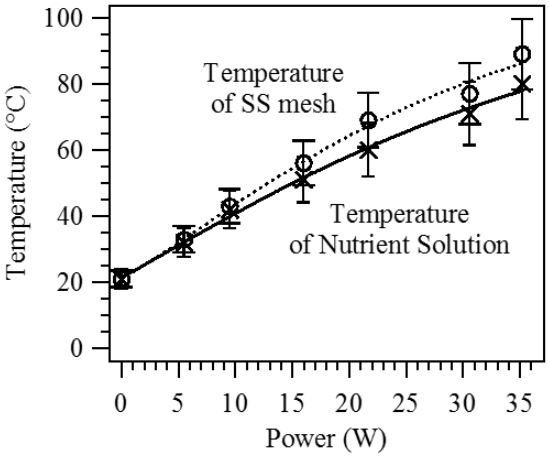

Figure 6.4 Temperature plots of SS mesh and nutrient solution as a function of applied heating power with nutrient solution volume of 150 ml and SS mesh dimension of 1×3 cm^2.

Both the temperatures of the SS mesh and nutrient solution were measured as a function of applied power, shown in Figure 6.4. A thermocouple was spot-welded onto the SS mesh in order to measure the temperature of the SS mesh. When the applied power was increased, both the temperatures of the SS mesh and nutrient solution were increased. It is noticeable that the temperature of the nutrient solution was almost similar to the temperature of the SS mesh at low applied power. When the applied power was above 10.0W, the temperature of the SS mesh was slightly higher than that of the solution temperature. This suggests that the heating rate at the SS mesh is relatively higher than the heat transfer rate from the SS mesh to the nutrient solution. Therefore, the temperature of the growth solution tends to be lower than the temperature at the SS mesh. Based on the power dependent experiment, at 33.0W, the quality of the

formed ZnO NRs are relative more c-oriented with good alignment. Furthermore, the temperature of the SS mesh at this applied power (~83°C) is similar to the temperature required for the decomposition of HMT (~85°C).

6.4.3 Growth Mechanism of ZnO NRs by PACBD

The growth mechanism of ZnO NRs using the PACBD method is very similar to that of the traditional CBD method, as discussed in section 3.4.2. Since the whole SS mesh is immersed in the growth solution, the generated heat will immediately decomposes the HMT to NH_4OH, which increases the pH of the solution. At higher pH, Zn^{2+} ions will be hydrolysed into $Zn(OH)_2$, which will then be deposited onto the heated SS mesh as ZnO. As mentioned before, the seed layer is formed during the growth process in PACBD. Therefore, the deposition of ZnO at the first few minutes will serve as the seed layer which will then assist the growth of vertically aligned arrays of ZnO NR.

It is important to note that the ZnO rods formed are tapered-like, as shown in Figure 6.3. This can be explained where the heat generated at SS mesh caused a rapid decomposition of the HMT, which results in the production of a large amount of OH^- ions at the beginning. These OH^- ions will react with the Zn^{2+} ions in the growth solution, resulting in a sufficient and thorough growth of ZnO, thus forming ZnO rods with a thicker base. As the duration of reaction is increased, the Zn^{2+} ions in the nutrient solution were gradually exhausted, limited by the initial concentration. Thus, the morphology of the NRs is determined by the depletion rate of the Zn^{2+} in the solution, which lead to the conical shape or tapered-like rods.

At low temperature (low applied power), only a small amount of randomly oriented ZnO NRs were grown on the surface of SS mesh with the presence of some

large crystals. This is because at low temperature, the growth rate is limited by the HMT decomposition rate. Meanwhile, the mobility and diffusion length of the ions on the substrate are limited, which prohibited the ions to diffuse around.[47] As a result, the NR density is low with some large size nuclei are formed on the surface of the SS wires. When the applied power is increased to 33.0W (~83°C), the ZnO NRs formed are relatively more vertically aligned with higher density. Under such condition, the nucleation and deposition rate is in a similar order as the HMT decomposition rate, therefore a steady growth with uniform morphology is achieved.

Further increased the heating power to 45.5W and above, there are some branched ZnO rods were formed. Such morphology is the result of rapid HMT decomposition at high temperature. When the formation of $Zn(OH)_2$ is faster than the NR growth rate, the surface energy difference between (002) and (100) planes is not sufficient to distinguish the growth kinetics between these faces. These ions will then also be deposited onto the (100) surface, forming new nucleation sites for the growth of ZnO NR branches. Consequently, tree-like ZnO NRs were created with high heating power. It is also worth mentioning that the SS mesh could reach a temperature of 112°C at an applied power of 60.0W, higher than the boiling point of the solvent (water). In order to compensate or control the growth kinetics between (002) and (100) faces at high temperature, one could use variable concentration of HMT, or an alternative chemical with lower decomposition rate.

6.4.4 Effect of Growth Duration on the Morphology of ZnO Rods

Other than the temperature of reaction, the growth duration of ZnO nanostructures is another parameter that will affect the morphology of the NR, which is important in optimising the optical properties. While maintaining other growth

parameters constant, such as the applied power (33.0W), dimension of SS mesh (1×3 cm^2) and volume of the nutrient solution (150 ml), the relationship between the growth duration and the morphology of ZnO NRs is investigated, shown in Figure 6.5. An applied power of 33.0W was chosen in this experiment due to the ZnO NRs grown under this power are relatively well-ordered with high density.

As shown in the top view SEM images (Figure 6.5A–6.5D), ZnO NRs were homogenously deposited throughout the SS meshes without any cracks or large defects. After different growth durations, vertically aligned ZnO NRs with different lengths and diameters were homogenously deposited on the surfaces around the SS wires throughout the whole SS mesh. As demonstrated in the SEM images, increased in the duration of reaction will result in the formation of longer, wider ZnO rods. The SEM images in Figure 6.5 reveal the cross sections of densely packed NRs were grown perpendicularly to the SS wires, except the sample which grown for 30 minutes (M30mW33 sample in Figure 6.5B). It is noteworthy that the adjacent NRs start to coalesce when the reaction time is 90 minutes and above, shown in the inset of Figure 6.5C and 6.5D. This can be explained where the longer growth duration will lead to the creation of larger NRs and thus reduce the gap between the neighbouring NRs, causing the adjacent NRs to merge into one big rod.

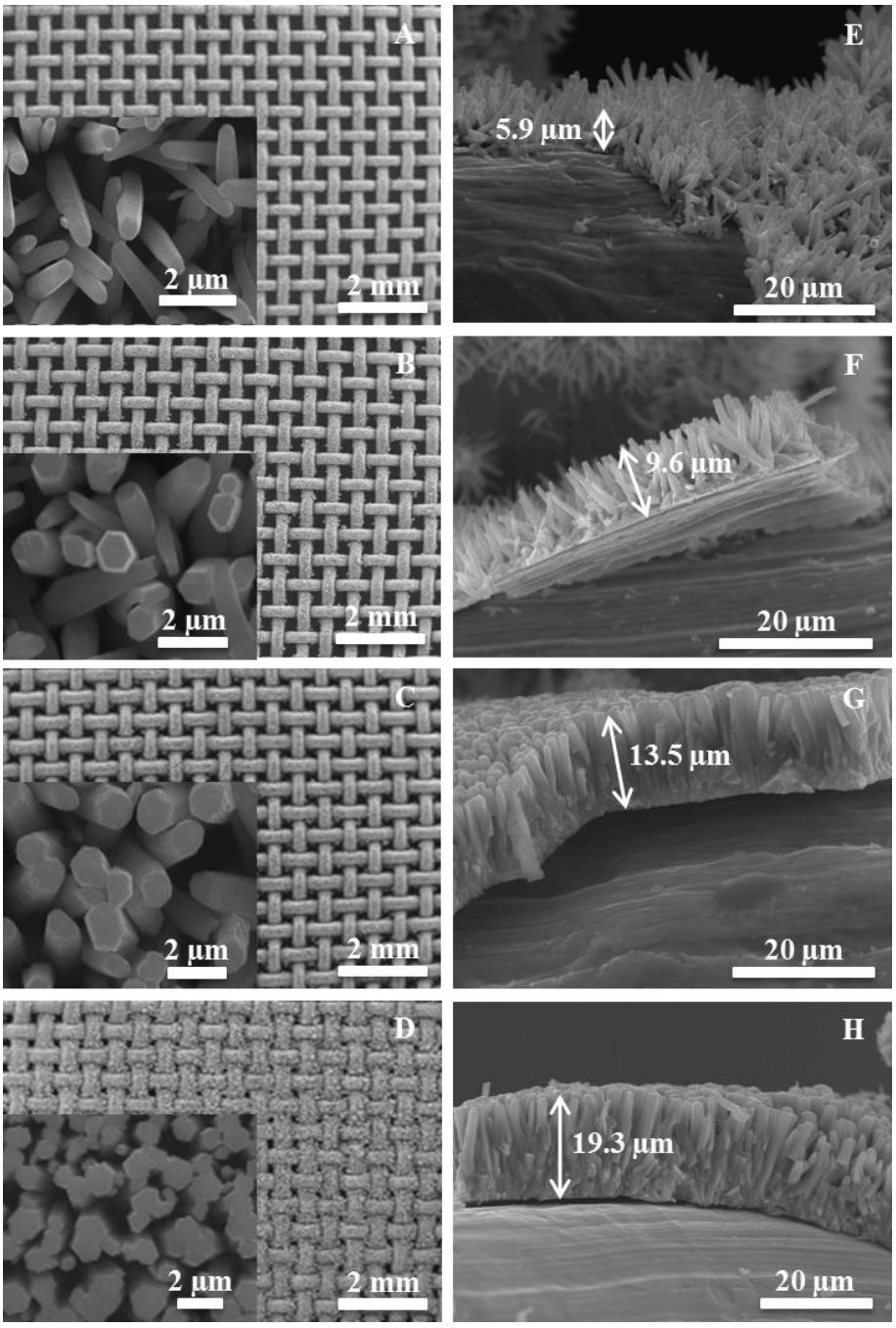

Figure 6.5 Top and cross-sectional view SEM images of ZnO NRs on SS meshes after different growth durations at an applied heating power of 33.0W in 150 ml of nutrient solution (The inset is the corresponding higher resolution of SEM image), (A,E) 30 minutes (M30mW33), (B,F) 60 minutes (M60mW33), (C,G) 90 minutes (M90mW33) and (D,H) 120 minutes (M120mW33).

The mean diameters and mean lengths of the ZnO rods grew at different durations were quantitatively measured from the SEM images in Figure 6.5. The results are plotted in Figure 6.6A and 6.6B. The diameters of all the samples are monodispersed with average diameters of 483, 670, 1040 and 1280 nm and FWHM values of 190, 172, 220 and 210 nm for the M30mW33, M60mW33, M90mW33 and M120mW33, respectively. Meanwhile, the length of the ZnO rods was increased from 5.9 µm to 19.3 µm (Figure 6.6B). From the plots, it is clear that both the diameters and lengths of NRs increase linearly as a function of growth time. This suggests that under these experimental conditions, for as long as 120 minutes of growth, the nutrient solution is not approaching exhaustion.

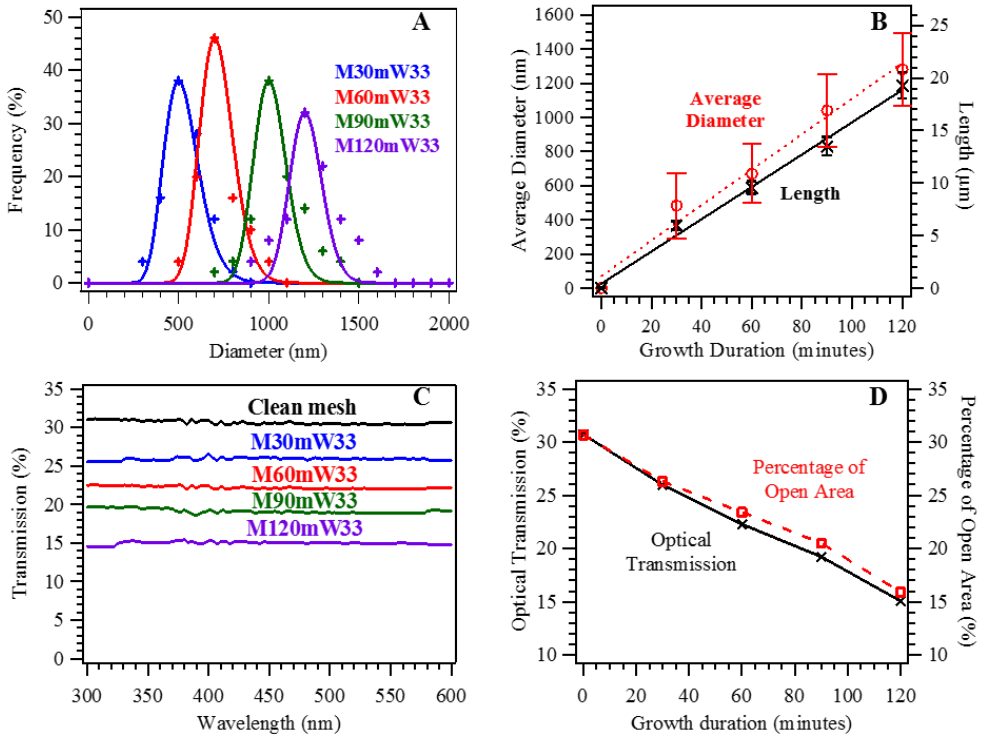

Figure 6.6 (A) Diameter distributions of ZnO NRs at different growth durations, (B) plots of average diameter and film thickness as a function of growth duration, (C) optical transmission spectra of ZnO NRs at different growth durations and (D) plots of optical transmission and percentage of open area as a function of growth duration.

In addition, the rate of growth of ZnO NR along (002) surface (length) and (100) surface (diameter) can also be evaluated from the gradients of the diameter and length plots in Figure 6.6B. The calculations reveal that the rate of growth of the ZnO NRs along the (002) plane (158.4 nm min^{-1}) is about 14 times faster than that along the (100) plane (11.2 nm min^{-1}). This can be explained by the higher surface energy of the (002) plane over the (100) plane, resulting in the anions favourably absorbed onto this polar surface and thus lead to the formation of 1D ZnO NRs.

It is noticeable that as the NRs become longer, the projected opening area and optical transmission were gradually decreased, as shown in Figure 6.6C to 6.6D. The percentages of open area of samples were calculated using equation 6.1, where 30.74%, 26.28%, 23.37%, 20.50% and 15.94% were achieved by the M30mW33, M60mW33, M90mW33 and M120mW33. In order to quantitatively assess the amount of light that passes through the mesh, the optical transmissions of the M30mW33, M60mW33, M90mW33 and M120mW33 were measured, as shown in Figure 6.6C. The optical measurements reveal that the optical transmission of electrodes were gradually decreased from 30.74% to 15.05% as increase in the duration of reaction. It is important to note that the calculated percentages of opening area of the samples are very similar to the recorded optical transmission, as shown in Figure 6.6D. Therefore, the optical transmission of SS mesh is exclusively determined by the opening area. Based on equation 6.1, the optical transmission of the sample could be precisely controlled by monitoring the length of the NRs.

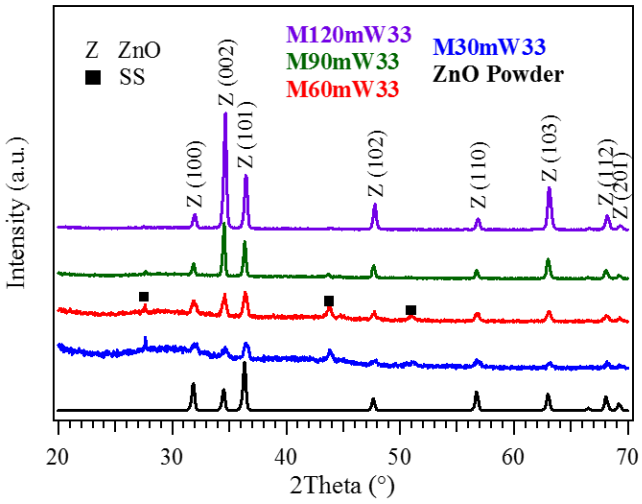

Figure 6.7 XRD patterns of ZnO NRs on SS meshes at different growth durations together with XRD pattern of ZnO powder. The miller indices of the crystal planes are labelled where Z and ■ are ZnO and SS, respectively.

The crystal structure and orientation of the as grown samples were investigated by powder XRD, shown in Figure 6.7. The XRD patterns of ZnO NRs on SS meshes are analysed based on the standard XRD database for wurtzite ZnO (JCPDS # 36-1451) and SS (JCPDS # 33-0397). The wurtzite ZnO gives the diffraction peaks located at 2θ = 31.89°, 34.56°, 36.38°, 47.65°, 56.71°, 62.97°, 68.05° and 69.26° (○) corresponding to (100), (002), (101), (102), (110), (103), (112) and (201) crystal planes. The SS gives the diffraction peaks located at 2θ = 27.69°, 43.76° and 50.81° (■). The ZnO diffraction peaks are getting more intense when the growth duration is increased. This can be explained where more ZnO is being deposited onto the SS mesh when the duration of reaction is increased, resulting in longer NRs with larger diameters. Meanwhile, the XRD intensities from the SS mesh substrate are gradually decreased as the thickness of the ZnO NRs film increases. The strongest diffraction intensity from the (002) plane is consistent to the fact that [0001] direction is the most favoured growth axis for 1D ZnO

nanomaterials.[281] This observation is in agreement with the hexagonal morphology of the ZnO rods which observed in SEM (Inset of Figure 6.5A–6.5D).

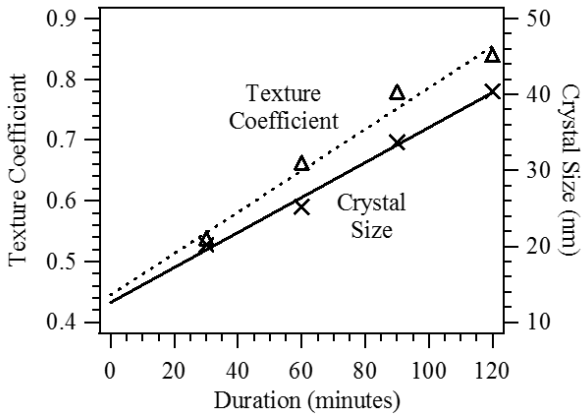

Figure 6.8 Plots of texture coefficient and crystal size of ZnO rods as a function of growth duration.

The relative texture coefficient (Equation 2.7, Section 2.3) and crystal domain size (Equation 2.5, Section 2.3) of ZnO rods grew at different durations were calculated, as shown in Figure 6.9. The relative texture coefficient values obtained for the M30mW33, M60mW33, M90mW33 and M120mW33 were 0.54, 0.66, 0.77 and 0.84, respectively. Compared to ZnO powder (0.50), all the samples demonstrate a higher relative texture coefficient value. This indicates the ZnO NRs grew on SS mesh are relatively more vertically aligned than the ZnO powder. Meanwhile, the crystal sizes of the samples were found to increase from 20.2 nm to 40.3 nm when the growth duration was increased from 30 to 120 minutes. These calculations demonstrate that increase in the duration of reactions, ZnO NRs grew on the SS meshes are more vertically aligned, along the [0001] direction with a larger crystal domain size.

6.5 PEC Hydrogen Generation Study

Here, the PEC performance of the ZnO NRs coated SS meshes will be evaluated in comparison with the ZnO NRs on a planar substrate. The effect of the ZnO morphology on SS mesh was also investigated in order to find optimum performance. More important, we constructed a multilayer SS mesh structured photoanode for PEC, which significantly improves the light absorption and results in an increase of photoconversion efficiency by ~158%.

6.5.1 PEC Activity of ZnO NRs on SS Plate and SS Mesh

The water photoelectrolysis activity of the M30mW33 photoanode was evaluated by measuring the photocurrent in 1.0 M KOH aquatic electrolyte under the illumination of a 100 mW cm^{-2} solar simulator with an AM1.5 G filter. The obtained photoactivity was compared with the vertically aligned ZnO NRs on SS plate after 15 hours of CBD growth (P15h). The NR length of P15h is very similar to the M30mW33 (5.5 µm; Figure 6.9B), where its mean length was 5.3 µm with a mean diameter of 216±56 nm (Figure 6.9A). Therefore, the direct comparison of PEC performance is generally valid.

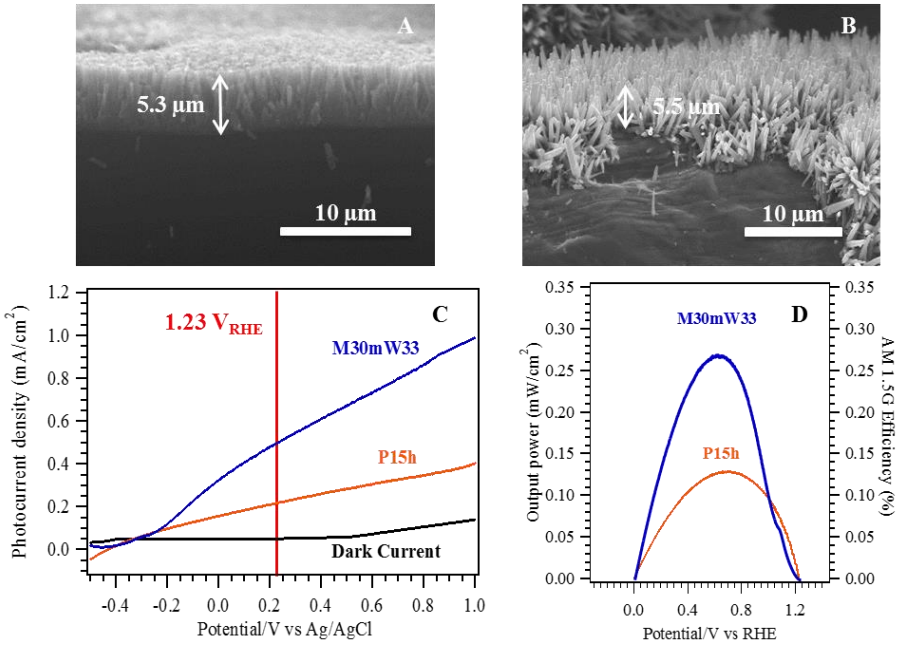

Figure 6.9 Cross-sectional view SEM images of (A) P15h, (B) M30mW33, (C) *I–V* curves of M30mW33 and P15h together with the dark current measured from M30mW33 in 1.0 M KOH aquatic electrolyte under the illumination of a 100 mW cm^{-2} solar simulator with an AM1.5 G filter and (D) corresponding PEC output power and conversion efficiency under AM1.5 G full solar spectrum irradiation.

The morphologies of the P15h and M30mW33 samples are shown in Figure 6.9A and 6.9B. Similar NR length were obtained, although the direct heating growth of ZnO NRs on SS mesh only takes 30 minutes, much faster than the conventional CBD growth on SS plate (15 hours). Carefully exam the SEM images in Figure 6.9A and 6.9B also reveal that the ZnO NRs on SS mesh is much less dense than that on the SS plate. Figure 6.9C compares the water photoelectrolysis *I–V* curves from the M30mW33 and P15h photoanodes under simulated sunlight together with the dark current recorded from the M30mW33 electrode. The applied potential ranges from –0.5 to 1.0 $V_{Ag/AgCl}$. With light on, the photocurrents generated from both the M30mW33 and P15h electrodes increase steeply at lower potential with an open circuit potential at

−0.40 $V_{Ag/AgCl}$. However, the photocurrent produced from the M30mW33 electrode increases much faster than the P15h electrode at more positive potentials. At 1.23 V_{RHE} (marked as red line in Figure 6.9C), the M30mW33 anode generates 0.49 mA cm^{-2}, but the P15 electrode only generates 0.21 mA cm^{-2}. This indicates a 133.33% enhancement from the SS mesh sample. This cannot be explained by the difference in the packing density of the ZnO NRs, as one would expect a higher density of ZnO NRs should result in a larger photocurrent, since it has a higher surface area.

For both samples, the photocurrents generated do not reach a plateau which suggest that the charge recombination and interface reaction kinetics did not limit the photocurrent under our experimental conditions. The photoconversion efficiencies of the samples were calculated (Equation 2.27, Section 2.6), presented in Figure 6.9D. A much higher output power density, and thus a higher photoconversion efficiency was found for the M30mW33 photoanode, with a maximum output power of 0.28 mW cm^{-2} with respect to 0.13 mW cm^{-2} from the P15h photoanode. These measured maximum PEC output powers correspond to the solar PEC efficiencies of 0.28% and 0.13%, respectively.

In order to understand the intrinsic electronic properties of the M30mW33 and P15h photoelectrodes in electrolyte, EIS measurements were carried out in the dark to evaluate the capacitances and flatband potential (V_{FB}) of the ZnO NRs in 0.5 M of Na_2SO_4 (pH 6.8) at 1 kHz with a 10 mV AC modulation (Equation 2.23, Section 2.5). The Mott–Schottky (M–S) plots in Figure 6.10A give the V_{FB} values of −0.38 $V_{Ag/AgCl}$ for both of the P15h and M30mW33 photoanodes.

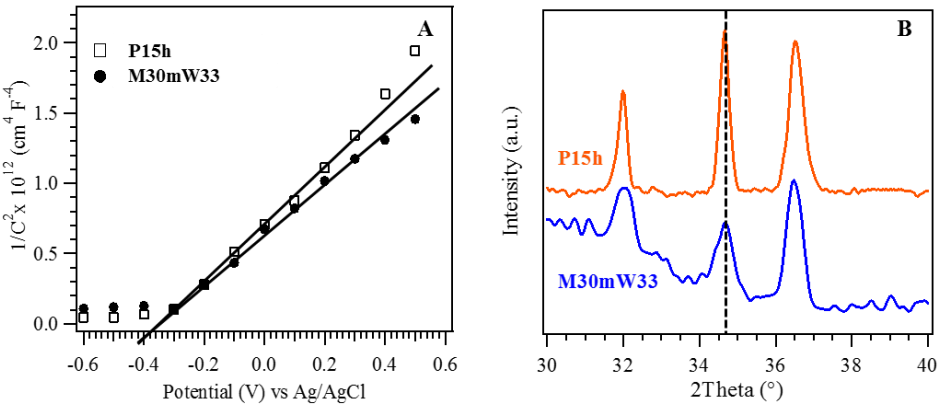

Figure 6.10 (A) M–S plots of P15h and M30mW33 photoanodes measured in 0.5 M Na_2SO_4 solution in the dark at a fixed frequency of 1 kHz. The amplitude of the sinusoidal wave was set at 10 mV. (B) Enlarge XRD spectra of P15h and M30mW33 at 2θ ranging from 30 to 40°.

The positive slopes of the M–S plots confirm that ZnO is an n-type semiconductor with the majority charge carriers are electrons. In addition, the slopes of the M–S plots from the M30mW33 is slightly less than that from the P15h, which suggests the charge carrier density in the M30mW33 is higher than that in the P15h. The electron densities of the P15h and M30mW33 photoanodes were calculated (Equation 2.24, Section 2.5) to be 6.15×10^{18} cm^{-3} and 8.22×10^{18} cm^{-3}, respectively. It is worth noting these values are comparable to the typical value of 6×10^{18} cm^{-3} for the ZnO NRs prepared by electrochemical deposition.[265] The charge carrier concentration of the M30mW33 electrode is about 33% higher than that of the P15h electrode. The higher carrier density can be attributed to the higher density of defects (oxygen vacancies) in the M30mW33 photoanode since the ZnO were rapidly deposited onto the SS mesh through the PACBD. Increased in the charge carrier density not only will enhance the charge transport in the ZnO but also improve the electron transfer at the interface between the ZnO and SS substrate.[89] The XRD spectra in Figure 6.10B

show that the (002) peak of the M30mW33 is much broader than that of the P15h. The FWHM values of the diffraction peak were measured to be 0.42° and 0.28°, corresponding to the crystal domain sizes (Equation 2.5, Section 2.3) of 19.2 and 28.4 nm for the M30mW33 and P15h, respectively. The smaller crystal domain size of the M30mW33 electrode confirms the presence of more defects (oxygen vacancies) and thus a higher charge carrier density, which can result in a higher PEC efficiency.

Other than that, the Zn–O bond lengths of the samples can also be calculated (Equation 2.3, Section 2.3) from the 2θ of the XRD in Figure 6.10B. The P15h and M30mW33 photoanodes were calculated to have Zn–O bond lengths of 1.97 Å and 1.92 Å. The bond length of Zn–O was previously reported to be 2.21 Å.[174] In comparison to the reported value, our samples show a shrinkage of the average bond length by 10.9% and 13.1%, respectively. The shorter Zn–O bond length also indicates the presence of the structural defects (oxygen vacancies) in the samples.[174] The Zn–O bond length of the M30mW33 electrode is 2.5% shorter than that of the P15h electrode, consistent with the higher charge carrier density in the M30mW33 as identified by the slope of the M–S plot in Figure 6.10A. Therefore, this could be one of the reasons for the improvement in the photoactivity of PEC water splitting for the M30mW33 photoanode over the P15h photoanode. Similar findings for heavily reduced TiO_2 nanomaterials have also been reported.[89]

In addition, the width of the space-charge layer (W), at the interface between the semiconductor and the electrolyte can also be derived from M–S plot relationship (Equation 2.25, Section 2.5). At a typical potential of 1.0 $V_{Ag/AgCl}$, the W values of P15h and M30mW33 photoelectrodes were calculated to be 20 nm and 17 nm, respectively. The W values obtained for both of the P15h and M30mW33 photoanodes are much smaller than the radius of the NR. Therefore, this suggests that the NRs of the P15h and

M30mW33 electrodes are not fully depleted at potential of 1.0 $V_{Ag/AgCl}$. The obtained results are in agreement with the *I–V* curves in Figure 6.9C where there is no limiting photocurrents observed.

The rates of electron-hole recombination of the M30mW33 and P15h electrodes were evaluated from the leading curvature of the time dependent amperometric plots measured at applied voltages of 0.80 V_{RHE} and 1.20 V_{RHE} under light on-off cycles for 150 s. These measurements reveal that the P15h (Figure 6.11A) and M30mW33 (Figure 6.11B) photoelectrodes are stable under our experimental conditions since there is no obvious decrease in the photocurrent density. Anodic photocurrent spikes were observed for both of the photoanodes at the beginning of illumination. This can be attributed to the slow oxygen evolution reaction kinetics at the carrier oxidised trap states of the semiconductor resulting in the accumulation of charges at the semiconductor-electrolyte interface.[255, 256]

It is noteworthy that the photocurrent spikes became smaller when the applied bias was increased from 0.80 V_{RHE} to 1.20 V_{RHE}. This phenomenon can be explained where increasing in the applied voltage would be beneficial to the charge separation since a larger proportion of holes have sufficient potentials to oxidise water, thus reducing the possibility of charge recombination.[256] Additionally, a more positive applied potential will cause the formation of potential gradient within the samples, which can accelerate the photogenerated electrons to transfer to the outer circuit, also resulting in decreased the electron-hole recombination.[299]

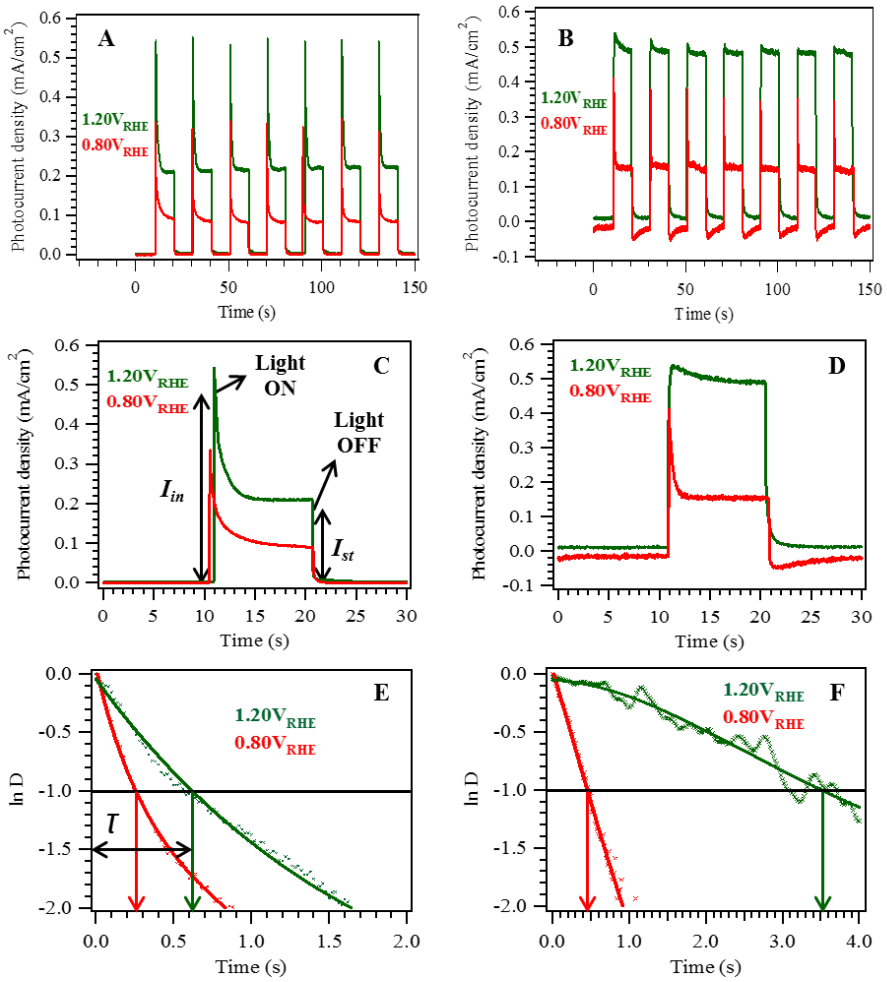

Figure 6.11 Amperometric *I–t* curves and anodic photocurrent dynamics of the P15h (A,C) and M30mW33 (B,D) anodes in 1.0 M KOH electrolyte (pH 13.6) at potentials of 0.80 V_{RHE} and 1.20 V_{RHE} at 100 mW cm^{-2}. Anodic transient dynamics analyses of the P15h (E) and M30mW33 (F).

It is noteworthy that the photocurrent spike of the M30mW33 photoanode is much smaller with respect to that generated from the P15h photoanode. This implies the rate of electron-hole recombination of the M30mW33 photoanode is much lesser than the P15h photoanode. The charge recombination behaviours of the samples can be quantitatively determined by fitting the exponential decay using equation 4.2 in section 4.5.2. Figure 6.11E and 6.11F present the plots of normalised ln *D* as a function of time

for the P15h and M30mW33, respectively. The transient time constant (τ) values measured at ln D = –1 for both of the photoanodes are increasing when the applied bias is increased. For the P15h photoanode, the τ values are 0.25 s (0.80 V_{RHE}) and 0.52 s (1.20 V_{RHE}), which are much smaller than the values by the M30mW33 photoanode of 0.45 s (0.80 V_{RHE}) and 3.53 s (1.20 V_{RHE}), respectively. These calculations reveal that, at an applied potential of 1.20 V_{RHE}, the charge recombination rate of the P15h photoanode is nearly 7 times faster than that of the M30mW33 photoanode. The reduction in the electron-hole recombination rate from the M30mW33 photoanode is possibly due to the presence of a certain amount of defects in the M30mW33 sample, which helps to improve charge separation. Such behaviour is further investigated by the illuminating light intensity dependent photocurrent analysis.

In the light intensity dependent experiment, the applied potential was fixed at 1.00 V_{RHE} with irradiation intensities set at 100 mW cm^{-2}, 200 mW cm^{-2} and 300 mW cm^{-2}. Figure 6.12A (P15h) and 6.12B (M30mW33) show that the anodic photocurrent dynamics for both of the photoanodes are reproducible under repeated light on-off cycles for 150 s under high light intensity. Figure 6.12C and 6.12D demonstrate the photocurrent densities from the P15h and M30mW33 photoanodes in a single step of light off-on-off. It is clear that both the steady photocurrent (I_{st}) and the initial photocurrent spikes (I_{in}) are increasing as the irradiation intensity increases.

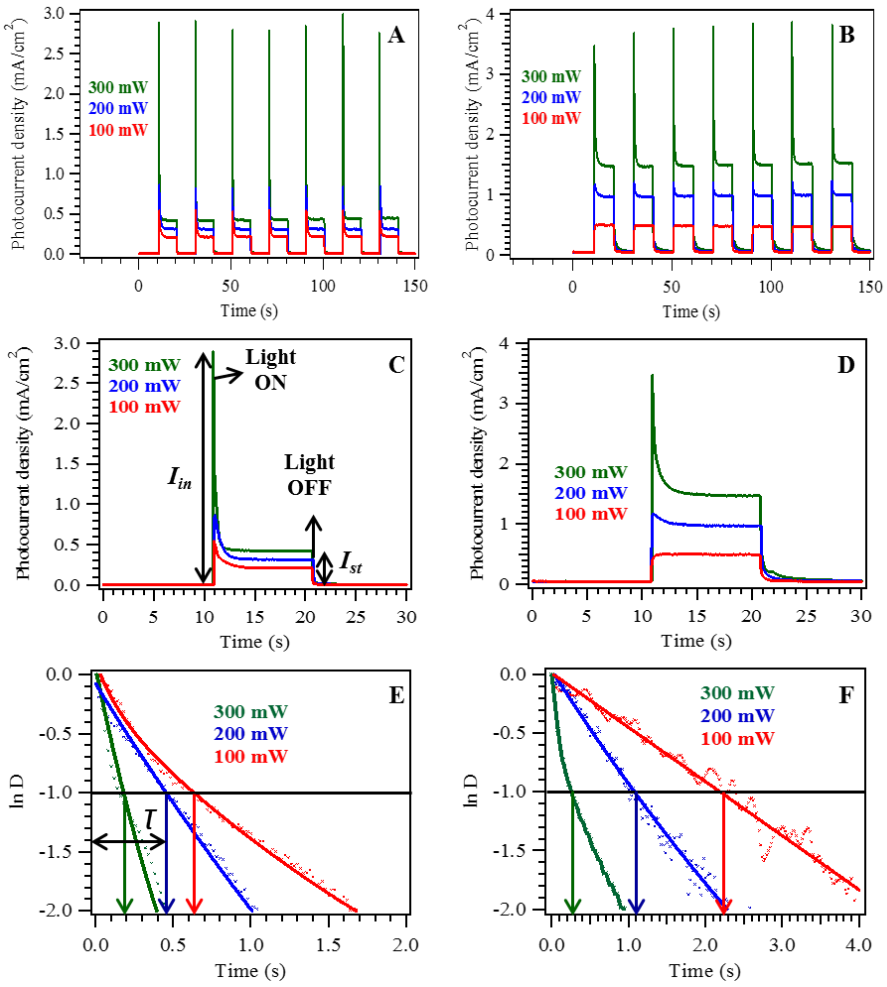

Figure 6.12 Transient dynamics of photocurrent by the P15h (A,C) and M30mW33 (B,D) measured in 1.0 M KOH electrolyte (pH 13.6) at an applied potential of 1.00 V_{RHE} at different irradiation intensities. The value of ln *D* is plotted at different incident light intensities for the P15h (E) and M30mW33 (F).

Under all illumination conditions, the M30mW33 anode generates a higher steady photocurrent than that from the P15h anode. For instance, at an incident light intensity of 200 mW cm^{-2}, the photocurrent density of M30mW33 electrode (0.97 mA cm^{-2}) is about three times higher than that from the P15h electrode (0.32 mA cm^{-2}). On the other hand, when compared with the P15h photoanode, the I_{in} of the M30mW33 photoanode is much smaller, suggesting a smaller electron-hole

recombination rate of the M30mW33. This was quantitatively analysed with the τ values calculated from equation 4.2 in section 4.5.2. The results are shown in the ln *D* plots in Figure 6.12E and 6.12F. It shows that the τ values for both of the electrodes are decreasing as the incident light intensity increases.

At irradiation intensities of 100 mW cm^{-2}, 200 mW cm^{-2} and 300 mW cm^{-2}, for the P15h electrode, the τ values were estimated to be 0.52 s, 0.44 s and 0.18 s, respectively, while, for the M30mW33 electrode, the τ values were 2.23 s, 1.09 s and 0.28 s, respectively. These measurements confirm that, as expected, the charge recombination rates are significantly affected by the incident light power intensity and with light intensity between 100 mW cm^{-2} to 300 mW cm^{-2}, the electron-hole recombination rates of the M30mW33 photoanode are much smaller than that of the P15h photoanode. It is worth noting that the I_{in} of the M30mW33 photoanode increases dramatically only with an irradiation intensity of 300 mW cm^{-2}. This observation suggests that the M30mW33 photoanode did not experience light saturation until the light irradiation intensity is higher than 200 mW cm^{-2}.

The next possible reason for the higher photocatalytic activity of the M30mW33 anode over the P15h anode can be attributed to the larger effective surface area of the M30mW33 anode. The illumination area during the PEC water splitting is fixed at 1 cm^2. The SS mesh is formed by SS wires with a diameter of 0.112 mm. The nature of the corrugated SS mesh surface offers an increased substrate surface area for the growth of ZnO NRs, with respect to the planar substrate, as illustrated in Figure 6.13.

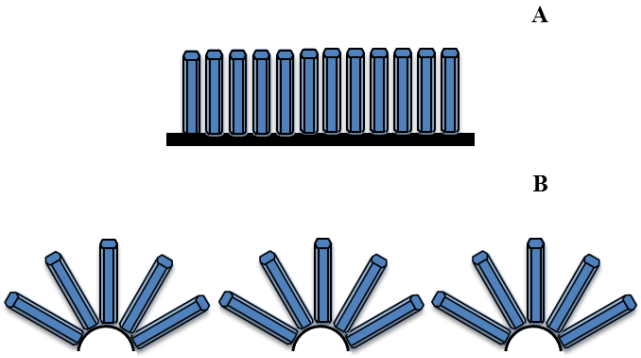

Figure 6.13 Schematic diagrams illustrating the surface area of (A) planar SS substrate and (B) SS mesh.

Considering the opening area of the SS mesh (~30.74%), the front illuminated area of the SS mesh can be calculated as below:

$$\text{Lateral surface area of the SS mesh (1 cm} \times \text{1 cm)} = {(\pi D_{ss} l_{ss} \times \text{ number of wires})}/{2}$$

$$= {[\pi\ (0.0112\ \text{cm})\ (1\ \text{cm})\ (80)]}/{2}$$

$$= 1.407\ \text{cm}^2$$

where D_{ss} and l_{ss} are the diameter and length of the SS wire, respectively. It is necessary to note that the cross knots of two SS wires should be taken into account. The total amount of the cross knots is determined to be ~1440 within 1 cm^2. Thus, the surface area of the cross knots of SS mesh is (0.112 cm × 0.112 cm)(1440) = 0.181 cm^2. The actual corrugated surface area of SS mesh is 1.407 cm^2 – 0.181 cm^2 = 1.23 cm^2.

When compared with the planar P15h photoanode (1 cm^2), the actual surface area of the M30mW33 photoanode is increased by at least 23%. The corrugated surface of the M30mW33 photoanode will be able to grow more ZnO NRs. On such surface, as shown in Figure 6.6A, ZnO NRs were grown in a radially outwards on the

circumference of the SS wire. This 3D feature offers a larger surface area and is beneficial for the larger reaction site density with improved light absorption, since some of the refracted light can also be captured by the ZnO NRs,[296] which in turn enhances the PEC water splitting performance.

6.5.2 Effect of Growth Duration on PEC Activity of ZnO NRs on SS Meshes

Both the length and diameter of the ZnO NRs can be controlled by the growth duration. Longer growth duration can achieve longer and larger NRs on SS meshes, which can affect the PEC performances. Figure 6.14A depicted the *I–V* curves of the M30mW33, M60mW33, M90mW33 and M120mW33 photoanodes together with the dark current from the M120 mW33 measured in 1.0 M KOH aquatic electrolyte under the illumination of a 100 mW cm^{-2} solar simulator with an AM1.5 G filter in the potential range of –0.5 to 1.0 $V_{Ag/AgCl}$.

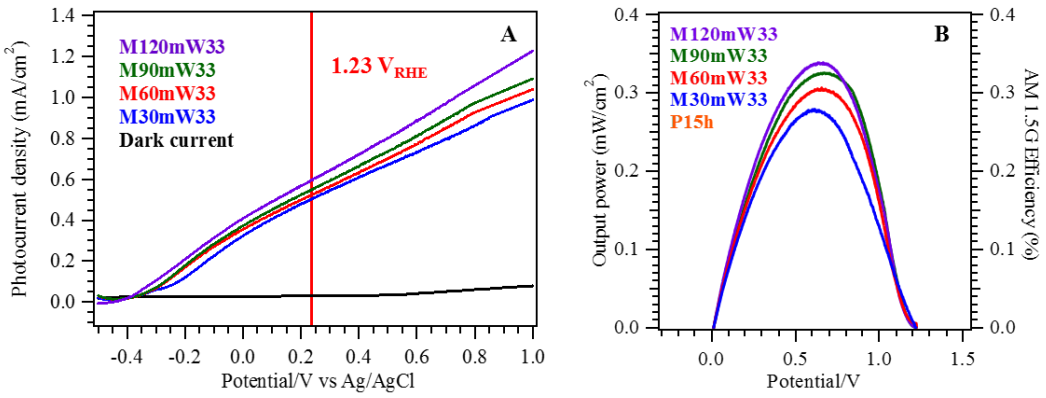

Figure 6.14 (A) *I–V* curves of ZnO NRs grew on SS meshes at different durations together with dark current measured from the M120mW33 measured in 1.0 M KOH aquatic electrolyte under the illumination of a 100 mW cm^{-2} solar simulator with an AM1.5 G filter and (B) corresponding PEC output power and photoconversion efficiency under AM1.5 G full solar spectrum irradiation.

The *I–V* curves reveal that increasing the growth durations do not have any obvious effect on the open-circuit potentials, however a large effect on the photocurrent density was found. At a typical potential of 1.23 V_{RHE} (marked as red line), the photocurrents generated from the M30mW33, M60mW33, M90mW33 and M120mW33 photoanodes were 0.44 mA cm^{-2}, 0.52 mA cm^{-2} , 0.55 mA cm^{-2} and 0.59 mA cm^{-2}, respectively.

Figure 6.14B presents the calculated PEC output power and photoconversion efficiency (Equation 2.27, Section 2.6) of the photoanodes at different growth durations. Consistent with the higher photocurrent, a higher PEC output power and photoconversion efficiency was found for the longest growth duration sample (M120mW33). The obtained film thickness together with the measured photoconversion efficiency were plotted as a function of growth duration in Figure 6.15A, in order to establish their correlation. It is clear that increasing in the growth duration will result in an increase of the NR length which will improve the PEC water splitting efficiency. Compared to the M30mW33 photoanode (0.27%), M120mW33 photoanode (0.34%) demonstrates an increase of ~26% in the photoconversion efficiency. This can be attributed to the large effective surface reaction centre density and better light absorption for the photoelectrolysis of water.

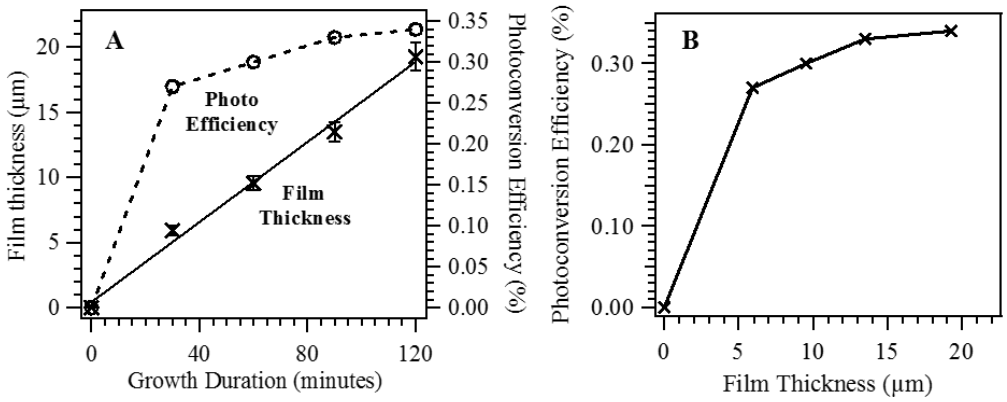

Figure 6.15 Plots of (A) film thickness and photoconversion efficiency as a function of growth duration (B) photoconversion efficiency as a function of film thickness.

Although increasing the growth duration will cause a higher photoconversion efficiency, it is necessary to note that the photoconversion efficiency enhancement is not linear proportional to the increment of the NRs length, shown in Figure 6.15B. As the NR length increases, it also increase the travelling length of the photoelectron within the ZnO NR to reach the SS substrate. This will increases the charge recombination probability. Furthermore, increasing the diameters of the NRs will also decrease the gaps between the adjacent NRs. This will decrease the surface porosity of the sample, which in turn reduced the photocurrent density. The surface porosities (Equation 3.8, Section 3.4.7) of the M30mW33, M60mW33, M90mW33 and M120mW33 electrodes were calculated to be 47%, 42%, 33% and 27%, respectively. A large surface porosity will allow better penetration of the electrolyte into the electrode and results in an increase in the contact area between the electrolyte and photoanode, thus a higher photocatalytic activity.

6.5.3 Effect of Number of Layers of M60mW33 on PEC Performance

A mesh substrate not only offers higher corrugated surface area, but it also allows a greater portion of light transmission. To take this advantage, I have designed a multilayer mesh system that allows to trap and capture most of the light between the meshes. The correlation between the number of layers of mesh and the PEC water splitting performance was investigated.

As shown in Figure 6.6G, M120mW33 is nearly fully covered by ZnO rods with a small opening area and the surface porosity of the sample is relatively low. Therefore, M60mW33 with an opening area of 23.37% was chosen for this experiment. All the samples were grown in 150 ml of nutrient solution with a mesh dimension of 1×3 cm^2 at an applied heating power of 33.0W for 60 minutes.

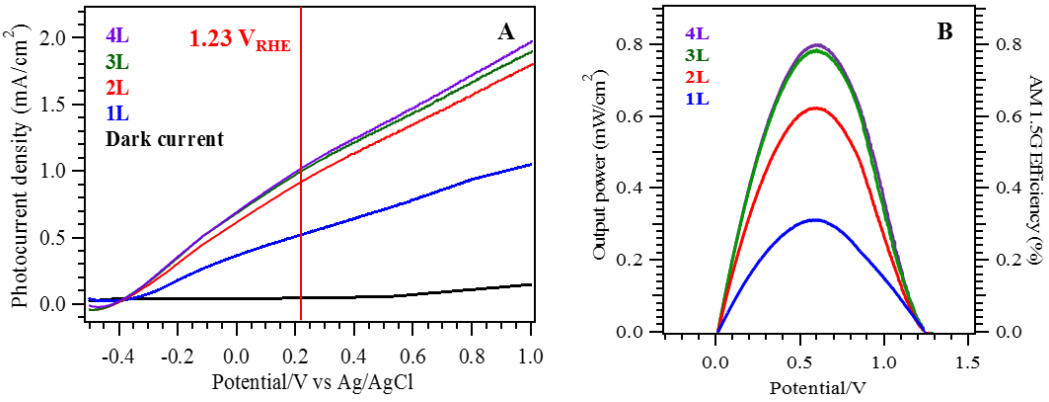

Figure 6.16 (A) *I–V* curves from different number of layers of M60mW33 together with dark current measured from the 4L in 1.0 M KOH aquatic electrolyte (pH 13.6) under the illumination of a 100 mW cm^{-2} solar simulator with an AM1.5 G filter and (B) corresponding PEC output power and photoconversion efficiency under AM1.5 G full solar spectrum irradiation.

Figure 6.16A displays the *I–V* curves from one to four layers of M60mW33 (named as 1L to 4L) under illumination (100 mW cm^{-2} with an AM1.5 G filter) between potentials of –0.5 and 1.0 $V_{Ag/AgCl}$ in 1.0 M of KOH electrolyte (pH 13.6). In comparison, the 2L and 3L photoanodes show progressively increasing photocurrent densities than the 1L photoanode. Photoanode with four layers of M60mW33 (4L, 1.91 mA cm^{-2} at 1.23 V_{RHE}) showing essentially the same photocurrent density as that using three layers of M60mW33 (3L, 1.85 mA cm^{-2} at 1.23 V_{RHE}). A comparison of the PEC output power and AM1.5 G efficiency of the photoanodes are presented in Figure 6.16B. The conversion efficiencies achieved by the 1L, 2L, 3L and 4L photoanodes were measured to be 0.31%, 0.62%, 0.78% and 0.80%, respectively. A maximum of ~158% of PEC water splitting efficiency increment was achieved by using the multilayer configuration.

The enhancement in the PEC water splitting efficiency can be attributed to two prominent advantageous characteristics of the multilayer of M60mW33 electrodes. Firstly, the total effective surface area of the 4L photoanode is increased as the number of layers of mesh were increased. The 23.37% opening allows a certain amount of light to pass through and illuminate the underneath layers. Therefore, the number of available reaction centres for the oxidation of water at the solid-liquid-gas interface for the multilayer photoanode are increased, which contribute to the higher efficiency in hydrogen generation.

Secondly, the light absorption of the 4L photoanode is improved by the internal light scattering and reflection as compared to the 1L photoanode or the planar electrode (P15h). For a single mesh or a planar electrode, the light reflection could decrease the apparent photoconversion efficiency. Many efforts have been focused on the trapping of light with surface waveguides or photonic crystals.[304] For the multilayer mesh electrode

(4L), a schematic diagram is proposed in Figure 6.17A to demonstrate the penetration and the internal reflection process of the incident light.

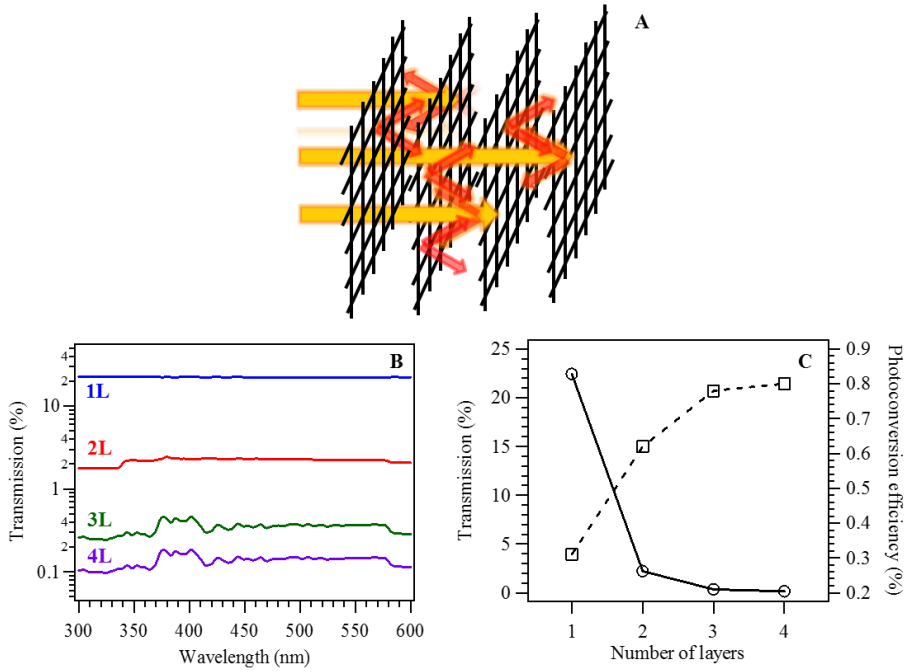

Figure 6.17 (A) A schematic diagram illustrating the penetration (orange) and reflection (red) process of the incident light, (B) optical transmission spectra of the samples with different number of layers of M60mW33 and (C) plots of optical transmission and photoconversion efficiency with respect to the number of layers of M60mW33.

As mentioned in section 6.4.4, the percentage of open area of the M60mW33 is ~23.37%. Therefore, some of the incident light will be able to penetrate through the apertures of the front mesh to reach to the following layers. Those light rays that passes through the front layer will then be absorbed by the ZnO NRs on the following layers. In addition, due to the special 3D feature of the multilayer photoanode, the reflected light can also be harvested by the ZnO NRs on the back of the first mesh as illustrated in the schematic diagram in Figure 6.17A. A UV-vis spectrophotometer was used to quantitatively assess the amount of light that passes through the multilayer photoanode,

as presented in Figure 6.17B. It reveals that the optical transmission is decreased when there is an increase of the number of layers of M60mW33. The optical transmissions obtained by the 1L, 2L, 3L and 4L electrodes were 22.43%, 2.20%, 0.34% and 0.14%. It is important to note that only 0.14% of the light passed through the 4L photoanode, which implies 99.86% of the light was absorbed by the electrode (including some reflected by the front of the first mesh). As presented in Figure 6.17C, an inverse correlation was observed between the optical transmission and the photoconversion efficiency of the multilayer photoanode. This indicates the total light absorption is improved by increasing the number of layers of M60mW33, where most of the light is harvested and utilised in the water splitting reaction, resulting in a higher photoconversion efficiency.

On a planar photoanode, such high efficient light absorption can only be achieved by using a thick layer of ZnO. However, the photoconversion efficiency from such geometry would be significantly limited by the charge transfer from the metal oxide to the conductive substrate. Thus, the approach becomes impractical for a planar electrode. Using a multilayer mesh electrode, while the light absorption is improved, the charge mobility will not limit the total photoconversion efficiency. Therefore, our unique multilayer mesh electrodes could offer an alternative effective way of maximising the light absorption.

In the practical application of solar energy harvesting, the response of the photoanode to the sun position is also important. For a planar device, this is usually facilitated by tracking the sun position, which will need sophisticated mechanical control. With our multilayer metal mesh photoanode, the internal reflection will allow it to be tolerant to the illumination angle. To demonstrate this advantage, the

photocurrents of the 4L photoanode were measured as a function of incident light angles relative to the surface normal, as depicted in Figure 6.18.

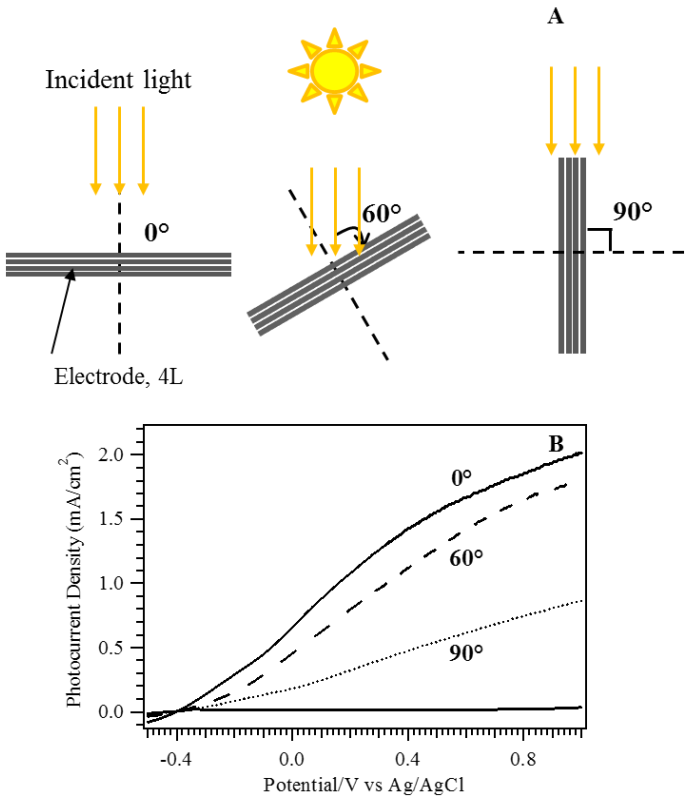

Figure 6.18 (A) Schematic diagrams demonstrating the PEC measurements of the 4L photoanode at different incident light angles relative to the surface normal and (B) *I*–*V* curves of the 4L photoanode recorded at incident light angles of 0°, 60° and 90°.

The schematic diagrams illustrate the light incident geometry is shown in Figure 6.18A. The measured photocurrent as a function of bias is presented in Figure 6.18B. It reveals that by changing the light incident angle from 0° to 60°, the photocurrent density (measured at 1.0 $V_{Ag/Ag/Cl}$) is only reduced by 10%. However, at 90° incidence with respect to the normal incidence, the photocurrent density (measured at 1.0 $V_{Ag/Ag/Cl}$) is reduced by 43%. The small reduction in the photocurrent density from 0° to 60° illumination suggest that the multilayer mesh photoanode has a wide light acceptance

angle, which is essential for harvesting solar energy. The result from our four layers mesh photoanode is much better than those published results for a single mesh photoanode.[299] In Liu Z. Y. *et al.* measurement, for a single layer mesh, the reduction of the photocurrent density from 0° to 60° was more than 20%. Such significant improvement by our 4L electrode can be attributed to the multiple internal light reflection effects. Consequently, more light is being trapped and utilised by the material in water splitting reaction, thus increases the photocurrent density. For a single mesh electrode, such internal light reflection is not expected.

In summary, the PEC performance of the nanostructures can be simply yet effectively improved by maximising the light absorption of the photoanode with high density corrugated morphologies (high surface area) and multilayer electrode configurations (internal light reflection).

6.6 Conclusions

We have demonstrated, for the first time, direct synthesis of vertically aligned crystalline ZnO NR arrays on SS meshes by PACBD. The final morphology of ZnO nanostructures was strongly affected by the applied power. Increased in the applied power to 45.5W and above resulted in the formation of tree-like ZnO nanostructures. Both the length and diameter of the ZnO rods can be controlled by varying the growth duration. The PEC water splitting measurements revealed that the NR arrays on the SS mesh was about two times more efficient than the NR arrays on the SS plate with similar film thicknesses. The possible mechanisms for the higher efficiency were also discussed. The PEC water splitting efficiency was further improved by 2.6 times when four layers of the NR arrays on SS mesh were used as the photoanode.

Chapter 7 Conductive Y-doped ZnO Nanorods Enhanced Gas Ionisation Sensor Performances

7.1 Abstract

A facile approach for the solution growth of Y-doped ZnO (YZO) NR arrays by hydrothermal method was demonstrated. The correlation between the Y/Zn molar ratio and the morphology of ZnO nanostructures was investigated. With increased the Y/Zn molar ratios, the aspect ratios of the ZnO NRs were increased. The effects of Y/Zn molar ratios on the optical and electrical properties of ZnO NRs were examined. The as-prepared ZnO and YZO NRs with different Y/Zn molar ratios were used as anodes in gas ionisation sensor (GIS) application. The measurements revealed that, in comparison to the undoped ZnO, the sensitivity of GIS was increased by 7–fold with a lower breakdown voltage when the YZO NRs (1% doped) were used. The reduced breakdown voltage and increased sensitivity can be attributed to the increase in the conductivity of the YZO NRs. Both the stability and repeatability of the GISs were investigated. The effect of UV illumination on the gas sensor performance was studied. When compared to that in the dark (130.7 μA), the UV illuminated GIS (144.6 μA) showed an increased in the discharge current by ~10%, which indicates the sensitivity of the sensor was improved.

7.2 Introduction

Gas sensors have attracted considerable attention in the recent years owing to their widespread applications in industry, for instance, pollution detection, environmental monitoring, biomedical and pharmaceuticals.[70, 149] Gas sensors can be

classified into two different categories which are chemical and physical types of sensors. Most of the conventional gas sensors are chemical type in which metal oxides,[69] porous silicon[155] and carbon nanotubes (CNTs)[21, 156] were used as the active layer. The responses of their electrical property to gas adsorption were used to quantify the gas concentration (partial pressure). There are a few limitations for these types of sensors where they suffer from selectivity issue since different types of gases might exhibit the similar electrical responses.[162, 163] Other than that, it has potential difficulties in detecting gases with low adsorption energies such as inert gases and normally high working temperature is required to establish the adsorption/desorption equilibrium.[70, 164]

Therefore, GISs had been introduced to qualitative and quantitative measurement of gas. As a physical type of gas sensor, it measures the ionisation energy and the ionisation current of gases. The characteristic ionisation energy is used to identify gases, while the amplitude of the ionisation current is proportional to the partial pressure of the gas components.[72, 305] This type of gas sensors could be used in advanced gas analysers for chromatography and mass spectrograph. The main drawback of GISs is that a high voltage is required.[69] Recently, a novel CNT arrays based GIS has been demonstrated to detect many gas species (NH_3, CO_2, N_2, O_2, He and air) regardless of the magnitude of the gas adsorption energy and the electronegativity.[72] Although the nanostructured CNTs could generate a very high electric fields at relatively low voltages which make it an ideal candidate as GIS, it suffers oxidation under oxygen environment and degradation at a high discharge current.[306] Other than CNTs, metallic NWs is one of the possible materials for GIS because it provides low breakdown voltage. However, the metallic NWs based GISs will lose the sensitivity after several cycles of operation due to the induced voltage degrades the NWs tips.[71]

Other than CNTs, 1D metal oxide nanomaterials had attracted great attention in the application of GIS. It has been reported that ZnO NWs,[69] CuO NWs,[164] silicon NWs[166] and the TiO_2 NTs[165] have shown promising potential in the GIS applications. Among these metal oxides, ZnO nanostructures have been widely explored owing to its chemical stability, sharp nanotips, high melting point (1975°C) and strong ionic bonding energy.[235] Previous finding reported that the modification of the ZnO NRs surface by capping with palladium nanoparticles will increase the sensitivity of gas sensor and lower the breakdown voltage.[70]

For a high performance GIS, it requires high conductivities with conical shapes and high aspect ratios.[71] ZnO NRs based GISs require a higher breakdown voltage in comparison to CNTs based GISs, due to its low conductivity. Here, we developed doped ZnO NRs with improved conductivity for reducing the breakdown voltages and improving the GIS sensitivity. Both the optical and electrical properties of the ZnO and YZO NRs were studied. The gas ionisation sensing tests reveal that the YZO NRs based GISs require a much smaller breakdown voltage in comparison to the ZnO NRs based GIS. More important, the sensitivity of the GIS can be further improved by the UV illumination.

7.3 Experimental Details

7.3.1 Preparation for Growing ZnO and YZO NRs

All the chemicals used were analytical grade and purchased from Sigma-Aldrich. The substrates, high purity copper plate with a thickness of 2 mm (1 × 1.5 cm^2; Rudgwick Metals) were polished with diamond paste of 3 μm. The polished copper plates were cleaned under sonication in an IPA bath for 15 minutes and rinsed with DI water, followed by drying in air.

Hydrothermal method was used to grow ZnO NRs on a copper plate. The synthesis process involves two main steps: seeding and growth processes. The seeding solution was prepared by dissolving 0.219 g of zinc acetate in 10.0 ml of DI water and magnetically stirred for 2 hours to form a 0.10 M seeding solution. The samples were spin coated (speed $\approx$ 300 rpm, time $\approx$ 30 s) with the seeding solution followed by annealing at 250°C for 20 minutes in order to convert the zinc acetate into ZnO seeds. The reaction solution was prepared by dissolving 0.136 g of zinc chloride in 10 ml of DI water to yield a 0.10 M solution. For YZO nanostructures, different concentrations of yttrium nitrate hexahydrate with Y/Zn molar percentages of 0.5, 1.0, 2.0 and 3.0 were prepared. While magnetically stirring, a 0.5 ml of ammonia solution (25%) was added dropwise into the growth solution to increase the solution pH to 10.0. The solution became milky due to the formation of $Zn(OH)_2$ sol-gel. Then, 8 ml of the as-prepared nutrient solution was poured into a 10 ml Teflon vessel with a seeded copper plate immersed into the reaction solution. The sealed hydrothermal vessel was heated in an oven at 95°C for 120 minutes. Subsequently, the vessel was cooled down to room temperature. The as-grown sample was rinsed with DI water three times and dried at room temperature.

7.3.2 Characterisation

The surface morphologies of the samples were studied by SEM (JSM 820M, Jeol). The crystallinity of the nanostructures were analysed by powder XRD (Siemens D500). The average diameters and average film thicknesses were measured from top- and side-view SEM images using Image J (National Institutes of Health, USA). The UV-vis absorption spectra were recorded using UV-vis spectrophotometer (Thermospectronic UV 300). The electrical resistances of the samples were measured

using a four-point probe with probe diameter of 1.80 mm and inter probes gap of 3.40 mm. The actual concentrations of Zn and Y were measured using ICP–MS (Agilent 7500ce).

7.3.3 Gas Ionisation Sensor Measurement

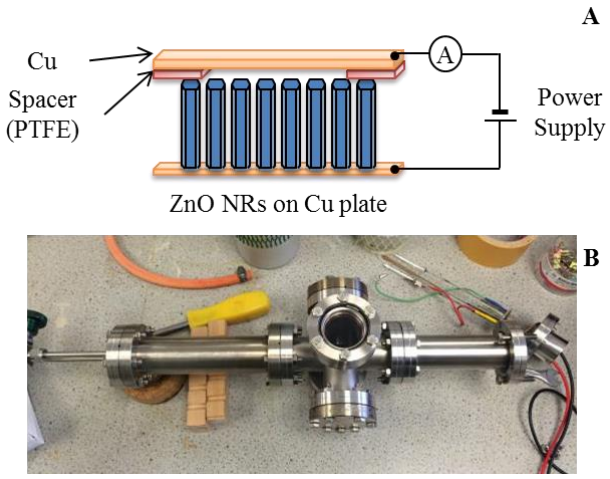

Figure 7.1 (A) A schematic diagram of ZnO NRs based GIS device and (B) the reaction chamber.

Figure 7.1A is a schematic diagram illustrates the construction of ZnO NRs based GIS device. It consists of two electrodes where ZnO NRs were used as the anode and a parallel copper plate as the counter electrode, separated by polytetrafluoroethylene (PTFE) film with the gap distance adjusted in the range from 30 to 200 µm. The GIS device was loaded into a reaction chamber, shown in Figure 7.1B, and a DC voltage was applied in the target gas environment. The applied voltage of the anode can be varied from 0 V to 3 kV (Pharmacia, ECPS 3000/150) and the current is recorded by a multimetre (VC97). The test chamber was evacuated with a rotary pump and the desired gas was introduced through a leak valve with its pressure monitored by a digital Pirani gauge (KJLC, 317 series).

7.4 Results and Discussion

7.4.1 Morphology of Hydrothermal ZnO and YZO Nanostructures

ZnO and YZO NRs were successfully synthesised through hydrothermal method. Figure 7.2 demonstrates the morphology of homogenously aligned array of NRs on the copper substrates. Figure 7.2A represents the SEM image of the typical ZnO NRs, while Figure 7.2B–E show the SEM images of the YZO NRs with Y in the growth solution of 0.5, 1.0, 2.0 and 3.0% respectively. The SEM images reveal that the presence of Y ions in the nutrient solution did not affect the growth direction of the ZnO NRs. However, the morphology of the YZO NRs is slightly different from the ZnO NRs. As increased in the Y/Zn molar ratios, the average diameter of the NRs is decreased, forming needle-like ZnO nanostructures.

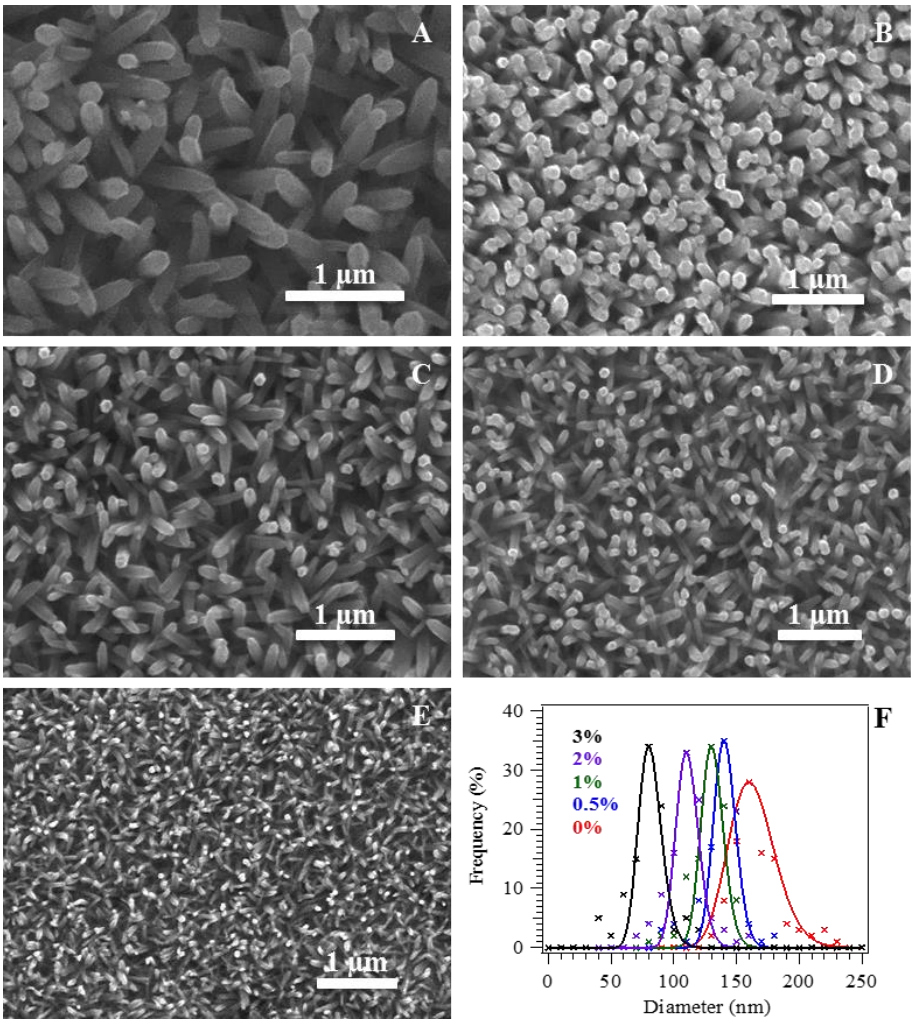

Figure 7.2 Top view SEM images of (A) ZnO NRs and YZO NRs grew for 120 minutes with Y molar percentages of (B) 0.5, (C) 1.0, (D) 2.0 and (E) 3.0 in the growth solutions. (F) Diameter distributions of the NRs.

The average diameters and mean errors of the NRs were evaluated from 100 measurements through their top view SEM images, shown in Figure 7.2F. The average diameters of the ZnO NRs and YZO NRs with Y/Zn molar percentages of 0.5, 1, 2 and 3 were measured to be 158.6, 142.7, 134.6, 115.7 and 86.2 nm with FWHM values of 44, 20, 26, 22 and 23 nm, respectively. These measurements reveal that the Y doping has the inversed effect on the NR diameter, as shown in Figure 7.3F. Although all of the

NRs are monodispersed in their diameters, the diameters of the YZO NRs are narrower distributed than that of the ZnO NRs.

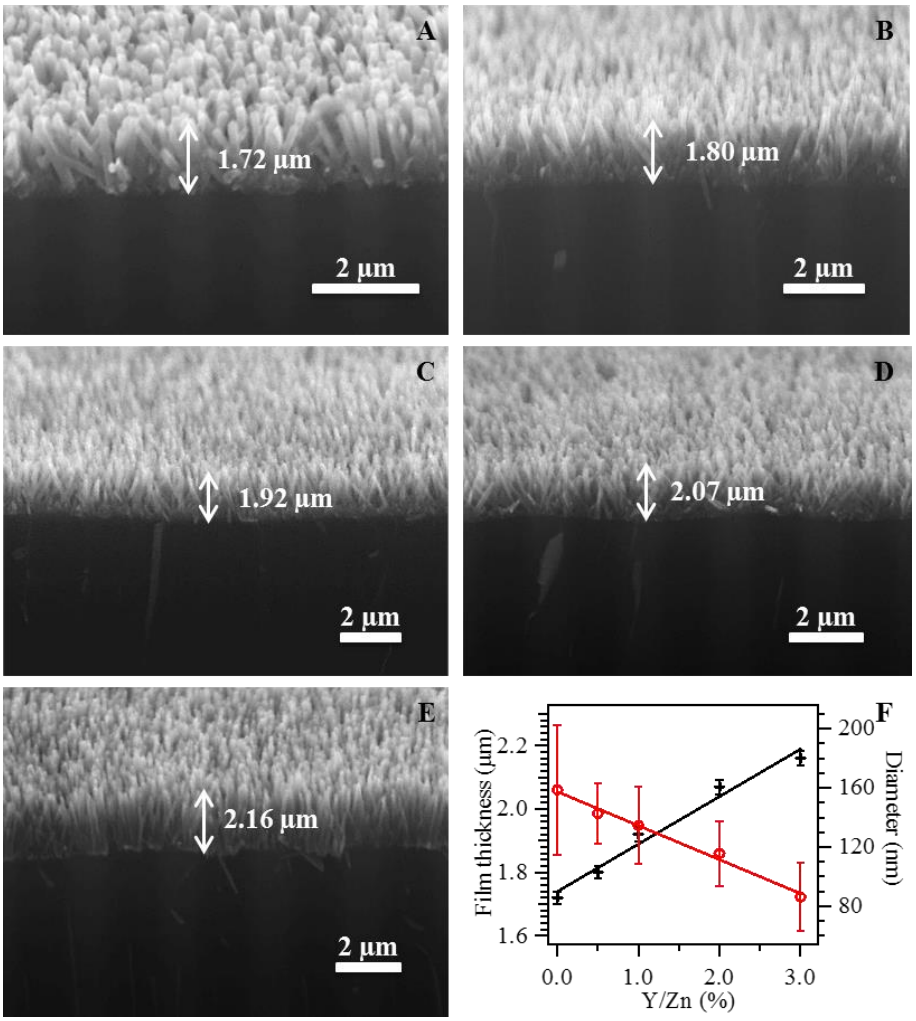

Figure 7.3 Cross-sectional view SEM images of (A) ZnO NRs and YZO NRs grew for 120 minutes with Y molar percentages of (B) 0.5, (C) 1.0, (D) 2.0 and (E) 3.0 in the growth solutions. (F) Plots of film thickness and average diameter as a function of Y/Zn molar percentage.

In addition, the Y doping can also affect the NR's length, shown in Figure 7.3. The cross-sectional view SEM images of the ZnO NRs (Figure 7.3A) and YZO NRs (Figure 7.3B–E) show that as the Y molar percentage in the growth solution increases,

the overall length of the YZO NRs also increases. The average lengths of the ZnO NRs and YZO NRs with Y/Zn molar percentages of 0.5, 1.0, 2.0 and 3.0 were measured to be 1.72, 1.80, 1.92, 2.07 and 2.16 μm, respectively. As shown in Figure 7.3F, the length of the NRs is linearly increased as increases in the Y/Zn molar ratio. In comparison to the ZnO NRs, the length of the 3.0% YZO NRs shows an increase of 25.6%. This revealed that the Y doping had some influence on the length of the NRs. The mechanism of the Y dopant affecting the ZnO morphology will be discussed below.

7.4.2 Effect of Y on the Morphology of ZnO NRs

It is obvious that the morphology of the ZnO NRs is strongly affected by the amount of Y ions in the growth solution. As mentioned in section 5.4.3, different dopants will form different charged complex ions in the nutrient solutions, which will cause a change in the growth direction of the NRs, either along the (002) top face or (100) sidewalls. This is because the ZnO (002) plane is negatively charged and (100) is positively charged.[279]

In our experiment, increasing in the Y/Zn molar ratio, the NRs will be longer with smaller diameters, forming needle-like ZnO nanostructures (Figure 7.2 and Figure 7.3). The aspect ratios (length/outer diameter) of the ZnO NRs and YZO NRs with Y/Zn molar percentages of 0.5, 1.0, 2.0 and 3.0 were determined to be 10.8, 12.6, 14.3, 17.9 and 25.1, respectively. This suggests the Y^{3+} ions will form negatively charged complex ions in the nutrient solutions at pH 11, which encourage the growth along [0001] direction and suppressed the sidewall deposition. As discussed in section 5.4.3, the most common group of metal ions that form negatively charged complex ions in the nutrient solution at pH 11 are the group 13 elements, including aluminium, gallium and indium. Y is technically classified as a transition metal, however it bears some

similarities to the group 13 elements. It has a near identical ionic radius to Holmium (1.015 Å compared to 1.019 Å) which can form 8-coordinate aqueous complex ions.[307] The similarity in the oxidation state and ionic radius make it feasible to suggest Y is also capable of forming 8-coordinate aqueous complex ions in nutrient solution at pH 11, which will form negatively charged complexes by coordination of hydroxide ions, prohibiting the growth along the positively charged (100) plane.

7.4.3 XRD Characterisation of ZnO NRs and YZO NRs

Power XRD was carried out to investigate the crystal structure and crystal orientation of the as grown samples. The XRD patterns of the ZnO NRs and YZO NRs are analysed based on the standard XRD database for wurtzite ZnO (JCPDS # 36-1451) and copper (JCPDS # 04-0836).

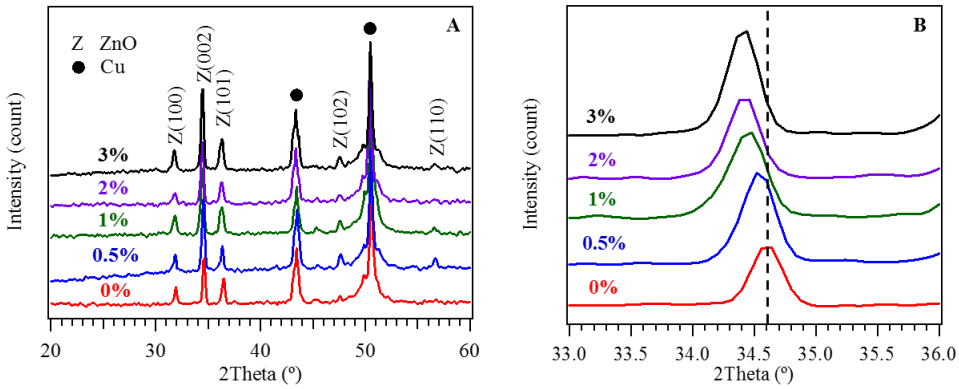

Figure 7.4 XRD patterns of ZnO NRs and YZO NRs with various Y/Zn molar percentages, (A) full spectra and (B) enlarged of (002) peak from 33–36°. The miller indices of crystal planes are labelled where Z and ● are ZnO and copper, respectively.

As shown in Figure 7.4A, the wurtzite ZnO gives the diffraction peaks located at 2θ = 31.89°, 34.60°, 36.39°, 47.68° and 56.74° (Z) corresponding to (100), (002), (101),

(102) and (110) crystal planes. The copper substrate gives the diffraction peaks located at 2θ = 43.51° and 50.63 (●), corresponding to (111) and (200) crystal planes. For the YZO NRs, all the XRD diffraction peaks were indexed to the typical wurtzite hexagonal phase of ZnO where there is no other metal oxides phases or additional peaks are observed. This suggests that the Y^{3+} ions were either very low concentration or homogeneously distributed in the ZnO crystal.

Figure 7.4A demonstrates that the ZnO NRs and YZO NRs are having the strong characteristic peak for the (002) plane. This suggests that the c-axis of the NRs is perpendicular to the substrate, typical for ZnO NRs. In addition, the (002) diffraction peak positions of the YZO NRs are systematically shifted towards the smaller angles, shown in Figure 7.4B. Compared with pristine ZnO (34.60°), the (002) peaks of the YZO NRs are shifted down by 0.05–0.16° when the Y/Zn molar percentage in the growth solution is increased from 0.5 to 3.0. Such shift indicates there is a systematic increase in the ZnO lattice parameters. The c-lattice parameters (Equation 2.2, Section 2.3) of ZnO NRs and YZO NRs were calculated, shown in Figure 7.5. The results demonstrate that the c-lattice constants of the samples are increased from 5.182 Å to 5.205 Å as increases the Y/Zn molar ratio. This can be attributed to the zinc sites are being substituted by Y^{3+} ions, whereby the incorporation of the Y^{3+} sites generates strain, as well as alter the ZnO lattice.[79] The expansion of the unit cell was due to the ionic radius of Y^{3+} is much larger than that of Zn^{2+} ions. According to Shannon R.D., the ionic radii of Y^{3+} and Zn^{2+} ions are 1.015 Å and 0.74 Å, respectively.[283] Thus, the variation of the c-lattice constants further confirm that Y^{3+} ions were successfully replaced in the Zn^{2+} lattice sites.

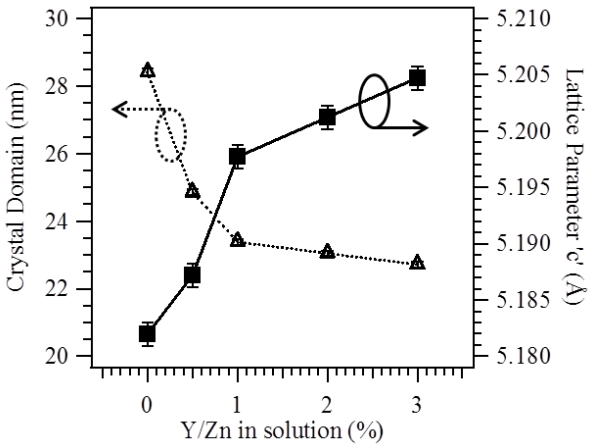

Figure 7.5 Crystal domain and c-lattice parameter as a function of Y/Zn molar percentage.

It is worth noting that the (002) diffraction peaks of the YZO NRs are broader than that of the ZnO NRs. Larger line width is the result of a smaller crystal domain size. The calculated crystal domain size (Equation 2.5, Section 2.3) of the ZnO NRs and YZO NRs as a function of Y concentration is presented in Figure 7.5. The crystal sizes of the ZnO NRs and YZO NRs with Y/Zn molar percentages of 0.5, 1.0, 2.0 and 3.0 were calculated to be 28.4, 24.8, 23.4, 23.0 and 22.7 nm, respectively. Thus, the higher the Y doping concentration, the smaller the crystal domain. This is consistent with the substitution doping of the Y in ZnO which causes the deterioration of the ZnO lattice.

In order to determine the actual dopant concentration, ICP–MS was used to measure the Y in the films after dissolving the as-grown YZO samples in 2 ml of 1.50% nitric acid and diluted to 50 ml by DI water. The obtained Y/Zn molar percentages are presented in Table 7.1. The measurements show that the concentration of the Y^{3+} ion in the YZO NRs samples is increased as the Y solution concentration is increased, although the actual Y/Zn molar percentages in the films were much lower than the initial molar ratios in the growth solution. The atom efficiency of the samples was calculated, as shown in Table 7.1. The calculations reveal that the atom efficiency is

decreased when the concentration of Y in the nutrient solution is increased. Such behaviour is similar to the previous finding for doping of manganese and aluminium.[308, 309]

Table 7.1 Actual Y/Zn molar percentages in the as-prepared films.

NRs Samples	Y/Zn molar percentage (at%)		Atom efficiency (%)
	Solution	Film	
0.5% YZO	0.5	0.05±0.005	10.0
1.0%YZO	1.0	0.10±0.012	10.0
2.0% YZO	2.0	0.13±0.017	6.5
3.0% YZO	3.0	0.17±0.023	5.7

The low dopant concentrations can be reasoned by a few factors, such as the difference in valence charge between the Y^{3+} and Zn^{2+}, difference in ion radius and also different crystal types of ZnO (tetrahedral coordinated) and Y_2O_3 (octahedral coordinated), resulting in the mismatch of the lattice constant. In addition, the bond energy of Y–O (4.94 eV)[310] is much higher than that of the Zn–O (1.67 eV)[311], so more energy will be required in order to allow the Y^{3+} ion to incorporate into the ZnO lattice to form Y–O bond.[308] Therefore, the number of Y^{3+} ions that replace the zinc sites is very low since more energy is required in the substituted samples to form the Zn–O–Y structure.

7.4.4 Optical Properties of ZnO NRs and YZO NRs

The effect of Y doping on the optical properties of the ZnO NRs was investigated using UV-vis spectrophotometer, in order to establish how the defects and dopants could affect the electronic structures of the ZnO nanomaterials. In these cases, samples were prepared on glass substrates.

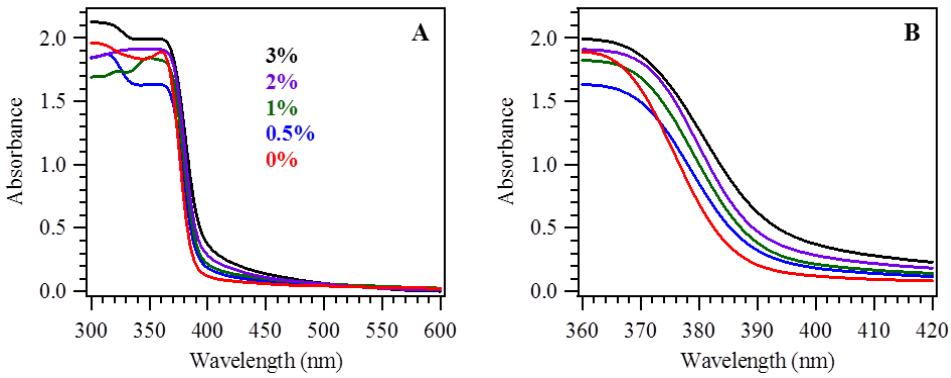

Figure 7.6 Absorption spectra of ZnO NRs and YZO NRs with various Y/Zn molar percentages, (A) full spectra and (B) enlarged region from 360–420 nm.

The absorption of the samples were recorded at room temperature from 300 nm to 600 nm wavelength, shown in Figure 7.6A. The UV-vis absorptions cut off were observed at 388, 393, 394, 395 and 398 nm for ZnO NRs and YZO NRs with Y/Zn molar percentages of 0.5, 1.0, 2.0 and 3.0, respectively. The absorption edges of the YZO NRs show a red shift up to 2.6% when compared to the ZnO NRs, suggesting the decreasing in the optical band gaps. The band gap energies of the samples were estimated using Tauc relation (Equation 2.11, Section 2.4), as presented in Figure 7.7A and 7.7B.

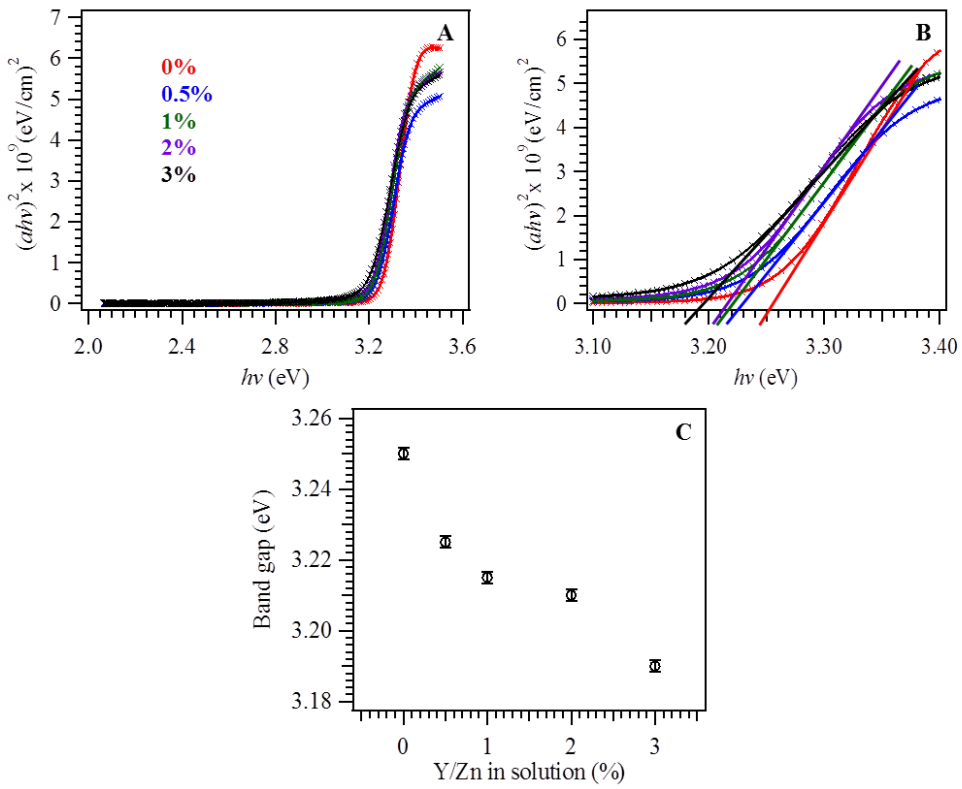

Figure 7.7 Tauc plots of ZnO NRs and YZO NRs with various Y/Zn molar ratios, (A) full spectra, (B) enlarged region between 3.1 to 3.4 eV and (C) plot of band gap as a function of Y/Zn molar percentage.

Figure 7.7A displays the plots of $(\alpha hv)^2$ vs hv for the ZnO NRs and YZO NRs with various Y/Zn molar percentages. The optical band gaps of the samples were obtained from the intercept of the *x*-axis of the extrapolated linear line (αhv = 0), as shown in Figure 7.7B. The band gap energies of the ZnO NRs and YZO NRs with Y/Zn molar percentages of 0.5, 1.0, 2.0 and 3.0 were estimated to be 3.25, 3.23, 3.22, 3.21 and 3.19 eV, respectively. It is clear that the optical band gaps of the samples were decreased with increasing in the doping level (Figure 7.7C). Yogamalar R. *et al.* have reported the similar band gaps narrowing observation for the Y-doped ZnO nanostructures.[312]

The band gaps narrowing for the YZO NRs can be attributed to the different phenomena, for instance, the merging of the donor states and conduction band by the presence of impurities.[313] The Y^{3+} ions incorporated in the ZnO will require the incorporating of Zn^{2+} vacancies and act as donor where the donor energy level is positioned close to the conduction band of ZnO. Since the ionic radius of Y^{3+} is bigger than that of Zn^{2+}, the donor wave functions of the Y electrons start to overlap with the neighbourhood. As increased in the Y dopant concentration, the electron density overlap will increase. This will cause the split in the donor energy level and broaden into an impurity band.[312] The broadening of the donor energy level will result in the merging of the donor and conduction band, which cause the Fermi energy level of ZnO to shift into the conduction band. Therefore, the optical energy band gap and more important, the electrical resistivity of the material is reduced.

7.4.5 Electrical Properties of ZnO and YZO NRs

The electrical resistances of the ZnO NRs and YZO NRs were investigated by a four-point probe measurement. Since the outer diameter of the probe (1.80 mm) is much larger than the average diameter of the as-grown ZnO NRs (< 160 nm), therefore the thin film could be considered as a continuous substrate. The electrical resistivity and conductivity of the sample can be calculated using equations 7.1 and 7.2:[314]

$$\rho = R \times t \qquad \text{(Equation 7.1)}$$

$$\sigma = {}^{1}/_{\rho} \qquad \text{(Equation 7.2)}$$

where ρ is the electrical resistivity (Ω cm), R is the sheet resistance (Ω), t is the film thickness (cm) and σ is the conductivity (S cm^{-1}).

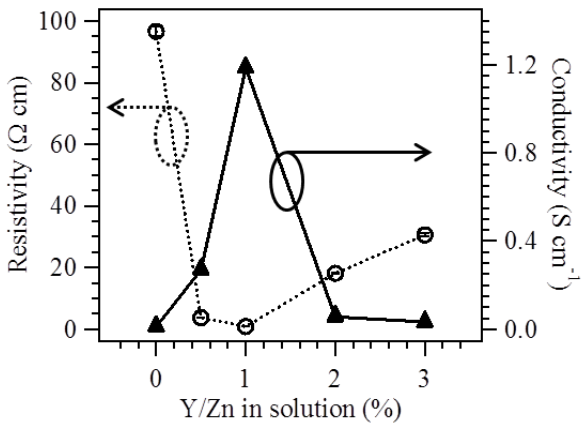

Figure 7.8 Electrical resistivity and conductivity as a function of Y/Zn molar percentage.

Figure 7.8 displays the plots of electrical resistivity and conductivity of ZnO NRs and YZO NRs with various Y/Zn molar ratios. By introducing Y atom into the ZnO lattice, the electrical resistivity of the sample will be reduced significantly. As shown in Figure 7.8, the electrical resistivity of the samples was first decreased with increasing in the Y/Zn molar ratio. A minimum electrical resistivity of 0.84 Ω cm was obtained for the 1% YZO NRs, and this corresponds to electrical conductivity of 1.19 S cm^{-1}. However, as the Y/Zn molar ratio is above 1%, the electrical resistivity of the samples started to increase. This suggests that the amount of Y in the ZnO need to be deliberately optimised in order to get highly conducting YZO NRs.

The decrease of the conductivity as the Y doping content exceed 1% Y/Zn molar ratio suggests that not all the Y atoms in the ZnO film are contributed to the donor dopants.[274] When a small amount of Y dopant is introduced into ZnO lattice, they are mostly replaced the existing Zn^{2+} at the lattice sites as donors. However, when the concentration of the Y dopant is increased, additional Y atoms will present at the interstitial sites instead of substituting in the ZnO lattice as donors. Excess of the Y atoms in the films may cause the grain boundary segregation with reduced crystal

domain size, which will act as donor passivation to decrease the electron concentration.[315] Thus, the electrical conductivity of the sample is reduced.

7.5 Gas Ionisation Sensors

After the characterisation, ZnO NRs and YZO NRs samples were applied as anodes for application in GIS. Bare copper plate and ZnO NRs were first tested in air, as shown in Figure 7.9, at atmospheric pressure with an electrode gap of 80 µm.

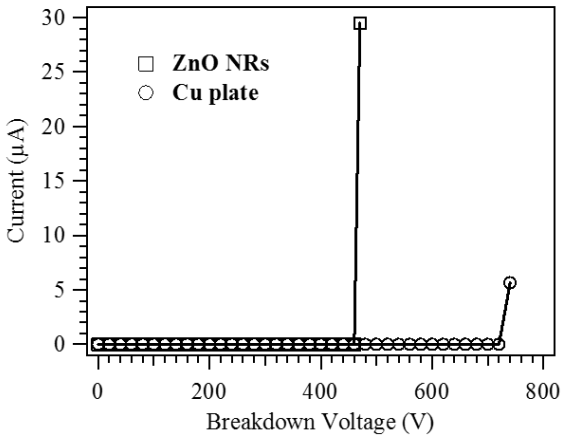

Figure 7.9 *I–V* curves for electrical breakdown of ZnO NRs and copper plate based GISs.

For ZnO NRs based GIS, the breakdown voltage of air was at 470 V with a continuous current discharge of 29.5 µA was generated. The same test was carried out by replacing the ZnO NRs anode to copper plate. A much higher breakdown voltage of air was required for the copper plate, which is 740 V, with a much smaller discharge current of 6.1 µA. This shows that by using ZnO NRs as the anode material will massively reduce the breakdown voltage of air as compared to the copper plate. The NR morphology is helping to focus the electrical field and leading to a lower discharge barrier.

Before comparison of the YZO NRs based GISs against the ZnO NRs based GIS, various parameters relating to the experiment needed to be investigated for their effects on the breakdown voltage and discharge current. These included the gap between two electrodes and the gas pressure. All optimisations were carried out using ZnO NRs and air was used as the target gas.

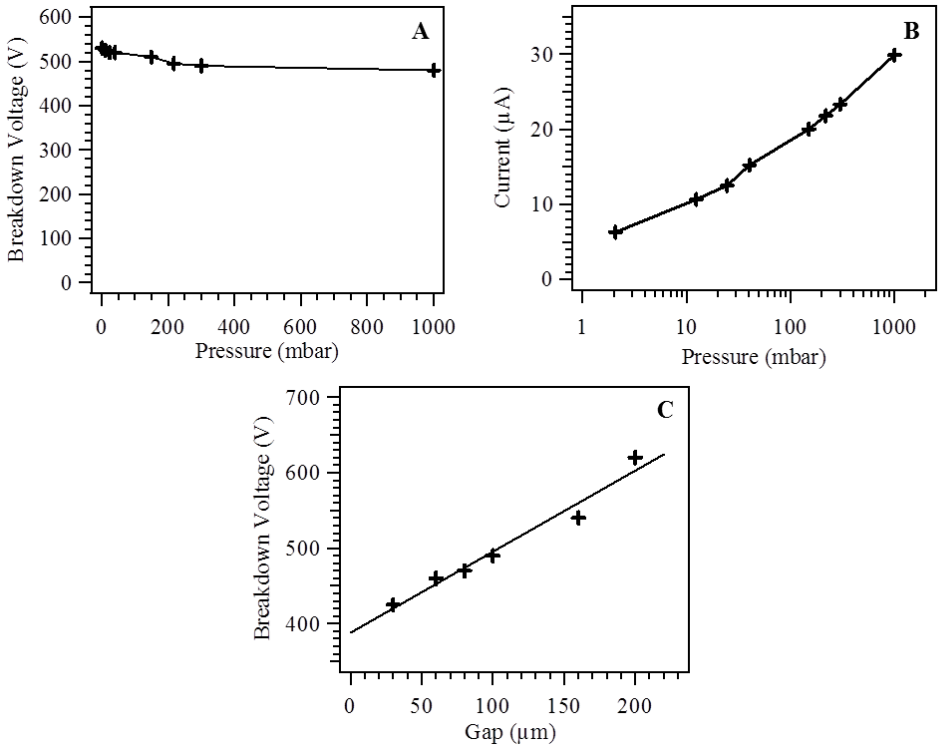

Figure 7.10 Plots of (A) breakdown voltage and (B) discharge current as a function of gas pressure of ZnO based GIS with a fixed electrode separation of 80 µm. (C) Plot of breakdown voltage as a function of electrode gap of ZnO based GIS at 1000 mbar.

Figure 7.10A shows the relationship between the air pressure and the breakdown voltage from a ZnO NRs based GIS with a fixed electrode separation of 80 µm. As the gas pressure decreased from 1000 mbar to 2 mbar, the breakdown voltage of air was increased from 480 V to 530 V. This is because the electrical breakdown is dominated

by the highly focused electric field near the tips of NRs. The same observation has also been discussed for the GIS using ZnO NWs and palladium NP-capped ZnO NRs.[69, 70]

The correlation between the discharge current at breakdown voltage and gas pressure was also investigated, as presented in Figure 7.10B. The discharge current varies logarithmically with respect to the gas pressure, ranging from 1000 mbar downwards to 2 mbar. This relationship suggests that the discharge current at breakdown voltage is proportional to the quantity of gas molecules per unit volume that may contribute to the conduction between the gaps. Therefore, this highlights the possibility of using the discharge current to quantify the gas pressure of the species being detected in future.

Figure 7.10C demonstrates the effect of the inter-electrode spacing as a function of the breakdown voltage at 1000 mbar. The breakdown voltage of air was found to increase when the gap between the electrodes is increased, following a linear relationship. For instance, at an electrode separation of 160 μm, the breakdown voltage of air is 540 V, which decreases to 460 V when the inter-electrode spacing is reduced to 60 μm. This linear relationship can be attributed to the requirement of increasing the voltage to maintain the electric field strength within the gap. However, there are some stability issues for very the small electrode gaps, ranging from 30–60 μm. Short circuit would destroy the response for gas sensing. Therefore, an electrode separation of 80 μm was chosen with the best trade-off between device stability and reasonably low breakdown voltage.

Using the optimal gap distance of 80 μm, ZnO NRs and YZO NRs with various Y/Zn molar percentages were used to sense several gas species, including air, O_2, N_2, CO_2, CH_4 and Ar at a fixed standard atmospheric gas pressure (1000 mbar).

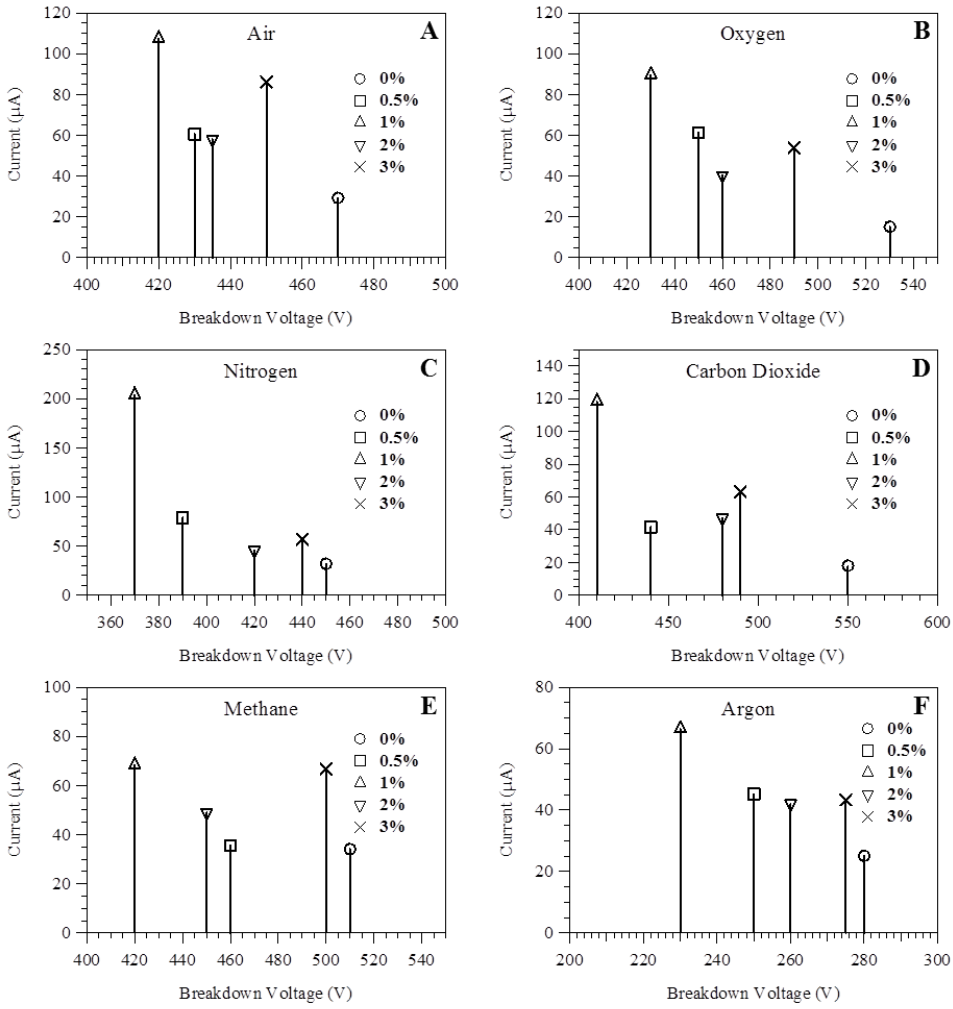

Figure 7.11 *I–V* curves for electrical breakdown of ZnO NRs and YZO NRs with various Y/Zn molar percentages based GISs for (A) air, (B) O_2 (C) N_2, (D) CO_2, (E) CH_4 and (F) Ar.

Figure 7.11A–F demonstrate the *I–V* curves for electrical breakdown of ZnO NRs and YZO NRs based GISs at different gas species environments. It is noticeable that each gases exhibits a distinct breakdown voltage. With undoped ZnO NRs, the breakdown voltages were found to be 282, 450, 470, 511, 529 and 550 V for Ar, N_2, air, CH_4, O_2 and CO_2, respectively. The different of breakdown voltage provides a "fingerprint" property and this reveals the potential for gas identification within a gas mixture. It is clear that, in comparison to ZnO NRs based GIS, YZO NRs based GISs

require a much smaller breakdown voltage for all the target gas species. For instance, the breakdown voltages of N_2 for ZnO NRs and YZO NRs with 0.5, 1.0, 2.0 and 3.0 of Y/Zn molar percentages based GISs were measured to be 450, 390, 370, 420 and 440 V, respectively. It is important to note that the 1% YZO NRs based GIS shows the lowest breakdown voltage for all the gas species. The reduction of the breakdown voltage for YZO NRs based GISs can be attributed to the increase in the conductivity of the NRs.

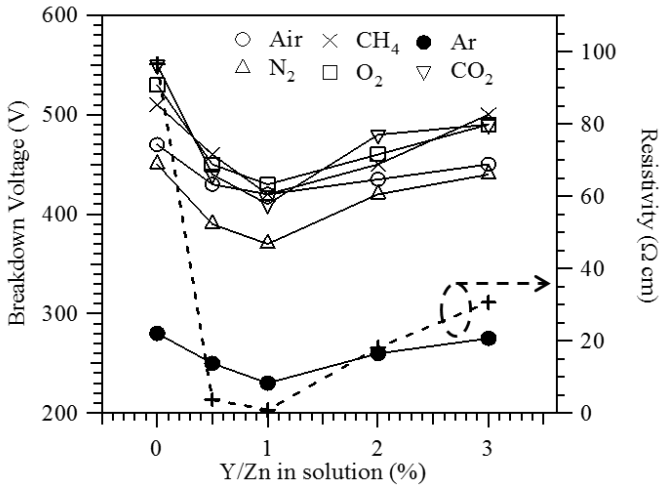

Figure 7.12 Plots of breakdown voltage of different gas species and resistivity as a function of Y/Zn molar percentage.

From Figure 7.12, the correlation between the resistivity of the NRs and the breakdown voltages for different gases can be clearly identified. A similar relationship was observed between the resistivity of the NRs and the breakdown voltage of gases. The breakdown voltages of the gases were reduced at first when the resistivity of the NRs is decreased and reaching minima at YZO NRs with 1% Y/Zn molar ratio. However, further increased the Y/Zn molar ratio above 1% will lead to an increase of the breakdown voltage since the resistivity of the NRs is increased.

As mentioned in section 7.4.4, the Fermi level of ZnO is shifted closer to the conduction band after the introduction of Y atom. This will lead to an increase in the electron density, which will increase the conductivity of the NR with a reduced potential gradient across the NR. Therefore, a smaller voltage will be required in order to ionise the gas moving between the tip of the NR and counter electrode (copper plate).

In addition, the discharge current generated from all the YZO NRs based GISs are much higher than that of the ZnO NRs based GIS. As shown in Figure 7.11D, the discharge currents produced by ZnO NRs and YZO NRs with 0.5, 1.0, 2.0 and 3.0 of Y/Zn molar percentages in CO_2 environment were 18.1, 41.7, 118.3, 47.1 and 63.3 µA, respectively. Compared to ZnO NRs based GIS, the 1% YZO NRs based GIS demonstrates a 6.5–fold increase in the discharge current density. This increment indicates a significant improvement in the sensitivity and such improvement could also be related to the change of conductivity.

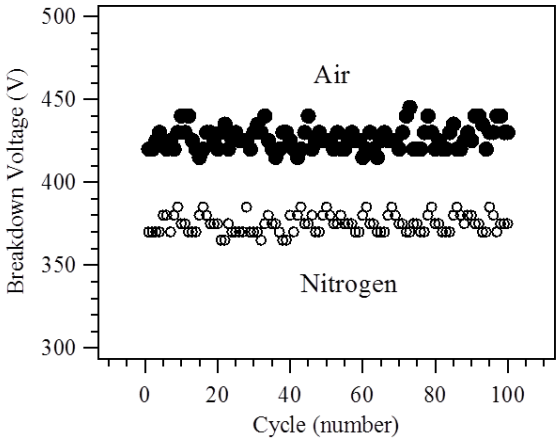

Figure 7.13 The stability test of 1% YZO NRs based GIS in air and N_2 environments.

The stability of the 1% YZO NRs based GIS was tested in air and N_2 ambients. Figure 7.13 shows the breakdown phenomena were generated continuously 100 cycles in air and N_2 at 1000 mbar. The duration of each cycle is 2 minutes. It is noticeable that

the breakdown voltage only fluctuates less than 5%. The obtained results reveal a better stability as compared to that of CNTs based GISs.[69] The low breakdown voltage with high sensitivity and high stability indicate that YZO NRs could be a better candidate as field ionisation gas sensor.

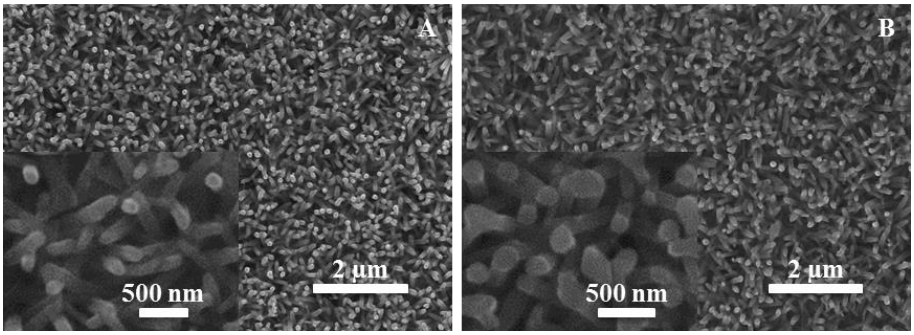

Figure 7.14 Top view SEM images of 1% YZO NRs (A) before and (B) after 100 cycles of continuous breakdown in N_2 environment. The inset is the corresponding higher resolution of SEM image.

The morphology of the YZO NRs after 100 cycles of continuous breakdown in N_2 environment was characterised by SEM, as displayed in Figure 7.14. It appears that most the NRs remain unchanged after 100 cycles of measurement as compared to the unused one (Figure 7.14A). However, some of the NR tips are flattened after the continuous breakdown, shown in the inset of Figure 7.14B. This can be attributed to the damage caused by plasma discharge during the ionisation process. Nevertheless, in comparison to CNTs based GISs,[69] the YZO NRs based GISs still offer a much higher stability in ionisation gas sensing applications.

7.6 Effect of UV illumination on GIS Performance

The conductivity of the metal oxide nanostructures can also be manipulated by photoexcitation by directly pumping electrons to the conduction band. Using UV excitation could also add extra energy to the electrons on the surface of the metal oxide by several electron volts (~3 eV). More important, a monochromated UV light could also selectively excite the electronic state of specific gas molecules, and the sensitivity towards that molecule could be expected to be enhanced against the others, resulting improved selectivity. For a classic metal oxide based resistance gas sensor, the enhanced performance with UV light has been demonstrated, although the mechanism is somehow different to the effects of UV light on GIS. Here, the effect of UV illumination on the GIS performance was investigated using the 1% YZO NRs, with a FTO glass used as the counter electrode to facilitate the light illumination. A 3W UV LED light source with a wavelength of 365 nm was used since the optical band gaps of the 1% YZO NRs was about 394 nm (3.1 eV), as demonstrated in section 7.4.4.

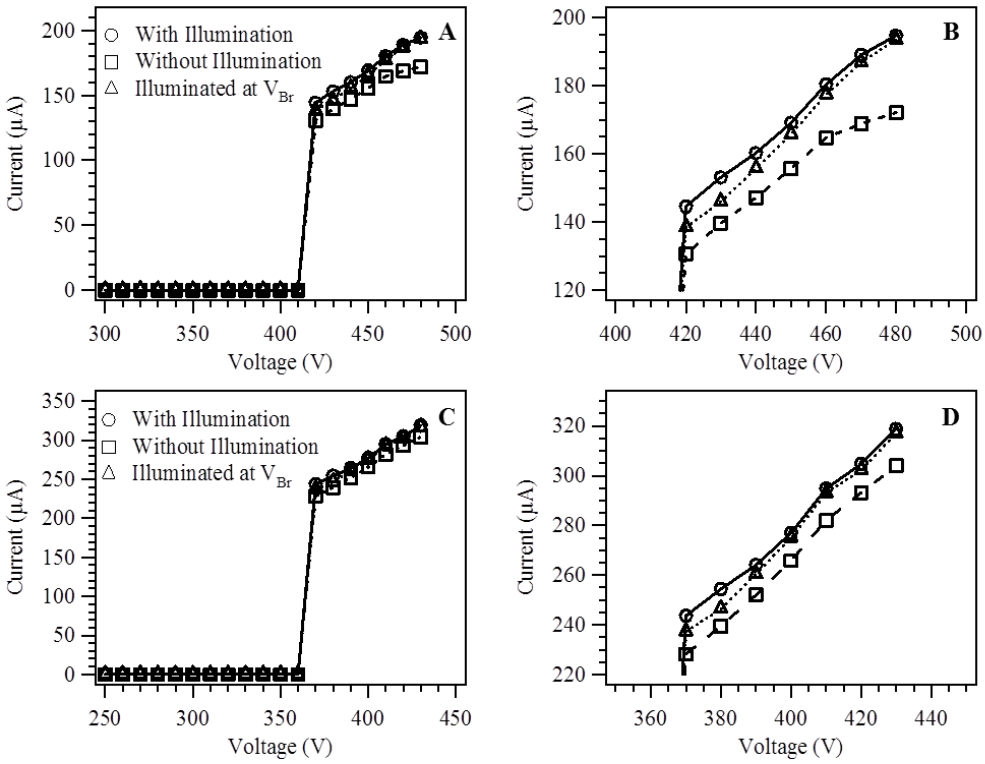

Figure 7.15 *I–V* curves for electrical breakdown of 1% YZO NRs based GIS in air (A,B) and N_2 (C,D) with, without UV illumination (365 nm) and UV illuminated at breakdown voltage.

Figure 7.15A and 7.15C are the *I–V* curves for the electrical breakdown of 1% YZO NRs based GIS in air and N_2 with and without UV illumination, as well as that illuminated at breakdown voltage. It is noticeable that the breakdown voltage of air and N_2 is not affected by the UV illumination. However, the discharge currents from air and N_2 were increased with the UV illumination. Figure 7.15B and 7.15D show the magnified *I–V* plots. Under the UV illumination, the discharge current generated in air was 144.6 μA, in comparison to 130.7 μA without UV light. This corresponds to an enhancement of ~10.6% in the discharge current, suggesting that the sensitivity of the gas sensor is improved upon UV illumination. In the N_2 gas, the discharge current was also increased from 228.2 μA to 242.2 μA under UV illumination. We propose that

under UV light, the excited electron-hole pairs were generated in the conduction and valence bands of ZnO, which further increase the electrical conductivity of the NRs. Thus, the effective electrical field between the tip of NRs and the counter electrode is enhanced, which in turn increases the discharge current density.

If the GIS is illuminated with bias from the breakdown voltage, the continuous discharge current generated was also higher than that unilluminated. However, in comparison with the continuous illumination from 0 V bias, the discharge currents were slightly lower. This could be attributed to the presence of a layer of chemisorbed oxygen species on the surface of NRs under dark, which reduces the conductance of ZnO.[168, 316] When the NRs are exposed to UV light, the adsorbed oxygen can be desorbed from the surface of the ZnO, which increases the surface conductivity of the NRs and thus increase the sensitivity of the gas sensor.

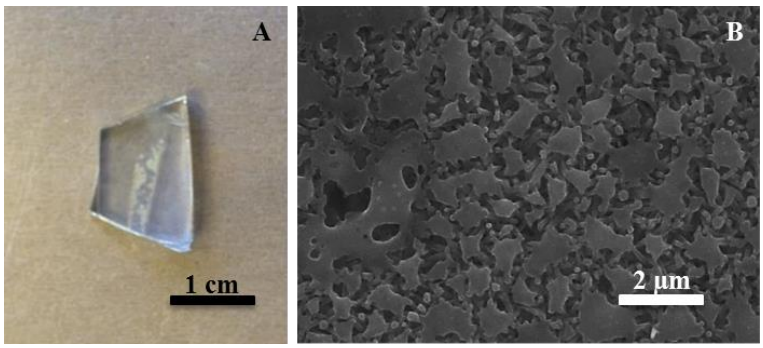

Figure 7.16 (A) Photograph of the FTO glass which acted as counter electrode and (B) top view SEM image of 1% YZO NRs based GIS after UV exposure of 20 minutes.

There were, however, some drawbacks to this UV light enhanced gas sensor application. After exposing the GIS device to UV light for 20 minutes, the conductive layer of FTO was etched off from the glass substrate by the plasma discharge, as shown in Figure 7.16A. Although the melting point of ZnO is very high, which is 1975°C,

most of the NRs were also melted or deteriorated after 20 minutes of UV light exposure during the gas ionisation measurement, as shown in Figure 7.16B. This may be due to a large amount of photoexcited electrons were generated under the UV illumination which caused the formation of defects and deformation of the ZnO structure. Furthermore, at the breakdown voltage, the immediate generation of a large discharge current density with the presence of UV illumination produces very high temperature on a focused area of the sample will also deteriorate the ZnO NRs.

7.7 Conclusions

We have demonstrated, for the first time, facile synthesis of vertically aligned crystalline YZO NR arrays by hydrothermal method. The surface morphology of the NRs was strongly affected by the Y/Zn molar ratio, where increased in the Y/Zn molar ratio lead to the formation of high aspect ratio ZnO NRs. The introduction of Y atoms into ZnO lattice caused the change in both the optical and electrical properties of the NRs. The GIS measurements revealed that the 1% YZO NRs based GIS had the highest sensitivity towards all the gas species with a smaller breakdown voltage was required. The possible reasons for the higher sensitivity and lower breakdown voltage were also discussed. The sensitivity of the GIS was further improved by UV illumination onto the GIS device during the GIS measurements.

Chapter 8 Efficient Solar Water Splitting by Highly Ordered 1D $BiVO_4$/ZnO Nanorods Heterojunction Film

8.1 Abstract

A novel material, highly ordered 1D $BiVO_4$/ZnO heterojunction film was successfully created through the combination of hydrothermal and metal organic decomposition (MOD)/spin coating methods. The correlation between the duration of reaction and the morphology of ZnO NRs was examined. The results revealed that 6 hours was the optimal growth duration for ZnO NRs. The top view SEM image of $BiVO_4$ demonstrated that the film was made of worm-like nanosized particles which were well-interconnected, forming a 3D porous material. The effect of the number of coats of $BiVO_4$ on ZnO NRs with respect to the PEC water splitting performance was investigated. A maximum conversion efficiency was achieved for that with 6 coats of $BiVO_4$ on top of ZnO NRs (0.22%). Compared with bare ZnO NRs (0.045%) and $BiVO_4$ (0.082%) photoanodes, the 1D $BiVO_4$/ZnO (0.22%) photoanode had revealed an increased photoconversion efficiency in water oxidation by a factor of five and three, respectively.

8.2 Introduction

The development of solar water splitting devices has created tremendous interest because it provides an attractive route to convert sunlight into chemical fuel in the form of hydrogen. The solar energy spectrum is composed of 44–47% visible light and 3–5% UV light.[317] Therefore, there have been intense research into the development of visible-light-responding photocatalysts for solar energy conversion. There are a number of

visible light photocatalysts, such as CdS[318, 319] and CdSe,[320] have attracted intensive attention as photoanode for photoelectrolysis of water, however these catalysts are chemically unstable upon illumination.[321] In addition, simple metal oxides, for instance WO_3[322] and Fe_2O_3,[267] are the popular photocatalytic materials because of their visible light activity, stability in aqueous electrolyte and low cost.[322, 323] Nevertheless, these metal oxides exhibit low photocatalytic activity in PEC water splitting. This is because the conduction band position of WO_3 is lower than the reduction potential of water[324] and hole diffusion length of Fe_2O_3 is very short (2–4 nm)[325] with high possibility of charge recombination.

Recently, n-type monoclinic $BiVO_4$ has emerged as a promising photocatalyst for water oxidation owing to its narrow band gap energy (~2.4 eV), which allow it absorbs a substantial portion of visible light.[326] Furthermore, the valence band of $BiVO_4$ is sufficiently positive for the water oxidation and its conduction band edge is very near the thermodynamic hydrogen evolution potential.[10, 121, 327] Although the theoretical conversion efficiency of monoclinic $BiVO_4$ was estimated to be 9.1%,[328] $BiVO_4$ photoanodes have exhibited low photon conversion efficiencies.[130] There are several reasons for this problem, including significant recombination of photogenerated electron-hole pairs, poor electron mobility and slow hole transfer kinetics for water oxidation.[121]

A number of available methods have been proposed to overcome these drawbacks. One of the approaches to improve the conversion efficiency of $BiVO_4$ is through the formation of heterojunction structure such as $BiVO_4/CuWO_4$[329] and $WO_3/BiVO_4$[326] to suppress the electron-hole recombination. However, WO_3 has the similar issue of poor electron mobility which limits the migration of photogenerated electrons to counter electrode and affects the hole transfer kinetics in $BiVO_4$.[324] The

introduction of oxygen evolving catalysts such as cobalt phosphate (Co–Pi)[265, 330, 331] and iron oxyhydroxide (FeOOH)[10, 129] on the surface of $BiVO_4$ is another way to enhance the conversion efficiency by reducing the recombination of electrons and holes. Unfortunately, the intrinsic problems of poor electron mobility and conductivity in $BiVO_4$ still remain.[332, 333]

In order to solve these problems, we use 1D ZnO NRs as the platform offering a nano-morphology owing to its extremely high electron mobility.[334] This will facilitate the charge injection and transportation. Coupling the $BiVO_4$ with wide band gap ZnO NRs will generate a heterojunction due to the difference in their Fermi levels, which will increase the charge separation and reduce the electron-hole recombination. The synergy of the narrow band gap material ($BiVO_4$) with a wide band gap material (ZnO) will also extend the spectrum range of the light absorption and thus increased the photoactivity of PEC water splitting under solar excitation. In the present work, we demonstrate the creation of highly ordered 1D $BiVO_4$/ZnO heterojunction film through the combination of hydrothermal and MOD/spin coating methods. The optical properties of ZnO NRs, $BiVO_4$ film and $BiVO_4$/ZnO film were also studied. The PEC measurements reveal that the heterojunction of $BiVO_4$/ZnO show a significant enhancement in the photocatalytic activity and stability relative to the bare ZnO NRs and $BiVO_4$ film in PEC water oxidation.

8.3 Experimental Details

8.3.1 Preparation for Growing ZnO NRs

All the chemicals used were analytical grade and purchased from Sigma-Aldrich. The substrates, FTO glasses (1×1.5 cm^2) were cleaned under sonication in an IPA bath for 15 minutes and rinsed with DI water, followed by dried in air.

Hydrothermal method was used to grow ZnO NRs on FTO glass. The synthesis process involves two main steps which are seeding and growth processes. The seeding solution was prepared by dissolving 0.219 g of zinc acetate in 10.0 ml of DI water and magnetically stirred for 2 hours to form a 0.10 M seeding solution. The seeded samples were then annealed at 350°C for 30 minutes to convert zinc acetate into ZnO seeds. The reaction solution was prepared by dissolving 0.136 g of $ZnCl_2$ in 10 ml of DI water to yield a 0.10 M solution. 0.5 ml of ammonia (25%) solution was added dropwise into the growth solution while stirring. Then, 8 ml of the as-prepared nutrient solution was poured into a 10 ml Teflon vessel with a seeded FTO glass was immersed into the reaction solution and sealed. The hydrothermal vessel was heated in an oven at 95°C for 3–7 hours. Subsequently, the vessel was cooled down to room temperature and the as-grown sample was rinsed three times with DI water, dried at room temperature.

8.3.2 Preparation of $BiVO_4$ Films

$BiVO_4$ films were fabricated using the published MOD/spin coating procedures.[125, 327] The solutions of vanadyl acetylacetonate [$VO(acac)_2$] and bismuth nitrate pentahydrate [$Bi(NO_3)_3 \cdot 5H_2O$] were prepared by dissolving 398 mg of $VO(acac)_2$ in 50 ml of acetylacetone and 728 mg of $Bi(NO_3)_3 \cdot 5H_2O$ in 7.5 ml of acetylacetone. These solutions were mixed ultrasonically in stoichiometric amounts for 30 minutes to yield a green precursor solution. The resulting precursor solution was spin cast ($\text{speed} \approx 1000$ rpm, $\text{time} \approx 10$ s) onto FTO glass or as-grown ZnO NRs, where 20 µL cm^{-2} of precursor was used for a single layer coating. After each coating cycle, the sample was annealed to 500°C for 10 minutes. The spin coating and calcination steps were repeated for several cycles in order to obtain a thick crystalline $BiVO_4$ film. After the last coating cycle, the sample was calcined at 500°C for 2 hours.

8.3.3 Characterisation

SEM (JSM 820M, Jeol) was used to examine the surface morphologies of the samples. The average diameters and average film thicknesses were measured from top- and side-view SEM images using Image J (National Institutes of Health, USA). Power XRD (Siemens D500) was carried out to analyse the crystallinity and structure orientation of the nanostructures. UV-vis spectrophotometer (Thermospectronic UV 300) was used to record the optical absorption of the samples. The PEC water splitting was measured using a standard three-electrode configuration in a 0.5 M Na_2SO_4 electrolyte (pH 6.8). A platinum foil was used as counter electrode and a KCl saturated Ag/AgCl electrode was used as a reference. A USB potentiostat (eDAQ) was used to control and record the photocurrent as a function of electrochemical potential. Sunlight was simulated with a 300W xenon arc lamp with an AM1.5 G filter and the output light power density was adjusted to 100 mW cm^{-2}. EIS (Palmsens 3.0) measurements were carried out in 0.5 M Na_2SO_4 solution (pH 6.8) and the amplitude of the sinusoidal wave was set at 10 mV and frequency varied from 10 kHz to 100 mHz.

8.4 Results and Discussion

8.4.1 Morphology of ZnO NRs

Crystallised ZnO NRs were successfully synthesised through hydrothermal method, as shown in Figure 8.1. The NRs were homogenously aligned array on the FTO substrate. The high magnification SEM image (Figure 8.1B) reveals that all the NRs have the typical hexagonal cross section. After 6 hours of growth, the length of the NRs was measured to be 2.6 μm, as presented in the cross-sectional view SEM image in Figure 8.1C. The average diameter and mean error of the NRs were evaluated from 100 measurements through their top view SEM images. The measurement shows that the

NRs are monodispersed in their diameters with an average diameter of 152.4 nm and a FWHM value of 32 nm, as demonstrated in Figure 8.1D.

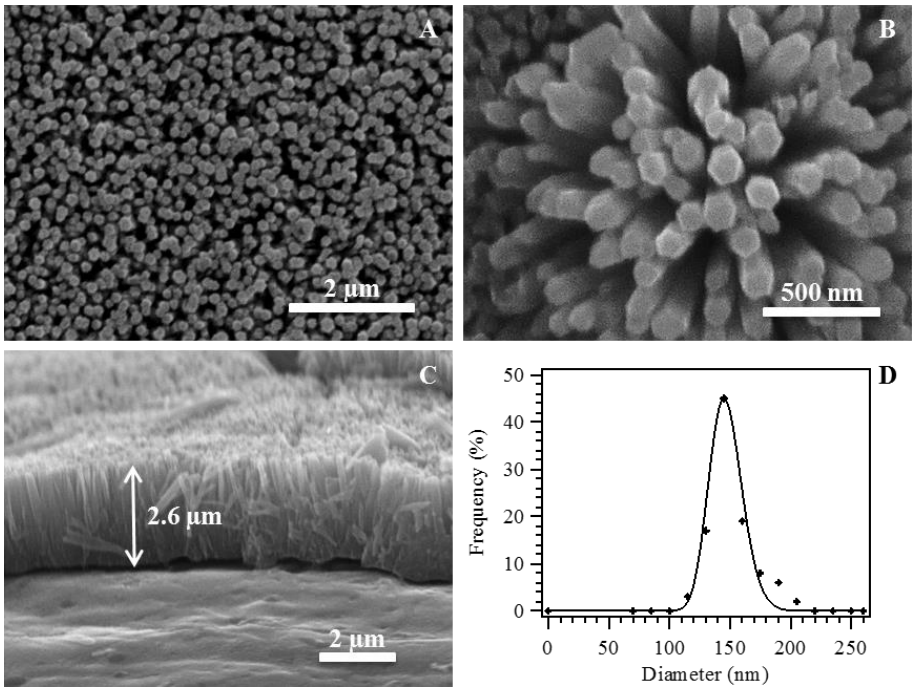

Figure 8.1 SEM images of ZnO NRs after 6 hours of growth at 95°C, (A) top view, (B) high magnification and (C) cross-sectional view. (D) Diameter distributions of the NRs.

The crystal structure and crystal orientation of the ZnO NRs were characterised by power XRD. The XRD pattern of ZnO NRs is analysed based on the standard XRD database for wurtzite ZnO (JCPDS # 36-1451). All the peaks were indexed to the wurtzite ZnO, which gives the diffraction peaks located at 2θ = 31.79°, 34.76°, 36.15°, 47.79° and 54.96° (Z), corresponding to (100), (002), (101), (102) and (110) crystal planes. The additional peaks located at 2θ = 26.83°, 36.55° and 51.84 (■) are the diffraction of SnO_2 from the FTO substrate.

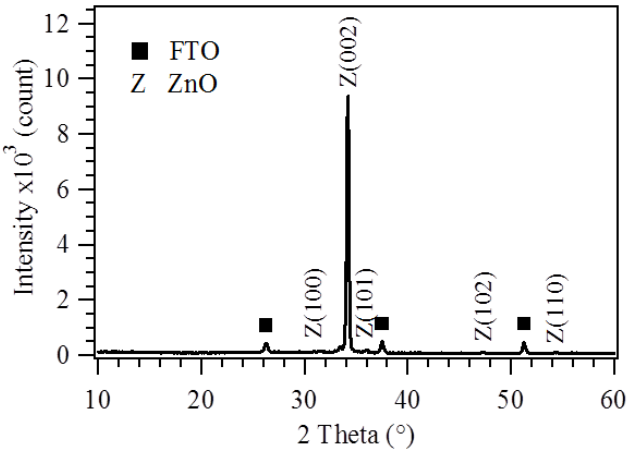

Figure 8.2 XRD pattern of ZnO NRs on FTO glass after 6 hours of growth. The miller indices of crystal planes are labelled where Z and ■ are ZnO and FTO, respectively.

As shown in Figure 8.2, (002) plane is the strongest diffraction peak of the ZnO NRs, which indicates the NRs are grown along the [0001] direction. This observation is in agreement with the SEM images (Figure 8.1), where all the NRs are grown along the c-axis. In addition, the crystal domain size (Equation 2.5, Section 2.3) and relative texture coefficient (Equation 2.7, Section 2.3) of the NRs were calculated, which are 34.3 nm and 0.99, respectively, indicating well-ordered and high quality of ZnO NRs were achieved.

8.4.2 Effect of Growth Duration on the Morphology of ZnO NRs

The correlation between the growth duration and the final morphology of ZnO NRs was investigated. All the experiment parameters were held constant, varying the duration of reaction to 3, 4, 5, 6 and 7 hours. Figure 8.3 shows the cross-sectional view SEM images of the ZnO NRs after different duration of reactions.

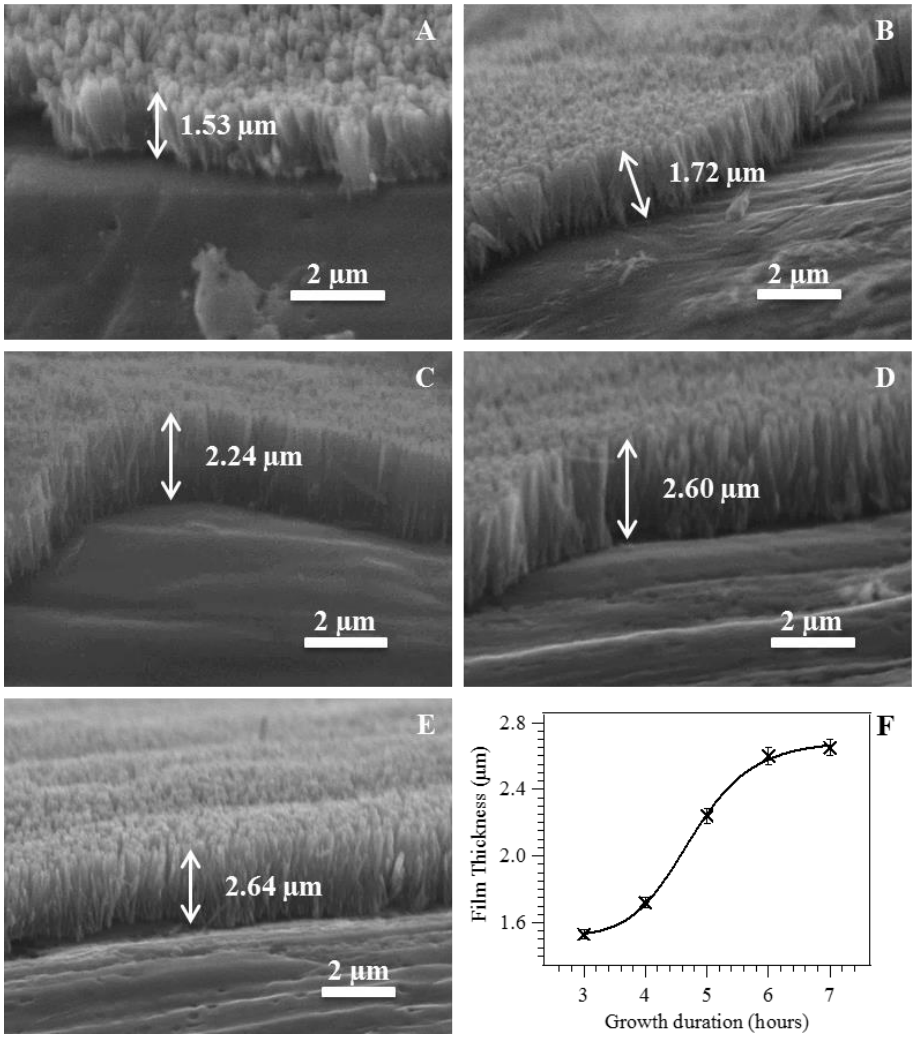

Figure 8.3 Cross-sectional view SEM images of ZnO NRs grew at (A) 3 hours, (B) 4 hours, (C) 5 hours, (D) 6 hours and (E) 7 hours. (F) Plot of film thickness as a function of growth duration.

It is obvious that the NR length is strongly dependent on the duration of reaction. The cross-sectional view SEM images reveal that the NR length is increased from 1.53 µm to 2.64 µm when the growth duration is increased from 4 to 7 hours. It is important to note that the NR length achieves plateau after 6 hours of growth, as shown in Figure 8.3F, where the NR grew for 7 hours (2.64 µm) showing essentially the same thickness as that grew for 6 hours (2.60 µm) due to the exhaustion of the nutrient solution.

8.4.3 Morphology of $BiVO_4$ Films

In order to establish the photoconversion efficiency of pure $BiVO_4$ film as benchmark for comparison with $BiVO_4$/ZnO composite structure, $BiVO_4$ film was generated directly on FTO substrate through the MOD/spin coating method. The top view SEM image (Figure 8.4A) reveals the particular structures of $BiVO_4$ film with some degree of coalescence.

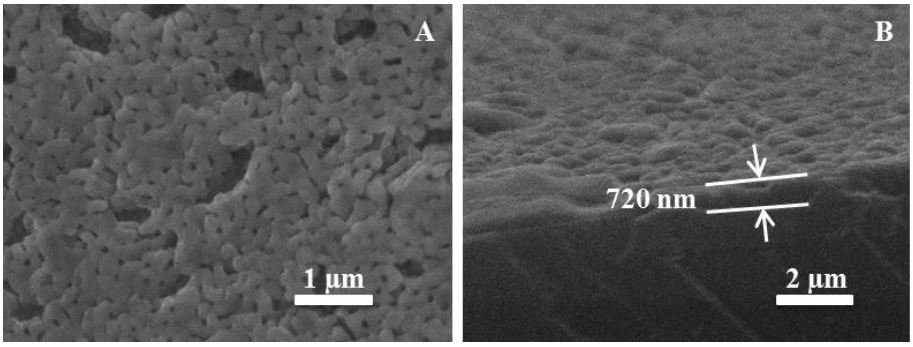

Figure 8.4 SEM images of $BiVO_4$ film after ten deposition cycles, (A) top view and (B) cross-sectional view.

The average diameter of the particles was measured to be 195±34 nm. The well-interconnected 3D porous networks in between the nanoparticles are important for reducing the grain boundary resistance of the films while maintaining the overall surface porosity of the film. This will allow a better penetration of the electrolyte into these films, with increased contact area between the electrolyte and the photoanodes. The obtained surface morphology of the nanoporous $BiVO_4$ films is similar to that reported before for the $BiVO_4$ films prepared by MOD technique.[130, 335] As shown in Figure 8.4B, the nanoporous $BiVO_4$ film is having a film thickness of ~720 nm after ten deposition cycles.

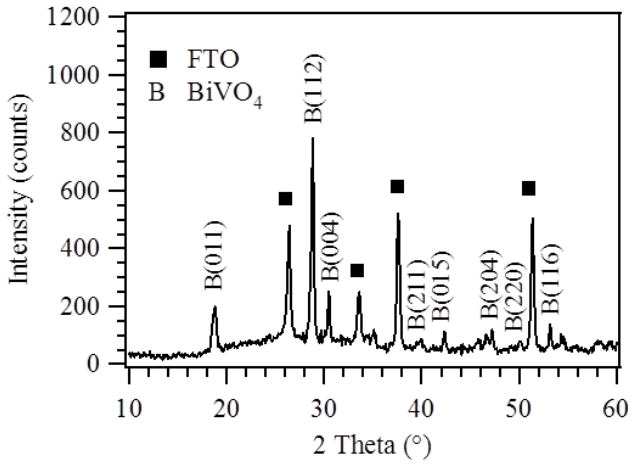

Figure 8.5 XRD pattern of nanoporous $BiVO_4$ film on FTO glass after ten deposition cycles. The miller indices of crystal planes are labelled where B and ■ are $BiVO_4$ and FTO, respectively.

The crystal structure of the nanoporous $BiVO_4$ film was examined by power XRD, as shown in Figure 8.5. The XRD pattern of $BiVO_4$ is analysed based on the standard XRD database for monoclinic $BiVO_4$ (JCPDS # 14-0688). All the peaks were indexed to the monoclinic phase of $BiVO_4$, which gives the diffraction peaks located at 2θ = 18.89°, 28.85°, 30.52°, 40.08°, 42.21°, 47.33°, 50.11° and 53.28° (B), corresponding to (011), (112), (004), (211), (015), (204), (220) and (116) crystal planes. This measurement confirms that the as-prepared $BiVO_4$ film is pure monoclinic phase of $BiVO_4$ possessing the scheelite structure. Similar to the XRD pattern of ZnO NRs, the four additional peaks marked as ■ in the spectrum are contributed by SnO_2 from the FTO substrate. As shown in the diffraction pattern, (112) is the dominant peak for $BiVO_4$ and the crystal domain size of the sample was calculated to be 24.3 nm, which is significantly smaller than the ZnO NRs.

8.4.4 Optical Properties of ZnO NRs and Nanoporous $BiVO_4$ Film

The optical properties of the ZnO NRs (6 hours of grew) and nanoporous $BiVO_4$ film (10 deposition cycles) were investigated using UV-vis spectrophotometer. Figure 8.6A is the UV-vis absorption spectra of ZnO and $BiVO_4$ that recorded between 350 nm to 600 nm at room temperature. The ZnO NR film is white colour, while the $BiVO_4$ thin film is bright yellow colour.

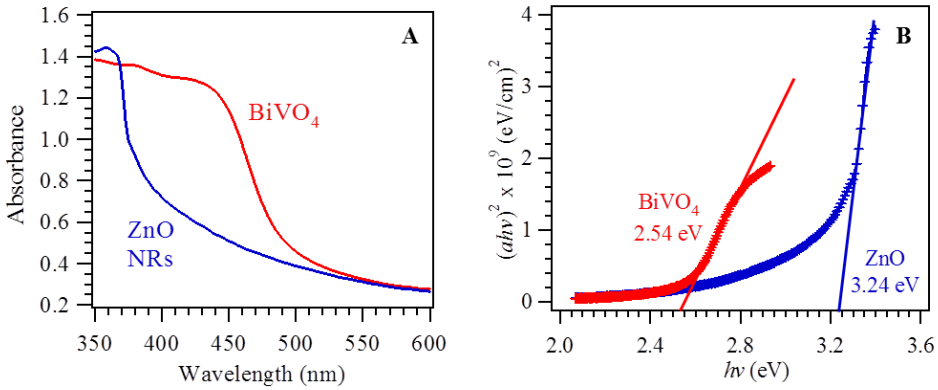

Figure 8.6 (A) UV-vis absorption spectra and (B) Tauc plots of ZnO NRs (6 hours grew) and nanoporous $BiVO_4$ film (10 deposition cycles).

As shown in Figure 8.6A, ZnO only absorb at the UV region, while $BiVO_4$ exhibited absorption in the visible region. The UV-vis absorptions cut-off of the ZnO and $BiVO_4$ were observed at around 390 nm (3.18 eV) and 500 nm (2.48 eV), respectively. It is noticeable that both the ZnO and $BiVO_4$ show sharp absorption edges, which indicates that both the samples have direct band gaps.[335] The absorption edges correspond to their optical band gap energies. The band gap energies were further calculated using Tauc expression (Equation 2.11, Section 2.4), as displayed in Figure 8.6B. The band gaps of the samples were estimated from the *x*-intercept of the tangent line in the plot of $(\alpha hv)^2$ as a function of hv. ZnO and $BiVO_4$ were determined to have

an optical band gap energy of 3.24 eV and 2.54 eV, respectively, very close to the absorption cut-off. The obtained results are comparable with the reported values.[293, 335] The band gap measurements suggest that ZnO absorbs the UV light while $BiVO_4$ is capable to absorb the blue and green light.

8.4.5 Creation of Electrode with $BiVO_4$ Coated ZnO NRs Heterogeneous Structure

In order to take advantage of the visible light absorption of $BiVO_4$ with improved charge mobility, heterogeneous $BiVO_4$ coated ZnO NRs electrodes were created. The tandem electrode of ZnO NRs with nanoporous $BiVO_4$ coating was prepared by the combination of hydrothermal (6 hours grew) and MOD/spin coating methods. The $BiVO_4$ precursor solution was spin cast onto the surface of ZnO NRs for six deposition cycles.

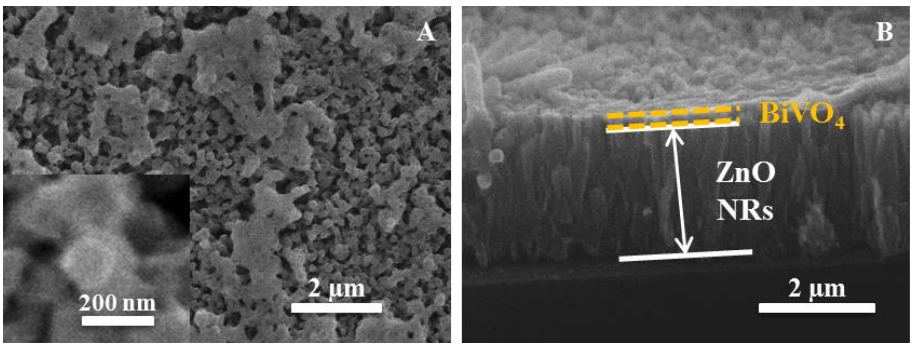

Figure 8.7 SEM images of $BiVO_4$/ZnO heterojunction film after six deposition cycles, (A) top view (The inset is the high resolution image of the sample) and (B) cross-sectional view.

Figure 8.7 shows the SEM images of the $BiVO_4$/ZnO heterostructures. The top view SEM image demonstrates that spin coating method introduced some $BiVO_4$ agglomerations at the top of ZnO NRs. This could be due to the limited spin speed for

the coating. As shown in the high magnification SEM image (inset of Figure 8.7A), the hexagonal morphology of the NRs became less well define due to the coating of $BiVO_4$. The cross-sectional view SEM image (Figure 8.7B) reveals that the coating procedure of $BiVO_4$ did not change the NR morphology. The $BiVO_4$ film on the surface of ZnO NRs after six deposition cycles was measured to have a thickness of ~300 nm.

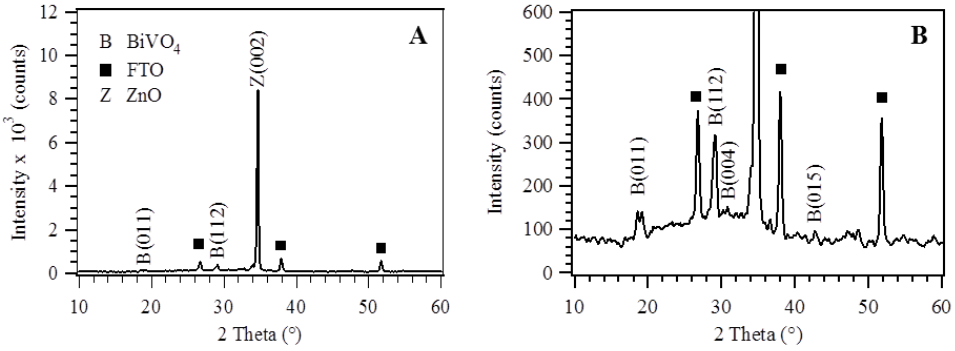

Figure 8.8 XRD pattern of $BiVO_4$/ZnO heterojunction film, (A) full spectra and (B) vertically enlarged. The miller indices of crystal planes are labelled where B, Z and ■ are $BiVO_4$, ZnO and FTO, respectively.

The XRD spectrum of $BiVO_4$/ZnO heterojunction film is presented in Figure 8.8. All the peaks were indexed to the monoclinic phase of $BiVO_4$, wurtzite structure of ZnO and FTO. The XRD spectrum confirmed the presence of ZnO with a strong (002) peak after the deposition of $BiVO_4$ film. This result is in agreement with the SEM image in Figure 8.7B, where the deposition of $BiVO_4$ film did not change the morphology of ZnO NRs. It is noteworthy that the diffraction peaks of $BiVO_4$ from the $BiVO_4$/ZnO electrode are relatively weak. The weak peaks were due to the low concentration of $BiVO_4$ on the surface of ZnO NRs, where the $BiVO_4$ film thickness is about 300 nm, as measured from Figure 8.7B. The crystal domain sizes of ZnO and $BiVO_4$ were calculated to be 40.2 and 23.8 nm, respectively. In comparison to bare ZnO

NRs, the crystal domain of the ZnO NRs from the $BiVO_4$/ZnO heterojunction film show an increase of ~17%. This can be explained by the increased in the crystallinity of ZnO after repeated annealing process.

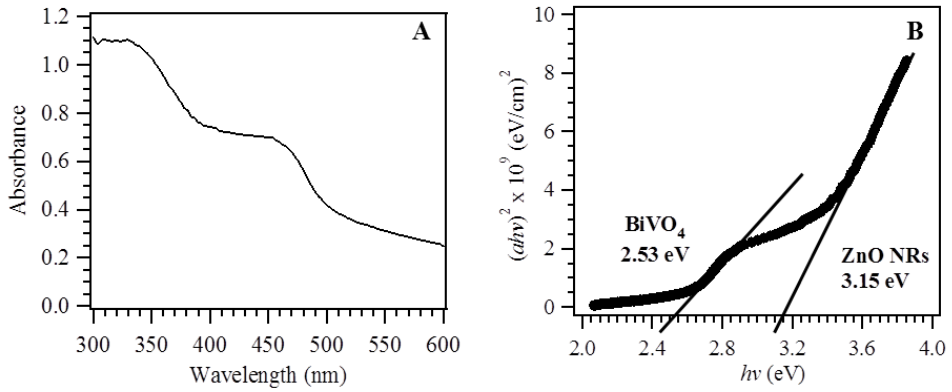

Figure 8.9 (A) UV-vis absorption spectrum and (B) Tauc plot of $BiVO_4$/ZnO heterojunction film.

The UV-vis absorption of the $BiVO_4$/ZnO heterojunction film was recorded as depicted in Figure 8.9A. There are two distinctive absorption features in the absorption spectrum with the absorption edges of ~400 nm and ~500 nm, indicating the presence of ZnO and $BiVO_4$ in the heterogeneous structure. The band gap energies of the samples were calculated from the UV-vis absorption spectrum using the Tauc relation (Equation 2.11, Section 2.4), as presented in Figure 8.9B. The band gap energies of ZnO and $BiVO_4$ were measured to be 3.15 eV and 2.53 eV, respectively. It is worth noting that the optical band gap of ZnO NRs in the composite electrode (3.15 eV) is slightly less than the bare ZnO NRs (3.25 eV; Figure 8.6B). The reduction of the band gap could possibly be due to the doping of bismuth or vanadium ions on the surface of the ZnO NRs.

8.5 PEC Water Splitting Measurements

8.5.1 Photocatalytic Activity of ZnO NRs and Nanoporous $BiVO_4$ Film

The PEC water splitting performances of ZnO NRs and nanoporous $BiVO_4$ film were directly compared by measuring the photocurrent in 0.5 M Na_2SO_4 electrolyte (pH = 6.8) under the illumination of solar simulator (100 mW cm^{-2}) with an AM1.5 G filter. Figure 8.10A presents the *I*–*V* curves of ZnO NRs (blue curve) and nanoporous $BiVO_4$ film (red curve) photoanodes under the sunlight in the potential range from –0.5 to 1.0 $V_{Ag/AgCl}$ together with the dark current measured from the $BiVO_4$ photoanode (black curve).

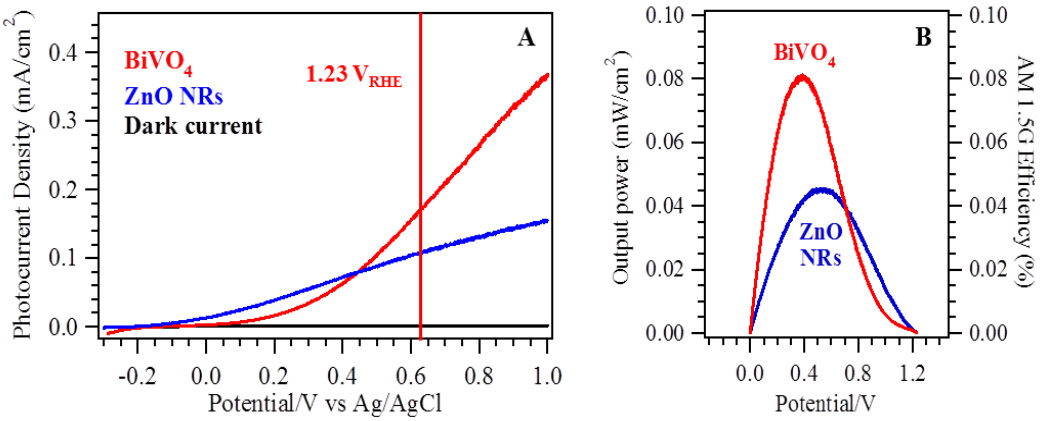

Figure 8.10 (A) *I*–*V* curves of ZnO NRs and nanoporous $BiVO_4$ film together with the dark current measured from $BiVO_4$ film in 0.5 M Na_2SO_4 electrolyte (pH = 6.8) under simulated sunlight of 100 mW cm^{-2} with an AM1.5 G filter and (B) corresponding output power and conversion efficiency under AM1.5 G full solar spectrum irradiation.

As shown in Figure 8.10A, the photocurrents generated from both the photoanodes increase steeply at a lower potential with onset photopotentials at –0.22 $V_{Ag/AgCl}$ for ZnO NRs and –0.18 $V_{Ag/AgCl}$ for nanoporous $BiVO_4$ film. For an electrolyte of 0.5 M Na_2SO_4 with pH 6.8, the reversible oxygen standard potential is at

0.63 $V_{Ag/AgCl}$, marked with the red line in Figure 8.10A. At a typical potential of 1.23 V_{RHE}, the ZnO NRs electrode generates a photocurrent density of 0.108 mA cm^{-2}, while $BiVO_4$ electrode generates a photocurrent density of 0.172 mA cm^{-2}. The photoconversion efficiencies of the ZnO NRs and $BiVO_4$ film photoanodes were calculated (Equation 2.27, Section 2.6), as presented in Figure 8.10B. Consistent with the higher photocurrent density, a much higher photoconversion output power was obtained by the $BiVO_4$ photoanode, with a maximum output power of 0.080 mW cm^{-2} with respect to 0.045 mW cm^{-2} from the ZnO electrode. The measured photoconversion output powers correspond to the photoconversion efficiencies of 0.080% and 0.045%. In comparison, the photoconversion efficiency of the $BiVO_4$ electrode is about 1.8 times higher than that of the ZnO NRs photoanode. This is expected as the smaller band gap of $BiVO_4$ (2.54 eV) with appropriate band edges offers a larger absorption spectrum region as demonstrated in the UV-vis absorption spectrum in Figure 8.6A. Consequently, as the solar intensity increases significantly from the UV to visible wavelength, the number of photogenerated electrons from $BiVO_4$ will increase and thus the photoactivity of PEC water splitting is increased.

8.5.2 Effect of $BiVO_4$ Coating Thickness on Photocatalytic Activity

The thickness of the $BiVO_4$ thin film is affected by the number of the coatings. As the thickness increases, the light absorption will be increased. However, due to the limitation of charge mobility and conductivity, an optimum film thickness should be identified by measuring the effect of the number of coats of $BiVO_4$ on the PEC water splitting performance. Figure 8.11A depicted the *I–V* curves of the $BiVO_4$/ZnO photoanodes with different number of coats of $BiVO_4$ together with the dark current measured from 6 coats $BiVO_4$/ZnO in 0.5 M Na_2SO_4 electrolyte (pH = 6.8) under

simulated sunlight of 100 mW cm^{-2} with an AM1.5 G filter in the potential range of –0.4 to 1.0 $V_{Ag/AgCl}$.

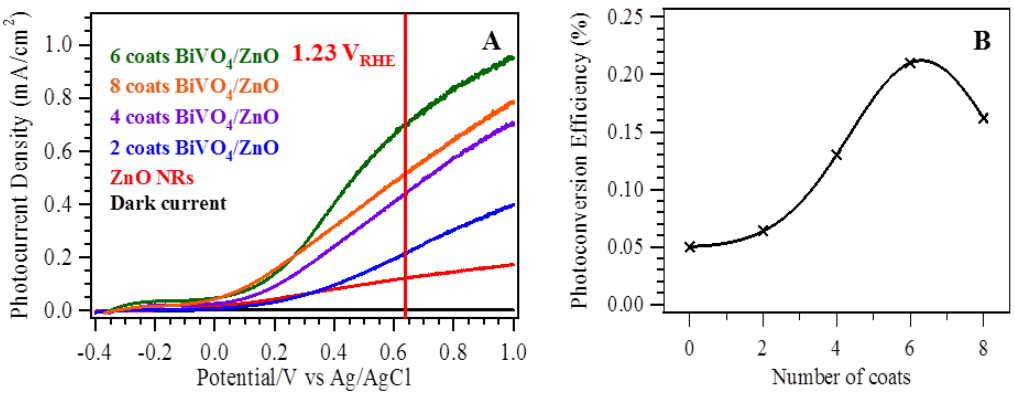

Figure 8.11 (A) *I–V* curves of $BiVO_4$/ZnO photoanodes with different number of coats of $BiVO_4$ in 0.5 M Na_2SO_4 electrolyte (pH = 6.8) under simulated sunlight of 100 mW cm^{-2} with an AM1.5 G filter and (B) plot of photoconversion efficiency with respect to the number of coats of $BiVO_4$.

It is noticeable that the PEC performance of the $BiVO_4$/ZnO photoanode is strongly affected by the number of coats of $BiVO_4$. Compared to the bare ZnO NRs photoanode (red curve), all the $BiVO_4$/ZnO electrodes demonstrate a much higher photocurrent density. The corresponding PEC water splitting parameters of the photoanodes with different number of coats of $BiVO_4$ film are summarised in Table 8.1.

As the $BiVO_4$ film thickness increases, the measured PEC photocurrent densities were also increased until the thickness reaches 300 nm. Meanwhile, the open circuit potentials follow the opposite trend and were decreased as the thickness of $BiVO_4$ increases until the thickness reaches 300 nm. With respect to the ZnO NRs (0.219 $V_{Ag/AgCl}$), the more negative onset potential of the $BiVO_4$ coated photoanode can be attributed to the improvement in the charge separation for the composite samples.[254]

Table 8.1 PEC performance parameters of ZnO NRs with different number of coats of $BiVO_4$ film.

Number of Coats of $BiVO_4$	$BiVO_4$ Film Thickness (nm)	Onset Potential ($V_{Ag/AgCl}$)	Photocurrent at 1.23 V_{RHE} (mA cm^{-2})	AM1.5 G efficiency (%)
0	–	–0.219	0.108	0.050
2	97	–0.306	0.303	0.064
4	223	–0.320	0.435	0.130
6	300	–0.352	0.693	0.210
8	392	–0.346	0.512	0.162

The photoconversion efficiencies of the photoanodes were also calculated from equation 2.27. The results are plotted in Figure 8.11B and summarised in Table 8.1. A maximum photoconversion efficiency of 0.21% was achieved for the photoanode with six coats of $BiVO_4$ (300 nm) on the ZnO NRs. Further increasing the $BiVO_4$ coating on the ZnO NRs will cause a drop in the conversion efficiency. We explain that the formation of a heterojunction in between the ZnO and $BiVO_4$; and the high charge mobility in the ZnO NRs will help to improve the charge separation and reduce the electron-hole recombination. However, with a thick layer of $BiVO_4$ in the $BiVO_4$/ZnO photoanode, the diffusion of the minority carrier (hole) from the $BiVO_4$ towards the ZnO NR core will be limited by the $BiVO_4$ hole diffusion length (100–200 nm).[132, 333] Nevertheless, the PEC water splitting tests reveal that the optimal photoconversion efficiency can be achieved with a layer of 300 nm $BiVO_4$ film on ZnO NRs.

8.5.3 Comparison of PEC Activity of ZnO NRs, Nanoporous $BiVO_4$ Film and $BiVO_4$/ZnO Film

In order to examine the synergy effects of the heterogeneous $BiVO_4$/ZnO photoanode for the improved PEC water splitting, a direct comparison between the ZnO NRs, nanoporous $BiVO_4$ film and $BiVO_4$/ZnO heterojunction film was carried out. Figure 8.12A represents the *I–V* curves of ZnO NRs (blue curve), nanoporous $BiVO_4$ film (red curve) and optimal $BiVO_4$/ZnO heterojunction film (dark green) in 0.5 M Na_2SO_4 electrolyte (pH = 6.8) under simulated sunlight of 100 mW cm^{-2} with an AM1.5 G filter in the potential range of –0.4 to 1.0 $V_{Ag/AgCl}$.

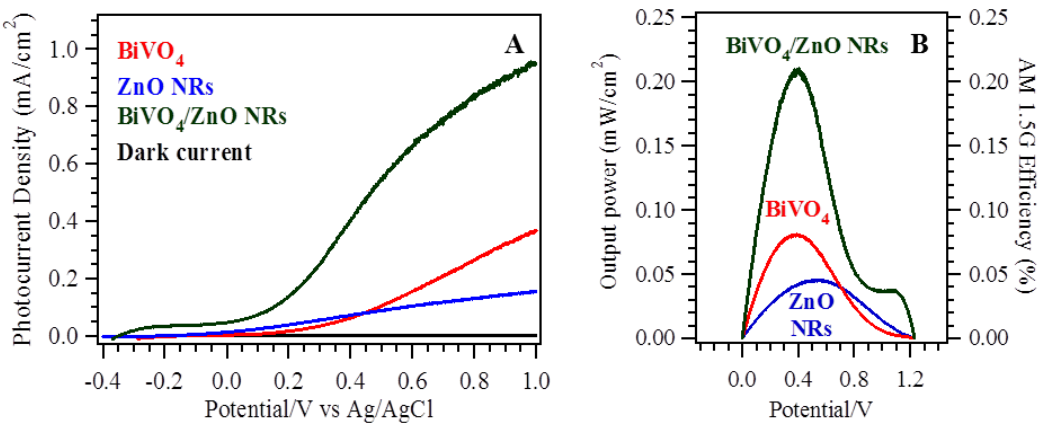

Figure 8.12 (A) *I–V* curves of ZnO NRs (blue), nanoporous $BiVO_4$ film (red) and $BiVO_4$/ZnO heterojunction film (dark green) together with dark current (black) measured from the composite sample in 0.5 M Na_2SO_4 electrolyte (pH = 6.8) under simulated sunlight of 100 mW cm^{-2} with an AM1.5 G filter and (B) corresponding PEC output power and conversion efficiency under AM1.5 G full solar spectrum irradiation.

As shown in Figure 8.12A, the $BiVO_4$/ZnO photoanode exhibits a much higher photocurrent density than that of the bare ZnO and $BiVO_4$ photoanodes. At a typical potential of 1.0 $V_{Ag/AgCl}$, the photocurrents generated from the ZnO, $BiVO_4$ and

$BiVO_4$/ZnO photoanodes were measured to be 0.155, 0.368 and 0.952 mA cm^{-2}, respectively. The onset potential of the $BiVO_4$/ZnO electrode (–0.352 $V_{Ag/AgCl}$) is also shifted to a more negative value relative to the ZnO (–0.219 $V_{Ag/AgCl}$) and $BiVO_4$ (–0.185 $V_{Ag/AgCl}$) photoanodes. This can be accredited to the appropriated alignment in the band gaps of ZnO and $BiVO_4$ which increases the charge separation.[259] The details of the band structures of the heterojunction between ZnO and $BiVO_4$ is discussed later in this section.

The PEC output powers and efficiencies of the samples were also evaluated using equation 2.27, shown in Figure 8.12B. The maximum conversion output powers of ZnO NRs, nanoporous $BiVO_4$ film and $BiVO_4$/ZnO electrodes were calculated to be 0.045, 0.082 and 0.212 mW cm^{-2}, respectively. The calculations reveal that the PEC output power of the $BiVO_4$/ZnO photoanode is being ~67% higher than the sum of the output powers of the ZnO and $BiVO_4$ photoanodes. This implies that the stacking of $BiVO_4$ film on top of ZnO NRs offers better charge separation and improved light adsorption with a synergistic effect.

Amperometric studies were conducted for ZnO, $BiVO_4$ and $BiVO_4$/ZnO photoanodes in 0.5 M Na_2SO_4 electrolyte (pH = 6.8) at an applied voltage of 0.63 $V_{Ag/AgCl}$ under light on-off cycles for 160 s, as shown in Figure 8.13A. The measurements display that there is no obvious decrease in the photocurrent density, which reveals the stability of the photoanodes under our experimental conditions. It is worth mentioning that the photocurrent on-off curve of the ZnO NRs anode is different from that of the $BiVO_4$ and $BiVO_4$/ZnO anodes. For ZnO NRs photoanode, the behaviour of the photocurrent represents by the surface charge accumulation rather than recombination which determines by the kinetics of water oxidation. For $BiVO_4$ photoanode, on the other hand, it absorbs visible light which has much higher light

intensity in the solar spectrum. Therefore, the exciton density is expected to be higher and thus results in an exponential decay in the photocurrent.

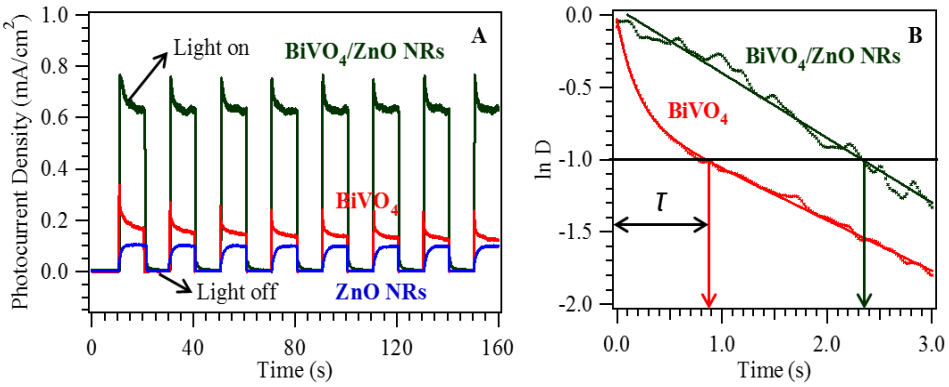

Figure 8.13 (A) Amperometric *I*–*t* curves of ZnO NRs, nanoporous $BiVO_4$ film and $BiVO_4$/ZnO heterojunction film in 0.5 M Na_2SO_4 electrolyte (pH = 6.8) at an applied voltage of 0.63 $V_{Ag/AgCl}$ at 100 mW cm^{-2} for 160 s with repeated light on-off cycles and (B) normalised plots of ln *D* as a function of illumination time.

The anodic photocurrent spikes of the $BiVO_4$ and $BiVO_4$/ZnO NRs electrodes can be used to assess the rate of electron-hole recombination of the photoanodes using equation 4.2. Figure 8.13B is the normalised plots of ln *D* as a function of illumination time for the $BiVO_4$ and $BiVO_4$/ZnO NRs electrodes. The transient time constant (τ) value of the $BiVO_4$/ZnO NRs electrode (2.35 s) measured at ln *D* = –1 is 2.6 times larger than that of the $BiVO_4$ electrode (0.89 s). The reduced in the electron-hole recombination rate from the $BiVO_4$/ZnO NRs photoanode is possibly due to the creation of a heterojunction in the composite sample, which helps to improve the charge separation.

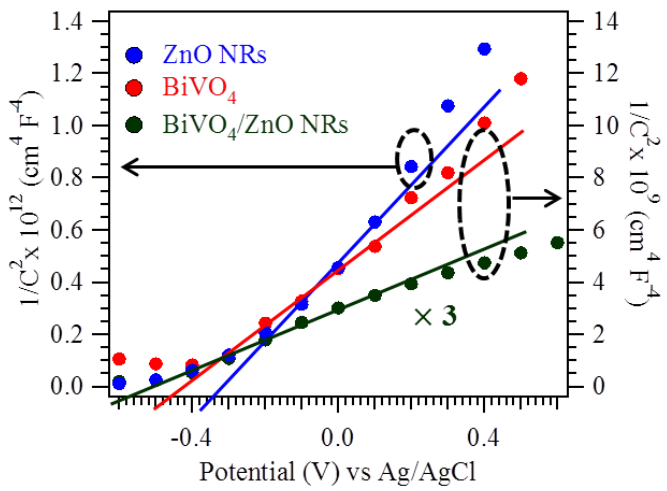

Figure 8.14 M–S plots of ZnO NRs, nanoporous $BiVO_4$ film and $BiVO_4$/ZnO film measured in 0.5 M Na_2SO_4 solution (pH 6.8) in the dark. The amplitude of the sinusoidal wave was set at 10 mV at a fixed frequency of 1 kHz.

In addition, EIS measurements were carried out to determine the capacitances and the flatband potential (V_{FB}) values of the semiconductors in 0.5 M Na_2SO_4 electrolyte in the dark at a fixed frequency of 1 kHz. Figure 8.14 shows the Mott–Schottky (M–S) plots of the ZnO NRs, nanoporous $BiVO_4$ film and $BiVO_4$/ZnO film. All the samples exhibit positive slopes which confirm the typical n-type semiconductor behaviour. The V_{FB} values of the electrodes were estimated to be –0.34, –0.46 and –0.57 $V_{Ag/AgCl}$ for the ZnO, $BiVO_4$ and $BiVO_4$/ZnO photoanodes. A more negative V_{FB} value will improve the charge carrier separation of the sample since the degree of band bending at the interface is increased.[109]

In addition, the slopes of the M–S plots were used to determine the donor densities of the samples using equation 2.24. The relative dielectric constants of ZnO and $BiVO_4$ are 10 and 55,[78, 333] thus the donor densities were calculated to be 7.31×10^{18} cm^{-3} and 3.82×10^{18} cm^{-3}, respectively. The obtained readings are comparable with the reported values.[265, 333] It is important to note that the slope of the

$BiVO_4$/ZnO electrode is much smaller as compared to the ZnO and $BiVO_4$ electrodes indicating a higher carrier concentration of the $BiVO_4$/ZnO electrode. The higher donor density for the $BiVO_4$/ZnO electrode can be explained on the basis that the $BiVO_4$ film acting as a passivation layer that reduces the surface trap state of the ZnO NRs. Therefore, the number of charge trapped on the surface states is reduced and consequently increasing the concentration of the electrons at the space charge depletion layer.[109] This could be one of the reasons for the improvement in the photoactivity of PEC water splitting for the $BiVO_4$/ZnO electrode over the bare ZnO and $BiVO_4$ photoanodes.

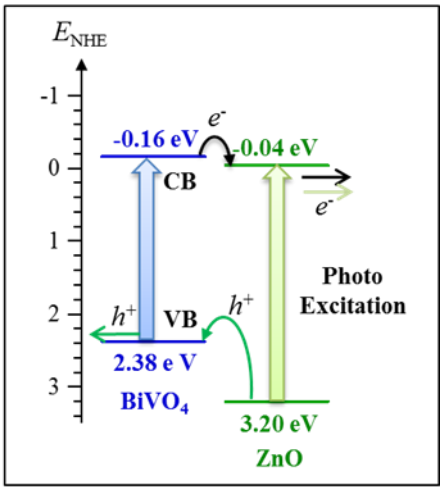

Figure 8.15 Band gap schematic diagram representing the charge-transfer process in $BiVO_4$/ZnO electrode.

Another possible reason for higher photocatalytic activity of the $BiVO_4$/ZnO electrode is the reduced in the electron-hole recombination. Based on the obtained V_{FB} values and optical band gap energies of ZnO and $BiVO_4$, a potential energy diagram for the $BiVO_4$/ZnO electrode can be constructed. The M–S plots reveal that the V_{FB} values of ZnO and $BiVO_4$ are –0.34 and –0.46 $V_{Ag/AgCl}$, corresponding to 0.26 and 0.14 V_{RHE},

respectively. It has been reported that the difference between the V_{FB} and the conduction band for an oxide semiconductor is approximated to 0.3 V.[336, 337] Therefore, the conduction bands of ZnO and $BiVO_4$ versus NHE at pH 0 are calculated to be −0.04 V and −0.16 V, respectively. The Tauc plots (Figure 8.6B) demonstrate that the optical band gap energies of ZnO and $BiVO_4$ were 3.24 eV and 2.54 eV, respectively. Hence, a potential energy diagram of the $BiVO_4$/ZnO photoanode is proposed in Figure 8.15.

As shown in Figure 8.15, the band edges of ZnO and $BiVO_4$ are appropriately aligned where the conduction band and valence band of $BiVO_4$ are more negative than the corresponding bands of ZnO. This energy alignment will favour the injection of the photogenerated electrons from $BiVO_4$ to ZnO and the photogenerated holes from ZnO to $BiVO_4$, which results in the improvement in charge separation and reduce the possibility of charge recombination. More important, due to the core-shell geometry of the $BiVO_4$ coated ZnO NRs, the hole transfer from ZnO to $BiVO_4$ will help to facilitate the surface water oxidation by the holes. Meanwhile, the electron transferred from the $BiVO_4$ to the ZnO NRs can benefit from the better electron conductivity of ZnO, allowing low internal energy consumption.

In order to prove that the electron-hole recombination rate of the $BiVO_4$/ZnO film is reduced, EIS measurements were carried out to determine the kinetics of charge transfer properties of the ZnO NRs, $BiVO_4$ film and $BiVO_4$/ZnO heterojunction film under illumination. Figure 8.16 displays the Nyquist plots of ZnO, $BiVO_4$ and $BiVO_4$/ZnO electrodes obtained in the frequency range of 10 kHz to 100 mHz. A simple Randles circuit model was used for the data fitting, as presented in Figure 8.16, where R_s is the solution resistance, Q_i is the constant phase element for the electrolyte/electrode interface and R_{ct} is the charge transfer resistance at the interface of the photoanode and electrolyte.

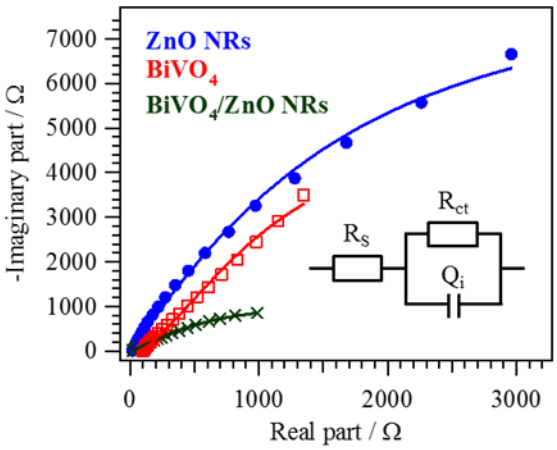

Figure 8.16 Nyquist plots of ZnO NRs, $BiVO_4$ film and $BiVO_4$/ZnO heterojunction film at 0.5 $V_{Ag/AgCl}$ under simulated solar illumination in 0.5 M Na_2SO_4 electrolyte (pH 6.8). The amplitude of the sinusoidal wave was set at 10 mV and frequency varied from 10 kHz to 100 mHz.

Figure 8.16 demonstrates that all the photoanodes exhibit one arc, suggesting that only the surface charge transfer step is involved in the photocatalytic reaction.[338] Normally, the smaller the semicircle/arc radius of the EIS Nyquist plot implies the larger the oxide layer capacitance which may lead to a higher charge density at the electrode/electrolyte interface. This will accelerate the interfacial charge transfer and thus reduce the charge recombination.[34, 193] From the Nyquist plots, the $BiVO_4$/ZnO electrode shows a smallest arc radius in comparison to the bare ZnO and $BiVO_4$ photoanodes. This indicates the $BiVO_4$ film on top of ZnO NRs assists the separation of the photogenerated electron-hole pairs and accelerate the charge transfer at the solid-liquid interface, which thus reduced the electron-hole recombination.

In summary, the $BiVO_4$/ZnO heterojunction film exhibits a significant improved in the PEC water splitting activity. The enhancement can be attributed to a number of factors, which are the improved in absorption region, increased carrier concentration,

reduced electron-hole recombination, enhanced charge separation and faster the interfacial charge transfer process.

8.6 Conclusions

Highly ordered 1D $BiVO_4$/ZnO heterojunction film was successfully created through the combination of hydrothermal and MOD/spin coating methods. The correlation between the growth duration and the morphology of ZnO NRs was investigated. The top view SEM image of $BiVO_4$ revealed that the as-prepared film was nanoporous. The effect of number of coats of $BiVO_4$ on ZnO NRs with respect to the PEC water splitting performance was examined. The results showed that six deposition cycles of $BiVO_4$ was the optimal thickness for the $BiVO_4$/ZnO film in PEC water splitting test. The PEC measurements demonstrated that the $BiVO_4$/ZnO electrode displayed a synergistic effect whereby its photoconversion output power was ~67% higher than the sum of the output powers of the ZnO NRs and nanoporous $BiVO_4$ film. Possible mechanisms for the high photoconversion efficiency were also discussed.

Chapter 9 Thesis Conclusions

In this thesis, metal oxide nanomaterials with different morphologies, optical and electrical properties were successfully created and applied in the PEC water splitting and GIS applications. The PEC water splitting tests revealed that the photocatalytic water splitting performances could be significantly affected by these properties. Here, the photoconversion efficiencies and some of the associated critical parameters of all the nanomaterials studied in this thesis were summarised and tabulated in Table 9.1.

The highest photoconversion efficiencies were achieved by urchin-like "ZT700" and multilayer of ZnO NRs on mesh "4L" photoanodes, which were 1.07 and 0.80%, respectively. A number of factors responsible for the higher PEC performance were identified. For the ZT700 photoanode, a thin layer of Zn_2TiO_4 (75 nm) at the interface between ZnO NRs and TiO_2 HHSs and the unique urchin-like morphology are essential for the high PEC water splitting efficiency. Here, the Zn_2TiO_4 layer acts as a charge barrier layer to prevent the back flow of the electrons, since the conduction band of the Zn_2TiO_4 is more negative than those of TiO_2 and ZnO. Therefore, the possibility of electron-hole recombination of this hybrid sample is further reduced. Meanwhile, the large surface area of the urchin-like structure allows an effective contact between the nanomaterials and the electrolyte to facilitate efficient surface reactions.

The high PEC water splitting efficiency of the 4L photoanodes can be attributed to the increased light absorption. For the 4L electrode, it is made up of 4 layers of M60mW33. Therefore, some of the light rays that pass through the apertures of the front layer will then be absorbed/scattered by the ZnO NRs on the following layers,

which help to achieve some multiple internal reflections. The optical transmission measurements revealed that 99.86% of the light was absorbed by the multilayer photoanode, resulting in a high photoconversion efficiency.

Table 9.1 PEC water splitting performances of metal oxide nanomaterials.

Sample	Length (μm)	Diameter (nm)	*SAVR* (nm^{-1})	E_g (eV)	η (%)
ZnO NRs	4.5	157±30	0.0171	3.21	0.15
ZnO NTs	5.0	159±24	0.0272	3.13	0.45
Co-doped ZnO NRs	3.1	200±24	0.0175	3.14	0.24
K-doped ZnO NRs	3.6	180±21	0.0184	3.15	0.26
Ni-doped ZnO NRs	2.2	440±66	0.0110	3.16	0.14
Na-doped ZnO NRs	3.8	170±24	0.0194	3.12	0.29
M30mW33	5.9	483±190	-	-	0.27
M60mW33	9.6	670±172	-	-	0.30
M90mW33	13.5	1040±220	-	-	0.33
M120mW33	19.3	1280±210	-	-	0.34
2L	-	-	-	-	0.62
3L	-	-	-	-	0.78
4L	-	-	-	-	0.80
ZT600	-	-	-	-	0.61
ZT700	-	-	-	-	1.07
$BiVO_4$/ZnO NRs	-	-	-	-	0.21

It is noticeable that the photoconversion efficiencies of ZnO NRs and Ni-doped ZnO NRs are the lowest, which were 0.15 and 0.14%, respectively. The low PEC water splitting efficiency by the ZnO NRs photoanode can be explained by the large band gap energy and poor charge transportation. Although the band gap energy of the Ni-doped ZnO NRs (3.16 eV) is smaller than the undoped ZnO NRs (3.21 eV), the photoconversion efficiency of the Ni-doped ZnO NRs still remained lower than that of the ZnO NRs. This can be attributed to the length of the Ni-doped ZnO NRs (2.2 μm) which is much shorter in comparison to the undoped ZnO NRs (4.5 μm), resulting in a smaller *SAVR* value and poor light absorption.

For the first time, conductive YZO NRs had been designed and prepared through hydrothermal method and applied in GIS application. The conductive YZO NRs were synthesised using a facile one-pot hydrothermal method. At higher Y/Zn molar ratios, the aspect ratio of the YZO NRs was increased from 11 to 25. Doping ZnO NRs with yttrium atoms decreased the electrical resistivity more than 100 fold. The GIS measurements revealed a 6.5-fold enhancement in the sensitivity accompanied with a significant reduction in breakdown voltages from the highly conductive YZO NRs. Further sensitivity improvements (~11%) were achieved with simultaneous UV illumination.

Chapter 10 Future Works

The future work will be focused on the understanding of the mechanism of doping in metal oxides and developing optimisation of PEC performance. At the time of preparing the doped ZnO NRs, X-ray photoelectron spectroscopy (XPS) was unavailable to determine whether the dopants are doped at the interstitial sites or lattice of the crystal. Therefore, the use of XPS is highly recommended in the future for the similar experiments in order to establish the oxidation states and dopant concentrations. For the PEC water splitting experiments, the stability tests of the photoelectrodes should be carried out at a longer duration (> 1 day) since the long term stability of the metal oxide nanostructures under illumination in the electrolytes used is not well characterised. In addition, the actual volume of the hydrogen and oxygen gases generated by the photoelectrodes should be measured using gas chromatography-mass spectrometer in order to obtain the actual solar-to-hydrogen conversion efficiency of the samples.

Other than that, one of the approaches to further increase the conversion efficiencies of the materials is to develop composite nanomaterials with small band gap photocatalysts, including $BiVO_4$,[130] Bi_2WO_6,[339] Fe_2O_3[323] and WO_3.[234] The created hybrid structures will result in the formation of heterojunctions at interfaces, which will increase the charge separation, reduce electron-hole recombination rate and also enhance the photon absorption. For the hybrid samples, the PEC performances can be enhanced further by the deposition of a layer of oxygen evolution catalyst (OEC) such as, FeOOH, NiOOH and Co-Pi.[10, 147, 148, 265, 318, 340] It has been reported that OEC will act

as the hole acceptors and catalytic sites to accelerate the rate of water oxidation reaction and suppress the charge recombination in the valence band.[147, 265]

For GIS application, materials will be developed to increase the stability of the GIS. Other than that, the creation of conductive ZnO nanostructures with a sharp tip, for instance, ZnO nanopencil[34] and nanocone,[341] will be another possible way of improving the GIS performances.

In summary, the insights drawn from these experiments can be developed and utilised in the creation of new hybrid metal oxide nanostructures as efficient anodes for potential applications in photoelectrolysis of water and photovoltaic, as well as gas ionisation sensor.

11 References and Bibliography

1. R. S. Devan, R. A. Patil, J. H. Lin and Y. R. Ma, *Adv. Funct. Mater.*, 2012, **22**, 3326-3370.
2. M. H. Huang, S. Mao, H. Feick, H. Q. Yan, Y. Y. Wu, H. Kind, E. Weber, R. Russo and P. D. Yang, *Science*, 2001, **292**, 1897-1899.
3. S. U. M. Khan, M. Al-Shahry and W. B. Ingler, *Science*, 2002, **297**, 2243-2245.
4. T. Hisatomi, J. Kubota and K. Domen, *Chem. Soc. Rev.*, 2014, **43**, 7520-7535.
5. Y. R. Ryu, T. S. Lee and H. W. White, *Appl. Phys. Lett.*, 2003, **83**, 87-89.
6. S. Y. Huang, G. Schlichthorl, A. J. Nozik, M. Gratzel and A. J. Frank, *J. Phys. Chem. B*, 1997, **101**, 2576-2582.
7. S. Iijima, *Nature*, 1991, **354**, 56-58.
8. F. Gyger, M. Hubner, C. Feldmann, N. Barsan and U. Weimar, *Chem. Mater.*, 2010, **22**, 4821-4827.
9. M. Ni, M. K. H. Leung, D. Y. C. Leung and K. Sumathy, *Renew. Sust. Energ. Rev.*, 2007, **11**, 401-425.
10. T. W. Kim and K. S. Choi, *Science*, 2014, **343**, 990-994.
11. T. Y. Zhai, X. S. Fang, M. Y. Liao, X. J. Xu, H. B. Zeng, B. Yoshio and D. Golberg, *Sensors*, 2009, **9**, 6504-6529.
12. G. R. Patzke, F. Krumeich and R. Nesper, *Angew. Chem. Int. Edit.*, 2002, **41**, 2446-2461.
13. D. V. Bavykin, J. M. Friedrich and F. C. Walsh, *Adv. Mater.*, 2006, **18**, 2807-2824.
14. J. N. Tiwari, R. N. Tiwari and K. S. Kim, *Prog. Mater. Sci.*, 2012, **57**, 724-803.
15. M. Armand and J. M. Tarascon, *Nature*, 2008, **451**, 652-657.
16. B. C. H. Steele and A. Heinzel, *Nature*, 2001, **414**, 345-352.
17. M. Law, L. E. Greene, J. C. Johnson, R. Saykally and P. D. Yang, *Nat. Mater.*, 2005, **4**, 455-459.
18. V. L. Colvin, M. C. Schlamp and A. P. Alivisatos, *Nature*, 1994, **370**, 354-357.
19. M. H. Habibi and M. Mikhak, *Appl. Surf. Sci.*, 2012, **258**, 6745-6752.

20. H. Kind, H. Q. Yan, B. Messer, M. Law and P. D. Yang, *Adv. Mater.*, 2002, **14**, 158-160.

21. J. Kong, N. R. Franklin, C. W. Zhou, M. G. Chapline, S. Peng, K. J. Cho and H. J. Dai, *Science*, 2000, **287**, 622-625.

22. S. J. Pearton, D. P. Norton, K. Ip, Y. W. Heo and T. Steiner, *Prog. Mater. Sci.*, 2005, **50**, 293-340.

23. U. Ozgur, Y. I. Alivov, C. Liu, A. Teke, M. A. Reshchikov, S. Dogan, V. Avrutin, S. J. Cho and H. Morkoc, *J. Appl. Phys.*, 2005, **98**, 041301.

24. G. H. Lee, T. Kawazoe and M. Ohtsu, *Solid State Commun.*, 2002, **124**, 163-165.

25. Z. L. Wang, *J. Phys.-Condens. Mat.*, 2004, **16**, R829-R858.

26. M. Skompska and K. Zarebska, *Electrochim. Acta*, 2014, **127**, 467-488.

27. A. Janotti and C. G. Van de Walle, *Rep. Prog. Phys.*, 2009, **72**, 126501.

28. C. H. Chia, T. Makino, K. Tamura, Y. Segawa, M. Kawasaki, A. Ohtomo and H. Koinuma, *Appl. Phys. Lett.*, 2003, **82**, 1848-1850.

29. A. Soudi, P. Dhakal and Y. Gu, *Appl. Phys. Lett.*, 2010, **96**, 253115.

30. Z. Y. Fan and J. G. Lu, *J. Nanosci. Nanotechno.*, 2005, **5**, 1561-1573.

31. D. C. Look, *Mat. Sci. Eng. B-Solid*, 2001, **80**, 383-387.

32. S. O. Kucheyev, J. S. Williams, C. Jagadish, J. Zou, C. Evans, A. J. Nelson and A. V. Hamza, *Phys. Rev. B*, 2003, **67**, 094115.

33. Z. Li, R. S. Yang, M. Yu, F. Bai, C. Li and Z. L. Wang, *J. Phys. Chem. C*, 2008, **112**, 20114-20117.

34. T. Wang, R. Lv, P. Zhang, C. J. Li and J. L. Gong, *Nanoscale*, 2015, **7**, 77-81.

35. C. J. Lee, T. J. Lee, S. C. Lyu, Y. Zhang, H. Ruh and H. J. Lee, *Appl. Phys. Lett.*, 2002, **81**, 3648-3650.

36. Y. Li, X.-Y. Yang, Y. Feng, Z.-Y. Yuan and B.-L. Su, *Crit. Rev. Solid State*, 2012, **37**, 1-74.

37. P. C. Chang, Z. Y. Fan, D. W. Wang, W. Y. Tseng, W. A. Chiou, J. Hong and J. G. Lu, *Chem. Mater.*, 2004, **16**, 5133-5137.

38. S. Fay, U. Kroll, C. Bucher, E. Vallat-Sauvain and A. Shah, *Sol. Energ. Mat. Sol. C.*, 2005, **86**, 385-397.

39. Y. J. Xing, Z. H. Xi, Z. Q. Xue, X. D. Zhang, J. H. Song, R. M. Wang, J. Xu, Y. Song, S. L. Zhang and D. P. Yu, *Appl. Phys. Lett.*, 2003, **83**, 1689-1691.

40. Y. J. Kim, H. Yoo, C. H. Lee, J. B. Park, H. Baek, M. Kim and G. C. Yi, *Adv. Mater.*, 2012, **24**, 5565-5569.

41. B. D. Yao, Y. F. Chan and N. Wang, *Appl. Phys. Lett.*, 2002, **81**, 757-759.

42. K. L. Choy, *Prog. Mater. Sci.*, 2003, **48**, 57-170.

43. L. Filipovic, S. Selberherr, G. C. Mutinati, E. Brunet, S. Steinhauer, A. Kock, J. Teva, J. Kraft, J. Siegert, F. Schrank, C. Gspan and W. Grogger, *IEEE T. Semiconduct. M.*, 2014, **27**, 269-277.

44. S. D. Shinde, G. E. Patil, D. D. Kajale, V. B. Gaikwad and G. H. Jain, *J. Alloy. Compd.*, 2012, **528**, 109-114.

45. M. Quintana, E. Ricra, J. Rodriguez and W. Estrada, *Catal. Today*, 2002, **76**, 141-148.

46. L. Vayssieres, *Adv. Mater.*, 2003, **15**, 464-466.

47. S. Xu, C. Lao, B. Weintraub and Z. L. Wang, *J. Mater. Res.*, 2008, **23**, 2072-2077.

48. S. H. Jung, E. Oh, K. H. Lee, Y. Yang, C. G. Park, W. J. Park and S. H. Jeong, *Cryst. Growth Des.*, 2008, **8**, 265-269.

49. S. Baruah and J. Dutta, *Sci. Technol. Adv. Mat.*, 2009, **10**, 013001.

50. B. Liu and H. C. Zeng, *J. Am. Chem. Soc.*, 2003, **125**, 4430-4431.

51. Y. H. Tong, Y. C. Liu, L. Dong, D. X. Zhao, J. Y. Zhang, Y. M. Lu, D. Z. Shen and X. W. Fan, *J. Phys. Chem. B*, 2006, **110**, 20263-20267.

52. J. M. Downing, M. P. Ryan and M. A. McLachlan, *Thin Solid Films*, 2013, **539**, 18-22.

53. P. V. Adhyapak, S. P. Meshram, D. P. Amalnerkar and I. S. Mulla, *Ceram. Int.*, 2014, **40**, 1951-1959.

54. H. Zhou, M. Wissinger, J. Fallert, R. Hauschild, F. Stelzl, C. Klingshirn and H. Kalt, *Appl. Phys. Lett.*, 2007, **91**, 181112.

55. L. M. Kukreja, S. Barik and P. Misra, *J. Cryst. Growth*, 2004, **268**, 531-535.

56. R. S. Yang, Y. Qin, C. Li, L. M. Dai and Z. L. Wang, *Appl. Phys. Lett.*, 2009, **94**, 022905.

57. K. Reimann, M. Steube, D. Frohlich and S. J. Clarke, *J. Cryst. Growth*, 1998, **189**, 652-655.

58. M. D. McCluskey and S. J. Jokela, *J. Appl. Phys.*, 2009, **106**, 071101.

59. A. K. Viswanath, E. J. Shin, J. I. Lee, S. Yu, D. Kim, B. Kim, Y. Choi and C. H. Hong, *J. Appl. Phys.*, 1998, **83**, 2272-2275.

60. G. F. Fine, L. M. Cavanagh, A. Afonja and R. Binions, *Sensors*, 2010, **10**, 5469-5502.

61. J. H. He, S. Singamaneni, C. H. Ho, Y. H. Lin, M. E. McConney and V. V. Tsukruk, *Nanotechnology*, 2009, **20**, 065502.

62. X. D. Wang, J. Zhou, J. H. Song, J. Liu, N. S. Xu and Z. L. Wang, *Nano Lett.*, 2006, **6**, 2768-2772.

63. Y. S. Zhang, K. Yu, D. S. Jiang, Z. Q. Zhu, H. R. Geng and L. Q. Luo, *Appl. Surf. Sci.*, 2005, **242**, 212-217.

64. J. X. Wang, X. W. Sun, A. Wei, Y. Lei, X. P. Cai, C. M. Li and Z. L. Dong, *Appl. Phys. Lett.*, 2006, **88**, 233106.

65. A. Wei, X. W. Sun, J. X. Wang, Y. Lei, X. P. Cai, C. M. Li, Z. L. Dong and W. Huang, *Appl. Phys. Lett.*, 2006, **89**, 123902.

66. P. R. Solanki, A. Kaushik, A. A. Ansari, G. Sumana and B. D. Malhotra, *Appl. Phys. Lett.*, 2008, **93**, 163903.

67. N. Kumar, A. Dorfman and J. Hahm, *Nanotechnology*, 2006, **17**, 2875-2881.

68. Z. Li and Z. L. Wang, *Adv. Mater.*, 2011, **23**, 84-89.

69. L. Liao, H. B. Lu, M. Shuai, J. C. Li, Y. L. Liu, C. Liu, Z. X. Shen and T. Yu, *Nanotechnology*, 2008, **19**, 175501.

70. H. J. Wang, C. W. Zou, C. X. Tian, L. Zhou, Z. S. Wang and D. J. Fu, *Nanoscale Res. Lett.*, 2011, **6**, 534.

71. S. Spitsina and M. Kahrizi, IECON 2012 - 38th Annual Conference on IEEE Industrial Electronics Society, 2012.

72. A. Modi, N. Koratkar, E. Lass, B. Q. Wei and P. M. Ajayan, *Nature*, 2003, **424**, 171-174.

73. Q. F. Zhang, C. S. Dandeneau, X. Y. Zhou and G. Z. Cao, *Adv. Mater.*, 2009, **21**, 4087-4108.

74. A. J. Bard and M. A. Fox, *Accounts Chem. Res.*, 1995, **28**, 141-145.

75. B. D. Alexander, P. J. Kulesza, L. Rutkowska, R. Solarska and J. Augustynski, *J. Mater. Chem.*, 2008, **18**, 2298-2303.

76. C. J. Lin, S. Y. Chen and Y. H. Liou, *Electrochem. Commun.*, 2010, **12**, 1513-1516.

77. J. W. Miao, H. B. Yang, S. Y. Khoo and B. Liu, *Nanoscale*, 2013, **5**, 11118-11124.

78. X. Yang, A. Wolcott, G. Wang, A. Sobo, R. C. Fitzmorris, F. Qian, J. Z. Zhang and Y. Li, *Nano Lett.*, 2009, **9**, 2331-2336.

79. C. K. Chen, Y. P. Shen, H. M. Chen, C. J. Chen, T. S. Chan, J. F. Lee and R. S. Liu, *Eur. J. Inorg. Chem.*, 2014, **2014**, 773-779.

80. H. Pan, J. Z. Luo, H. Sun, Y. P. Feng, C. K. Poh and J. Y. Lin, *Nanotechnology*, 2006, **17**, 2963-2967.

81. Q. Wan, C. L. Lin, X. B. Yu and T. H. Wang, *Appl. Phys. Lett.*, 2004, **84**, 124-126.

82. Z. Y. Liu, X. T. Zhang, S. Nishimoto, M. Jin, D. A. Tryk, T. Murakami and A. Fujishima, *Langmuir*, 2007, **23**, 10916-10919.

83. M. R. Ranade, A. Navrotsky, H. Z. Zhang, J. F. Banfield, S. H. Elder, A. Zaban, P. H. Borse, S. K. Kulkarni, G. S. Doran and H. J. Whitfield, *P. Natl. Acad. Sci. USA*, 2002, **99**, 6476-6481.

84. H. Z. Zhang and J. F. Banfield, *J. Phys. Chem. B*, 2000, **104**, 3481-3487.

85. D. O. Scanlon, C. W. Dunnill, J. Buckeridge, S. A. Shevlin, A. J. Logsdail, S. M. Woodley, C. R. A. Catlow, M. J. Powell, R. G. Palgrave, I. P. Parkin, G. W. Watson, T. W. Keal, P. Sherwood, A. Walsh and A. A. Sokol, *Nat. Mater.*, 2013, **12**, 798-801.

86. A. Fujishima, X. T. Zhang and D. A. Tryk, *Surf. Sci. Rep.*, 2008, **63**, 515-582.

87. K. Pan, Y. Z. Dong, W. Zhou, Q. J. Pan, Y. Xie, T. F. Xie, G. H. Tian and G. F. Wang, *ACS Appl. Mater. Interfaces*, 2013, **5**, 8314-8320.

88. A. Mazzarolo, K. Lee, A. Vicenzo and P. Schmuki, *Electrochem. Commun.*, 2012, **22**, 162-165.

89. G. M. Wang, H. Y. Wang, Y. C. Ling, Y. C. Tang, X. Y. Yang, R. C. Fitzmorris, C. C. Wang, J. Z. Zhang and Y. Li, *Nano Lett.*, 2011, **11**, 3026-3033.

90. J. Yang, S. Mei and J. M. F. Ferreira, *Mat. Sci. Eng. C-Bio. S.*, 2001, **15**, 183-185.

91. X. Chen and S. S. Mao, *Chem. Rev.*, 2007, **107**, 2891-2959.

92. H. H. Ou and S. L. Lo, *Sep. Purif. Technol.*, 2007, **58**, 179-191.

93. W. Q. Wu, Y. F. Xu, C. Y. Su and D. B. Kuang, *Energ. Environ. Sci.*, 2014, **7**, 644-649.

94. Z. Zhao, H. Q. Tan, H. F. Zhao, Y. Lv, L. J. Zhou, Y. J. Song and Z. C. Sun, *Chem. Commun.*, 2014, **50**, 2755-2757.

95. U. Bach, D. Lupo, P. Comte, J. E. Moser, F. Weissortel, J. Salbeck, H. Spreitzer and M. Gratzel, *Nature*, 1998, **395**, 583-585.

96. S. S. Watson, D. Beydoun, J. A. Scott and R. Amal, *Chem. Eng. J.*, 2003, **95**, 213-220.

97. D. Gong, C. A. Grimes, O. K. Varghese, W. C. Hu, R. S. Singh, Z. Chen and E. C. Dickey, *J. Mater. Res.*, 2001, **16**, 3331-3334.

98. Z. T. Y. Al-Abdullah, Y. Y. Shin, R. Kler, C. C. Perry, W. Z. Zhou and Q. Chen, *Nanotechnology*, 2010, **21**, 505601.

99. M. Paulose, K. Shankar, S. Yoriya, H. E. Prakasam, O. K. Varghese, G. K. Mor, T. A. Latempa, A. Fitzgerald and C. A. Grimes, *J. Phys. Chem. B*, 2006, **110**, 16179-16184.

100. G. K. Mor, O. K. Varghese, M. Paulose, K. Shankar and C. A. Grimes, *Sol. Energ. Mat. Sol. C.*, 2006, **90**, 2011-2075.

101. J. Zeleny, *Phys. Rev.*, 1914, **3**, 69-91.

102. J. S. Bedi, D. W. Lester, Y. X. Fang, J. F. C. Turner, J. Zhou, S. M. Alfadul, C. Perry and Q. Chen, *J. Polym. Eng.*, 2013, **33**, 453-461.

103. S. Cavaliere, S. Subianto, I. Savych, D. J. Jones and J. Roziere, *Energ. Environ. Sci.*, 2011, **4**, 4761-4785.

104. N. Bhardwaj and S. C. Kundu, *Biotechnol. Adv.*, 2010, **28**, 325-347.

105. Y. Q. Dai, C. M. Cobley, J. Zeng, Y. M. Sun and Y. N. Xia, *Nano Lett.*, 2009, **9**, 2455-2459.

106. A. Fujishima and K. Honda, *Nature*, 1972, **238**, 37-38.

107. H. J. Wu and Z. H. Zhang, *J. Solid State Chem.*, 2011, **184**, 3202-3207.

108. H. X. Li, Z. F. Bian, J. Zhu, D. Q. Zhang, G. S. Li, Y. N. Huo, H. Li and Y. F. Lu, *J. Am. Chem. Soc.*, 2007, **129**, 8406-8407.

109. H. I. Kim, D. Monllor-Satoca, W. Kim and W. Choi, *Energ. Environ. Sci.*, 2015, **8**, 247-257.

110. M. Xu, P. M. Da, H. Y. Wu, D. Y. Zhao and G. F. Zheng, *Nano Lett.*, 2012, **12**, 1503-1508.

111. B. Oregan and M. Gratzel, *Nature*, 1991, **353**, 737-740.

112. I. Robel, V. Subramanian, M. Kuno and P. V. Kamat, *J. Am. Chem. Soc.*, 2006, **128**, 2385-2393.

113. K. Y. Li, S. Y. C. Liu, C. P. Huang, S. Esariyaumpai and D. H. Chen, *J. Adv. Oxid. Technol.*, 2002, **5**, 227-232.

114. D. Losic and S. Simovic, *Expert Opin. Drug Del.*, 2009, **6**, 1363-1381.

115. J. J. Wykrzykowska, Y. Onuma and P. W. Serruys, *Expert Opin. Drug Del.*, 2009, **6**, 113-126.

116. K. C. Popat, M. Eltgroth, T. J. La Tempa, C. A. Grimes and T. A. Desai, *Small*, 2007, **3**, 1878-1881.

117. F. Schmidt-Stein, R. Hahn, J. F. Gnichwitz, Y. Y. Song, N. K. Shrestha, A. Hirsch and P. Schmuki, *Electrochem. Commun.*, 2009, **11**, 2077-2080.

118. Y. Y. Song, F. Schmidt-Stein, S. Bauer and P. Schmuki, *J. Am. Chem. Soc.*, 2009, **131**, 4230-4232.

119. A. Fujishima, T. N. Rao and D. A. Tryk, *J. Photoch. Photobio. C*, 2000, **1**, 1-21.

120. R. X. Cai, Y. Kubota, T. Shuin, H. Sakai, K. Hashimoto and A. Fujishima, *Cancer Res.*, 1992, **52**, 2346-2348.

121. Y. Park, K. J. McDonald and K. S. Choi, *Chem. Soc. Rev.*, 2013, **42**, 2321-2337.

122. A. Kudo, K. Omori and H. Kato, *J. Am. Chem. Soc.*, 1999, **121**, 11459-11467.

123. Z. F. Huang, L. Pan, J. J. Zou, X. W. Zhang and L. Wang, *Nanoscale*, 2014, **6**, 14044-14063.

124. S. Gu, W. Li, F. Wang, S. Wang, H. Zhou and H. Li, *Appl. Catal. B-Environ.*, 2015, **170**, 186-194.

125. K. P. S. Parmar, H. J. Kang, A. Bist, P. Dua, J. S. Jang and J. S. Lee, *ChemSusChem*, 2012, **5**, 1926-1934.

126. Y. Q. Ying, F. F. Tao, T. J. Hong and L. X. Wang, *Mater. Sci. Semicond. Process.*, 2015, **32**, 82-89.

127. X. Wang, H. Liu, J. Wang, L. Chang, N. Song, Z. Yan and X. Wan, *Res. Chem. Intermed.*, 2015, **41**, 2465-2477.

128. N. Myung, S. Ham, S. Choi, Y. Chae, W. G. Kim, Y. J. Jeon, K. J. Paeng, W. Chanmanee, N. R. de Tacconi and K. Rajeshwar, *J. Phys. Chem. C*, 2011, **115**, 7793-7800.

129. J. A. Seabold and K. S. Choi, *J. Am. Chem. Soc.*, 2012, **134**, 2186-2192.

130. W. J. Luo, Z. S. Yang, Z. S. Li, J. Y. Zhang, J. G. Liu, Z. Y. Zhao, Z. Q. Wang, S. C. Yan, T. Yu and Z. G. Zou, *Energ. Environ. Sci.*, 2011, **4**, 4046-4051.

131. K. Sayama, A. Nomura, Z. G. Zou, R. Abe, Y. Abe and H. Arakawa, *Chem. Commun.*, 2003, 2908-2909.

132. D. K. Zhong, S. Choi and D. R. Gamelin, *J. Am. Chem. Soc.*, 2011, **133**, 18370-18377.

133. S. P. Berglund, D. W. Flaherty, N. T. Hahn, A. J. Bard and C. B. Mullins, *J. Phys. Chem. C*, 2011, **115**, 3794-3802.

134. S. P. Berglund, A. J. E. Rettie, S. Hoang and C. B. Mullins, *Phys. Chem. Chem. Phys.*, 2012, **14**, 7065-7075.

135. H. M. Fan, T. F. Jiang, H. Y. Li, D. J. Wang, L. L. Wang, J. L. Zhai, D. Q. He, P. Wang and T. F. Xie, *J. Phys. Chem. C*, 2012, **116**, 2425-2430.

136. P. Bornoz, F. F. Abdi, S. D. Tilley, B. Dam, R. van de Krol, M. Graetzel and K. Sivula, *J. Phys. Chem. C*, 2014, **118**, 16959-16966.

137. M. D. Hernandez-Alonso, F. Fresno, S. Suarez and J. M. Coronado, *Energ. Environ. Sci.*, 2009, **2**, 1231-1257.

138. W. Ma, Z. Li and W. Liu, *Ceram. Int.*, 2015, **41**, 4340-4347.

139. K. Ji, J. Deng, H. Zang, J. Han, H. Arandiyan and H. Dai, *Appl. Catal. B-Environ.*, 2015, **165**, 285-295.

140. S. Kohtani, M. Tomohiro, K. Tokumura and R. Nakagaki, *Appl. Catal. B-Environ.*, 2005, **58**, 265-272.

141. M. Gratzel, *Nature*, 2001, **414**, 338-344.

142. X. B. Chen, S. H. Shen, L. J. Guo and S. S. Mao, *Chem. Rev.*, 2010, **110**, 6503-6570.

143. S. T. Nishanthi, B. Sundarakannan, E. Subramanian and D. P. Padiyan, *Renew. Energ.*, 2015, **77**, 300-307.

144. A. Zuttel, A. Remhof, A. Borgschulte and O. Friedrichs, *Philos. T. R. Soc. A*, 2010, **368**, 3329-3342.

145. M. G. Walter, E. L. Warren, J. R. McKone, S. W. Boettcher, Q. X. Mi, E. A. Santori and N. S. Lewis, *Chem. Rev.*, 2010, **110**, 6446-6473.

146. M. H. Lee, K. Takei, J. J. Zhang, R. Kapadia, M. Zheng, Y. Z. Chen, J. Nah, T. S. Matthews, Y. L. Chueh, J. W. Ager and A. Javey, *Angew. Chem. Int. Edit.*, 2012, **51**, 10760-10764.

147. J. S. Luo, J. H. Im, M. T. Mayer, M. Schreier, M. K. Nazeeruddin, N. G. Park, S. D. Tilley, H. J. Fan and M. Gratzel, *Science*, 2014, **345**, 1593-1596.

148. C. R. Jiang, S. J. A. Moniz, M. Khraisheh and J. W. Tang, *Chem. Eur. J.*, 2014, **20**, 12954-12961.

149. Y. Wang and J. T. W. Yeow, *J. Sensors*, 2009, **2009**, 493904.

150. Z. Y. Li, H. N. Zhang, W. Zheng, W. Wang, H. M. Huang, C. Wang, A. G. MacDiarmid and Y. Wei, *J. Am. Chem. Soc.*, 2008, **130**, 5036-5037.

151. J. Zhang, S. R. Wang, M. J. Xu, Y. Wang, B. L. Zhu, S. M. Zhang, W. P. Huang and S. H. Wu, *Cryst. Growth Des.*, 2009, **9**, 3532-3537.

152. Y. S. Kim, S. C. Ha, K. Kim, H. Yang, S. Y. Choi, Y. T. Kim, J. T. Park, C. H. Lee, J. Choi, J. Paek and K. Lee, *Appl. Phys. Lett.*, 2005, **86**, 213105.

153. Q. Y. Hao, S. A. Liu, X. M. Yin, Z. F. Du, M. Zhang, L. M. Li, Y. G. Wang, T. H. Wang and Q. H. Li, *CrystEngComm*, 2011, **13**, 806-812.

154. D. H. Zhang, Z. Q. Liu, C. Li, T. Tang, X. L. Liu, S. Han, B. Lei and C. W. Zhou, *Nano Lett.*, 2004, **4**, 1919-1924.

155. S. J. Kim, S. H. Lee and C. J. Lee, *J. Phys. D Appl. Phys.*, 2001, **34**, 3505-3509.

156. P. G. Collins, K. Bradley, M. Ishigami and A. Zettl, *Science*, 2000, **287**, 1801-1804.

157. L. Liao, H. B. Lu, J. C. Li, H. He, D. F. Wang, D. J. Fu, C. Liu and W. F. Zhang, *J. Phys. Chem. C*, 2007, **111**, 1900-1903.

158. L. Liao, H. B. Lu, J. C. Li, C. Liu, D. J. Fu and Y. L. Liu, *Appl. Phys. Lett.*, 2007, **91**, 173110.

159. C. Li, C. H. Feng, F. D. Qu, J. Liu, L. H. Zhu, Y. Lin, Y. Wang, F. Li, J. R. Zhou and S. P. Ruan, *Sensor. Actuat. B-Chem.*, 2015, **207**, 90-96.

160. C. Baratto, R. Kumar, G. Faglia, K. Vojisavljevic and B. Malic, *Sensor. Actuat. B-Chem.*, 2015, **209**, 287-296.

161. S. W. Choi, A. Katoch, J. H. Kim and S. S. Kim, *J. Mater. Chem. C*, 2015, **3**, 1521-1527.

162. S. Lakkis, R. Younes, Y. Alayli and M. Sawan, *Sensor Rev.*, 2014, **34**, 24-35.

163. S. J. Gentry and T. A. Jones, *Sensor. Actuator.*, 1986, **10**, 141-163.

164. R. Mohammadpour, H. Ahmadvand and A. I. Zad, *Sensor. Actuat. A-Phys.*, 2014, **216**, 202-206.

165. A. Nikfarjam, R. Mohammadpour and A. I. Zad, *Appl. Phys. A-Mater.*, 2014, **115**, 1387-1393.

166. R. Banan Sadeghian and M. Saif Islam, *Nat. Mater.*, 2011, **10**, 135-140.

167. M. B. Fang, X. L. Zhao, J. H. Li, Z. Wang, Y. F. Wang and Z. Y. Hou, *Appl. Mech. Mater.*, 2014, **551**, 460-465.

168. C. L. Hsu and Y. C. Tsai, *IEEE T. Nanotechnol.*, 2012, **11**, 1110-1116.

169. D. McMullan, *Scanning*, 1995, **17**, 175-185.

170. J. Goldstein, *Scanning Electron Microscopy and X-ray Microanalysis : A Text for Biologists, Materials Scientists, and Geologists*, Plenum Press, New York, 1981.

171. Zacharia.Wh, *Acta Crystallogr.*, 1967, **23**, 558-564.

172. W. H. Bragg, *P. R. Soc. Lond. A-Conta.*, 1914, **89**, 575-580.

173. S. M. Ramay, S. Atiq, M. Saleem, A. Mahmood, S. A. Siddiqi, S. Naseem, Y. Al-Zeghayer, N. S. Alzayed and M. Shahabuddin, *J. Nanomater.*, 2014, **2014**, 452468.

174. D. I. Rusu, G. G. Rusu and D. Luca, *Acta Phys. Pol. A*, 2011, **119**, 850-856.

175. G. I. N. Waterhouse and M. R. Waterland, *Polyhedron*, 2007, **26**, 356-368.

176. Y. Kajikawa, S. Noda and H. Komiyama, *Chem. Vapor Depos.*, 2002, **8**, 99-104.

177. D. F. Swinehart, *J. Chem. Educ.*, 1962, **39**, 333-335.

178. A. A. Tahir, M. A. Ehsan, M. Mazhar, K. G. U. Wijayantha, M. Zeller and A. D. Hunter, *Chem. Mater.*, 2010, **22**, 5084-5092.

179. L. Miao, P. Jin, K. Kaneko, A. Terai, N. Nabatova-Gabain and S. Tanemura, *Appl. Surf. Sci.*, 2003, **212**, 255-263.

180. J. Tauc, *Amorphous and Liquid Semiconductors*, Plenum, London, New York,, 1974.

181. A. B. Murphy, *Sol. Energ. Mat. Sol. C.*, 2007, **91**, 1326-1337.

182. P. Sharma, I. Sharma and S. C. Katyal, *J. Appl. Phys.*, 2009, **105**, 053509.

183. D. B. Buchholz, J. Liu, T. J. Marks, M. Zhang and R. P. H. Chang, *ACS Appl. Mater. Interfaces*, 2009, **1**, 2147-2153.

184. J. Tauc, Grigorov.R and A. Vancu, *Phys. Status Solidi*, 1966, **15**, 627-637.

185. S. J. Ikhmayies and R. N. Ahmad-Bitar, *J. Mater. Sci. Technol.*, 2013, **2**, 221-227.

186. S. John, C. Soukoulis, M. H. Cohen and E. N. Economou, *Phys. Rev. Lett.*, 1986, **57**, 1777-1780.

187. S. Ilican, *J. Alloy. Compd.*, 2013, **553**, 225-232.

188. P. M. Gomadam and J. W. Weidner, *Int. J. Energ. Res.*, 2005, **29**, 1133-1151.

189. E. Barsoukov and J. R. Macdonald, *Impedance Spectroscopy: Theory, Experiment, and Applications*, 2nd edn., Wiley, 2005.

190. G. Garcia-Belmonte, A. Munar, E. M. Barea, J. Bisquert, I. Ugarte and R. Pacios, *Org. Electron.*, 2008, **9**, 847-851.

191. K. Gelderman, L. Lee and S. W. Donne, *J. Chem. Educ.*, 2007, **84**, 685-688.

192. L. X. Sang, H. Y. Tan, X. M. Zhang, Y. T. Wu, C. F. Ma and C. Burda, *J. Phys. Chem. C*, 2012, **116**, 18633-18640.

193. F. X. Xiao, F. C. Wang, X. Z. Fu and Y. Zheng, *J. Mater. Chem.*, 2012, **22**, 2868-2877.

194. M. Wang, F. Ren, G. X. Cai, Y. C. Liu, S. H. Shen and L. J. Guo, *Nano Res.*, 2014, **7**, 353-364.

195. W. Schottky, *Z. Phys.*, 1942, **118**, 539-592.

196. R. Krishnan, in *Encyclopedia of Electrochemistry*, Wiley-VCH Verlag GmbH & Co. KGaA, 2007.

197. F. K. Meng, J. T. Li, S. K. Cushing, J. Bright, M. J. Zhi, J. D. Rowley, Z. L. Hong, A. Manivannan, A. D. Bristow and N. Q. Wu, *ACS Catal.*, 2013, **3**, 746-751.

198. R. Saito, Y. Miseki and K. Sayama, *Chem. Commun.*, 2012, **48**, 3833-3835.

199. N. de Jonge, Y. Lamy, K. Schoots and T. H. Oosterkamp, *Nature*, 2002, **420**, 393-395.

200. H. J. Fan, P. Werner and M. Zacharias, *Small*, 2006, **2**, 700-717.

201. J. R. Huang, J. H. Wang, C. P. Gu, K. Yu, F. L. Meng and J. H. Liu, *Sensor. Actuat. A-Phys.*, 2009, **150**, 218-223.

202. H. Ko, S. Park, S. Park and C. Lee, *J. Nanosci. Nanotechno.*, 2015, **15**, 5295-5300.

203. M. Nath and C. N. R. Rao, *J. Am. Chem. Soc.*, 2001, **123**, 4841-4842.

204. Y. Sun, G. M. Fuge, N. A. Fox, D. J. Riley and M. N. R. Ashfold, *Adv. Mater.*, 2005, **17**, 2477-2481.

205. H. Q. Hou, A. K. Schaper, Z. Jun, F. Weller and A. Greiner, *Chem. Mater.*, 2003, **15**, 580-585.

206. V. Bajpai, L. M. Dai and T. Ohashi, *J. Am. Chem. Soc.*, 2004, **126**, 5070-5071.

207. X. J. Zheng, D. Q. Yu, F. Q. Xiong, M. R. Li, Z. Yang, J. Zhu, W. H. Zhang and C. Li, *Chem. Commun.*, 2014, **50**, 4364-4367.

208. G. L. Chai, L. J. Zhou, C. S. Lin, Y. Yang and W. D. Cheng, *Chem. Phys. Lett.*, 2012, **529**, 49-53.

209. L. L. Yang, Z. Q. Zhang, J. H. Yang, Y. S. Yan, Y. F. Sun, J. Cao, M. Gao, M. B. Wei, J. H. Lang, F. Z. Liu and Z. Wang, *J. Alloy. Compd.*, 2012, **543**, 58-64.

210. J. Elias, J. Michler, L. Philippe, M. Y. Lin, C. Couteau, G. Lerondel and C. Levy-Clement, *J. Electron. Mater.*, 2011, **40**, 728-732.

211. C. Pholnak, C. Sirisathitkul, D. J. Harding and S. Suwanboon, *J. Ceram. Soc. Jpn.*, 2011, **119**, 535-537.

212. Y. H. Chang, S. M. Wang, C. M. Liu and C. Chen, *J. Electrochem. Soc.*, 2010, **157**, K236-K241.

213. Y. Xi, J. Song, S. Xu, R. Yang, Z. Gao, C. Hu and Z. L. Wang, *J. Mater. Chem.*, 2009, **19**, 9260-9264.

214. J. Elias, R. Tena-Zaera, G. Y. Wang and C. Levy-Clement, *Chem. Mater.*, 2008, **20**, 6633-6637.

215. A. Wei, X. W. Sun, C. X. Xu, Z. L. Dong, Y. Yang, S. T. Tan and W. Huang, *Nanotechnology*, 2006, **17**, 1740-1744.

216. K. K. Yang, C. K. Xu, L. W. Huang, L. F. Zou and H. Wang, *Nanotechnology*, 2011, **22**, 405401.

217. M. Lennox and S. Coulombe, *J. Nanopart. Res.*, 2012, **14**, 1245.

218. J. J. Wu, S. C. Liu, C. T. Wu, K. H. Chen and L. C. Chen, *Appl. Phys. Lett.*, 2002, **81**, 1312-1314.

219. C. Y. Yao, G. J. Chen and T. Y. Tseng, *J. Nanosci. Nanotechno.*, 2008, **8**, 4432-4435.

220. K. Itabashi, H. Tabata, W. Wongwiriyapan, S. Minami, K. Matsushita, R. Shimazaki, T. Ueda, T. Ito and M. Katayama, *Jpn. J. Appl. Phys.*, 2012, **51**, 055104.

221. Y. G. Yan, L. X. Zhou, J. Zhang, S. Q. Hu and S. Q. Sun, *J. Mater. Res.*, 2013, **28**, 897-904.

222. K. M. McPeak, M. A. Becker, N. G. Britton, H. Majidi, B. A. Bunker and J. B. Baxter, *Chem. Mater.*, 2010, **22**, 6162-6170.

223. R. D. Deegan, *Phys. Rev. E*, 2000, **61**, 475-485.

224. R. D. Deegan, O. Bakajin, T. F. Dupont, G. Huber, S. R. Nagel and T. A. Witten, *Nature*, 1997, **389**, 827-829.

225. A. Hasimi, A. Stavropoulou, K. G. Papadokostaki and M. Sanopoulou, *Eur. Polym. J.*, 2008, **44**, 4098-4107.

226. Z. H. Mbhele, M. G. Salemane, C. G. C. E. van Sittert, J. M. Nedeljkovic, V. Djokovic and A. S. Luyt, *Chem. Mater.*, 2003, **15**, 5019-5024.

227. B. H. Cipiriano, T. Kashiwagi, S. R. Raghavan, Y. Yang, E. A. Grulke, K. Yamamoto, J. R. Shields and J. F. Douglas, *Polymer*, 2007, **48**, 6086-6096.

228. Y. K. Hsu, Y. G. Lin and Y. C. Chen, *Electrochem. Commun.*, 2011, **13**, 1383-1386.

229. J. F. Muth, R. M. Kolbas, A. K. Sharma, S. Oktyabrsky and J. Narayan, *J. Appl. Phys.*, 1999, **85**, 7884-7887.

230. Y. I. Alivov, B. Xiao, S. Akarca-Biyikli, Q. Fan, H. Morkoc, D. Johnstone, O. Lopatiuk-Tirpak, L. Chernyak and W. Litton, *J. Phys.-Condens. Mat.*, 2008, **20**, 085201.

231. M. H. Kumar, N. Yantara, S. Dharani, M. Graetzel, S. Mhaisalkar, P. P. Boix and N. Mathews, *Chem. Commun.*, 2013, **49**, 11089-11091.

232. P. Thiyagarajan, H. J. Ahn, J. S. Lee, J. C. Yoon and J. H. Jang, *Small*, 2013, **9**, 2341-2347.

233. J. J. Tian, Q. F. Zhang, E. Uchaker, R. Gao, X. H. Qu, S. E. Zhang and G. Z. Cao, *Energ. Environ. Sci.*, 2013, **6**, 3542-3547.

234. S. S. Kalanur, Y. J. Hwang, S. Y. Chae and O. S. Joo, *J. Mater. Chem. A*, 2013, **1**, 3479-3488.

235. T. Nakajima, K. Shinoda and T. Tsuchiya, *Chem. Soc. Rev.*, 2014, **43**, 2027-2041.

236. J. Goldberger, R. R. He, Y. F. Zhang, S. W. Lee, H. Q. Yan, H. J. Choi and P. D. Yang, *Nature*, 2003, **422**, 599-602.

237. X. Qi, G. She, M. Wang, L. Mu and W. Shi, *Chem. Commun. (Camb.)*, 2013, **49**, 5742-5744.

238. Z. H. Zhang, L. B. Zhang, M. N. Hedhili, H. N. Zhang and P. Wang, *Nano Lett.*, 2013, **13**, 14-20.

239. Z. H. Zhang and P. Wang, *Energ. Environ. Sci.*, 2012, **5**, 6506-6512.

240. S. Xu and Z. L. Wang, *Nano Res.*, 2011, **4**, 1013-1098.

241. Z. H. Zhang, M. F. Hossain and T. Takahashi, *Int. J. Hydrogen Energ.*, 2010, **35**, 8528-8535.

242. S. Mathew, A. Yella, P. Gao, R. Humphry-Baker, B. F. Curchod, N. Ashari-Astani, I. Tavernelli, U. Rothlisberger, M. K. Nazeeruddin and M. Gratzel, *Nat. Chem.*, 2014, **6**, 242-247.

243. K. S. Ahn, S. Shet, T. Deutsch, C. S. Jiang, Y. F. Yan, M. Al-Jassim and J. Turner, *J. Power Sources*, 2008, **176**, 387-392.

244. G. Marci, V. Augugliaro, M. J. Lopez-Munoz, C. Martin, L. Palmisano, V. Rives, M. Schiavello, R. J. D. Tilley and A. M. Venezia, *J. Phys. Chem. B*, 2001, **105**, 1026-1032.

245. C. W. Cheng, H. F. Zhang, W. N. Ren, W. J. Dong and Y. Sun, *Nano Energy*, 2013, **2**, 779-786.

246. L. Kavan, M. Gratzel, S. E. Gilbert, C. Klemenz and H. J. Scheel, *J. Am. Chem. Soc.*, 1996, **118**, 6716-6723.

247. Z. Cai, J. Li and Y. Wang, *J. Alloy. Compd.*, 2010, **489**, 167-169.

248. N. T. Nolan, M. K. Seery and S. C. Pillai, *Chem. Mater.*, 2011, **23**, 1496-1504.

249. M. Gajewska, J. Dutkiewicz and J. Morgiel, *Arch. Metall. Mater.*, 2013, **58**, 433-436.

250. D. A. H. Hanaor and C. C. Sorrell, *J. Mater. Sci.*, 2011, **46**, 855-874.

251. J. F. Porter, Y. G. Li and C. K. Chan, *J. Mater. Sci.*, 1999, **34**, 1523-1531.

252. H. Cai, Q. H. You, Z. G. Hu, Z. H. Duan, Y. Cui, J. Sun, N. Xu and J. D. Wu, *Sol. Energ. Mat. Sol. C.*, 2014, **123**, 233-238.

253. E. M. P. Steinmiller and K. S. Choi, *P. Natl. Acad. Sci. USA*, 2009, **106**, 20633-20636.

254. S. Hernandez, D. Hidalgo, A. Sacco, A. Chiodoni, A. Lamberti, V. Cauda, E. Tresso and G. Saracco, *Phys. Chem. Chem. Phys.*, 2015, **17**, 7775-7786.

255. Z. D. Li, C. H. Yao, Y. H. Yu, Z. Y. Cai and X. D. Wang, *Adv. Mater.*, 2014, **26**, 2262-2267.

256. J. T. Li, S. K. Cushing, P. Zheng, F. K. Meng, D. Chu and N. Q. Wu, *Nat. Commun.*, 2013, **4**, 2651.

257. D. Tafalla, P. Salvador and R. M. Benito, *J. Electrochem. Soc.*, 1990, **137**, 1810-1815.

258. J. Elias, M. Bechelany, I. Utke, R. Erni, D. Hosseini, J. Michler and L. Philippe, *Nano Energy*, 2012, **1**, 696-705.

259. R. H. Tao, J. M. Wu, J. Z. Xiao, Y. P. Zhao, W. W. Dong and X. D. Fang, *Appl. Surf. Sci.*, 2013, **279**, 324-328.

260. W. Lee, S. H. Kang, J. Y. Kim, G. B. Kolekar, Y. E. Sung and S. H. Han, *Nanotechnology*, 2009, **20**, 335706.

261. S. Huang, W. J. Luo and Z. G. Zou, *J. Phys. D Appl. Phys.*, 2013, **46**, 235108.

262. J. S. Jang, P. H. Borse, J. S. Lee, K. T. Lim, O. S. Jung, E. D. Jeong, J. S. Bae, M. S. Won and H. G. Kim, *B. Korean Chem. Soc.*, 2009, **30**, 3021-3024.

263. M. Razavy, *Quantum Theory of Tunneling*, World Scientific, River Edge, NJ, 2003.

264. J. C. Vickerman, *Surface analysis: the principal techniques*, Wiley, Chichester, 1997.

265. Y.-G. Lin, Y.-K. Hsu, Y.-C. Chen, B.-W. Lee, J.-S. Hwang, L.-C. Chen and K.-H. Chen, *ChemSusChem*, 2014, **7**, 2748-2754.

266. H. M. Chen, C. K. Chen, Y. C. Chang, C. W. Tsai, R. S. Liu, S. F. Hu, W. S. Chang and K. H. Chen, *Angew. Chem. Int. Edit.*, 2010, **49**, 5966-5969.

267. K. Sivula, F. Le Formal and M. Gratzel, *ChemSusChem*, 2011, **4**, 432-449.

268. R. Liu, Y. J. Lin, L. Y. Chou, S. W. Sheehan, W. S. He, F. Zhang, H. J. M. Hou and D. W. Wang, *Angew. Chem. Int. Edit.*, 2011, **50**, 499-502.

269. Y.-G. Lin, Y.-K. Hsu, Y.-C. Chen, S.-B. Wang, J. T. Miller, L.-C. Chen and K.-H. Chen, *Energ. Environ. Sci.*, 2012, **5**, 8917-8922.

270. Y. H. Lu, W. H. Lin, C. Y. Yang, Y. H. Chiu, Y. C. Pu, M. H. Lee, Y. C. Tseng and Y. J. Hsu, *Nanoscale*, 2014, **6**, 8796-8803.

271. K. J. Kim and Y. R. Park, *Appl. Phys. Lett.*, 2002, **81**, 1420-1422.

272. V. Bharathi, M. Sivakumar, R. Udayabhaskar, H. Takebe and B. Karthikeyan, *Appl. Phys. A-Mater.*, 2014, **116**, 395-401.

273. B. Panigrahy, M. Aslam and D. Bahadur, *J. Phys. Chem. C*, 2010, **114**, 11758-11763.

274. Q. J. Yu, W. Y. Fu, C. L. Yu, H. B. Yang, R. H. Wei, Y. M. Sui, S. K. Liu, Z. L. Liu, M. H. Li, G. R. Wang, C. L. Shao, Y. H. Liu and G. T. Zou, *J. Phys. D Appl. Phys.*, 2007, **40**, 5592-5597.

275. F. Wang, J.-H. Seo, Z. Li, A. V. Kvit, Z. Ma and X. Wang, *ACS Appl. Mater. Interfaces*, 2014, **6**, 1288-1293.

276. M. Anusha and D. Arivuoli, *J. Alloy. Compd.*, 2013, **580**, 131-136.

277. W. J. Sheng, B. Sun, T. L. Shi, X. H. Tan, Z. C. Peng and G. L. Liao, *ACS Nano*, 2014, **8**, 7163-7169.

278. Z. W. Jin, T. Fukumura, M. Kawasaki, K. Ando, H. Saito, T. Sekiguchi, Y. Z. Yoo, M. Murakami, Y. Matsumoto, T. Hasegawa and H. Koinuma, *Appl. Phys. Lett.*, 2001, **78**, 3824-3826.

279. J. Joo, B. Y. Chow, M. Prakash, E. S. Boyden and J. M. Jacobson, *Nat. Mater.*, 2011, **10**, 596-601.

280. N. P. Dasgupta, J. W. Sun, C. Liu, S. Brittman, S. C. Andrews, J. Lim, H. W. Gao, R. X. Yan and P. D. Yang, *Adv. Mater.*, 2014, **26**, 2137-2184.

281. Z. R. R. Tian, J. A. Voigt, J. Liu, B. McKenzie, M. J. McDermott, M. A. Rodriguez, H. Konishi and H. F. Xu, *Nat. Mater.*, 2003, **2**, 821-826.

282. B. J. Boyle, E. G. King and K. C. Conway, *J. Am. Chem. Soc.*, 1954, **76**, 3835-3837.

283. R. D. Shannon, *Acta Crystallogr. A*, 1976, **32**, 751-767.

284. Z. W. Qiu, X. P. Yang, J. Han, P. Zhang, B. Q. Cao, Z. F. Dai, G. T. Duan and W. P. Cai, *J. Am. Ceram. Soc.*, 2014, **97**, 2177-2184.

285. C. W. Liu, S. J. Chang, C. H. Hsiao, K. Y. Lo, T. H. Kao, B. C. Wang, S. J. Young, K. S. Tsai and S. L. Wu, *IEEE J. Sel. Top. Quant.*, 2014, **20**, 3800707.

286. S. H. Chiu and J. C. A. Huang, *J. Non-Cryst. Solids*, 2012, **358**, 2453-2457.

287. P. Y. Ma, Y. Wu, Z. Y. Fu and W. M. Wang, *Adv. Mater. Res.*, 2011, **328-330**, 1198-1201.

288. T. Fukumura, Z. W. Jin, A. Ohtomo, H. Koinuma and M. Kawasaki, *Appl. Phys. Lett.*, 1999, **75**, 3366-3368.

289. D. Y. Inamdar, A. D. Lad, A. K. Pathak, I. Dubenko, N. Ali and S. Mahamuni, *J. Phys. Chem. C*, 2010, **114**, 1451-1459.

290. Z. B. Chen, T. F. Jaramillo, T. G. Deutsch, A. Kleiman-Shwarsctein, A. J. Forman, N. Gaillard, R. Garland, K. Takanabe, C. Heske, M. Sunkara, E. W. McFarland, K. Domen, E. L. Miller, J. A. Turner and H. N. Dinh, *J. Mater. Res.*, 2010, **25**, 3-16.

291. I. Mora-Sero, F. Fabregat-Santiago, B. Denier, J. Bisquert, R. Tena-Zaera, J. Elias and C. Levy-Clement, *Appl. Phys. Lett.*, 2006, **89**, 203117.

292. Z. G. Zou, J. H. Ye, K. Sayama and H. Arakawa, *Nature*, 2001, **414**, 625-627.

293. W. C. Lee, Y. X. Fang, R. Kler, G. E. Canciani, T. C. Draper, Z. T. Y. Al-Abdullah, S. M. Alfadul, C. C. Perry, H. Y. He and Q. Chen, *Mater. Chem. Phys.*, 2015, **149-150**, 12-16.

294. X. Fan, F. Z. Wang, Z. Z. Chu, L. Chen, C. Zhang and D. C. Zou, *Appl. Phys. Lett.*, 2007, **90**, 073501.

295. W. X. Guo, C. Xu, X. Wang, S. H. Wang, C. F. Pan, C. J. Lin and Z. L. Wang, *J. Am. Chem. Soc.*, 2012, **134**, 4437-4441.

296. Z. Y. Liu and M. Misra, *ACS Nano*, 2010, **4**, 2196-2200.

297. H. Dai, Y. Zhou, L. Chen, B. L. Guo, A. D. Li, J. G. Liu, T. Yu and Z. G. Zou, *Nanoscale*, 2013, **5**, 5102-5108.

298. M. R. Lee, R. D. Eckert, K. Forberich, G. Dennler, C. J. Brabec and R. A. Gaudiana, *Science*, 2009, **324**, 232-235.

299. Z. Y. Liu, Q. Q. Zhang, T. Y. Zhao, J. Zhai and L. Jiang, *J. Mater. Chem.*, 2011, **21**, 10354-10358.

300. Z. Y. Liu, V. Subramania and M. Misra, *J. Phys. Chem. C*, 2009, **113**, 14028-14033.

301. H. Dai, Y. Zhou, Q. Liu, Z. D. Li, C. X. Bao, T. Yu and Z. G. Zhou, *Nanoscale*, 2012, **4**, 5454-5460.

302. J. T. Zhang, M. He, N. Q. Fu, J. Y. Li and X. Yin, *Nanoscale*, 2014, **6**, 4211-4216.

303. C. C. Wu, L. Wei, Y. T. Li, C. Liu, J. Jiao, Y. X. Chen and L. M. Mei, *Nanoscale Res. Lett.*, 2014, **9**, 112.

304. T. Tanabe, M. Notomi, E. Kuramochi, A. Shinya and H. Taniyama, *Nat. Photonics*, 2007, **1**, 49-52.

305. C. T. Chang, C. Y. Huang, Y. R. Li and H. C. Cheng, *Sensor. Actuat. A-Phys.*, 2013, **203**, 137-141.

306. M. S. Wang, L. M. Peng, J. Y. Wang and Q. Chen, *J. Phys. Chem. B*, 2005, **109**, 110-113.

307. D. T. Richens, *The Chemistry of Aqua Ions : Synthesis, Structure, and Reactivity : A Tour Through the Periodic Table of the Elements*, J. Wiley, Chichester; New York, 1997.

308. D. W. Wu, Z. B. Huang, G. F. Yin, Y. D. Yao, X. M. Liao, D. Han, X. Huang and J. W. Gu, *CrystEngComm*, 2010, **12**, 192-198.

309. C. H. Hsu and D. H. Chen, *Nanotechnology*, 2010, **21**, 285603.

310. R. Chang and W. A. Goddard, *Surf. Sci.*, 1985, **149**, 341-348.

311. D. E. Clemmer, N. F. Dalleska and P. B. Armentrout, *J. Chem. Phys.*, 1991, **95**, 7263-7268.

312. R. Yogamalar, P. S. Venkateswaran, M. R. Benzigar, K. Ariga, A. Vinu and A. C. Bose, *J. Nanosci. Nanotechno.*, 2012, **12**, 75-83.

313. H. Vancong, S. Charar and S. Brunet, *Phys. Status Solidi B*, 1988, **147**, 253-260.

314. X. F. Han, K. Han and M. Tao, *J. Electrochem. Soc.*, 2010, **157**, H593-H597.

315. S. Heo, S. K. Sharma, S. Lee, Y. Lee, C. Kim, B. Lee, H. Lee and D. Y. Kim, *Thin Solid Films*, 2014, **558**, 27-30.

316. S. W. Fan, A. K. Srivastava and V. P. Dravid, *Appl. Phys. Lett.*, 2009, **95**, 142106.

317. S. Cho, J. W. Jang, J. Kim, J. S. Lee, W. Choi and K. H. Lee, *Langmuir*, 2011, **27**, 10243-10250.

318. Y. Xu, X. Yin, Y. Huang, P. Du and B. Zhang, *Chem. Eur. J.*, 2015, **21**, 4571-4575.

319. X. T. Wang, C. Liow, D. P. Qi, B. W. Zhu, W. R. Leow, H. Wang, C. Xue, X. D. Chen and S. Z. Li, *Adv. Mater.*, 2014, **26**, 3506-3512.

320. M. A. Holmes, T. K. Townsend and F. E. Osterloh, *Chem. Commun.*, 2012, **48**, 371-373.

321. D. Meissner, R. Memming and B. Kastening, *J. Phys. Chem.*, 1988, **92**, 3476-3483.

322. S. Emin, M. de Respinis, M. Fanetti, W. Smith, M. Valant and B. Dam, *Appl. Catal. B-Environ.*, 2015, **166**, 406-412.

323. M. Barroso, C. A. Mesa, S. R. Pendlebury, A. J. Cowan, T. Hisatomi, K. Sivula, M. Gratzel, D. R. Klug and J. R. Durrant, *P. Natl. Acad. Sci. USA*, 2012, **109**, 15640-15645.

324. F. G. Wang, C. Di Valentin and G. Pacchioni, *J. Phys. Chem. C*, 2012, **116**, 8901-8909.

325. H. J. Ahn, M. J. Kwak, J. S. Lee, K. Y. Yoon and J. H. Jang, *J. Mater. Chem. A*, 2014, **2**, 19999-20003.

326. S. J. Hong, S. Lee, J. S. Jang and J. S. Lee, *Energ. Environ. Sci.*, 2011, **4**, 1781-1787.

327. M. F. Lichterman, M. R. Shaner, S. G. Handler, B. S. Brunschwig, H. B. Gray, N. S. Lewis and J. M. Spurgeon, *J. Phys. Chem. Lett.*, 2013, **4**, 4188-4191.

328. A. B. Murphy, P. R. F. Barnes, L. K. Randeniya, I. C. Plumb, I. E. Grey, M. D. Horne and J. A. Glasscock, *Int. J. Hydrogen Energ.*, 2006, **31**, 1999-2017.

329. S. K. Pilli, T. G. Deutsch, T. E. Furtak, L. D. Brown, J. A. Turner and A. M. Herring, *Phys. Chem. Chem. Phys.*, 2013, **15**, 3273-3278.

330. M. W. Kanan and D. G. Nocera, *Science*, 2008, **321**, 1072-1075.

331. F. F. Abdi and R. van de Krol, *J. Phys. Chem. C*, 2012, **116**, 9398-9404.

332. F. F. Abdi, T. J. Savenije, M. M. May, B. Dam and R. van de Krol, *J. Phys. Chem. Lett.*, 2013, **4**, 2752-2757.

333. A. J. E. Rettie, H. C. Lee, L. G. Marshall, J. F. Lin, C. Capan, J. Lindemuth, J. S. McCloy, J. S. Zhou, A. J. Bard and C. B. Mullins, *J. Am. Chem. Soc.*, 2013, **135**, 11389-11396.

334. F. M. Li, G. W. Hsieh, S. Dalal, M. C. Newton, J. E. Stott, P. Hiralal, A. Nathan, P. A. Warburton, H. E. Unalan, P. Beecher, A. J. Flewitt, I. Robinson, G. Amaratunga and W. I. Milne, *IEEE T. Electron. Dev.*, 2008, **55**, 3001-3011.

335. E. S. Kim, H. J. Kang, G. Magesh, J. Y. Kim, J.-W. Jang and J. S. Lee, *ACS Appl. Mater. Interfaces*, 2014, **6**, 17762-17769.

336. Y. Matsumoto, *J. Solid State Chem.*, 1996, **126**, 227-234.

337. W. J. Chun, A. Ishikawa, H. Fujisawa, T. Takata, J. N. Kondo, M. Hara, M. Kawai, Y. Matsumoto and K. Domen, *J. Phys. Chem. B*, 2003, **107**, 1798-1803.

338. W. H. Leng, Z. Zhang, J. Q. Zhang and C. N. Cao, *J. Phys. Chem. B*, 2005, **109**, 15008-15023.

339. H. B. Fu, L. W. Zhang, W. Q. Yao and Y. F. Zhu, *Appl. Catal. B-Environ.*, 2006, **66**, 100-110.

340. S. J. A. Moniz, J. Zhu and J. W. Tang, *Adv. Energy Mater.*, 2014, **4**, 1301590.

341. Y. H. Yang, Y. Zhang, N. W. Wang, C. X. Wang, B. J. Li and G. W. Yang, *Nanoscale*, 2011, **3**, 592-597.